Brain microstructure mapping using quantitative and diffsusion MRI

Alice Lebois

UNIVERSITÉ PARIS-SUD

ÉCOLE DOCTORALE : Sciences et Technologie de l'Information, des Télécommunications et des Systèmes

LABORATOIRE: Unité d'Imagerie RMN et de Spectroscopie, NeuroSpin, CEA

DISCIPLINE : Physique

THÈSE DE DOCTORAT

Soutenue le 23/07/2014

par

Alice LEBOIS

Brain microstructure mapping using quantitative and diffusion MRI

Directeur de thèse :	Cyril POUPON	Directeur de Recherche (UNIRS)
Composition du jury :		
Présidente du Jury :	Petra HUPPI	Professeur (Université de Genève)
Rapporteurs :	Emmanuel BARBIER	Directeur de Recherche (Université J. F. de Grenoble)
	Christophe DESTRIEUX	Directeur de Recherche (Université F. R. de Tours)
Examinateurs :	Daniel ALEXANDER	Professeur (University College of London)
	Jean-Christophe GINEFRI	Maître de Conférence (Université Paris Sud)
Membres invités :	Denis LE BIHAN	Directeur (NeuroSpin/CEA)
	Jean-François MANGIN	Directeur de Recherche (NeuroSpin/CEA)

Acknowledgements

Je tiens tout d'abord à remercier mon directeur de thèse, Cyril Poupon qui a su m'encourager et me faire confiance tout au long de ma thèse : merci pour ton optimisme, ta gentillesse et ton aide dans les moments difficiles.

Je remercie également tous les membres du jury, Drs Emmanuel Barbier et Christophe Destrieux pour l'intérêt qu'ils ont porté à mon mémoire de thèse et leurs remarques constructives sur mon sujet, Drs Daniel Alexander, Petra Hüppi et Jean-Christophe Ginefri, pour avoir accepté de faire partie de ce jury et d'avoir fait le déplacement pour ma soutenance. Je remercie enfin Drs Denis Le Bihan et Jean-François Mangin pour avoir accepté mon invitation à cette soutenance. Merci à tout mon jury pour les questions et discussions lors de ma soutenance.

Je voudrais remercier les personnes avec qui j'ai collaboré : Irina qui m'a accueillie et encadrée la première année de ma thèse, Ivana de l'University College of London mais aussi Chung Hung Yeh, (a.k.a Jimmy !) avec qui j'ai partagé les derniers mois de sa thèse et à qui nous avons pu rendre visite à Taiwan grâce à la bourse ORCHID. Plus un ami qu'un collègue, j'ai apprécié les bons moments passés en ta présence au laboratoire et à Taiwan, ta gentillesse, ta patience et ton humour.

Un grand merci à tous mes collègues de Neurospin, à commencer par mes collègues du laboratoire de diffusion : Fabrice, Refka, Alaitz, Anne, Cyril, Achille, Cyrille, Véronique, Linda, Pamela, Josselin, Christine et surtout, mes trois (adorables !) collègues de bureau: Clarisse, Delphine et Urielle. Merci à tous et à toutes pour votre bonne humeur, votre humour et votre gentillesse. Merci tout spécialement à Fabrice, pour son calme et ses conseils avisés et pour avoir partagé quelques séances de badminton et de tir à l'arc avec nous. Merci à Véronique qui a su me transmettre son optimisme, sa sagesse et sa bonne humeur. Egalement merci à Achille, Cyrille et Urielle pour les sorties et festivals qui m'ont permis de décompresser au bon moment ! Je finis par mes remerciements à Clarisse et Delphine, sans qui ces trois ans et demi auraient été bien plus difficiles. Merci à vous pour votre amitié, pour nos longues discussions, nos sorties, nos fous rires, nos moments de joie, nos réflexions sur la vie, vos conseils, ... Grâce à vous, cette expérience a été une réelle expérience humaine, où j'ai pu trouver de vraies amies avec qui j'espère pouvoir garder contact.

Je n'oublierai certainement pas mes collègues qui, avec nous, ont partagé le moment précieux du Glunch: Laurent, Marie-France, Jérémy, Yann, Nathalie, Denis, Lionel... Merci à vous tous pour ces grands moments et grandes discussions que nous avons pu partager autour d'une abondance de nourriture en tout genre qui en a étonné plus d'un !

Merci à vous, Yohanna et Dominique pour les potins et toutes ces discussions que nous avons pu avoir pendant ces trois ans.

Merci aussi aux manips radio et infirmières : Gaëlle, Bernadette, Véronique, Christine, Séverine D., Séverine R., Chantal et Laurence. Merci à vous d'avoir rendu agréables les moments passés à la console, et merci spécialement à Chantal, pour tous ses conseils, pour son sourire quotidien et pour avoir accepté de jouer au badminton avec moi !

Enfin, je remercie toutes les personnes que j'ai pu croiser et avec qui j'ai pu discuter durant mon passage à NeuroSpin : Ileana, Julien, Benjamin, Nadya, Alfredo, Aurélien, Alexis, Nicolas, Fawzi, Luisa, Boucif, ...

Je souhaite également remercier mes ami(e)s du lycée et de fac qui m'ont supportée moralement : Laetitia, Justine, Olga, Héloise, Soraya, Rémi et Stéphane.

J'aimerais dire aussi un immense merci à ma famille et à ma belle-famille sans qui tout aurait été aussi très dur. Merci à vous, Maman et Papa, votre soutien à tous les deux m'a été très précieux. Merci à toi, Félix, pour tes conseils de grand frère et pour m'avoir remonté le moral et donné confiance en moi. Merci à vous, Coco et Doudou, pour votre présence, votre gentillesse, votre sagesse, vous avez su m'accompagner dans chaque étape de ma vie. Merci également à mes tantes, Tata Monique, Tata Cathy et Tata Sylvie ainsi qu'à mes cousins. J'ai également une pensée pour ma grand-mère, Mémé Lucette qui nous a quittés en Août dernier mais dont la bonne humeur et les bons petits plats ont ponctué ces années de thèse. Merci à Valérie, Bertrand, Manon, Chloé, Geoffrey, Chantal, Pierre, Madeleine, Patrice, Christophe, Fabienne, Sam et toute ma belle famille pour les discussions et le soutien qu'ils m'ont apporté lors des week-ends passés en Normandie.

Finalement, je remercie tout spécialement Quentin, qui mérite certainement un diplôme pour avoir supporté mes moments de questionnement et de stress durant ces trois ans. Merci à toi, pour ton immense patience, ta gentillesse et ta tendresse.

Je dédie cette thèse à mes grands-parents, Jeannine et Roland alias Coco et Doudou, qui m'ont tant apporté.

Contents

Acknowledgements i

Contents iii

List of Figures x

List of Tables xvi

Symbols xvii

1 Introduction 1
- 1.1 Context . . . 1
- 1.2 Motivations . . . 2
- 1.3 Thesis organization . . . 4
  - 1.3.1 Chapitre 2: Human Brain Anatomy . . . 4
  - 1.3.2 Chapitre 3: MRI modalities dedicated to tissue microstructure . . . 4
  - 1.3.3 Chapitre 4: Brain white matter relaxometric atlases . . . 5
  - 1.3.4 Chapitre 5: Microstructure mapping using diffusion MRI . . . 5
  - 1.3.5 Chapitre 6: Brain microstructure mapping . . . 5
  - 1.3.6 Chapter 7: Conclusion and future work . . . 5

2 Human Brain Anatomy 6
- 2.1 Introduction . . . 6
- 2.2 Macroscopic Anatomy . . . 6
- 2.3 Global description . . . 6
- 2.4 Cortex lobes, gyri, and sulci . . . 7
  - 2.4.1 Frontal lobe . . . 8
  - 2.4.2 Parietal lobe . . . 8
  - 2.4.3 Occipital lobe . . . 8
  - 2.4.4 Temporal lobe . . . 8
  - 2.4.5 Insula and limbic lobe . . . 9
  - 2.4.6 Brodmann areas . . . 9
- 2.5 Internal anatomy . . . 10
  - 2.5.1 Blood supply of the brain . . . 10
  - 2.5.2 Ventricles . . . 10
  - 2.5.3 Grey matter . . . 11

2.5.3.1 Nuclei of the cerebellum, the brain stem and the mesencephalon . . . 11
2.5.3.2 Grey matter of the diencephalon . . . 11
2.5.3.3 Grey matter of the telencephalon . . . 12
Deep nuclei . . . 12
Cortex . . . 12
2.5.4 White matter . . . 13
2.5.4.1 Projection fibers . . . 13
2.5.4.2 Association fibers . . . 14
2.5.4.3 Interhemispheric commissures . . . 15
2.6 Brain tissue microstructure . . . 15
2.6.1 Brain cells . . . 16
2.6.1.1 Neurons . . . 16
2.6.1.2 Oligodendrocytes . . . 17
2.6.1.3 Astrocytes . . . 18
2.6.1.4 Microglia . . . 18
2.6.2 Cortex histology . . . 18
2.6.3 White matter histology . . . 20
2.7 Brain diseases and microstructure . . . 20
2.8 Conclusion . . . 21

3 MRI modalities dedicated to the study of tissue microstructure 22
3.1 Introduction . . . 22
3.2 Principles of magnetic resonance imaging . . . 23
3.2.1 Magnetic resonance phenomenon . . . 23
3.2.1.1 Magnetic moments of protons . . . 23
3.2.1.2 Equilibrium state in the presence of a magnetic field B_0 24
3.2.1.3 Perturbation of the equilibrium by a radio frequence B_1 : excitation . . . 24
3.2.1.4 Bloch equations, T_1 and T_2 relaxation times . . . 25
3.2.1.5 T_1 and T_2 relaxation times for different tissues and different fields . . . 27
3.2.2 Origin of the signal acquired in MRI . . . 27
3.2.3 From FID to image . . . 29
3.2.4 Spatial encoding . . . 29
3.2.4.1 Slice gradient . . . 30
3.2.4.2 Phase encoding . . . 31
3.2.4.3 Frequency encoding . . . 31
3.2.4.4 3D imaging . . . 31
3.2.5 K-space and FFT . . . 31
3.2.6 Parallel imaging . . . 32
3.2.7 MRI sequences used in this thesis . . . 33
3.2.7.1 Spin Echo Sequence . . . 34
3.2.7.2 Gradient Echo Sequence . . . 34
3.2.7.3 Fast K-space acquisition: Echo Planar Imaging . . . 35
3.2.8 Contrast . . . 36
3.3 Relaxometry and quantitative imaging . . . 36

3.3.1 Common T_1 and T_2 sequences . . . 39
3.3.1.1 T_1 mapping : Inversion/Recovery sequence . . . 39
3.3.2 T_2 mapping : multiple echo times Spin-Echo . . . 40
3.3.3 Advanced Sequences . . . 40
3.3.3.1 T_1 mapping using RF spoiling . . . 41
3.3.3.2 T_2 mapping using steady state free precession . . . 42
3.4 Diffusion weighted imaging . . . 43
3.4.1 Diffusion process in tissues . . . 44
3.4.1.1 Free diffusion . . . 44
3.4.1.2 Anisotropy and restricted diffusion . . . 45
3.4.2 Basic sequence dedicated to diffusion MRI and signal equation . . . 46
3.4.2.1 Pulse Gradient Spin Echo . . . 46
3.4.2.2 Artefacts and noise in diffusion MRI . . . 47
3.4.2.3 Diffusion signal expression . . . 51
3.4.3 Review of local models . . . 52
3.4.3.1 Q-space analysis : dODF, fODF and diffusion propagator 52
3.4.3.2 Local modeling review . . . 53
3.4.3.3 DTI . . . 55
3.4.3.4 Numerical and analytical Qball imaging . . . 58
3.4.3.5 Spherical Deconvolution Techniques . . . 60
3.4.4 Application of the diffusion weighted imaging . . . 60
3.4.4.1 Inference of structural connectivity using tractography . 61
3.5 Conclusion . . . 63

4 Brain white matter relaxometry atlases 64
4.1 Introduction . . . 64
4.2 The ARCHI database . . . 65
4.3 Inference of an atlas of the structural connectivity . . . 67
4.3.1 Quality check and correction of imaging artefacts . . . 68
4.3.2 Local modeling and tractography . . . 69
4.3.3 Intra-subject and inter-subjects clustering . . . 70
4.3.4 Labelling . . . 70
4.3.5 Diffeomorphic registration of subjects using DTI-TK . . . 72
4.3.6 Super resolved quantitative atlases . . . 74
4.3.7 Connectivity Atlas . . . 74
4.4 High resolution relaxometric 3D atlases . . . 76
4.4.1 Inference of individual relaxometry maps . . . 76
4.4.2 Inference of high resolution atlases . . . 77
4.5 T_1 and T_2 profiles along white matter bundles . . . 78
4.5.1 Profile Computation . . . 78
4.5.2 Validation of the symmetrized centroids . . . 81
4.5.3 Profiles of T_1 and T_2 along WM bundles . . . 82
4.5.4 Anatomical analysis of the profiles . . . 82
4.5.4.1 General observations . . . 82
4.5.4.2 Arcuate Group (Figures 4.13-4.15) . . . 83
4.5.4.3 Cingulum Tract (Figure 4.16) . . . 83
4.5.4.4 CorticoSpinal fasciculus (Figure 4.17) . . . 83

4.5.4.5 Inferior Fronto Occipital fasciculus (Figure 4.18) 83
4.5.4.6 Inferior Longitudinal Fasciculus (Figure 4.19) 84
4.5.4.7 Uncinate fasciculus (Figure 4.20) 84
4.5.4.8 Corpus Callosum 84
4.6 Study of inter-hemispheric asymmetries 84
4.6.1 Arcuate asymmetries (Figure 4.13-4.15) 85
4.6.2 Cingulum asymmetries (Figure 4.16) 85
4.6.3 CorticoSpinal asymmetries (Figure 4.17) 85
4.6.4 Inferior Fronto Occipital asymmetries (Figure 4.18) 86
4.6.5 Inferior Longitudinal asymmetries (Figure 4.19) 86
4.6.6 Uncinate asymmetries (Figure 4.20) 86
4.7 Comparison with the profiles of diffusion structural parameters 86
4.8 Conclusion 101

5 Microstructure mapping using diffusion MRI 103
5.1 Microstructure modeling of the brain tissue 104
5.1.1 Compartmentalization and exchange 105
5.1.2 Compartmentalization of the brain tissue 105
5.1.3 Exchange between compartments 106
5.2 State of the art of tissue modeling 107
5.2.1 Current white matter models 107
5.2.1.1 Beyond monoexponential model : biexponential model of white matter 108
5.2.1.2 First analytical model with cell geometrical model 108
5.2.1.3 Ball and Stick model 109
5.2.1.4 The composite hindered and restricted model of diffusion (CHARMED) 110
5.2.1.5 Extension of CHARMED model for orientation dispersion 111
5.2.1.6 Models including myelin sheaths 111
5.2.1.7 Comparison of the white matter models 112
5.2.2 Grey matter models and mixed models 112
5.3 Beyond the CHARMED model : axon model using a two-pool model cylinder 114
5.3.1 Do the fast and slow pools correspond to extra and intra-cellular space ? 114
5.3.2 A biexponential diffusion behaviour inside the cell 114
5.4 Cytoarchitectural modeling of the grey matter : beyond the sphere model 115
5.5 Diffusion MR microscopy 116
5.5.1 Principles of diffusion MRI microscopy 116
5.5.1.1 Using varying diffusion time to probe tissue microstructure 116
5.5.1.2 Diffusion MRI simulation 117
5.5.1.3 Mathematical framework of signal attenuation computation : Short Pulse Gradient and Gaussian Phase Distribution approximations 117
5.5.1.4 Equation of the diffusion propagator 120
Diffusion propagator expression for the axon : cylinder geometry 120

Diffusion propagator expression for neural cells : sphere geometry . . . 120
5.5.2 Diffusion MRI microscopy using Pulse Gradient Spin Echo . . . 121
5.5.2.1 AxCaliber Framework . . . 121
5.5.2.2 ActiveAx Framework : optimization of acquisition scheme for clinical routine . . . 123
Signal model : . . . 125
Results and Limits : . . . 126
5.5.2.3 Second contribution : signal attenuation for the two-pool model . . . 131
Development of the PGSE signal attenuation for the two-pool cylinder model: . . . 131
Signal attenuation for the thick layer sphere using PGSE: . . . 134
5.5.2.4 Long time limit : diffusive-diffraction experiments . . . 136
5.5.3 Diffusion MRI microscopy using double PGSE . . . 138
5.5.3.1 Extracting microstructure features from diffraction patterns . . . 138
5.5.3.2 Signal angular dependency . . . 139
Application to white matter structure . . . 139
5.5.4 Oscillating gradient sequences : OGSE and SW-OGSE . . . 140
5.5.4.1 OGSE and temporal diffusion spectroscopy . . . 141
5.5.4.2 OGSE for cell calibration . . . 142
5.5.5 Beyond the PGSE : spin echo sequence diffusion weighted with arbitrary gradient waveforms (AGWSE) . . . 143
5.5.5.1 Developpment and implementation of an AGSWE sequence in a clinical routine at 3 Teslas and 7 Teslas . . . 145
5.6 Conclusion of this chapter . . . 148

6 White Matter Microstructure Mapping 151
6.1 Mapping the white matter using the PGSE sequence . . . 152
6.1.1 Methods . . . 152
6.1.1.1 MRI data acquisition . . . 152
6.1.1.2 White matter model . . . 153
6.1.1.3 Axon Calibration Algorithm . . . 153
6.1.1.4 Post-processing . . . 155
6.1.2 Results . . . 156
6.1.2.1 Microstructure mapping . . . 156
6.1.2.2 Average profile . . . 156
6.1.3 Discussion . . . 161
6.1.3.1 Results versus histology . . . 161
6.1.3.2 Intra and Inter-subject variability . . . 161
6.1.3.3 Stability of the results . . . 162
6.1.3.4 Comparison with 4 profiles . . . 164
6.1.3.5 Comparison with our previous study . . . 164
6.1.3.6 Correlations between microstructure parameters and dti parameters . . . 165
6.1.3.7 Conclusion and discussion . . . 167

6.2 Theoretical study of the two-pool model to improve axon calibration . . 168
6.2.1 Single-pool vs the two-pool model 168
6.2.2 Origin of the overestimation 169
6.2.3 Limitations of the model 171
6.3 Ongoing studies 171
6.3.1 Arbitrary Gradient Waveform Spin Echo versus PGSE : *in vivo* comparison 171
6.3.2 Towards characterization of diseases through axon calibration : application to a cohort of autistic patients 172
6.3.2.1 MRI protocol and methods 173
6.3.2.2 Preliminary results 174
6.4 Conclusion 176

7 Conclusion and Future Work 178
7.1 General conclusion and contributions 178
7.1.1 Atlas of T1 and T2 relaxation times from the 79 subjects of the CONNECT/Archi database 178
7.1.2 Contributions to axon calibration methods 179
7.1.2.1 Implementation and validation of an Arbitrary Gradient Waveform Spin Echo sequence 179
7.1.2.2 A novel geometrical model of the axon 179
7.1.2.3 Axon radii and density mapping of the corpus callosum at 7T 179
7.1.3 Software contribution 180
7.2 Future Work 180
7.2.1 Construction of further atlases based on the CONNECT/Archi MRI database 180
7.2.2 *In vivo* axon calibration at 7T 180
7.2.3 *In vivo* comparative study of AGWSE vs PGSE 180
7.2.4 Towards clinical applications 181
7.2.5 Real-time axon calibration 181
7.2.6 Extension of the study to grey matter 182
7.2.7 Human Brain Project 182
7.2.8 Publications 182
7.2.8.1 Journal Papers 182
7.2.8.2 Conference Papers 182

A Mathematical Functions used in this thesis 184
A.1 Bessel Functions 184
A.1.1 Bessel Functions of the first kind 184
A.1.2 Neuman Functions (second kind) 184
A.2 Modified Bessel Functions of the first kind 184
A.3 Spherical Bessel Functions 185
A.3.1 Spherical Bessel Functions of the first kind 185
A.3.2 Spherical Bessel Functions of the second kind 185
A.4 Legendre Polynomials 185

A.5 Confluent hypergeometric function 185

B MCMC Procedure **186**

C Corpus Callosum T1 and T2 profiles **188**

Bibliography **189**

List of Figures

2.1 The four brain lobes . . . 7
2.2 Brodmann's areas. . . . 9
2.3 Brain blood supply. . . . 10
2.4 Ventricles system . . . 11
2.5 Nuclei of the telencephalon on an axial slice. . . . 12
2.6 Projection fibers and corpus callosum . . . 13
2.7 Association fibers . . . 14
2.8 Corpus Callosum sections from [Highley et al., 1999] . . . 15
2.9 Description of the different parts of the neuron. . . . 16
2.10 Transmission electron micrograph of a myelinated axon . . . 16
2.11 Oligodendrocyte. Adapted from http://cnx.org . . . 17
2.12 Astrocyte. Adapted from http://cnx.org . . . 18
2.13 Cortex microstructure . . . 19
2.14 Brain tissue microstructure . . . 20

3.1 Magnetic Moment of a proton . . . 23
3.2 Left : Protons behavior in the absence of magnetic field , Right : Alignment in the presence of an external magnetic moment . . . 24
3.3 Excitation and relaxation phenomena. . . . 25
3.4 Laboratory frame and rotative frame. . . . 26
3.5 Temporal longitudinal and transverse magnetization evolution . . . 28
3.6 T_1-weighted image (left) and T_2-weighted image (right) from one subject of the Archi database . . . 29
3.7 MRI system : With G_ϕ the phase encoding gradient, G_s the slice gradient, G_ω the frequency encoding gradient, B_0 the static magnetic field . . . 30
3.8 Spatial encoding. Top line : spatial encoding, bottom line : basic MRI sequence diagram . . . 32
3.9 K-space from `www.imaios.fr` . . . 33
3.10 Spin Echo sequence adapted from `www.imaios.fr` . . . 35
3.11 Spin Echo Echo Planar Imaging sequence from `www.imaios.fr`. . . . 36
3.12 MRI contrast with varying TR and TE. TR is constant across rows and increasing down columns (TR=500ms, 1000ms, 2000ms, 4000ms, 8000ms, 12000ms from the top to the bottom line). TE is constant across the columns and increases across the rows (TE=25ms, 50ms,75ms,100ms from left to right). . . . 37
3.13 Inversion Recovery sequence `www.imaios.fr` . . . 39
3.14 T_1 and T_2 mapping sequences : a) IR-EPI b) EPI. . . . 40
3.15 Spoiled Gradient Recalled Echo sequence. . . . 41

3.16 Stead State Free Precession sequence. 42
3.17 Restricted diffusion phenomenon [Assaf et al., 2008]: Δ_x is the mean-squared displacement and Δ the diffusion time 45
3.18 Pulse Gradient Spin Echo Sequence. 46
3.19 N/2 Ghosting Artefact. 47
3.20 Susceptibility artefact 48
3.21 nc-χ noise in diffusion MRI data (adapted from [Brion, 2013]) 49
3.22 Rician probability distribution function (figure from [Brion, 2013]) for different ratios S/σ. 50
3.23 Diffusion weighted images (b=1500 $s.mm^2$) for three different orientations 53
3.24 Reprenstation of the diffusion tensor D in the cases of isotropic and anisotropic diffusion 56
3.25 RGB and FA maps 57
3.26 Analytical QBall field (computed using CONNECTOMIST 2.0). 59
3.27 Streamline deterministic tractography (from one subject of the Archi Database). 62
3.28 Deterministic versus Probabilistic tractography. 63

4.1 Connectomist pipeline leading to the fiber bundle labelling 68
4.2 Robust Tractography mask (figure from [Guevara et al., 2011a]).First line: mask with a simple FA threshold, second line: T_1-based mask. many important areas of white matter are missed when using FA based masks . 70
4.3 Clustering. Step 1 : hierarchical decomposition, Step 2: length-based segmentation, Step 3: voxel-based clustering, Step 4: extremity-based clustering, and Step 5: fascicle merge. From [Guevara et al., 2012]. 71
4.4 Major white matter bundles of the 79 subjects of the ARCHI database: corpus callosum (rostrum: dark pink, genu: dark blue, body: dark green, splenium : brown), arcuate tracts (arcuate: red, anterior arcuate: green, posterior arcuate: yellow), uncinate tract: cyan, Inferior Fronto Occipital tract: pink, Inferior Longitudinal Tract: purple, Cingulum: brown 72
4.5 Super resolution technique 74
4.6 Super resolution technique : FA maps obtained from the combination of the 79 subjects' maps from the initial resolution 1.7mm isotropic (a) to 1mm (b), 0.75mm (c) and 0.5mm (d) 75
4.7 Super-resolved (0.5mm isotropic) FA map (top line), ADC map (second line), Axial Diffusivity (third line), Radial Diffusivity (bottom line) . . . 76
4.8 Individual T_1 maps of 6 subjects from the Archi database using a T1-based mask 77
4.9 Individual T_2 maps of 6 subjects from the Archi database using a T1-based mask 78
4.10 First line: 1.7 mm isotropic resolution atlases of quantitative T_1(left) and T_2(right) relaxation times obtained from the 79 subjects of the CONNECT/Archi database, second line : 500μm isotropic resolution atlases using the super resolution technique 79
4.11 Profile computation. Top : Computed centroid of left corticospinal tract and corresponding density map. Bottom : sections computed from the centroid defining the domain of integration 80
4.12 Differences between profiles using orignal centroids and symmetrized centroids 81

4.13 Left Columns : Average T_1, T_2, FA, ADC, $\lambda_{\|}$ and $\lambda_{\perp}$ profiles of the anterior arcuate tracts (In green : right bundle profiles, in blue left bundle profiles). Individual profiles are also plotted. Right Columns : Interhemispheric asymmetries (red lines correspond to regions with at least 4 significantly asymmetric sections) 87
4.14 Left Columns : Average T_1, T_2, FA, ADC, $\lambda_{\|}$ and $\lambda_{\perp}$ profiles of the posterior arcuate tracts In green : right bundle profiles, in blue left bundle profiles. Individual profiles are also plotted. Right Columns : Interhemispheric asymmetries (red lines correspond to regions with at least 4 significantly asymmetric sections) 88
4.15 Left Columns : Average T_1, T_2, FA, ADC, $\lambda_{\|}$ and $\lambda_{\perp}$ profiles of the arcuate tracts In green : right bundle profiles, in blue left bundle profiles. Individual profiles are also plotted. Right Columns : Interhemispheric asymmetries (red lines correspond to regions with at least 4 significantly asymmetric sections) 89
4.16 Left Columns : Average T_1, T_2, FA, ADC, $\lambda_{\|}$ and $\lambda_{\perp}$ profiles of the cingulum tracts In green : right bundle profiles, in blue left bundle profiles. Individual profiles are also plotted. Right Columns : Interhemispheric asymmetries (red lines correspond to regions with at least 4 significantly asymmetric sections) 90
4.17 Left Columns : Average T_1, T_2, FA, ADC, $\lambda_{\|}$ and $\lambda_{\perp}$ profiles of the right/left corticospinal tracts. In green : right bundle profiles, in blue left bundle profiles. Individual profiles are also plotted. Right Columns : Interhemispheric asymmetries (red lines correspond to regions with at least 4 significantly asymmetric sections) 91
4.18 Left Columns : Average T_1, T_2, FA, ADC, $\lambda_{\|}$ and $\lambda_{\perp}$ profiles of the right/left inferior fronto occipital tracts. In green : right bundle profiles, in blue left bundle profiles Right Columns : Interhemispheric asymmetries (red lines correspond to regions with at least 4 significantly asymmetric sections) 92
4.19 Left Columns : Average T_1, T_2, FA, ADC, $\lambda_{\|}$ and $\lambda_{\perp}$ profiles of the right/left inferior longitudinal tracts. In green : right bundle profiles, in blue left bundle profiles. Individual profiles are also plotted. Right Columns : Interhemispheric asymmetries (red lines correspond to regions with at least 4 significantly asymmetric sections) 93
4.20 Left Columns : Average T_1, T_2, FA, ADC, $\lambda_{\|}$ and $\lambda_{\perp}$ profiles of the right/left uncinate tracts. In green : right bundle profiles, in blue left bundle profiles. Individual profiles are also plotted. Right Columns : Interhemispheric asymmetries (red lines correspond to regions with at least 4 significantly asymmetric sections) 94
4.21 Correlation between T_1/T_2 relaxation times and diffusion parameters : Anterior/Posterior Arcuate tracts 96
4.22 Correlation between T_1/T_2 relaxation times and diffusion parameters : arcuate and cingulum tracts 97
4.23 Correlation between T_1/T_2 relaxation times and diffusion parameters :corticospinal and inferior occipital tracts 98
4.24 Correlation between T_1/T_2 relaxation times and diffusion parameters : inferior longitudinal and uncinate tracts 99

5.1 Tissue microstructure (astrocyte and oligodendrocytes) (from http://www.db-gersite.com) . . . 105
5.2 Cell membrane structure adapted from wikipedia . . . 106
5.3 Cell membrane and molecules transfers from [Ayus et al., 2008] . . . 107
5.4 Optic nerve model : axons are modelled as prolate ellipsoid with a axial radius r_p and the transverse radius r_t, glial cells are modeled as spheres of radius r_s and an additional compartment corresponds to the extra-cellular space . . . 109
5.5 CHARMED model of white matter [Assaf et al., 2004] . . . 110
5.6 Geometrical models of brain tissue components . . . 113
5.7 Two-pool cylinder model . . . 113
5.8 Two-pool sphere model . . . 116
5.9 AxCaliber Framework results from [Assaf et al., 2008] for ex-vivo porcine optic and sciatic nerves : a. Multi diffusion time diffusion spectroscopy signal decay of an optic nerve sample. b. Multi diffusion time diffusion spectroscopy signal decay of a sciatic nerve sample. c. Extracted AxCaliber axon diameter distribution based on the signal decays given in (a) and (b). d. Axon diameter distribution derived from electron microscopy section of the two nerve samples. e,f. Electron microscope section of one optic nerve (e) and one sciatic nerve samples upon which the data in (a–d) is based. . . . 124
5.10 Human optimized protocol extracted from [Alexander et al., 2010] (RF pulses are also shown) . . . 127
5.11 Results of ActiveAx framework on the corpus callosum of human subjects from [Alexander et al., 2010] . . . 128
5.12 Comparison of the estimated axon radius a' versus the ideal axon diameter index α from simulated data at different gradient strength (60mT/m, 140 mT/m, 200 mT/m, 300mT/m) and with various SNR (from [Dyrby et al., 2013]). In blue: the mean of the repetitions of the fitting, in red: the estimates for each repetition . . . 130
5.13 Two-pool cylinder and sphere model : in blue the slow pool, in red the fast pool . . . 131
5.14 PGSE signal expression in long time limit for several geometries . . . 137
5.15 Diffraction pattern for parallel planes separated by a 2R distance (left) and in a sphere of radius R (right). Figures extracted from [Price, 1997] . 137
5.16 Double PGSE diagram . . . 138
5.17 OGSE diagram . . . 140
5.18 AGWSE diagram from [Drobnjak et al., 2010] . . . 144
5.19 PGSE, OGSE and totally arbitrary gradient waveform from the AGWSE sequence . . . 146
5.20 Panel dedicated to our novel diffusion sequence. For an AGWSE sequence, it is possible to set the time duration between each time point, the maximum gradient strength along each axis, the number of T2-weighted images, the number of diffusion orientations, the number of profiles, the number of orientation blocks and finally the kind of sequence . . . 147
5.21 FiberCup phantom. Fiber pathways are highlighted in colors. Arrows indicate the directions of the synthetic fiber bundles. . . . 148
5.22 AGWSE tests at 3T on the fibercup phantom : comparison between the PGSE and the AGWSE protocol . . . 148

5.23 AGWSE tests at 3T on the fibercup phantom : zoom on the odf field . . 149
5.24 AGWSE tests at 3T on a human subject : RGB map and ODF fields . . . 150

6.1 Diffusion PGSE protocol 154
6.2 Comparison between the protocol of [Duclap et al., 2013a] and our protocol 155
6.3 Processing steps from the data acquisition to the computation of the average profiles 157
6.4 Individual axon calibration obtained on 7 of 14 healthy subjects using the protocol described in section 6.1.1.1 at 7T (50mT/m, SR=333mT/m) including 10 different diffusion times and b-values. On the right : axon radius maps, in the middle : white matter fraction, on the left : density index. 158
6.5 Individual axon calibration obtained on 7 of 14 healthy subjects using the protocol described in section 6.1.1.1 at 7T (50mT/m, SR=333mT/m) including 10 different diffusion times and b-values. On the right : axon radius maps, in the middle : white matter fraction, on the left : density index. 159
6.6 Average profile of white matter fraction and radius estimates and the derived axon density along the Corpus Callosum from 14 subjects 160
6.7 Standard deviations of the radius posterior distribution from the MCMC fitting on the mid-sagittal plane of one subject. Top : radius estimates, bottom: radius standard deviation 162
6.8 Standard deviations of the radius posterior distribution from the MCMC fitting on the mid-sagittal plane of one subject. Top : white matter fraction estimates, bottom: white matter fraction standard deviation . . 162
6.9 Comparison of the radius estimates with different initial values (on one subject) 163
6.10 Comparison of the white matter fraction estimates with different initial values (on one subject) 163
6.11 Comparison of the radius estimates using 4 and 10 PGSE profiles 164
6.12 Comparison of the white matter fraction estimates using 4 and 10 PGSE profiles 164
6.13 Wm fraction and radius profiles from the 10 subjects of the Archi database using the protocol of [Duclap et al., 2013a] 165
6.14 Correlations between microstructure parameters derived from the model and dti parameters (pvalue<0.05). First row : FA vs radius/WM fraction/ Axon density, second row : $\lambda_{\|}$ vs radius/WM fraction/ Axon density, third row : $\lambda_{\perp}$ vs radius/WM fraction/ Axon density, fourth row : *ADC* vs radius/WM fraction/ Axon density. 166
6.15 Correlations between microstructure parameters (pvalue<0.05). 167
6.16 Signal attenuation for an axon of radius of 1μm; Left: using the two-pool model and right: using the simple cylinder model 169
6.17 Signal attenuation for an axon of radius of 2μm; Left: using the two-pool model and right: using the simple cylinder model 170
6.18 Signal attenuation for an axon of radius of 3μm; Left: using the two-pool model and right: using the simple cylinder model 170
6.19 Diffusion in a circular layer : the attenuation comes from the attenuation along the boundaries and perpendicular to them 171

6.20 Optimized protocol using trapezoidal oscillating gradients (courtesy of Dr. I. Drobnjak) . . . 172
6.21 Average profiles of axon radii and white matter fraction. On the left : autistic patients. On the right : controls . . . 174
6.22 Significative regions ($p < 0.05$) for radius, white matter fraction and FA along the corpus callosum . . . 175

List of Tables

3.1 T_1 and T_2 relaxation times of gray and white matter at 1.5T (from http://users.fmrib.ox.ac.uk/ peterj/lectures/), 3T (from [Wansapura et al., 1999]) and 7T ([Rooney et al., 2007]) 27

Symbols

$\lambda_{\parallel}$	Axial diffusivity
$\lambda_{\perp}$	Radial diffusivity
μdMRI	diffusion Magnetic Resonance Imaging Microscopy
ADC	Apparent Diffusion Coefficient
$AGWSE$	Arbitrary Gradient Waveform Spin Echo
$dMRI$	diffusion Magnetic Resonance Imaging
$dODF$	diffusion Orientation Distribution Function
$dPGSE$	Double Pulse Gradient Spin Echo
$fODF$	fiber Orientation Distribution Function
DSI	Diffusion Spectrum Imaging
DTI	Diffusion Tensor Imaging
FA	Fraction Anisotropy
GFA	Generalized Fraction Anisotropy
$HARDI$	High Angular Resolution Diffusion Imaging
$HYDI$	Hybrid Diffusion Imaging
$MCMC$	Monte Carlo Markov Chain
MRI	Magnetic Resonance Imaging
$OGSE$	Oscillating Gradient Spin Echo
$PGSE$	Pulse Gradient Spin Echo
QBI	Q-ball Imaging
SDT	Spherical Deconvolution Transform
WM	White matter

Chapter 1

Introduction

1.1 Context

Magnetic resonance imaging (MRI) has become a key tool to investigate brain function and anatomy *in vivo*. More than understanding which brain structures and functional networks are damaged for any pathology, clinicians are now willing to understand what are the pathophysiological mechanisms involved at the cellular scale. To answer this, MR physicists are now developing novel methods going beyond the use of conventional T1-weighted and T2-weighted MRI contrasts which are not quantitative and replacing them by quantitative approaches based on multicompartmental biophysical modelling of brain tissues. Quantitative relaxometry (qMRI) and diffusion MR microscopy (μ-dMRI) are the two emerging modalities that successfully allowed to push forward this strategy to go beyond the imaging in resolution. Both modalities now provide insights about the microstructure of white matter, and this thesis is fully dedicated to investigate their potential to finally analyse the structure of white matter at the cellular scale.
For instance, in white matter, water can be separated in two compartments, the first one corresponding to the bulk of extra and intracellular water characterized by long T1 and T2 relaxation times and the second one corresponding to the bulk of water trapped in the myelin sheath with shorter T1 and T2 relaxation times due to their interaction with macromolecules such as cholesterol. By means of observation of differences in such relaxation times, and using a multicompartment model of the NMR signal, it is possible to have access to their respective volume fraction and thus characterizing the myelin content of white matter. Such a model offers novel biomarkers of myelin water fraction useful for instance to characterize diseases where myelin damage occurs or to probe the myelination process occuring during the early brain development.

Looking at the displacement of water molecules in brain tissues with diffusion MRI is another way to characterize its cellular environment. Indeed, due to their interaction with natural barriers such as cell membranes, the diffusion pattern of water molecules embeds unique information on the tissue microstructure corresponding to a kind of fingerprint of their membrane geometry restricting or hindering their displacement. Diffusion MRI has been very popular to probe the geometry of myelinated axons revealed by the strong anisotropy of the displacement of water molecules where the probability of motion is much higher along the direction of axons than other directions, thus allowing to infer the anatomical connectivity of the human brain *in vivo* using now well-established tractography techniques. More recently, more elaborated multicompartmental models have been introduced to go a step beyond, not only by looking at the angular profile of anisotropy of the diffusion process, but also by aiming at characterizing cell species and trying to infer more specifically their characteristics such as the local distribution of their dimensions and density. Such microstructural models also rely on a multicompartmental modelling of the diffusion-weighted MR signal attenuation. One example of these models is the CHARMED model ([Assaf et al., 2004]) dedicated to the white matter including two compartments, one corresponding to the bulk of restricted water within the axons modeled as simple cylinders, and the other gathering the extra-cellular space and glial cells where the diffusion process is assumed to be hindered only. Such a model was successfully investigated to characterize locally the axon radii and density and yield a novel modality called diffusion MR microscopy (μ-dMRI).

1.2 Motivations

The main goal of this thesis is to take advantage of these two modalities to set up the methodology to study white matter microstructure of the human brain *in vivo* in order to develop normative atlases. Nowadays, the use of both quantitative and diffusion MRI in clinical routine is extremely limited due to the high constraint on scan duration. However, these modalities could provide useful biomarkers to diagnose diseases affecting the brain microstructure: myelin water fraction has been shown to reveal myelin loss in multiple sclerosis while the inference of axon radius by diffusion MRI could help to observe any modification of the brain microstructure thus being potentially useful to fully characterize alterations of tissues occuring during the evolution of disease. The scan duration associated with these modalities is still quite long for clinical routine, but some studies ([Deoni et al., 2005a],[Alexander, 2008]) are focused on their clinical feasibility. On one hand, the challenge is to to keep the accuracy of inferred microstructural parameters (validated using histological data) while reducing the scan duration. Hopefully

high and ultra field MRI systems together with improved gradient open a new opportunity to reduce the scan duration while providing accurate quantitative parameters. On the other hand, the relationship between the actual underlying microstructure and these parameters extracted at a resolution of the order of 1mm remains unclear. This is one of the reason that motivated the two international consortium focused on human brain microstructure: the European project CONNECT (Consortium of NeuroImagers for the Non-invasive Exploration of Brain connectivity and Tracts) and the American Human Connectome Project both focused on the compilation of data from a large number of subjects to better understand the brain microstructure and connectivity.

The first part of this thesis is directly linked to the CONNECT project and aims at developing high resolution healthy normative atlases of T1 and T2 relaxation times from the individual maps of the 79 healthy subjects of the Archi database acquired in the frame of this project at NeuroSpin on the 3T Tim Trio Siemens MRI system. Profiles of quantitative relaxometric and diffusion parameters were computed along major white matter bundles using T1, T2 and connectivity atlases (Fractional Anisotropy, Apparent Diffusion Coefficient, axial and radial diffusivity maps) and were analyzed from an anatomical point of view and compared to study their correlation. Interhemispheric asymmetry was addressed comparing the left and right profile for each bundle. This part therefore provides the first high resolution atlases of T1 and T2 from a large database that can be used as a reference for comparative studies. Moreover, the ARCHI connectivity atlas allows to project any kind of information along the white matter bundles, thus providing an unique way to study microstructure along major white matter bundles.

Because common diffusion parameters remain global and suffer from a lack of specificity about the microstructural organization of the tissue, the second part of this thesis focuses on the field of diffusion MR microscopy to characterize the microstructure of white matter bundle providing maps of their axonradii and axonal density and to provide tools to perform it in clinical conditions. Two aspects have been considered : the diffusion sequence used to infer the signal and the tissue model itself. A variety of sequences have been derived from the common PGSE sequence, varying the diffusion gradient waveform. For example, using oscillating gradient waveforms allows to reach smaller diffusion time and therefore to be more sensitive to smallest structure than when using two squared gradients. However, in clinical conditions such waveforms lead to a reduced diffusion weighting of the signal and therefore are inappropriate because of a loss of sensitivity to microstructure due to the limited gradient strength (since the weighting is proportional to the area of the waveform). Recent studies ([Drobnjak et al., 2010]) have shown that it is possible to increase sensitivity to microstructure using an optimization scheme taking into account the tissue model and the hardware constraints to provide optimized waveforms that can be played on clinical scanner. Following this idea, we developed an unique diffusion sequence on the 3T and 7T Siemens clinical MRI systems

of NeuroSpin, able to play any kind of gradient waveforms from PGSE scheme to totally arbitrary gradient waveforms. This sequence allows for the first time to acquire diffusion data of human brain subjects with arbitrary waveforms. This sequence was first used to map the axon radii and density in the corpus callosum of 14 healthy subjects on the 7T clinical MRI system of NeuroSpin. The aim of this study was to take advantage of the high static field and to study the profile of the axon radii and density at the group level. An ongoing study aims at comparing the results obtained using an optimized oscillating trapezoidal gradient waveform to those obtained using PGSE schemes. Finally, we proposed a new model taking into account the biphasic behavior of the water in the living tissue, dividing the water molecules into two pools characterized by a slow and fast diffusivity. This new model could help to limit the overestimation of the smallest radii occuring in the majority of axon calibration frameworks. This work allows to open up new prospects by using our sequence to perform axon calibration on patients suffering from diseases where the white matter could be affected and also in the future to compare PGSE sequence and optimized arbitrary gradient waveforms on healthy subjects. Next section will describe in details the organization of this manuscript.

1.3 Thesis organization

This thesis is organized in seven chapters, including introduction and conclusion.

1.3.1 Chapitre 2: Human Brain Anatomy

This chapter describes the basis of human brain anatomy required for this thesis from a macroscopic level to the cell level, describing the tissue organization and the specificities of grey and white matter.

1.3.2 Chapitre 3: MRI modalities dedicated to tissue microstructure

This chapter first presents the basis of Magnetic Resonance Imaging, before focusing on specific sequences dedicated to microstructure imaging : relaxometry and diffusion MRI.

1.3.3 Chapitre 4: Brain white matter relaxometric atlases

This chapter describes our first contribution: the construction of two super-resolved atlases of the T1 and T2 relaxation times ant their combination to the connectivity atlas built from the CONNECT/Archi database.

1.3.4 Chapitre 5: Microstructure mapping using diffusion MRI

This chapter exposes the state of the art of diffusion MRI microscopy, describing the different white matter models and diffusion sequences. We describe then two other contributions: the development of a novel clinical diffusion sequence able to play general gradient waveform and we propose an alternative model to the CHARMED model of white matter: the two-pool model.

1.3.5 Chapitre 6: Brain microstructure mapping

This chapter summarizes our contribution on microstructure mapping : the construction of the first atlas of axon radii and density at 7T, the description of the two-pool model and how it could help to overcome the overestimation of smaller radii; finally we expose the ongoing studies focusing on the comparison of Arbitray Gradient Wave Spin Echo and PGSE sequences and the first clinical application to Asperger's autism.

1.3.6 Chapter 7: Conclusion and future work

This chapter summarizes the contributions of this thesis and discusses future work on this topic.

Chapter 2

Human Brain Anatomy

2.1 Introduction

This thesis aims at inferring microstructure information from MRI data. We expose in this chapter the basic features of the human brain anatomy. The first part of this chapter deals with macroscopic anatomy, starting from the global description of the encephalon followed by the description of grey and white matter major structures. The second part goes deeper in the tissue at the cell level, describing the main neural cells of the brain, establishing the frame where this MRI application is conducted. The information related in this part principally comes from the book "Anatomie" of C. Cabrol, the websites http://teachinganatomy.blogspot.fr/ and http://www.db-gersite.com, from [Marrakchi-Kacem, 2011] and some illustrations are taken from wikipedia.

2.2 Macroscopic Anatomy

2.3 Global description

The human brain is one part of the encephalon, which also includes the cerebrum, the cerebellum and the brain stem composing the central nervous system with the spinal cord. The brain is protected by the skull, and surrounded by several layers of meninges : the dura mater (the thicker layer), the arachnoid and the pia maters. The pia mater covers the entire surface of the central nervous system and is surrounded by the arachnoid. The cerebrospinal fluid is located between the pia mater and the arachnoid, in the subarachnoid space. Its surface, called the cortex, is composed of layers of grey matter. We can divide the internal brain anatomy into two main parts : the telencephalon

(composed by the left and right hemispheres) and the diencephalon or "interbrain". As part of the brain stem, we find the mesencephalon. The two hemispheres are linked by the inter-hemispheric commissures and the diencephalon and separated by the medial longitudinal fissure, where the falx cerebri relies. Each hemisphere is divided into lobes.

2.4 Cortex lobes, gyri, and sulci

The surface of the brain, which corresponds to the grey matter of the cortex, has a complex structure. It is characterized by circonvolutions, also called gyri, delineated by the sulci, which are depressions of the surface. The main sulci, the lateral (or Sylvian) and the central (or Rolandic) fissures allow to segment the lateral part of the cortex of each hemisphere into four lobes: the frontal, parietal, occipital and temporal lobes (see Figure 2.1). Two additional lobes could be added: the insula, located deep in the lateral fissure, completely hidden on a lateral view by the neighboring parts of the frontal, parietal and temporal lobes (opercula); and the limbic lobe, reunion of several structures located at the medial aspect of the hemisphere, around the corpus callosum and diencephalon. Each of them is implicated in different functional tasks.

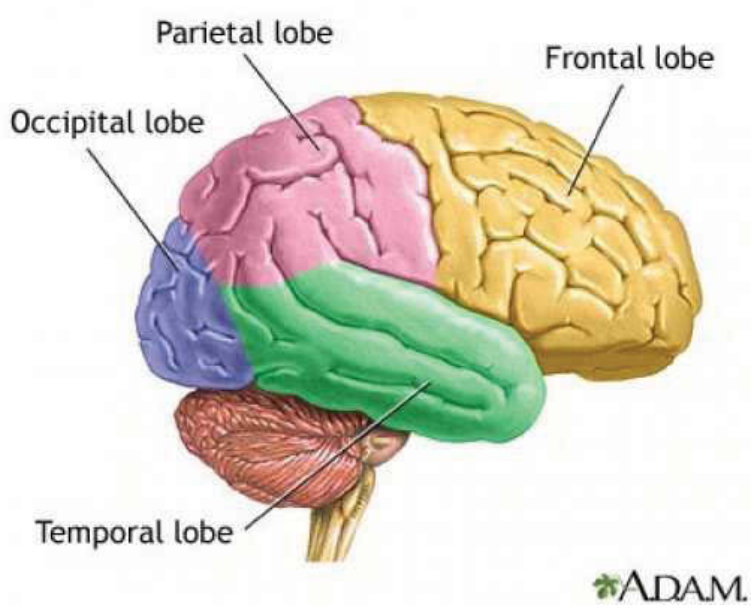

FIGURE 2.1: The four brain lobes
http://www.md-health.com/Lobes-Of-The-Brain.html

2.4.1 Frontal lobe

The frontal lobe is separated from the parietal lobe by the central sulcus, and from the temporal lobe by the lateral sulcus. Its lateral aspect is subdivided into the precentral gyrus (motor area), the superior, inferior (that includes Broca area on the left hemisphere, one of the language area) and middle frontal gyri. Its inferior aspect contains the orbital and rectus gyri, whereas its medial aspect surrounds the cingulate gyrus. The frontal lobe can be functionally divided into four different areas : the prefrontal cortex (involved in reasoning skills), the orbitofrontal cortex (involved in risk and reward assessment, and moral judgment), the primary motor cortex (involved in the control of movements), and the premotor cortex (involved for example in planification and organization of movements or in charge of attention). The frontal lobe also plays a role in decision-making.

2.4.2 Parietal lobe

It contains the postcentral gyrus anteriorly and is divided into superior and inferior parietal lobules posteriorly. The parietal lobe is involved in the integration of information coming from different senses : vision, touch, sense of smell and audition. It receives sensory information from the tongue and skin, and visual and auditory information from the other lobes.

2.4.3 Occipital lobe

It contains the primary and secondary visual cortex. Several sulci go through the occipital lobe : the superior, middle and inferior sulci on its lateral aspect occipital and the calcarinus sulcus on its medial aspect. The occipital lobe processes the visual information (received from the retina) and sends it to the temporal and parietal lobes for complementary processes.

2.4.4 Temporal lobe

The temporal lobe is separated from the frontal and parietal lobes by the lateral fissure and contains three circonvolutions on its lateral aspect, called inferior, middle and superior temporal gyri, separated by the superior and inferior temporal sulci. Its ventro medial aspect contains 2 other gyri, which are continued into the occipital lobe : the lateral (or fusiform) and medial occipito-temporal gyri. The medial occipito-temporal gyrus is subdivided into temporal (parahippocampal gyrus) and occipital parts (lingual

gyrus). The temporal lobe is also involved in auditory and visual information processing and receives information from the occipital lobe. It plays a major role in object and pattern recognition (faces for example).

2.4.5 Insula and limbic lobe

The insual is a triangular piece of cortex limited from the frontal, temporal and parietal opercular by the circular sulcus, and subdivided in short and long insular gyri. It is involved in vegetative control and emotions. The limbic lobe is a circle of gyru located around the junction between both hemispheres (corpus callosum and diencephalon). It contains the subcalllosal area anteriorly, the cingulate gyrus and also includes the parahippocampal gyrus of the temporal lobe. It is involved in emotions, mood and memory.

2.4.6 Brodmann areas

This brain division into different lobes has been extended from the observations by microscopy of differences in the organization of the cortex cytoarchitecture. Several atlases of cortical areas had been proposed. The most known was proposed by Brodmann in 1909, dividing the surface of the cortex into 52 areas. Each area participates to a specific function (see Figure 2.2). A similar atlas was proposed by Campbell (1905) and a topographic atlas of the cortex was published by Smith (1907). Alternative atlases were proposed by Von Economo and Koskinas in 1925, Sarkisov in 1949 and Bailey and Von Bonin in 1951. All these atlases are still used in clinical studies.

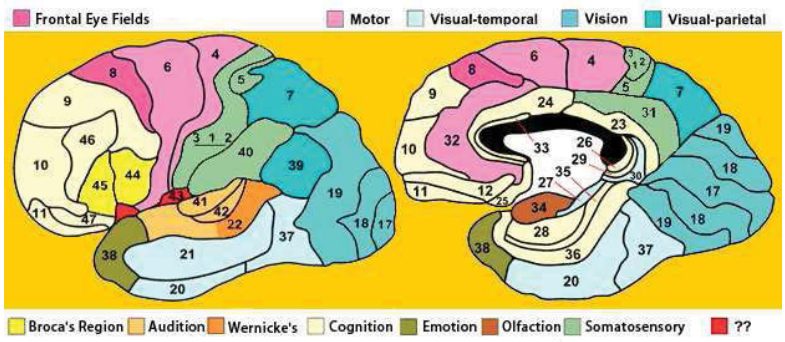

FIGURE 2.2: Brodmann's areas.
http://spot.colorado.edu

2.5 Internal anatomy

The internal anatomy of the brain is divided into three main parts : grey matter, white matter and ventricles.

2.5.1 Blood supply of the brain

Blood supply of the brain originates from an anastomotic system located at the surface of the inferior aspect of the brain. This arterial circle of the brain is fed by the paired internal carotid arteries and by the basilar artery (fusion of both vertebral arteries). The arterial circle gives rise to several types of branches : cortical branches (for the surface of the brain), ventricular branches for the choroid plexuses and deep brain and perforators for the deep brain (basal ganglia, internal capsule...).

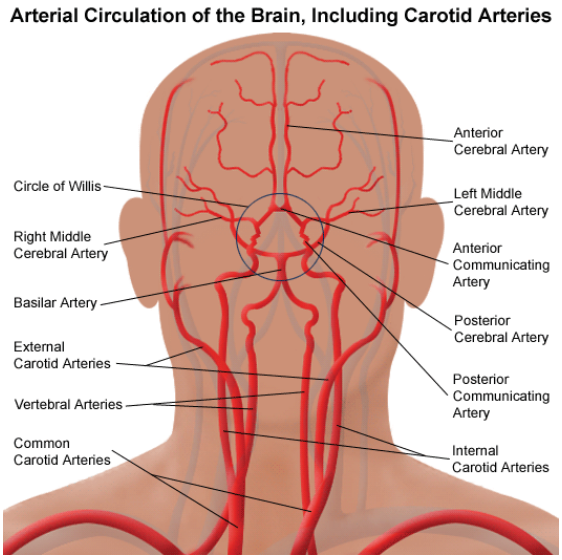

FIGURE 2.3: Brain blood supply.
http://surgery.med.miami.edu

2.5.2 Ventricles

The cerebro-spinal fluid (CSF) bathes the human brain, protecting it from mechanical shocks. It is secreted by the plexus choroideus and circulates from two central cavities (located in each hemispheres), called lateral ventricles (see Figure 2.4). Each lateral ventricle has three horns (temporal, frontal and occipital). The CSF leaves the lateral ventricles to a third ventricle located in the diencephalon (through the Monroe intraventricular foramen) and finally to the fourth ventricle, located in the brain stem through the cerebral aqueduct (of Sylvius). Outside the brain, the CSF is bounded by the arachnoid mater.

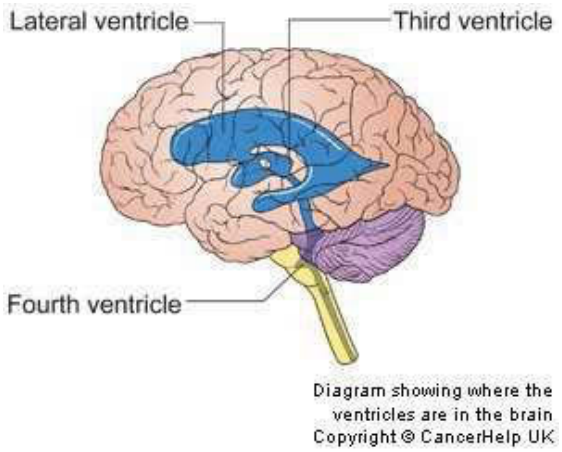

FIGURE 2.4: Ventricles system

2.5.3 Grey matter

Grey matter that composes the surface of the brain is called the cortical mantel or cortex and has a thickness varying from 1 to 4.5 mm. The cerebral cortex depicts three main kind of cortices : the neocortex (external aspects of the hemispheres), including six different cortical layers, characterized by different types of cells and density (described in the section 2.6), the paleocortex with four or five layers, covering the olfactory bulb and in the parahippocampal gyrus and the archicortex (with three cortical layers), found in the hippocampus. Another type of grey matter is located deeper in the brain, forming the central nuclei, which will be described below.

2.5.3.1 Nuclei of the cerebellum, the brain stem and the mesencephalon

The cerebellum contains four major nuclei : the dentate, the globose and emboliform nuclei and the fastigial nucleus. The nuclei of the cranial nerves are located in the brain stem. The mesencephalon also contains the substantia nigra, near the crus cerebri. Dopaminergic neurons are found in this region that mainly acts on the motor control. It also contains the red nucleus.

2.5.3.2 Grey matter of the diencephalon

The diencephalon regroups the thalamus, the hypothalamus, the epithalamus and the subthalamus. The thalamus, which forms the side walls of the third ventricle represents 80% of the diencephalon and is located on the top of the brain stem. It plays a role in the sensory and sensitive functions, in the motor control, in the consciousness and the regulation of the states of sleep and wakefulness. It contains several nuclei. The

hypothalamus contains several vegetatives nuclei and has an endocrinian role. The mammillar body is part of the hypothalamus and is implicated in the limbic system. The hypothalamus is separated from the thalamus by the Monro sulcus. Below, the subthalamic nucleus or corpus of Luys has a sensitive and motor role. Finally the epithalamus is characterized by the epiphyse and the habenula.

2.5.3.3 Grey matter of the telencephalon

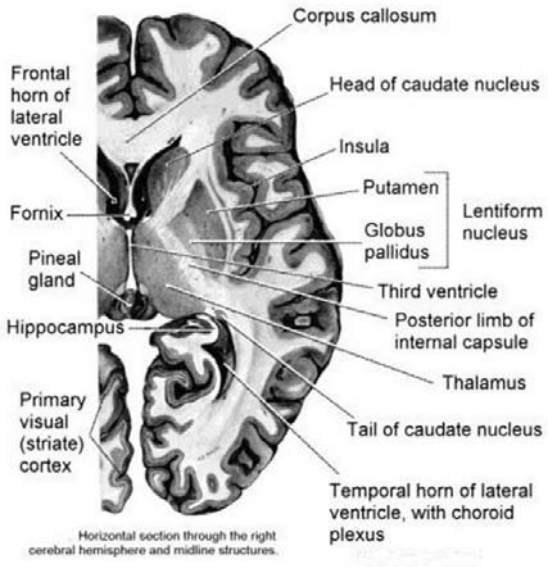

FIGURE 2.5: Nuclei of the telencephalon on an axial slice.
http://brainmind.com

Deep nuclei In the telencephalon, we can distinguish several nuclei in the deep grey matter (see Figure 2.5). The striated nuclei designate the caudate nucleus and the putamen, forming the basal ganglia with the globus pallidum, the subthalamus nuclei and the substantia nigra. The internal capsule separates, in its anterior limb the caudate nucleus from the lenticular nucleus and the thalamus from the lenticular nuclus in its posterior part. Together with the claustrum, they play a role in the motor control and equilibrium.

Cortex The deep grey matter also includes limbic system, composed of the hippocampus (the Amon Horn and the gyrus dentatus) and the amygdala. They control emotions, memory and representation of space. Finally, the insula is a also a part of the telencephalon cortex.

2.5.4 White matter

This thesis is particularly focused on the white matter microstructure. The white matter is located under the cortex and is made of fibers, corresponding to the axons of the neurons, responsible for the connections between different functional areas of the brain. These connections allow to carry signals from one location to another, in the form of action potentials. The fibers, of a diameter from $1\mu m$ to 25 μm, appear white because of the myelin sheath (mainly composed of lipids) covering their membranes. But in the brain, myelinated and unmyelinated axons coexist. The unmyelinated axons are generally small and slowly conduct the signals in comparison with the myelinated fibers. The fibers can be divided into three major classes : the projection fibers, the association fibers and the commissural fibers. In the next subsections, we define these three classes of fibers which are of main interest in the scope of this thesis.

2.5.4.1 Projection fibers

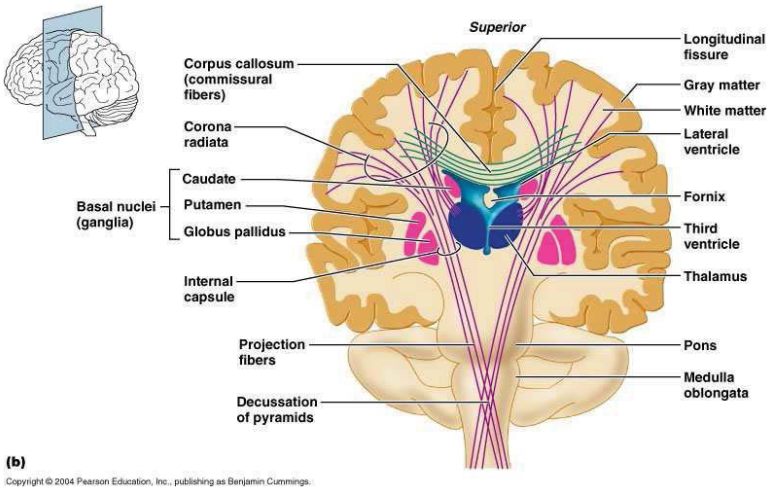

FIGURE 2.6: Projection fibers and corpus callosum
http://apbrwww5.apsu.edu

They designate the afferent and efferent fibers, connecting the cortex to the deep structures (see Figure 2.6). They project onto/from the cortex with a fanning configuration, corresponding to the corona radiata. The principal descending pathway is the corticospinal fasciculus, regrouping all the fibers of the motor tract. These fibers pass through the posterior limb and the genu of the internal capsule, between the thalamus and the lenticulate nucleus. The corticobulbar and corticopontine fibers, connecting the cortex to the brainstem run into the genu of the internal capsule. Some projection fibers form the external capsule, passing between the lenticular nucleus and the claustrum, and other forms the extreme capsule, passing between the claustrum and the cortex. At the

level of the mesencephalon, the descending projection fibers composes the middle part of the cerebral peduncles. Ascending fibers project from the thalamus to the cortex : they include the thalamic radiations, auditory and optic radiations.

2.5.4.2 Association fibers

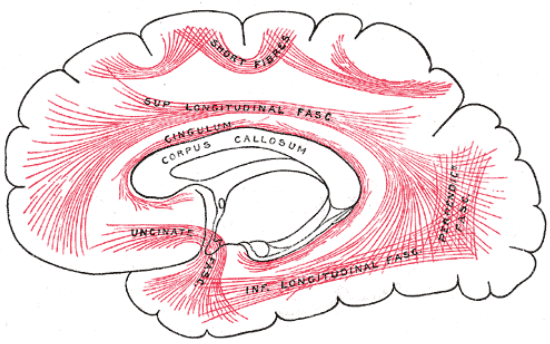

FIGURE 2.7: Association fibers
wikipedia

Association fibers link different areas of the same hemisphere (see Figure 2.7). The short association fibers, called "U-fibers" are located under the cortical mantel, connecting different gyri. The long association fibers include :

- The cingulum fasciculus, connecting the cingulate gyrus to the enthorinal cortex (cortex between the neocortex and hippocampus). These fibers have therefore a major role in communication of the limbic system. The anterior part plays a role in emotion and the posterior part is rather linked to cognitive functions,
- The uncinate fasciculus, connecting the frontal lobe to the temporal lobe is also considered as part of the limbic system,
- The superior longitudinal fasciculus including arcuate fasciculus, connecting the frontal lobe to the temporal and parietal lobes is involved in the language function. It connects Wernicke's and Broca's language areas in the left hemisphere,
- The inferior longitudinal fasciculus connecting the occipital lobe to the temporal lobe,
- The inferior-fronto-occipital fasciculus, connecting the occipital lobe to the frontal lobe.

The fornix connects the hippocampus to the mammillar corpus in each hemispheres. It contains fibers coming from the hippocampus. From the alveus, the fibers converge to form the fimbria. The fimbria of each hemisphre finally merge in the midline of the brain to form the body of the fornix. The body also divides near the anterior commissure.

2.5.4.3 Interhemispheric commissures

The interhemispheric commissures are white matter pathways connecting the hemispheres of the brain. The corpus callosum is the wider one, located deep in the interhemispheric fissure and is separated from the fornix by the septum lucidum. It connects the hemispheres and exhibits four major parts, in the antero-posterior direction : the genu, the body, the isthmus and the splenium (see Figure 2.8). The anterior commissure

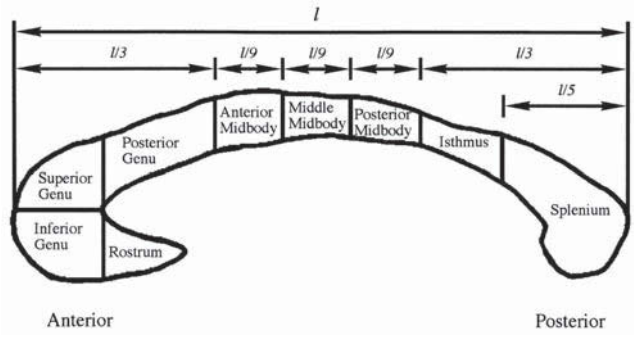

FIGURE 2.8: Corpus Callosum sections from [Highley et al., 1999]

crosses perpendicularly the anterior wall of the third ventricle connecting the olfactory bulbs, while the posterior commissure crosses the posterior wall of the third ventricle. The two fimbria are connected by the hippocampal commissure, connecting the two hippocampus. The Habenular commisure, a smaller bundle of fibers passing in the superior stalk of the epiphyse, connects the habenular nuclei.

We have defined the major macroscopic structures of the brain, dividing the cerebral matter into two major parts : the grey and white matter. This thesis focusing on the brain microstructure, the following section goes deeper in the tissue, describing white and grey matter at the cellular level.

2.6 Brain tissue microstructure

The brain microstructure is very complex exhibiting various types of cells, of different sizes and shapes. The macroscopic brain division into grey and white matter comes from their cytoarchitectural differences : the white matter is mainly composed of myelinated axons (giving the white color) and cells responsible for the myelination while the grey matter contains neuron cell bodies and astrocytes. We here describe the main components of the cytoarchitecture of the brain.

2.6.1 Brain cells

2.6.1.1 Neurons

Responsible for the transmission of the nerve signals, it is the main cellular corpus we can find in the brain. There are about 100 billion of neurons in a human brain. Their size varies from 4 microns to 100 microns. We can separate the neurons into the cell body, called pericaryon, the signal receivers called dendrites, and the projections, the axons (the main part of the white matter), conducting the nerve impulse (see Figure 2.9).

In the cell body, we find the nucleus that contains the DNA with the nucleole, containing proteins and RNA. Surrounding the nucleus, the cytoplasm contains the Nissl corpus (granular endoplasmic reticulum) and free ribosomes, synthesizing the proteins. We also find neurofilaments and neurotubules, organizing themselves in parallel within the axons. They are responsible for chemical transport. Finally, as we can find in other cells, the neuron cell contains different organites, such as mitochondrion (breathing of the cell and energy supply), the Golgi apparatus, which regulates the transport of molecules through the membranes and transforms the proteins and the lysosomes (digestion of the cell).

The dendrite contains the same types of organites as the cell body does, excepting the nucleus and the lysosome.

The axon part emerging from the neuron is not myelinated, but further from the cell body, a myelin sheath covers the axon.

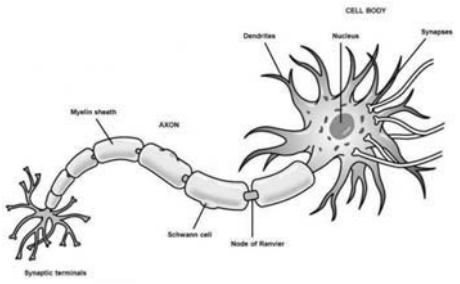

FIGURE 2.9: Description of the different parts of the neuron.
http://www.positscience.com/

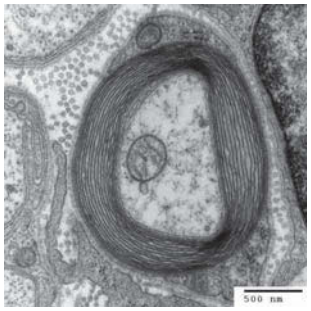

FIGURE 2.10: Transmission electron micrograph of a myelinated axon
http://commons.wikimedia.org/

This myelin sheath (Figure 2.10) is regularly interrupted by the Ranvier nodes, playing a major part in the action potential propagation. The myelin contains several layers, alternating bewteen protein (30%) and lipid (70%) susbtances. This layer has an average length of 12 μm. The axons exhibits further ramifications to nerve or muscular cells. Those ramifications end with synapses, responsible of the transmission of the neuron

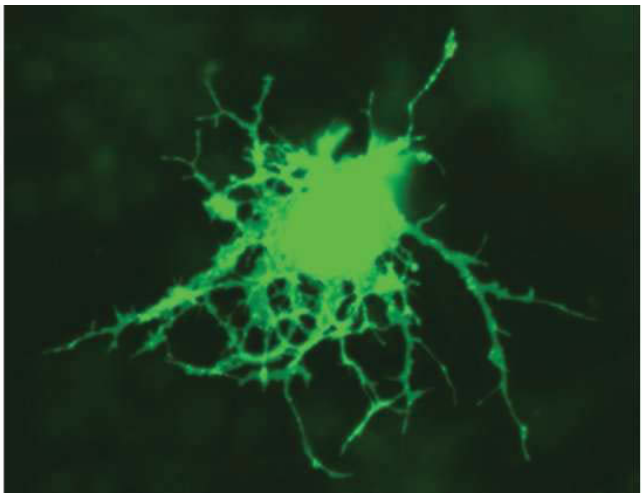

FIGURE 2.11: Oligodendrocyte. Adapted from http://cnx.org

signal. A neuron could be either efferent (motor neurons) or afferent (sensory neurons), the former carrying away the nerve impulses, the latter from receptors to the central nervous system.
In the cortex, several kind of neurons can be found :

- The pyramidal cells, characterized by a pyramidal cell body. Their diameters varie from 10 to 70 microns. They have long axons leaving the cortex to connect other cortical areas.
- The granular cells which are smaller (diameters lower than 10 microns). They are interneurons, their axons stay in the cortex.
- The cells of Martinotti, having small dendrites and their axons run towards the surface and turn to follow the superficial layers of the cortex. They make contact with pyramidal cells through their synapses.
- Fusiform cells : their axons reach the surface and their dendrites connect other cortical layers.

2.6.1.2 Oligodendrocytes

The oligodendrocytes are mainly responsible for the myelin production. These cells are present in the grey matter, where they play a metabolic role and in the white matter, where they product the myelin, surrounding the axon with their prolongations. Their cell bodies, appearing oval or round, have an average length of 6-8μm. Few processes emanate from the cell body (see Figure 2.11).

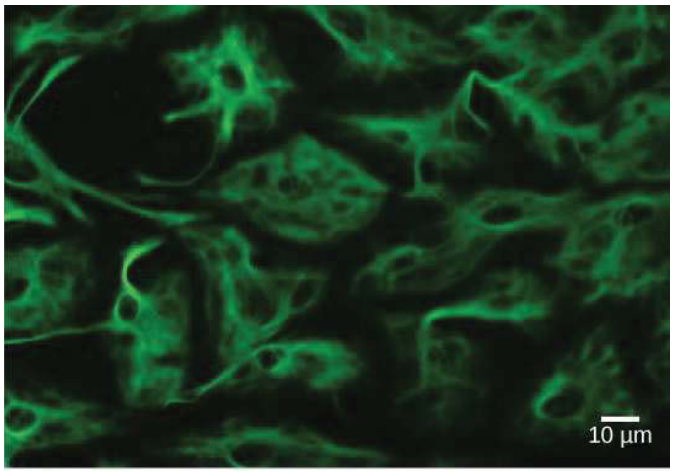

FIGURE 2.12: Astrocyte. Adapted from http://cnx.org

2.6.1.3 Astrocytes

Astrocytes are part of the conjunctive tissue and highly present in the brain (see Figure 2.12). These cells have big nuclei. The astrocytes are narrow, with several prolongations and they have a star-like shape. In the grey matter, the protoplasmic astrocytes exhibit short prolongations. In the white matter, they have fewer but longer prolongations, they are called fibrous astrocytes and they have an average size of 10-12μm. Their processes form the glial sheets between axons. Astrocytes play several roles in the nervous tissue : they regulate the blood flow, they sustain the hemato-encephalic barrier, they maintain the pH level, and the ionic concentration, they participate to the brain fixing in case of damages (gliosi) and nerve communication, they secrete substances for oligodendrocyte survey, myelin formation and myelin reformation.

2.6.1.4 Microglia

The last cells of the glia are the microglia cells. We can find them in both grey and white matter, but their density varies from a region to another. They represent about 13 % of the cells but are more present in white matter than in grey matter. They have an ovoid nucleus ($\approx$ 5.1μm by 2.2μm) and a small cell body but their shape varies. They are macrophage cells.

2.6.2 Cortex histology

The previously described cells are found in the neocortex which can be divided into six different cell layers (see Figure 2.13) :

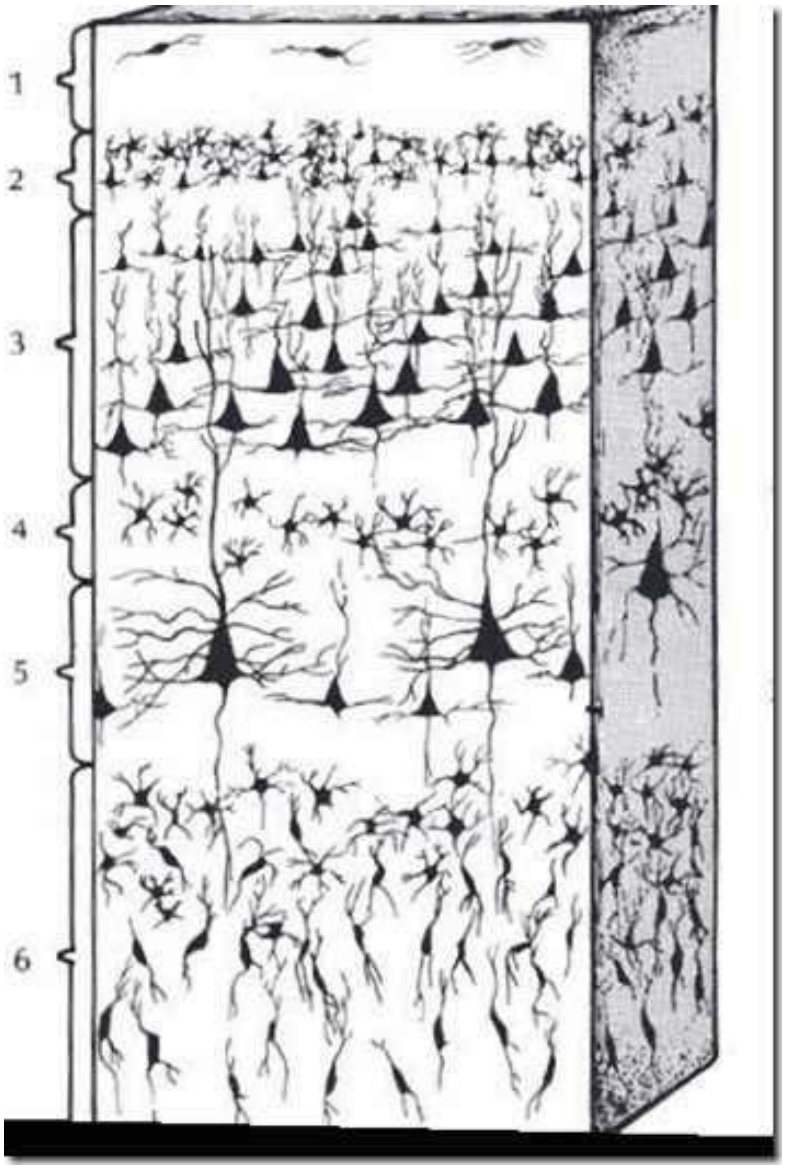

FIGURE 2.13: Cortex microstructure

- Layer I : the molecular layer, with few neurons, several dendrites and axons in contact through their synapses,
- Layer II : the external granular layer with granular, star-shaped, pyramidal cells and axons/dendrites connections,
- Layer III : the external pyramidal layer, including medium sized pyramidal cells and Martinotti cells,
- Layer IV : the internal granular layer, including dense packing of granular cells,
- Layer V : the ganglonic layer, with big pyramidal cells and Martinotti cells,
- Layer VI : the polymorph layer, including all type of cells

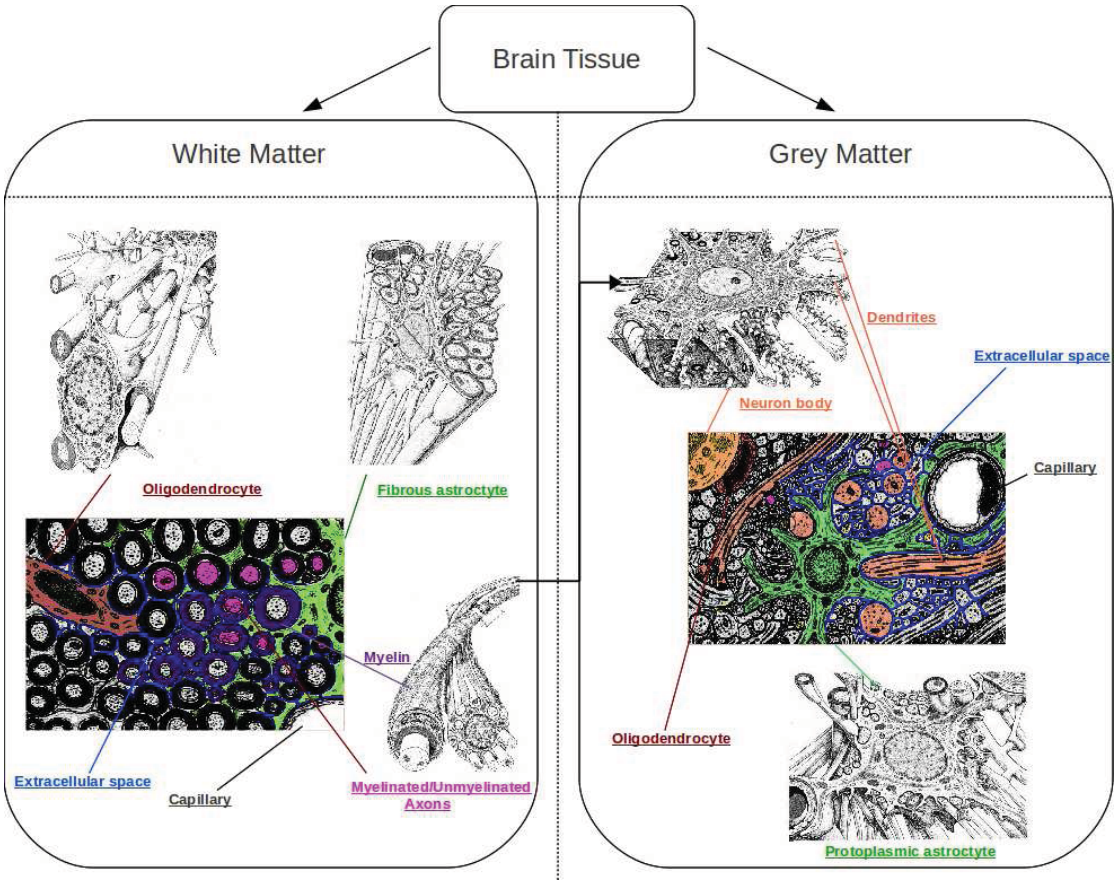

FIGURE 2.14: Brain tissue microstructure

2.6.3 White matter histology

White matter mainly contains myelinated and unmyelinated axons, surrouned by oligodendrocytes and fibrous astrocytes.

2.7 Brain diseases and microstructure

Brain pathologies affect the microstructure. In the case of neurodegenerative diseases, neuron death occurs in different regions of the brain. In Parkinson's, for example, we observe a loss of dopaminergic neurons in the substantia nigra. This kind of modifications changes the local organization of the microstructure, for example a reduced neuron density. Accessing to the brain microstructure *in vivo* could therefore help to study the evolution of brain pathologies.

2.8 Conclusion

We described here the main features of human brain anatomy, at both macroscopic and microscopic levels. The human brain has a very complex structure, and the task of studying its microstructure by MRI is therefore very difficult. The idea behind the work of this thesis is to extract indirect or more direct parameters able to characterize the microstructure, despite its complexity. We need then to explore the hidden information contained in the MRI signal, and the potential of the wide variety of MRI sequences to get closer to the microscopy by MRI. The following chapter describes the principle of MRI and the sequences used in this work.

Chapter 3

MRI modalities dedicated to the study of tissue microstructure

3.1 Introduction

Magnetic Resonance Imaging, introduced by [Lauterbur, 1973] and [Mansfield, 1977] is a key modality in the human brain study, since it relies on the magnetic resonance phenomenon of water protons, which represent around 80% of the brain. Moreover, it gives access to different kinds of information. First, mapping the anatomy of the brain structures is possible thanks to T_1 and T_2 weighted contrasts, T_1 and T_2 being the two characteristic times of the relaxation phenomenon. Second, a functional analysis of the brain is accessible using the susceptibility effects in activated regions induced by the oxyhemoglobine carying the oxygen required to brain activity. Finally, MRI has became a powerful tool to probe brain architecture at the cellular scale, corresponding to a scale inferior to the resolution of the acquired images. There is growing interest in quantitative MRI of T_1 and T_2 parameters since various multi-compartment models allow today to quantify the volume fractions of the different pools of water in the tissue. Diffusion MRI or dMRI is sensitive to the movement of water molecules in the tissue and thus allows to measure for example the orientation of axons, packed in large fascicles of fibers, paving the way in the last decade for exploring the anatomical connectivity of the brain and considering the study of the anatomical and functional networks of the human brain *in vivo*. Moreover, dMRI is becoming a way to explore not only the anatomical connectivity but also its microstructural organization. Indeed, the membrane geometry of the different cells of the brain hindering or restricting the movement of water molecules, leaving its signature in the diffusion weighted signal. The community presently works to develop biophysical models from which it is possible to extract characteristic quantities

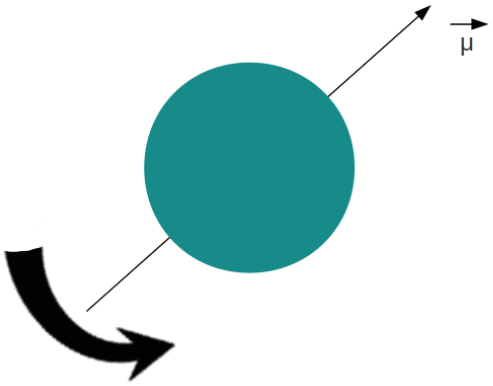

FIGURE 3.1: Magnetic Moment of a proton

of the various populations of cells. This thesis being focused on quantitative T_1 and T_2 MRI and diffusion MRI microscopy, it is important to introduce here the physical basis of MRI and present in particular the sequences related to quantitative and diffusion MRI.

3.2 Principles of magnetic resonance imaging

This section describes the basic principles of magnetic resonance imaging (MRI). We explain how it is possible to obain contrast between tissues from the induced magnetic resonance of the protons of water molecules. This chapter is inspired by the book [Kastler et al., 2001], the courses of Pr Fessler (http://web.eecs.umich.edu) and the website www.imaios.fr, the chapters of [Brion, 2013], [Marrakchi-Kacem, 2011], .

3.2.1 Magnetic resonance phenomenon

3.2.1.1 Magnetic moments of protons

The magnetic resonance imaging finds its basis in the magnetic resonance of protons, [Bloch, 1946], and mainly from protons from the hydrogene nucleus. These particles have the characteristic of rotating on themselves, around an axis passing through their centers (see Figure 3.1). Protons are also charged particles, and while spinning, they create a magnetic moment $\overrightarrow{\mu}$, called spin. The summation of all these spins gives a net magnetization $\overrightarrow{M}$. In the absence of any additional magnetic field, the individual spins have random orientations, resulting in a null magnetization : $\sum \overrightarrow{\mu} = \overrightarrow{M} = \overrightarrow{0}$.

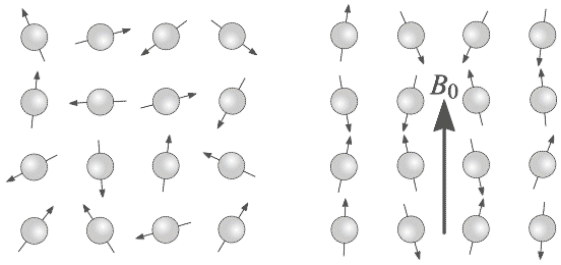

FIGURE 3.2: Left : Protons behavior in the absence of magnetic field , Right : Alignment in the presence of an external magnetic moment

3.2.1.2 Equilibrium state in the presence of a magnetic field B_0

But in the presence of a static magnetic field B_0, all the spins align with it, giving birth to two populations of spins : those having spins parallel to B_0 and those having spins antiparallel to it (see Figure 3.2). The protons precess around B0 with the angular frequency equals to the Larmor frequency ω_0 :

$$\omega_0 = \gamma B_0,$$

with γ the gyromanetic ratio ($\gamma = 267,5 \times 10^6$ rad s^{-1} T^{-1} for the hydrogene nucleus). This phenomenon of precession was first described by [Purcell et al., 1946] as a double precession, with a transversal and longitudinal component. Higher number of protons precesses in the parallel direction, giving a non-null magnetic moment aligned in the same direction as B_0, along the longitudinal direction. In the transversal direction, spins are not phased, leading to a null component on average.

3.2.1.3 Perturbation of the equilibrium by a radio frequence B_1 : excitation

If we perpendicularly add to B_0 a rotating electro-magnetic field B_1 (called radio frequence, RF), with an angular frequency equals to the Larmor frequency, there is a transfer of energy to the protons aligned with B_0: this is the magnetic resonance phenomenon. This rotating field excites the protons, that precess not only around B_0, but also around B_1. It "tilts" the global magnetization into the orthogonal plane to B_0 (in the case of a 90° pulse), inducing a magnetic resonance. At the microscopic level, the protons change of energy level, from parallel state to antiparallel state. The longitudinal magnetization then decays, and a tranversal component appears, stemming from in phase spins. Depending on the duration of the B_1 application, one can get a 90° tilt yielding a transverse magnetization, or a 180° tilt where the entire macroscopic magnetization is inversed along the longitudinal axis. When B_1 is stopped, the system returns

back to its equilibrium state : this is the relaxation phenomenon. This phenomenon is described in Figure 3.3.

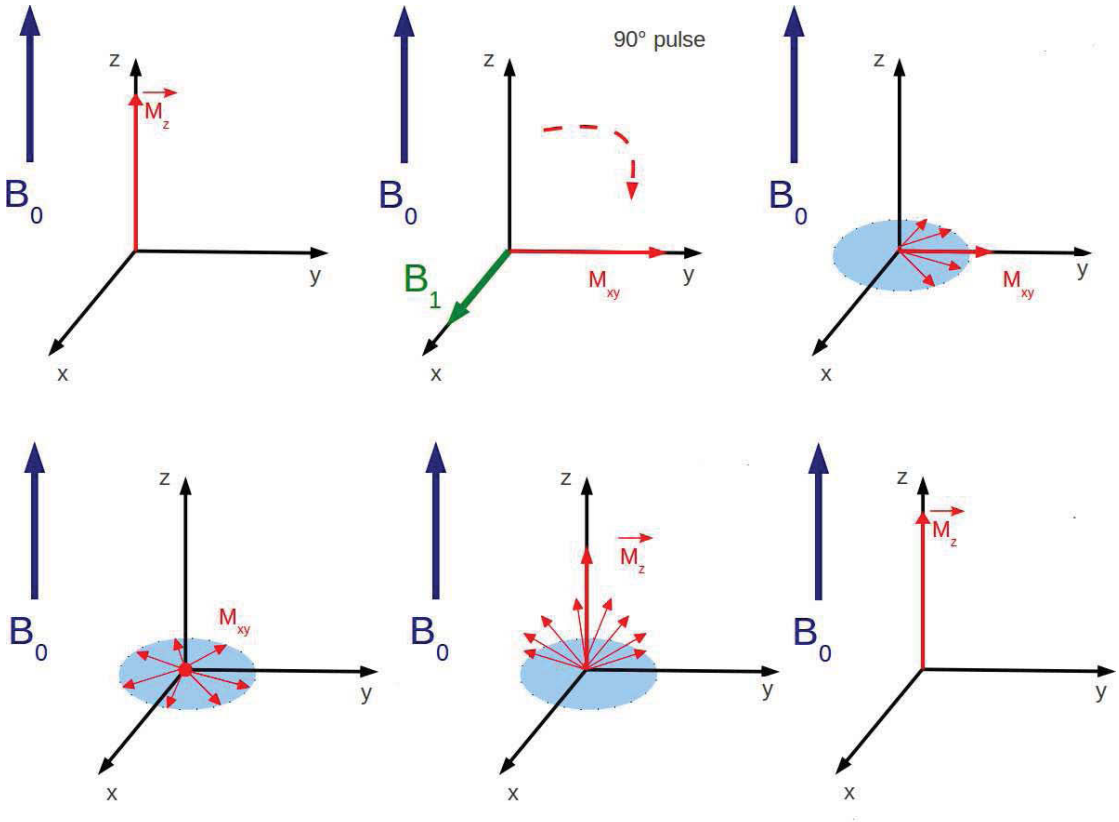

FIGURE 3.3: Excitation and relaxation phenomena.

3.2.1.4 Bloch equations, T_1 and T_2 relaxation times

We assume a referential (x,y,z) where B_0 is aligned in the z direction and B_1 is applied perpendicularly, in the (xOy) plane. The temporal evolution of magnetization can be described with the Bloch equations, [Bloch, 1946]:

$$\frac{dM_x(t)}{dt} = \gamma\left(M_y(t)B_z(t) - M_z(t)B_y(t)\right) - \frac{M_x(t)}{T_2}, \tag{3.1}$$

$$\frac{dM_y(t)}{dt} = \gamma\left(M_z(t)B_x(t) - M_x(t)B_z(t)\right) - \frac{M_y(t)}{T_2}, \tag{3.2}$$

$$\frac{dM_z(t)}{dt} = \gamma\left(M_x(t)B_y(t) + M_y(t)B_x(t)\right) - \frac{M_z(t)-M_0}{T_1}, \tag{3.3}$$

where M is the magnetization, γ the gyromagnetic ratio, B the magnetic field, T_1 and T_2 two characteristic relaxation times. If we apply an RF B_1 of frequency ω_1 :

$$B_{1x}(t) = B_1 cos(\omega_1 t), \tag{3.4}$$

$$B_{1y}(t) = B_1 sin(\omega_1 t), \tag{3.5}$$

$$B_{1z}(t) = 0. \tag{3.6}$$

We introduce the rotative frame (x'Oy') where B_1 is aligned to the axis (Ox') (see Figure 3.4). We define the transverse magnetization as : $M_{x'y'} = M_{x'} + iM_{y'}$. Right after the

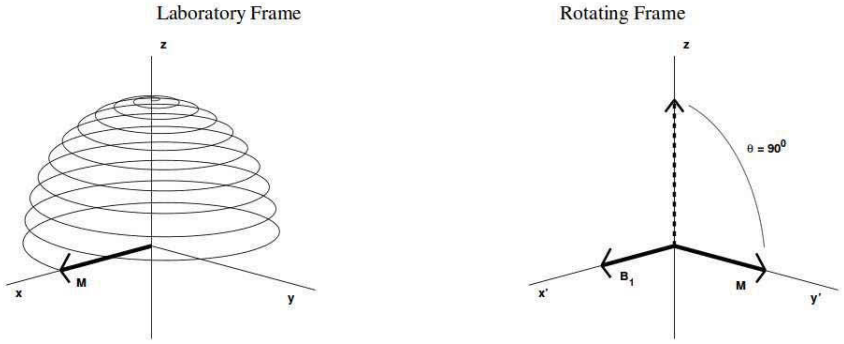

FIGURE 3.4: Laboratory frame and rotative frame.
http://web.eecs.umich.edu

90° RF application, $M_z = 0$ and $M_{xy} = iM_{zeq}$. Then the relaxation phenomenon can be expressed as follows in the new referential (x',y',z) :

$$M_{x'y'}(t) = M_{zeq} \exp(\frac{-t}{T_2}), \tag{3.7}$$

$$M_z(t) = M_z(0) \exp(-\frac{t}{T_1}) + M_{zeq}(1 - \exp(-\frac{t}{T_1})), \tag{3.8}$$

with M_{zeq} the longitudinal magnetization at the equilibrium, $M_z(0)$ is the longitudinal magnetization immediately after the RF pulse. Equation 3.8 describes the behaviour of the longitudinal relaxation : during the phase of the relaxation, protons which have moved from parallel to antiparallel state will return to their original state, exchanging the energy with their molecular environment, leading to a growth of the longitudinal magnetization, going back to its original value. The longitudinal growth of the global magnetization follows an exponential behaviour, characterized by the T_1 relaxation time defining the necessary duration to recover 63% of the initial value. T_1 is called spin-lattice relaxation time because it involves an exchange of energy between water molecules and proteins, lipids and macromolecules. This T_1 depends on the characteristics of the tissue and of B_0, and varies with the molecular environment. For example, T_1 is longer in liquids. Equation 3.8 describes the behaviour of the transverse magnetization. Inhomogeneities of the B_0 field induced by different molecular environments create a

dephasing between the spins, thus having an angular frequency slightly different from ω_0. During the excitation, the spins are all phased but when B_1 is stopped, they naturally return back to a dephased state, and the transverse global magnetization reduces. This reduction follows an exponential decay, characterized by the T_2 relaxation time defining the necessary duration to the transverse magnetization to decrease of 37% of its initial value. The temporal evolutions of the longitudinal and transverse magnetizations after a 90° are depicted in Figure 3.5. Like T_1, T_2 depends on the tissue and its molecular composition, and it is longer in liquids. It is called spin-spin relaxation time, because T_2 relaxation involves the dephasing of protons due to interactions with each other. T_2 relaxation is faster than T_1 relaxation, so T_2 is always longer than T_1. Both T_1 and T_2 depends on the static magnetic field.

3.2.1.5 T_1 and T_2 relaxation times for different tissues and different fields

Table 3.1 shows some T_1 and T_2 values for gray and white matter at different fields. The T_1 and T_2 differences among the tissues creates the MRI contrast with proton

	T_1-GM	T_1-WM	T_2-GM	T_2-WM
1.5 Teslas	1000 ms	700ms	110ms	100ms
3 Teslas	1330 ms	830ms	90ms	80ms
7 Teslas	2130 ms	1220ms	55ms	45ms

TABLE 3.1: T_1 and T_2 relaxation times of gray and white matter at 1.5T (from http://users.fmrib.ox.ac.uk/ peterj/lectures/), 3T (from [Wansapura et al., 1999]) and 7T ([Rooney et al., 2007])

density. Depending on the MRI sequence used to acquire the signal, we can get different constrast weighting in T_1, T_2 or ρ. The T_1 contrast is called "anatomical contrast" since the gray matter appears gray and the white matter appears brighter. We find the inverse contrast in a T_2-weighted image. Figure 3.6 shows T_1 and T_2-weighted images obtained at 3 Teslas. Mechanisms of T_1 and T_2 weighted contrasts will be described later.

3.2.2 Origin of the signal acquired in MRI

The variation of the transverse and longitudinal magnetization is used to get the MRI signal. The reception coil, placed in the transverse plane of the MRI system (see figure 3.7) receives the signal coming from the transverse magnetization, called Free Induction Decay (FID). This signal is a sinusoid weighted by the T_2 exponential. Back into the initial referential we have from 3.8 :

$$M_{xy}(t) = M_{x'y'}(t) * \exp(-i\omega_0 t) = M_{zeq} * \exp(-i\omega_0 t) * \exp(-\frac{t}{T_2}).$$

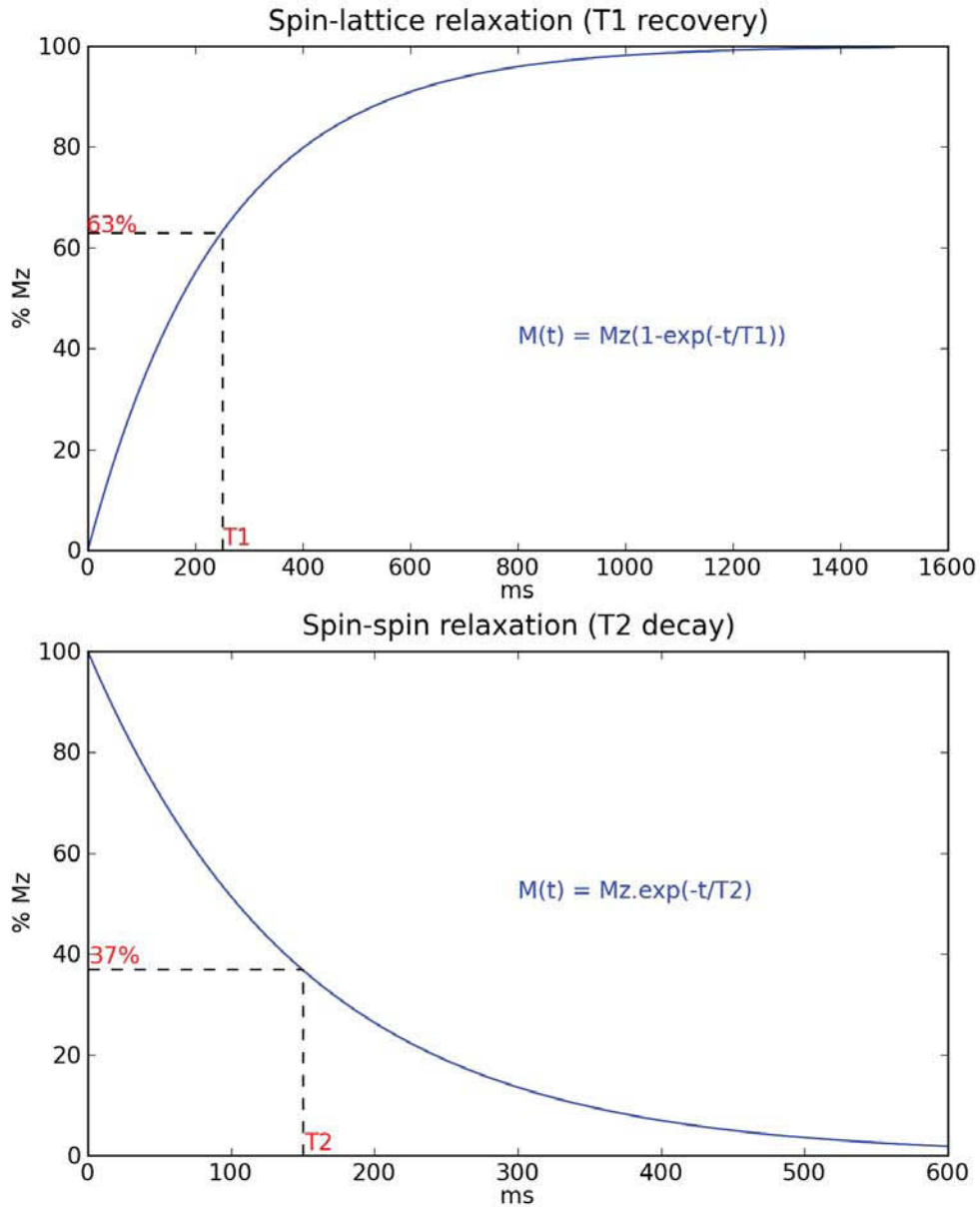

FIGURE 3.5: Temporal longitudinal and transverse magnetization evolution

In fact, this signal doesn't depend on T_2 but on T_2^* because of molecular inhomogeneities and B_0 microscopic inhomogenities. We define : $\frac{1}{T_2^*} = \frac{1}{T_2} + \gamma \Delta B_0$. Then the transverse magnetization follows :

$$M_{xy}(t) = M_{zeq} \exp(-i\omega_0 t) \exp(-\frac{t}{T_2^*}) \tag{3.9}$$

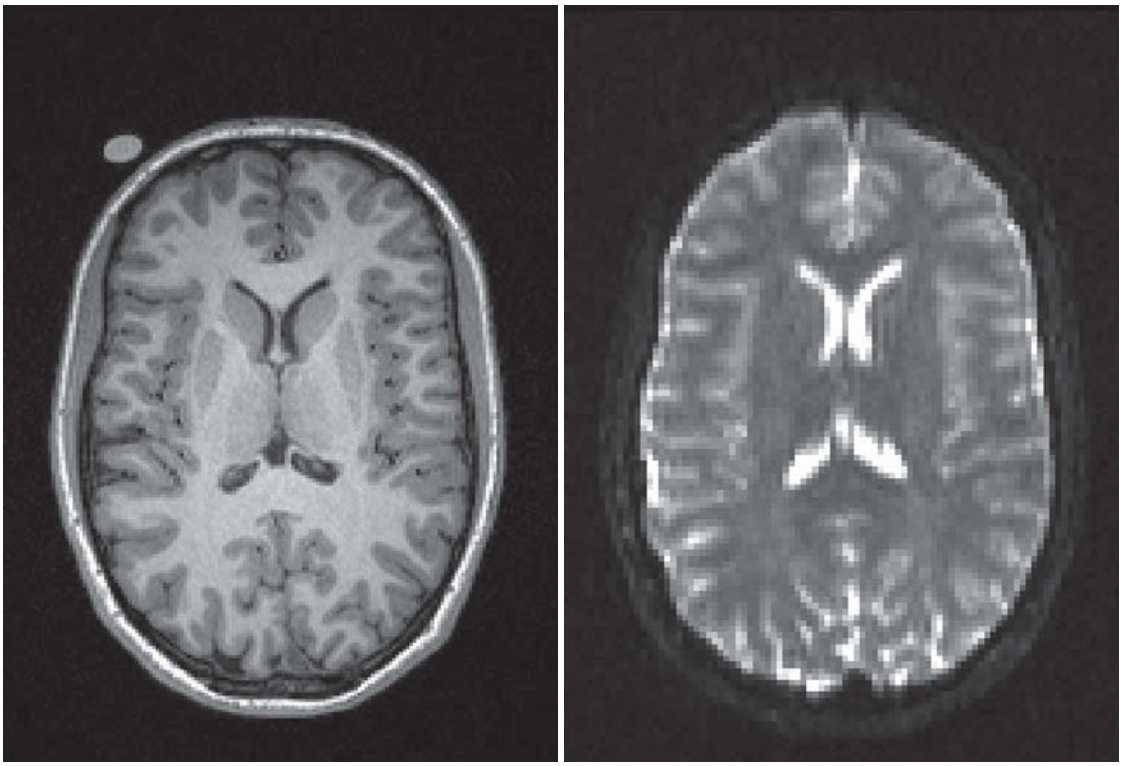

FIGURE 3.6: T_1-weighted image (left) and T_2-weighted image (right) from one subject of the Archi database

By using combinations of 90° and 180° impulsions, in MRI sequences,we can acquire signal more or less sensitive to either T_1 or T_2 relaxation times. The following section presents the basis of the MRI sequences.

3.2.3 From FID to image

3.2.4 Spatial encoding

We just explained the origin of the signal acquired by the coil of the MRI scanner, the FID. But how can we form the image from this signal ? In fact, during a typical MRI sequence, several magnetic gradients will be applied in different directions in order to encode the information (see Figure 3.8). There exists 2D and 3D imaging. In the case of 2D imaging, one gradient is applied along the z direction, in order to select the slice, another one is applied in the x direction, the phase gradient, and finally the readout gradient is applied in the y direction. These gradients, differentiating the spins by their phases and frequencies, encode them by their frequencies and dephasing.

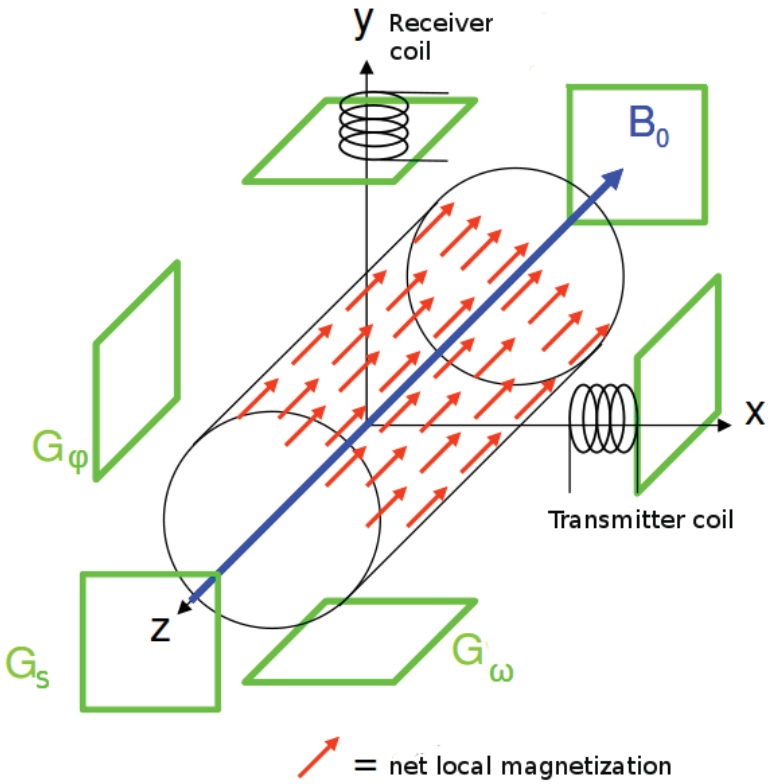

FIGURE 3.7: MRI system : With G_ϕ the phase encoding gradient, G_s the slice gradient, G_ω the frequency encoding gradient, B_0 the static magnetic field

3.2.4.1 Slice gradient

A magnetic gradient of strength G_s is applied in the same direction as B_0, perpendicularly to the slice to acquire. Thanks to the gradient, a different gradient field, proportionnal to G_s, will be applied in each position along z. The protons at the position z precess with the same Larmor frequency, corresponding to $\omega_z = \gamma(B_0 + G_s * z)$. On each slice of the volume, the protons all process at the same frequency, but this frequency differs from one slice to another. A rotating magnetic field B_1 at the frequency ω_1 corresponding to the frequency of one slice is applied. Finally, only the protons of this slice will be excited, this is the slice selection. This gradient is applied during the RF application, allowing to select only the desired spins. The resolution in z is defined by the width of the RF or by the gradient strength. In fact, in the common MRI sequences, the slice selection gradient has two lobes, one negative and one positive, allowing to rephase the spins because applying a gradient will necessarly involve a dephasing : the first lobe will dephase the spins, while applying the desired frequency, and the second lobe will rephase them, in order to get rid of the dephasing. when the gradient is turned off, all the spins are rephased : this is called "a gradient echo".

3.2.4.2 Phase encoding

A second gradient G_ϕ is applied, perpendicularly to the future lines of the image, this is the phase gradient. This gradient is applied during a short time, and induces a dephasing of the spins depending on the lines where they belong to, all the spin on one line have therefore the same phase at the end of the gradient application. This encoding has to be repeated the number of lines, with different gradient strength.

3.2.4.3 Frequency encoding

Once G_s and G_ϕ are applied, each line of the selected slice can be distinguished because there spins present different dephasing. One final gradient, the readout gradient, G_ω, is applied perpendicularly to the columns, so each columns is encoded with its own frequency. Finally, each proton is characterized by a single association (phase, frequency). The same problem of cumulated dephasing between the acquisitions occurs for the frequency gradient, this is the reason why it will also be bipolar, allowing to rephase the spins. But, in this case, the measure of the signal is located at the time of the spin echo but it is not immediate, so the reader gradient has to have one negative lobe followed by two positive lobes, since the gradient echo will occur at the end of the second lobe. The three gradients G_ϕ, G_ω and G_s ensure the 3D encoding and localization (see Figure 3.8), however this does not take place in a cartesian space but in the Fourier domain, called K-space and described in the next subsection.

3.2.4.4 3D imaging

We have described the specificity of spatial encoding in 2D MRI acquisition. This encoding can be generalized for 3D acquisition. In this case, a whole volume is excited. The third direction is phase encoded using a second phase-encoding gradient.

3.2.5 K-space and FFT

During the acquisition, each couple frequency/phase is registered in a matrix called "K-space" (see Figure 3.9). Each FID contains the informations coming from all the spins and a decoding part is necessary to recover the initial image. This is possible thanks to the 2D-Fourier transform. In each point (k_x,k_y) of the k-space, we can write :

$$S(k_x(t), k_y(t)) = \int_x \int_y M(x, y)(t) \exp -i(k_x(t)x + k_y(t)y)dxdy \tag{3.10}$$

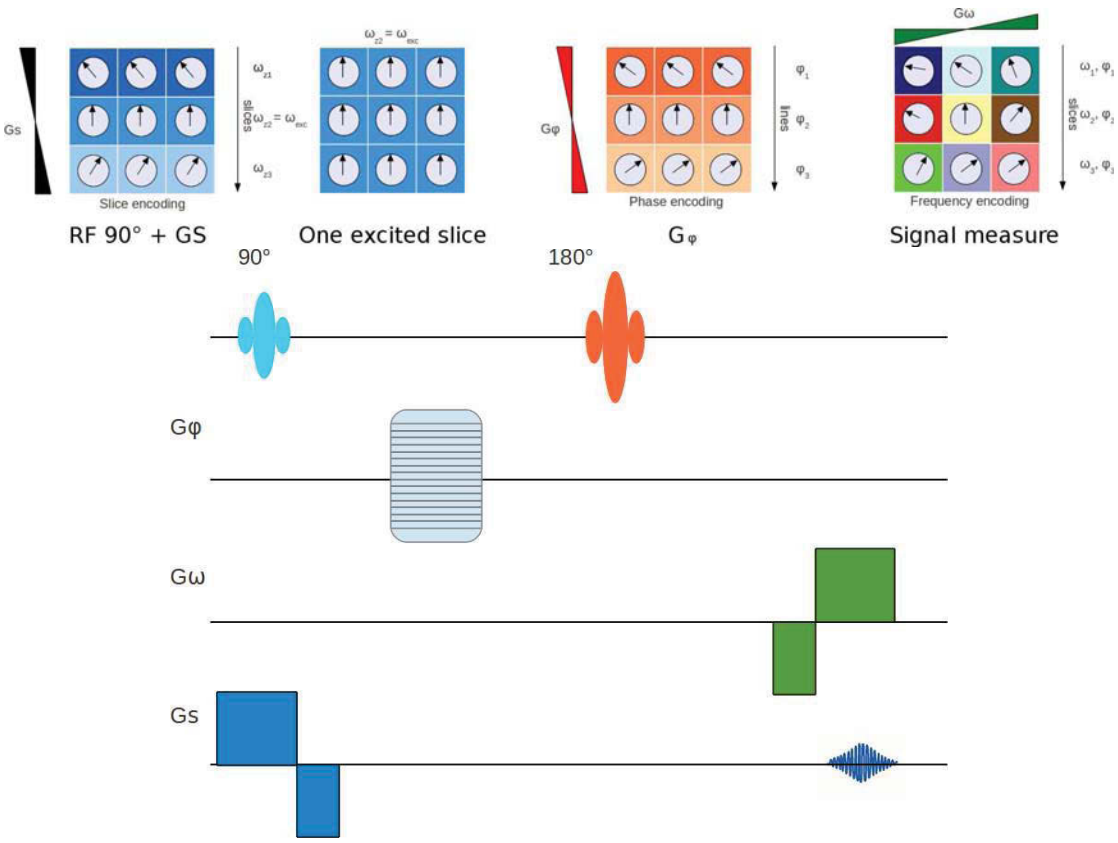

FIGURE 3.8: Spatial encoding. Top line : spatial encoding, bottom line : basic MRI sequence diagram

where $k_x(t) = \gamma \int_0^t G_\omega(t')dt'$ and $k_y(t) = \gamma \int_0^t G_\phi(t')dt'$ The maximum value of k_x will determine, the resolution of the final image taking its inverse value. Therefore, the higher the gradient strength, the higher the resolution. Equation 3.10 shows that a simple 2D Fourier transform links the image to its signal measurement in the K-space. As a consequence, applying an inverse 2D-Fast Fourier Transform, one can reconstruct the image from the mix of all signals coming from protons. In the case of 3D acquisition, a 3D K-space is filled and the image is reconstructed using a 3D-FFT. This way, the center of the k-space corresponds to low frequencies and the extremities to high frequencies. One particularity of the K-Space, coming from the general property of the Fourier space, is the conjugate symmetry between all quadrants. This property can be used to reduce the acquisition time, acquiring only a subset of the lines of the K-space and re-building the entire space by symmetry.

3.2.6 Parallel imaging

It is possible to increase the signal to noise ratio and reduce the acquisition time using parallel imaging technique. Instead of using a single reception coil, several coils can be combined to measure the signal, each of them receiving the signal from each region

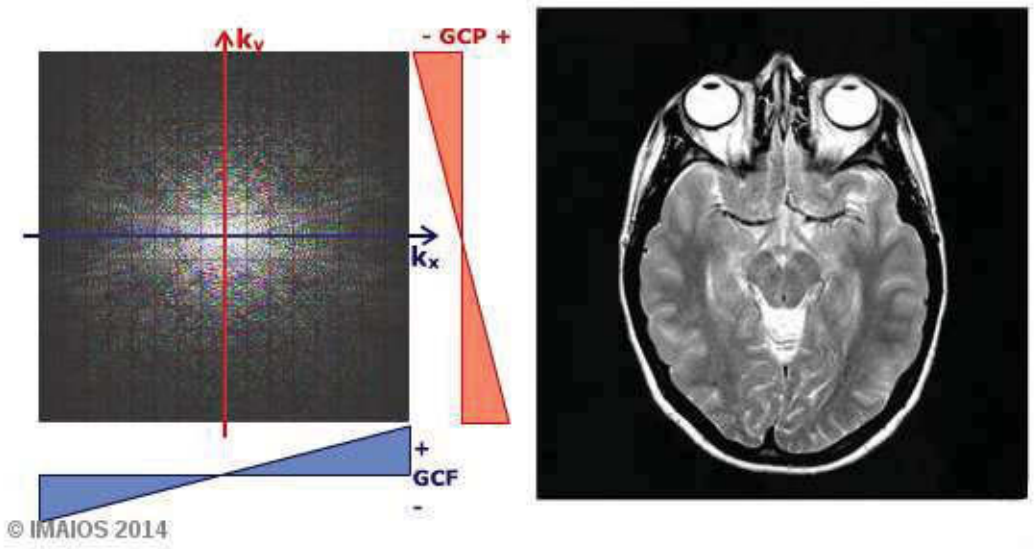

FIGURE 3.9: K-space from www.imaios.fr

located in front of them. The array of reception coils (or channels) allows to acquire a reduced amount of K-space data. Different algorithms have been developed to reconstruct the image from the different signals : the SENSE (sensitivity encoding for fast MRI, [Pruessmann et al., 1999]) algorithm merges the field of view acquired by each coil to reconstruct the image using the sensitivity of the coils while techniques such as GRAPPA (generalized autocalibrating partially parallel acquisition, [Griswold et al., 2002]) method compute the missing lines of the K-space before reconstructing the image using the Fourier transform.

3.2.7 MRI sequences used in this thesis

We previously introduced the phenomenon of excitation-relaxation of the spins in the tissue and how to exploit this phenomenon to obtain tissue images thanks to magnetic gradients applied along the three space directions. The basic sequence therefore requires an excitation pulse, and the encoding gradients. From this basis, a wide variety of MRI sequences was developed, depending on the desired contrast or acquisition duration. One of the first sequence, called Spin Echo was introduced by [Hahn, 1950]. It contains one 90° excitation pulse, spatial encoding gradients and one 180° refocusing pulse. Only one K-space line is filled between two excitation pulses (i.e during the repetition time TR of the sequence).

Usually, the K-space is filled line by line and one line is read thanks to the frequency encoding gradient. One needs to increment the phase gradient to go from one line

to another. But in clinical applications the acquisition duration has to be limited. Several sequences use different strategies of displacement to cover the K-space, acquiring several lines in one TR (MultiShot RARE, Echo Planar Imaging (EPI), Fast Spin Echo), reducing the repetition time using gradient echo (reducing the flip angle) or exploiting the symmetry properties of the K-space (Half-Fourier acquisition, Spiral acquisition). We limit our presentation of the MRI sequences to Spin Echo, Echo Planar Imaging and Gradient Echo used in the frame of this thesis. Some specific sequences derived from Spin Echo and EPI dedicated to relaxometry and diffusion studies will be introduced in the next sections.

3.2.7.1 Spin Echo Sequence

The first MRI sequence is the spin echo sequence [Hahn, 1950] depending on T_1 and T_2 relaxation time. After a 90° pulse, all the spins are phased and will progressively dephase because of molecular inhomogeneities. After a given time TE/2 (TE being the echo time), a 180° pulse is applied, so the spins are rephased at TE, inducing a spin echo. This trick allows to get rid of B_0 inhomogeneities, and to have access to the real T_2, and not T_2* corresponding to the relaxation time integrating B_0 inhomogeneities. The sequence diagram is shown in Figure 3.10. In a Spin Echo sequence, only one line is acquired between the 90° and the 180° pulses. The duration between the two 90° pulses corresponding to two consecutive lines is called the repetition time (TR). To cover the entire k-space, one needs as many TR as lines in the K-space. In sequences like the RARE sequence, additional 180° pulses create other echoes following the first one and a new phase encoding is applied before the next echo to acquire several lines of the K-Space. In the case of the Spin Echo sequence, the transverse magnetization can be expressed as follows for $t > TE$:

$$\boxed{M_\perp = M_z(0)exp(1 - TR/T_1)exp(-TE/T_2)}. \tag{3.11}$$

3.2.7.2 Gradient Echo Sequence

We already described the phenomenon for the gradient echo when two negative and positive gradients of the same strength are applied successively. The gradient echo sequence differs from the spin echo by the use of a flip angle below 90° and the abscence of 180° refocussing pulse. The required angle to get the maximal information, called Ernst angle is defined as $\theta = acos(exp(-TR/T_1))$. Using greater angle (in particular a 90° angle)

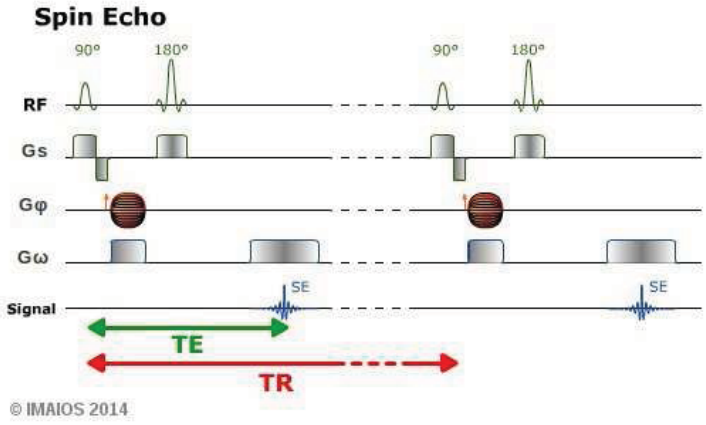

FIGURE 3.10: Spin Echo sequence adapted from www.imaios.fr

doesn't provide more information. These sequence also allows to decrease the acquisition time : the longitudinal magnetization regrows faster for lower flip angles. It allows shorter TR and TE. The measured signal is weighted in T_2* since the inhomogeneities are not corrected in this sequence, since the flip angle is low, the transverse magnetization is lower too. The gradient echo is created by a bipolar gradient, corresponding to the frequency encoding gradient. During this sequence, reduction of TR below T_2 will induce residual transverse magnetization for the next repetition. This drawback can be managed using spoiling techniques such as RF spoiling or gradient spoiling.

3.2.7.3 Fast K-space acquisition: Echo Planar Imaging

The Echo Planar Imaging, EPI, (Figure 3.11) introduced by [Mansfield, 1977] allows to acquire the entire K-space in a single shot, but the resolution is limited and the acquisition is prone to many sources of artefacts. In a single RF excitation scheme (one TR), EPI allows to acquire several or the entire K-space. This technique uses the phenomenon of gradient echoes. After the combination of 90° and 180° pulses, G_ω, the gradient encoding for the frequency is applied, alternating quickly and therefore generating a spin echo for each oscillation. Each oscillation corresponds to a given line of the K-space. Phase-encoding blips are then applied for each echo, moving from one line to the next. EPI imaging can be either single or multi-shots, depending on the number of TR required to cover the k-space. This kind of imaging suffers from any field inhomogeneity that is integrated along the echo train, thus increasing its effect. Artefacts will be discuss later.

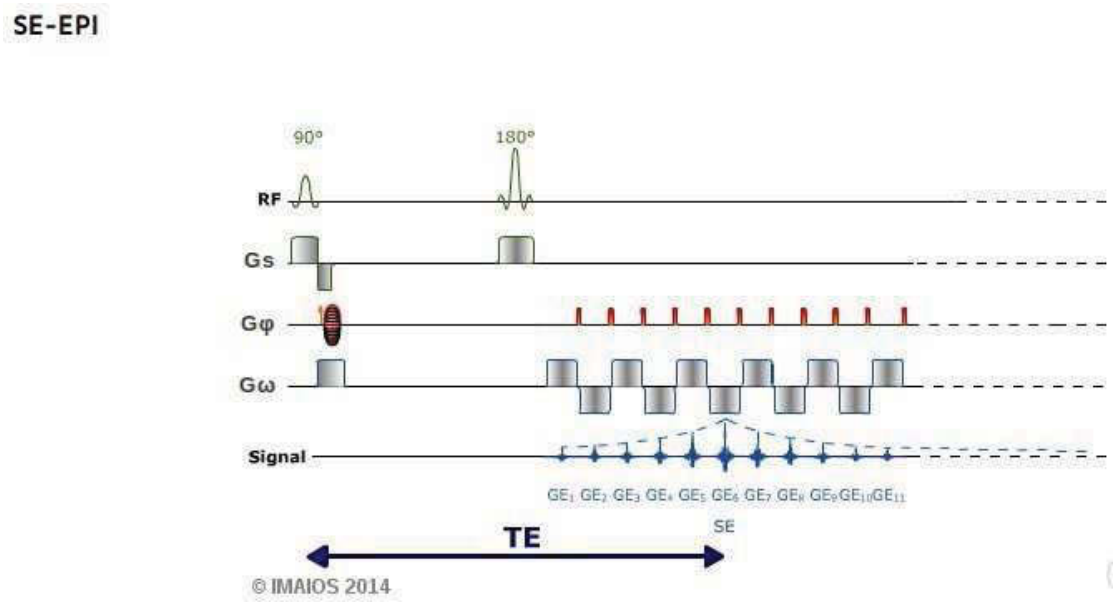

FIGURE 3.11: Spin Echo Echo Planar Imaging sequence from www.imaios.fr.

3.2.8 Contrast

The final constrast of the image comes from a trade-off between proton density, T_1 and T_2 ponderation, depending on the values of TR and TE. The repetition time influences directly the T_1-weigthing : if TR is long, the longitudinal magnetization of all the different tissues will be totally recovered, but if TR is short, the tissues having different T_1 times won't totally recover their longitudinal magnetization, so the tissue with the shorter T_1 will appear brighter than the tissue with a longer T_1. In the same manner, a short TE won't allow to differentiate two tissues with different T_2 and the T_2-weighting will be obtained with longer TE. Finally, T_1-weighted is obtained with short TR and TE, T_2-weighting with long TR and TE and a proton density contrast is obtained with long TR and short TE, to reduce the T_1 and T_2-weighting. Figure 3.12 shows different constrast with varying TR and TE.

In this section, we described Spin Echo and EPI sequences, used to obtain T_1-weighted, T_2-weighted or proton density-weighted images. The next sections will expose sequences dedicated to the extraction of parameters close to tissue microstructure.

3.3 Relaxometry and quantitative imaging

As we previously exposed, the contrast of images obtained by Spin Echo sequence are a mix of ρ, T_1 and T_2 weighting and are acquisition-dependent. This kind of sequences cannot directly provide quantitative parameters. Quantitative MRI, and in particular

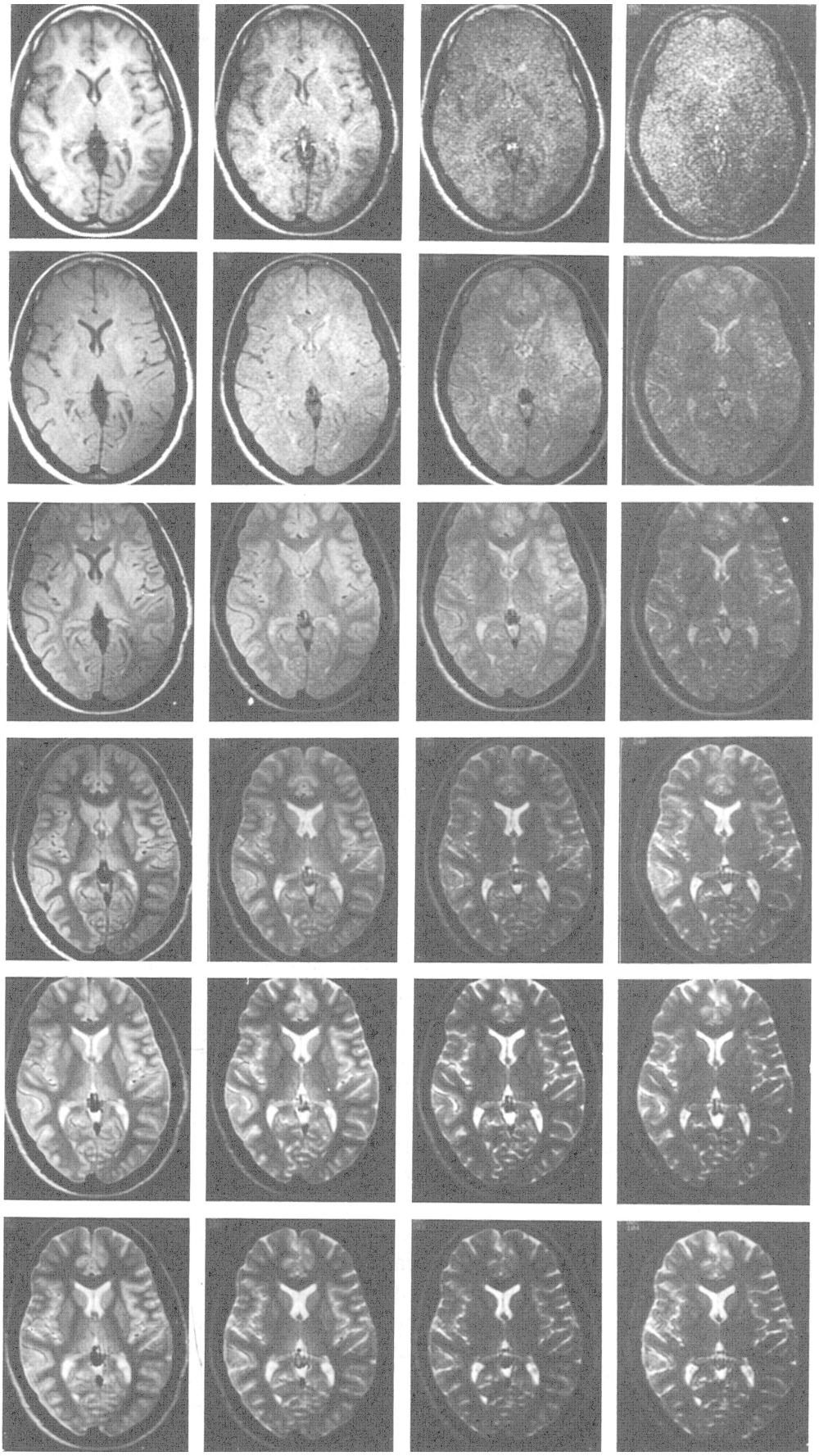

FIGURE 3.12: MRI contrast with varying TR and TE. TR is constant across rows and increasing down columns (TR=500ms, 1000ms, 2000ms, 4000ms, 8000ms, 12000ms from the top to the bottom line). TE is constant across the columns and increases across the rows (TE=25ms, 50ms,75ms,100ms from left to right).

relaxometry studies focus on the extraction of parameters such as magnetization transfer ratio (MTR), T_1, T_2 and T_2* relaxations times, etc... These parameters can be directly used to characterize a tissue and differentiate it from another.

Magnetization transfer sequences [Wolff and Balaban, 1989] provide a contrast dependent on the magnetization exchange between free protons and protons restricted to macromolecules. The latter have an extremely short T_2 relaxation times and cannot be directly imaged. This modality is widely used in the study of myelin and its destruction, in particular in the Multiple-Sclerosis disease, because, as we presented it in the chapter 2, myelin sheath contains macromolecules such as cholesterol. MT thus gives a quantitative information through the computation of the magnetization transfer ratio, on the microstructure through the signal arising from the protons bounded to these macromolecules. Magnetization transfer studies are beyond the scope of this work, this section, partly inspired by [Deoni, 2010] and [Hashemi et al., 2010], will focus on a particular field of quantitative MRI : T_1 and T_2 relaxometry.

T_1 and T_2 relaxation times provide contrast between tissues in clinical routine and they have been shown to be clearly related to the brain microstructure, and more precisely to the different water compartments defined by the cytoarchitecture of the white matter tissue: mainly the pool of water molecules trapped in the myelin sheats and the water in the extra and intra cellular spaces [Barkovich, 2000]. The former is characterized by short T_1 and T_2, because of the interaction of water molecules with large molecules such as cholesterol, highly present in myelin, the latter exhibits longer T_1 and T_2 times since molecules don't interact with such molecules, the water is more free. Therefore, mapping these times may certainly provide insights about the brain microstructure and imaging-based biomarkers of pathological tissues [Stevenson et al., 2000]. The T_2 relaxation time has been popular to map the iron content of the humain brain [Hasan et al., 2012], but one even more popular application of relaxometry study is the characterization of myelination maturation [Deoni et al., 2012] or demyelination in pathologies thanks to the sensitivity of relaxation times to myelin water content [Deoni et al., 2010]. In this kind of studies, the T_1-weighted and T_2-weighted signals are modelled using linear mixtures of signals stemming from several compartments [Deoni et al., 2008], [Deoni et al., 2012], with a short time compartment (corresponding to the water trapped in the myelin), a long time compartment (intra/extra cellular water) and sometimes an additional compartment corresponding to free water to deal with Cerebrospinal Fluid contamination. In order to be feasible in clinical routine, T_1 and T_2 mappings should remain short but fully reliable. The next subsections present the sequences used to map T_1 and T_2 relaxation times.

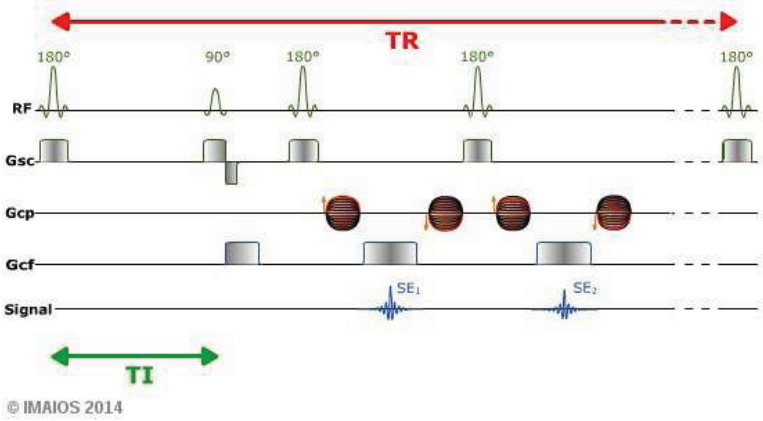

FIGURE 3.13: Inversion Recovery sequence www.imaios.fr .

3.3.1 Common T_1 and T_2 sequences

Usually, the T_2 relaxation time is computed from several spin echo sequences with varying echo times and T_1 relaxation time is computed from several inversion times from gradient spin echo sequences. But to obtain a good accuracy of the estimation of the parameters, we have to densely sample echo times or inversion times, and this requires an acquisition time that is too long for clinical use. [Deoni et al., 2005a] proposed alternative approaches to historical spin echo and inversion recovery spin echo sequences to efficiently map the T_1 and T_2 relaxation times on the entire brain in a clinical acceptable time (on the order of half an hour). Another alternative is to use EPI sequences ([Poupon et al., 2010]), reducing the achievable resolution in comparison to spin echo but allowing to acquire several inversion and echo times in an acceptable time (5 minutes for each T_1, T_2 maps for a tens of sample points). However, the price to pay is the presence of more geometrical distorsions, that must be corrected afterwards. The following sections present the common sequences used to map T_1 and T_2 relaxometry times.

3.3.1.1 T_1 mapping : Inversion/Recovery sequence

This sequence has been designed to obtain a strong T_1-weighted constrast. We have explained before that Spin Echo sequence provides a contrast dependent on ρ, T_1 and T_2. In order to double the constrast to noise ratio, this sequence begins with a 180° pulse, leading to the complete inversion of the macroscopic longitudinal magnetization : M_z becomes $-M_z$. Then a 90° pulse is applied after a duration TI, called inversion time (see Figure 3.13). This pulse will occur during the regrowth of M_z and will tilt the residual longitudinal magnetization in the transverse plane. A simple spin echo follows the magnetization preparation. This sequence is therefore weighted in T_1 and can also be used for fat signal supression. One particularity of this sequence is that TR has to

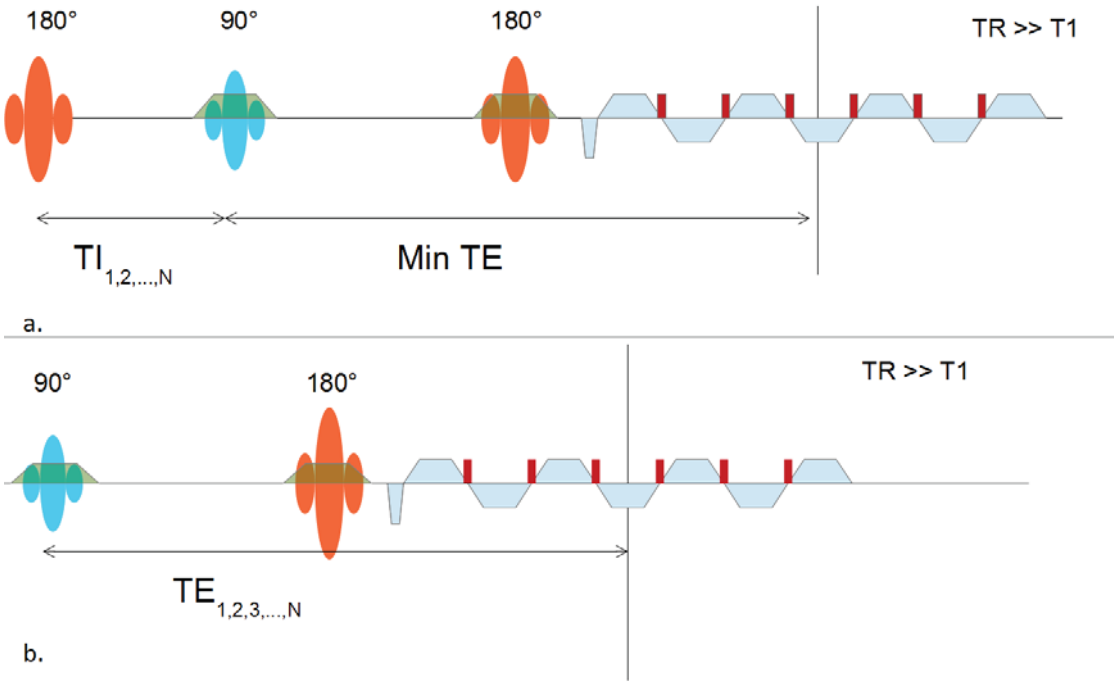

FIGURE 3.14: T_1 and T_2 mapping sequences : a) IR-EPI b) EPI.

be long to allow the total longitudinal regrowth of the magnetization before the next acquisition. The final signal at the end of an IR sequence is then given by :

$$S(TI) = \rho \left| 1 - 2\exp\left(-\frac{TI}{T_1}\right) \right| \tag{3.12}$$

Therefore, varying the inversion times provides a set of measurements that can be fitted to equation 3.12 to retrieve the T_1 relaxation time at each voxel.

3.3.2 T_2 mapping : multiple echo times Spin-Echo

The T_2 can be directly inferred from the usual spin echo sequence. The signal follows the equation :

$$S(TE) = \rho \exp\left(-\frac{TE}{T_2}\right) \tag{3.13}$$

The T_2 value can then be extracted acquiring a set of images at different echo times. Figure 3.14 depicts the inversion-recovery sequence and the multiple echo time Spin-Echo.

3.3.3 Advanced Sequences

The basic sequences presented in the previous section required long acquisition times, to obtain sufficient number of samples and therefore a good accuracy of the parameter

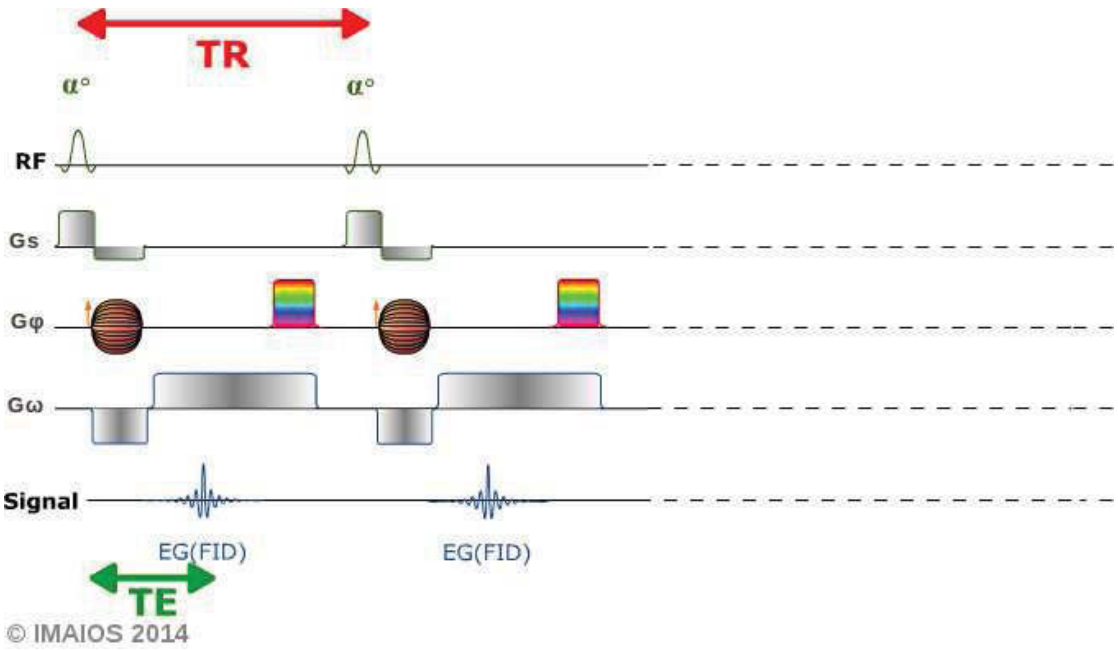

FIGURE 3.15: Spoiled Gradient Recalled Echo sequence.

estimates. T_1 and T_2 mapping are widely used in clinical applications, since they can provide quantitatives markers of diseases in comparison to the conventional T_1-weighted and T_2-weighted MRI. The scan duration is limited in clinical routine (it must not exceed 1 hour, and is quite often restricted to half an hour). For this reason, novel sequence schemes have been introduced (DESPOT1(driven equilibrium single pulse observation of T_1)/DESPOT2(driven equilibrium single pulse observation of T_2)) [Deoni et al., 2003], [Deoni et al., 2005a], mcDESPOT [Deoni et al., 2008] to accurately map T_1 and T_2 relaxation times in a reduced scan time. These new sequences rely on variable flip angles instead of the inversion trick : a Spoiled Gradient Recalled-Echo sequence (SPGR) for T_1 mapping and the Steady-State free precession sequence (SSFP) for T_2 mapping.

3.3.3.1 T_1 mapping using RF spoiling

The T_1 relaxation time can be inferred using a spoiled gradient recalled-echo sequence (SPGR) over a range of flip angle α (DESPOT1, [Deoni et al., 2003]), keeping a constant TR described in Figure 3.15. This sequence relies on gradient echoes obtained applying a negative gradient followed by the same gradient but with opposite sign. After the gradient echo, a residual transverse magnetization could be observed and this magnetization reaches a steady state after several subsequent TR. This residual magnetization will be added to the transverse magnetization induced by the RF pulse and will lead to an increase of the T_2* weighting. For T_1 mapping, a reducing effect of the T_2* weighting is desired. This is the reason why the SPGR starts by the destruction of this transverse

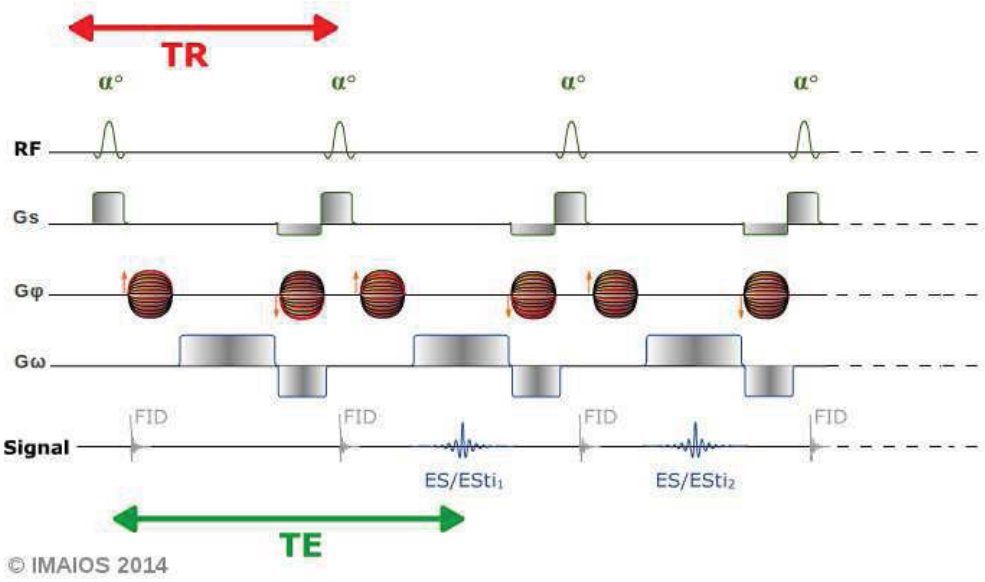

FIGURE 3.16: Stead State Free Precession sequence.

magnetization by RF spoiling. At each RF pulse, a phase offset is added inducing the cancellation of the residual transverse magnetization. To summarize, variable flip angles α are applied to obtain T_1-weighting (this experiment needs a long TR and a relatively low flip angle to reduce T_2* and ρ weighting) through the following equation :

$$\frac{S_{SPGR}}{sin(\alpha)} = \frac{S_{SPGR}\exp(-TR/T_1)}{tan(\alpha)} + M_0(1-\exp(-TR/T_1)). \tag{3.14}$$

3.3.3.2 T_2 mapping using steady state free precession

The T_2 relaxation time can be inferred using a steady-state free precession sequence (SSFP), over a range of flip angle α (DESPOT2([Deoni et al., 2003]) see Figure 3.16). In this sequence, steady state is induced by the rapid excitation of the spins using low flip angles, with a short TR. Here, the transverse magnetization has to be preserved and is therefore refocused between two successive RF pulses. Because this technique uses a repetition time such that $TR < T_2$ and $TR < T_1$, both transverse and longitudinal magnetizations reach a steady-state, leading to a signal depending on T_1 and T_2 (see equation 3.15). Practically, successive RF pulses create additional "Hahn echoes" from the residual transverse magnetization and act as refocussing pulses.

The obtained signal follows the equation :

$$\frac{S_{SSFP}}{sin(\alpha)} = \frac{S_{SSFP}(\exp(-TR/T_1)-\exp(-TR/T_2))}{tan(\alpha)(1-\exp(-TR/T_1)\exp(-TR/T_2))} + \frac{M_0(1-\exp(-TR/T_1))}{1-\exp(-TR/T_1)\exp(-TR/T_2)}. \tag{3.15}$$

Then, using previous estimation of T_1 obtained with DESPOT1 technique, one can easily derive T_2 values, measuring the signal varying the flip angle α. These two techniques allow to reach a good accuracy in T_1 and T_2 mappings with a reduced time in comparison with the commonly used inversion recovery and multi echoes spin echo sequences (half an hour instead of several hours required with conventional spin echo or in recovery spin echo). However, this technique is sensitive to B_0 and B_1 inhomogeneities and therefore requires additional B_1 and B_0 mappings.

Quite recently, qMRI was proven to be useful to somewhat characterize the microstructure of tissues through its water content and multiple compartment modeling. The same stands for diffusion MRI that we propose to introduce in the following section.

3.4 Diffusion weighted imaging

During the last two decades, diffusion MRI has become a key tool to probe the anatomical connectivity in vivo : within the brain, the displacement of water molecules is random due to interactions between molecules, but also to phenomena of hindrance and restriction caused by the barriers present along their trajectories, such as cell membranes. As a consequence, observing and decoding these displacements may provide a unique way to probe the local microstructure of brain tissues *in vivo*.
Back in 1950, [Hahn, 1950] was the first to report the attenuation of the NMR signal of the spin echo, because of the movement of spins during the application of the different gradients pulses of a sequence, leading to an unperfect rephasing of spins. [Carr and Purcell, 1954] established the first basics for diffusion measurement, followed by [Stejskal and Tanner, 1965a] who introduced the Pulse Gradient Spin Echo (PGSE) a few years later, giving the first MRI sequence providing information about the displacement of water molecules and enabling the inference of apparent diffusion coefficients.
This sequence has been widely used in the clinical setting, allowing for example a quick diagnosis of acute ischemia (characterized by the reduction of the Apparent Diffusion Coefficient, representing the average diffusion coefficient of water) or cerebrovascular accident as well as the study of white matter damages in several pathologies ([Moseley et al., 1990], [Le Bihan et al., 1992], [Benveniste et al., 1992]). The most popular application of diffusion is obviously the *in vivo* inference of the structural brain connectivity and microstructure, using the motion of the water molecules and its preferential directionnality to probe the direction of white matter fibers. More recently, the diffusion MRI has became a new tool able to perfom *in vivo* microscropy, allowing for instance to measure axon diameters and density locally. This chapter describes the diffusion process of water molecules in brain tissues before explaining the main principles of the PGSE

sequence, followed by the presentation of the local modelings of the diffusion process. This part is inspired by the courses of C. Poupon and the book [Johansen-Berg and Behren, 2009].

3.4.1 Diffusion process in tissues

Water molecules naturally moves randomly and interact with each other because of thermal agitation. In the presence of a free environment, without restrictions, the water molecules undergo a Brownian motion. The process of diffusion can be described mathematically as follows.
The diffusion of the water molecules follows the first Fick's law :

$$J = -D\nabla C, \tag{3.16}$$

with D the diffusion coefficient ($m^2 s^{-1}$), J the flux ($mol\ m^{-2}\ s^{-1}$), C the concentration ($mol\ m^{-3}$). The second law describes the evolution of the concentration in the time :

$$\frac{\partial C}{\partial t} = D\nabla^2 C. \tag{3.17}$$

In diffusion MRI, the concentration is replaced by the diffusion propagator $\mathbf{P(r,t)}$, the probability that a particle, initially at the position r_0 moves to the position r_1 during a time t. The diffusion propagator then follows the second Fick's law :

$$\frac{\partial P(r_0, r_1, t)}{\partial t} = D\nabla^2 P(r_0, r_1, t). \tag{3.18}$$

3.4.1.1 Free diffusion

The process of free diffusion, detailed by [Einstein, 1905], is described as a random walk of water molecules in an environment without restriction. This behavior can be found, for instance, in the ventricular system of the brain. In this case, the mean-squared displacement (the average length travelled by water molecules during a given time t) is a linear function of the time, following Einstein's equation :

$$x = \sqrt{2nD\Delta t}. \tag{3.19}$$

with D the diffusion coefficient (around $2 \times 10^{-9} m^2 s^{-1}$ for pure water at 20°) and Δt the time allowed to the water molecules to diffuse, n the dimensionality. In the case of free diffusion, the diffusion propagator is modeled by a Gaussian distribution of the

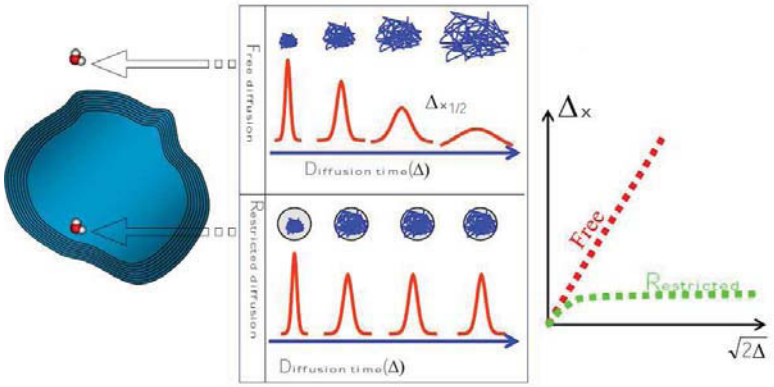

FIGURE 3.17: Restricted diffusion phenomenon [Assaf et al., 2008]: Δ_x is the mean-squared displacement and Δ the diffusion time

form :

$$P(r_0, r_1, t) = \frac{\exp(-\frac{(r_1-r_0)^2}{4Dt})}{\sqrt{4\pi Dt}}. \tag{3.20}$$

Equation (3.19) can be found using the mean-squared displacement expression with the gaussian propagator :

$$\langle (r_1 - r_0)^2 \rangle = \int_{-\infty}^{\infty} (r_1 - r_0)^2 \rho(r_0) P(r_o, r_1, t) dr_0 dr_1. \tag{3.21}$$

3.4.1.2 Anisotropy and restricted diffusion

The phenomenon of restricted diffusion allows, to infer structural parameters from diffusion MRI. Indeed, when water molecules move in the brain tissue, they encounter several barriers such as membranes, etc, structuring the tissue. In white matter, the mean-displacement depends on the direction : along the fibers the motion is not really constrained and the mean-displacement is greater than the perpendicular one, where the diffusion is highly restricted by the myelin sheath of axons. The diffusion is therefore anisotropic. In an even more complex environment, water molecule motion is either hindered or fully restricted, and the propagator is no longer Gaussian, the mean displacement is quickly restricted in any direction and the diffusion time therefore defines this mean-displacement, that is shortened (see Figure 3.17). From a given model of the tissue, one can infer the diffusion propagator. It is possible to infer structural parameters of the tissue from a model of this restricted diffusion phenomenon. Advanced local models of tissues will be discussed later in 3.4.3.

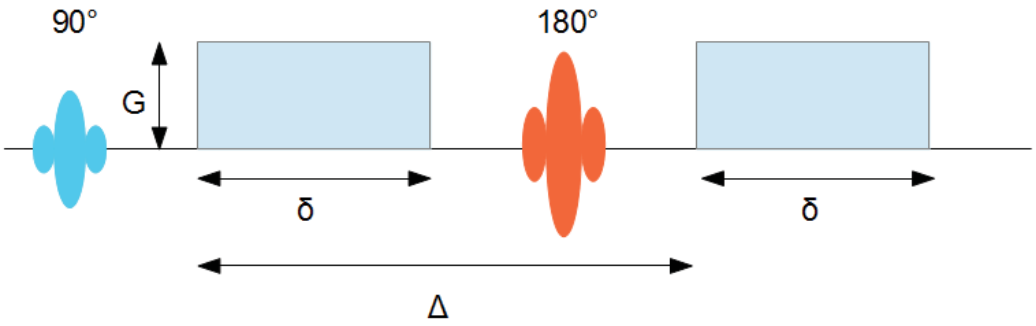

FIGURE 3.18: Pulse Gradient Spin Echo Sequence.

3.4.2 Basic sequence dedicated to diffusion MRI and signal equation

Diffusion MRI data are obtained using a specific MRI sequence, including strong diffusion gradients to "tag" the position of spins. The simpler diffusion scheme is called Pulse Gradient Spin Echo (PGSE, [Stejskal and Tanner, 1965b]). This subsection presents the details of the PGSE sequence and describes the common artefacts that may occur in diffusion MRI, followed by the expression of the diffusion signal obtained with this sequence.

3.4.2.1 Pulse Gradient Spin Echo

In [Hahn, 1950], it was noticed that the diffusion of spins during the spin echo leads to a natural attenuation of the signal. [Torrey, 1956] modified the Bloch equations to take the effect of spin diffusion into account. [Stejskal and Tanner, 1965b] introduced the first sequence able to enhanced this diffusion phenomenon : the Pulse Gradient Spin Echo (PGSE). [Lebihan and Breton, 1985] developed the idea to use the PGSE sequence in a clinical context to visualize ischemia for example. The basic diffusion sequence is the Pulse Gradient Spin Echo, depicted in Figure 3.18. It consists in applying two linear gradients before and after the 180° pulse in the spin echo. The gradient strengths and durations have to be the same on each side. The first gradient induces a dephasing of the spins along the direction of application. The second rephases them. But when a spin moves between the two gradients, it won't be rephased, its contribution to the signal is "lost". The signal from a diffusion sequence is therefore an attenuation from the initial signal S_0, without any gradient of diffusion. Major parameters of this sequence is the gradient strength G, the duration of the gradients δ, the separation between the two gradients Δ. The spin echo readout sequence is often replaced by an EPI echo train.

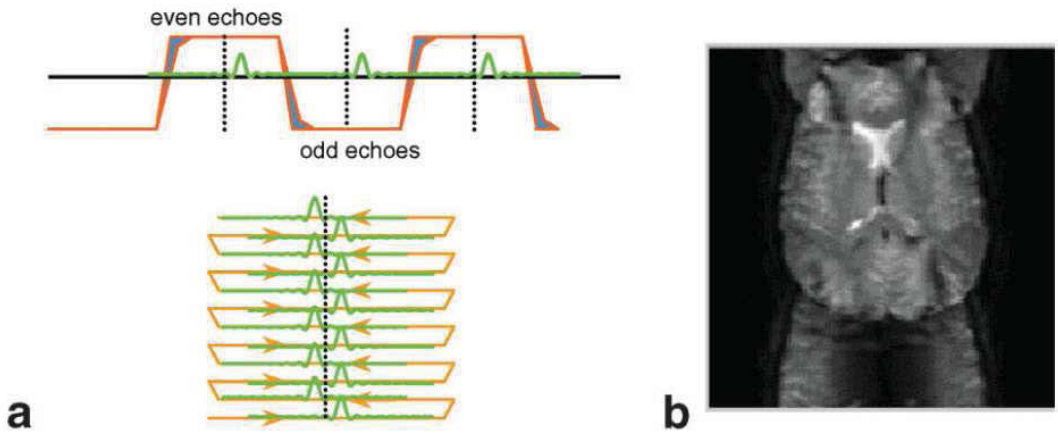

FIGURE 3.19: N/2 Ghosting Artefact.

3.4.2.2 Artefacts and noise in diffusion MRI

Several artefacts, stemming from the use of EPI echo train for diffusion experiments are listed here. These artefacts were described in [Le Bihan et al., 2006].

- **Eddy Currents :** When strong gradients are switched during the MRI sequences, currents, called eddy currents, are created in the conductive structures of the scanner. These currents create additional magnetic field, combined with gradient pulses, that modify the initial magnetic field experienced by the spins, leading to geometrical distortions (shrinking, dilation, scaling, translation, shearing) in the final image. In diffusion MRI, the extracted parameters come from a large set of data acquired with different diffusion sensitizations thus giving birth to different eddy currents and consequently different geometrical distorsions. It is therefore important to correct them adequately previous to any advanced analysis ([Mangin et al., 2001],[Reese et al., 2003]).

- **Ghosting :** The additional magnetic field created by Eddy Currents, inducing modification of gradient shape and area can lead to a phase offset between odd and even echoes using EPI, because of the particular manner of filling the K-space using oscillating readout gradients and a back-and-forth trajectory (the negative lobe of the readout gradient won't be the exact opposite of the positive lobe, due to the presence of Eddy Currents). This will lead to a misalignment of the acquired echoes in the K-space, leading to the creation of a "ghost" image in the phase direction, shifted by N/2, N corresponding to the number of lines. This is called N/2 ghosting (see Figure 3.19).

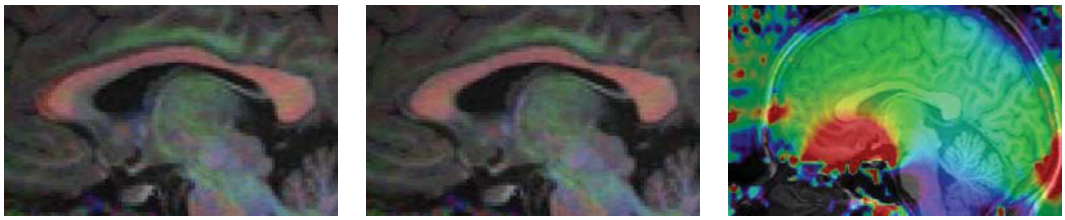

(a) Effect of the susceptibility artefact on the corpus callosum (Fusion of RGB map and T_1-weighted image

(b) Corrected image using the phase map

(c) Phase Map superimposed to the anatomical image

FIGURE 3.20: Susceptibility artefact

- **Gradient Non-Linearity :**
  The non-linearity of the gradient system can also induce geometrical distorsions in the image and the diffusion weighting won't be exactly the same, depending on the position. This can be corrected by the estimation of the deformation using the spherical harmonics decomposition of the non linearities usually provided by the gradient manufacturer or estimated using hardware grid phantoms. In addition, gradient non linearities lead to unhomogeneous b-value over the field of view.

- **Motion artefact:** If a motion occurs during the acquisition (respiratory, heartbeat...)in the direction of the phase encoding gradient, it will induce errors in the phase : if a voxel is moving, it will be present at different phase and frequency in the K-space, and will then appear at several positions). Moreover, in diffusion experiments, the observed dephasing have to be the result of the application of diffusion gradients but in case of motion, this is no longer the spin motion itself that is encoded but also the patient motion, leading to errors in parameter estimation.

- **Susceptibility effects :** The susceptibility artefact comes from the juxtaposition between two kind of tissue having too different magnetic susceptibilities and inducing a local magnetic field, leading to distortion of the image (geometrical as well as intensity distorsions). This problem typically occurs at the air/tissue interface (sinus). The image can be corrected using the acquisition of further calibration field map ([Jezzard and Balaban, 1995],see Figure 3.20).

- **Noise :** A major problem, commonly met in diffusion MRI is the noise. This part has been documented from [Brion, 2013]. Like for all kind of MRI images, the diffusion data suffers from non-central χ noise (nc-χ). In the case of diffusion, the bias introduced by nc-χ noise is very important since, as we just exposed, the diffusion experiment is in fact, a measure of a signal loss. The highest the diffusion gradient strength will be, the greater the signal attenuation will be. In case of signal loss, it is straightforward that the signal to noise ratio (SNR) for this kind of data could be extremely low (see Figure 3.21).

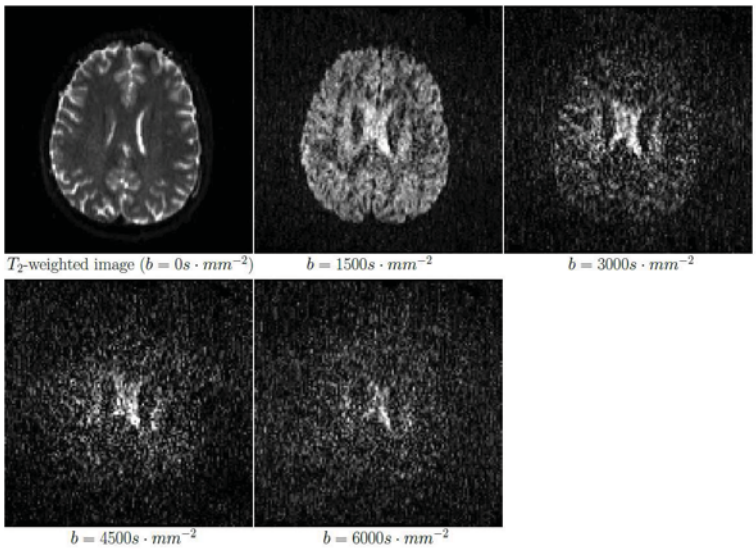

FIGURE 3.21: nc-χ noise in diffusion MRI data (adapted from [Brion, 2013])

In MRI, thermal noise coming from random motion of charge carriers in electrical conductors of the MRI scanner system, but also in the subject's body, which is also conductive. The SNR form of the spin echo EPI commonly used in diffusion studies is given by :

$$SNR \propto \frac{\exp(-TE/T_2)(\Delta x \Delta y \Delta z)(\sqrt{NxNyN_{acq}})B_0}{\sqrt{(RBW)}\sqrt{(R)}\mathcal{G}}. \tag{3.22}$$

where TE is the echo time, T_2 the transverse relaxation time, Δx Δy Δz the resolution of the image (size of the voxel), Nx and Ny are the acquisition matrix dimensions, N_{acq} is the number of repetitions, R is the parallel accelaration factor, RBW is the read bandwith of the electronic chain, B_0 is the static magnetic field and $\mathcal{G}$ is the quality factor of the receiving antenna. From this equation, it is clear that the SNR could increase with higher static fields. But T_2 values decrease when the static field increase. Thus, one has to pay attention to the exponential part that will also decrease the SNR. The acquisitions must have reasonable TE to limit this effect, requiring strong gradients. The read bandwith, filtering around the MRI signal frequency, can be lowered in order to reduce SNR but this will inevitably lead to geometrical distortions.

As we already mentionned, the signal measured on the N channels of the receiving coil is a complex signal, but in MRI images this is the magnitude of this signal that is exploited:

$$M = \sqrt{\sum_{c=1}^{N}(S_{rc} + noise_{rc})^2 + (S_{ic} + noise_{ic})^2}. \tag{3.23}$$

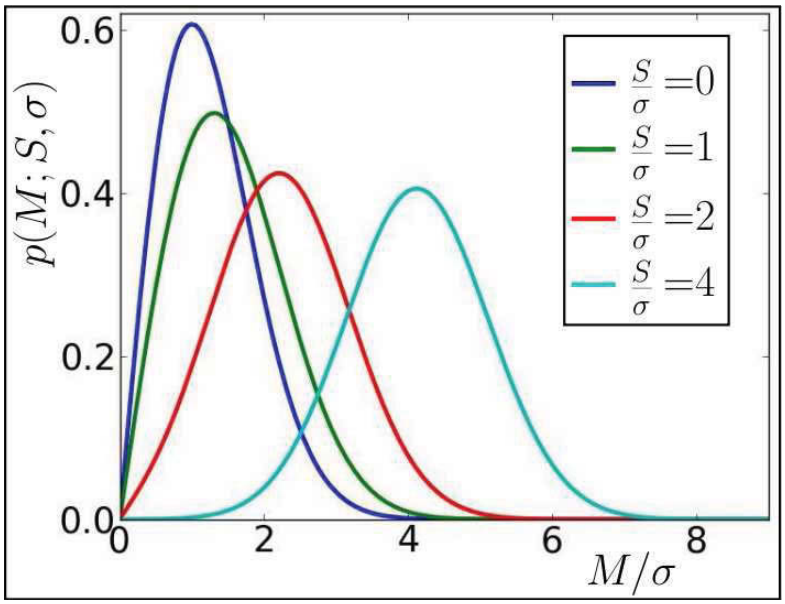

FIGURE 3.22: Rician probability distribution function (figure from [Brion, 2013]) for different ratios S/σ.

where r and i indicates real and imaginary parts of the signal or the noise. The noise is initially considered as gaussian for real and imaginary part. But when the modulus of the signal is performed on the signal measured from multiple channels, it is not longer Gaussian, it becomes a non-central χ noise ([Constantinides et al., 1997]). Assuming the same standard deviation for each channel, σ, the probability distribution is then :

$$\boxed{p(M,\sigma) = \frac{S}{\sigma^2}(\frac{M}{S})^n \exp(-\frac{M^2+S^2}{2\sigma^2})I_{n-1}(\frac{MS}{\sigma^2})} \tag{3.24}$$

where M is the measured signal and I_{n-1} is the modified bessel function of n-1 order. When only one coil is used, the noise becomes Rician ([Bernstein et al., 1989], [Rice, 1952])and has the following form :

$$\boxed{p(M,\sigma) = \frac{M}{\sigma^2} \exp(-\frac{M^2+S^2}{2\sigma^2})I_0(\frac{MS}{\sigma^2})} \tag{3.25}$$

where I_0 is the modified bessel function of zero order. The figure 3.22 shows the probability density function for several values of S/σ. In the case of $S = 0$, the noise follows a Rayleigh distribution function (dark blue curve on the figure). Different methods have been developed to denoise the diffusion data, but they are beyond the scope of this thesis, and are well described in [Brion, 2013].

3.4.2.3 Diffusion signal expression

We here present the expression of the diffusion signal obtained using the PGSE sequence.[Torrey, 1956] extended the initial Bloch equations of the temporal evolution of the magnetization to include a diffusion term. This evolution can then be expressed as :

$$\boxed{\frac{\partial M(r,t)}{\partial t} = \gamma \mathbf{M} \times \mathbf{B}(\mathbf{r},\mathbf{t}) - \frac{(M_z - M_0)\mathbf{z}}{T_1} - \frac{M_x \mathbf{x} - M_y \mathbf{y}}{T_2} + \nabla(\mathbf{D}\nabla\mathbf{M})} \tag{3.26}$$

with $M = M_x + M_y + M_z$. In case of anisotropy, the signal expression is :

$$\frac{S(t)}{S_0} = exp(-\int_0^t k(t')^T D k(t') dt'), \tag{3.27}$$

with $k(t) = \gamma \int_0^t G(t')dt'$, S_0 the signal without diffusion weighting, D the diffusion tensor and G the diffusion gradient. When the sample is isotropic, the signal 3.27 becomes :

$$S(t) = S_0 exp(-bD). \tag{3.28}$$

The b-value expresses the diffusion weighting of the sequence. The higher this value, the higher the attenuation. In the PGSE framework : assuming rectangular diffusion gradient pulses, one obtains :

$$b = \gamma^2 G^2 \delta^2 (\Delta - \frac{\delta}{3}). \tag{3.29}$$

From this value, we can extract a effective diffusion time : $\Delta - \frac{\delta}{3}$. These expressions above are valid in the case of free water, for the Gaussian diffusion propagator. If the environment exhibits restrictions, one can replace the diffusion coefficient D by the Apparent Diffusion Coefficient (ADC), that does not correspond to the true diffusion coefficient but that represents an average diffusion coefficient, integrating the constraints of displacements of water molecules by the natural barriers of tissue. In the case of a hindered environment, where the restrictions not fully constrain the mobility of water molecules, the ADC can be defined as the ratio between the true diffusion coefficient and a tortuosity coefficient Λ. The ADC can be sufficient to characterize some brain damages, even if the environment is not free. In fact, diffusion MRI experiments can provide more information than just the ADC, and different local models were established to infer angular and radial information of the probability of displacement of water molecules getting closer and closer to the tissue microstructure. The next section proposes a summary of the various models introduced during the last decade aiming at modeling the diffusion propagator, or more simply, the orientation distribution function.

3.4.3 Review of local models

3.4.3.1 Q-space analysis : dODF, fODF and diffusion propagator

We have introduced in the previous section the b-value, depending on the diffusion time and the gradient strength. [Callaghan, 1991] introduced the Q-space formalism, based on the relationship between the diffusion propagator and the diffusion signal measured in the space of the wave vector using the Fourier Transform [Callaghan, 1991] :

$$\boxed{E(\mathbf{q},\tau) = \int_{\mathbb{R}^3} P(\mathbf{r},\tau)\exp(-i\pi\mathbf{q}^T\mathbf{r})dr}, \tag{3.30}$$

where E is the signal attenuation, P the diffusion propagator, $\mathbf{q}$ the wavevector :

$$q = \gamma G\delta\mathbf{q} \tag{3.31}$$

The Q-space is therefore the dual space to the propagator space. The b-value can then be expressed by : $b = q^2 T_{diff}$, T_{diff} being the diffusion time. This relation is valid if the gradient pulses are very short but it is not technically possible to reach short enough gradient pulses. If this assumption is not verified, the relationship only allows to retrieve the ensemble average propagator, that still can provide significant angular and radial information on the diffusion process. This equation is the basis of a number of techniques developed to access to angular information of the propagator : different local models were proposed, trying to recover a probabilistic information on water diffusion, and exploit it to better understand the tissue microstructure. Usually, the propagator is not easily accessible and requires long acquisition schemes. In the community two other measures is often use to characterize the diffusion process in the white matter: the orientation distribution function of the diffusion process (dODF) or the orientation distribution function of the fibers (fODF). They both give angular information about the local displacement. The dODF is the integration of the propagator along all the distances r :

$$dODF(\mathbf{o}) = \int_0^\infty P(r,t)r^2 dr. \tag{3.32}$$

The fODF ([Tournier et al., 2004]) gives the fraction of fibers aligned along a certain orientation, thus providing a direct information on fibers configuration. The dODF and fODF give angular but no radial information, while diffusion propagator gives both information. These probabilistic functions can be inferred, as it is done for the diffusion propagator by Q-space sampling of the diffusion signal using relation 3.30. Different models were derived from this equation. We present some of them in the next section.

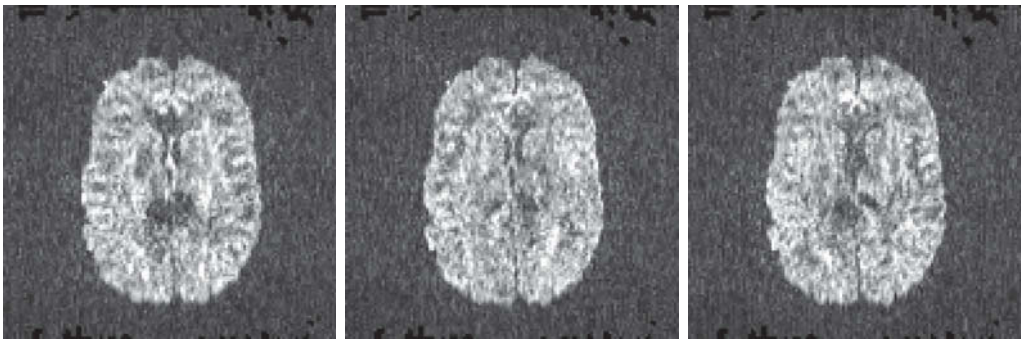

FIGURE 3.23: Diffusion weighted images (b=1500 $s.mm^2$) for three different orientations

3.4.3.2 Local modeling review

[Basser et al., 1994] introduced the popular Diffusion Tensor Imaging (DTI) model, assuming a Gaussian distribution of displacements. This technique has been widely used, even now in clinical applications because of is reasonable acquition time. But this technique suffers from several drawbacks, in particular because of its incapacity to detect more than one fiber population within a voxel and therefore to not detect fiber crossings. In [Wedeen et al., 2000], using the Fourier relationship between Q-space and the propagator space introduced in [Callaghan, 1991], Van Wedeen published the Diffusion Spectrum Imaging model (DSI), discretizing the relationship into a Cartesian grid limited to a sphere in the Q-space of radius corresponding to a large b-value. While providing access directly to the 3D probability density function of spin displacement (PDF), DSI requires long acquisitions not always compatible with clinical applications. In order to overcome the limitations of the DTI model, new models such as multi-Gaussian models [Tuch, 2002] were introduced, considering that each fiber population follows a Gaussian diffusion process and the final model being the sum of the contributions of each population. Following the idea of [Wedeen et al., 2000] and to be able to approach the real fiber configuration within a voxel, a pletora of high angular resolution diffusion imaging (HARDI) models and hybrid diffusion imaging (HYDI) models were developed. Most of these models inherit the former Fourier relationship and aim at decomposing the diffusion weighted signal on a basis of spherical functions. In these models, the Q-space sampling is optimized and is performed on a sphere, with optimized gradient orientations to cover the sphere (see Figure 3.23). Only few of the models exploit the radial component of the diffusion propagator, using multi-shell sampling ([Assaf and Basser, 2005], [Assemlal et al., 2009], [Descoteaux et al., 2011], [Alexander et al., 2006]), and most of them only rely on its angular profile. While the diffusion propagator is supposed to be the holy grail, few microstructural scalar features have been introduced but they generally suffer from a lack of specificity : a drop of the GFA value in a region cannot be directly linked to tissue microstructural modifications. More recently, [Assaf

et al., 2008] have demonstrated that modeling the diffusion process with two separated hindered and restricted compartments and measuring the diffusion weighted signal at different diffusion times can create the adequate contrast to infer the local axon density and radii, thus turning diffusion MRI into virtual microscopy. The challenge is then to be able to get an analytical solution of the diffusion attenuation within a geometrical shape mimicking the membrane restricting the displacement of molecules as well as optimizing the number of samples (corresponding to a specific gradient magnitude, orientation and diffusion time) in order to maintain the feasibility of the scan in clinical routine ([Alexander, 2008], [Drobnjak et al., 2010], [Zhang et al., 2011a]). [Zhang et al., 2012] went further, starting to investigate the grey matter introducing the NODDI model to infer neurite orientation dispersion and density within the cortical mantle. These models will be discussed in Chapter 5.

All the methods issued from HARDI acquisitions can be separated into two major groups: model-free techniques and model-depedent techniques. The latter use a-priori knowledge on the diffusion propagator. We summarize here the major techniques of these two groups, and we may not be exhaustive due to the pletora of models introduced since the last decade.

Model-free techniques :

- Diffusion Spectrum Imaging (DSI, [Wedeen et al., 2000]),
- The Q-Ball Imaging (QBI) ([Tuch, 2002]) introduces a spherical sampling of the Q-space, reducing the acquisition time of the DSI technique despite the decrease in angular resolution. It reconstructs the dODF from equation 3.32 using the Funk-Radon Transform,
- The Analytical QBall Imaging (aQBI) ([Descoteaux et al., 2007]) uses the same acquisition scheme as QBI but decomposes the signal into a modified spherical harmonics basis,
- The Diffusion Orientation Transform (DOT) ([Özarslan et al., 2006] provides an alternative to the dODF function, giving the propagator at a unique radius,
- The General Diffusion Tensor Imaging (gDTI)/Higher Order Tensor (HOT) ([Liu et al., 2003]) extends the diffusion tensor using a generalization of Fick's Law to a higher-order differential equation,
- The Persistent Angular Structure Imaging (PAS-MRI, [Jansons and Alexander, 2003]) also extracts an alternative to the dODF, called Persistent Angular Structure, representing the mobility of spins in each direction,

- The Kurtosis Imaging technique (DKI, [Jensen et al., 2005]) quantifies the degree of non gaussianity of the diffusion process.

Model-based techniques :

- Composite hindered and restricted model of diffusion (CHARMED, [Assaf and Basser, 2005] combines a hindered diffusion process corresponding to the extra-cellular compartment in the white matter voxel and a restricted compartment defined by the diffusion process in axons, modeled by a cylinder. The acquisition scheme required several b-values and several diffusion times,
- The Spherical Deconvolution (SD) ([Tournier et al., 2004])allows to retrieve the fODF, considering that each measurement is the convolution of the fODF with the impulse response of one homogeneous fiber population to the fiber process. The deconvolution technique uses a decomposition of the signal in spherical harmonics,
- The Constrained super-resolved spherical deconvolution (CSD, [Tournier et al., 2007]) follows the idea of the SD,
- The Spherical Deconvolution Transform (SDT)([Descoteaux, 2008] described in the next subsections,
- The Ball and Stick model ([Behrens et al., 2003]) considers two compartments, the first one undergoing a Gaussian and highly anisotropic diffusion process (corresponding to fibers) and the second one corresponds to a fully isotropic gaussian diffusion process. Similar models were derived, using stick, cylinder or a distribution of cylinder for the restricted compartments, and ball, tensor or zeppelin for the extra-cellular part where an additional isotropically restricted compartment can sometimes be inserted (see [Panagiotaki et al., 2012]),
- Multi Gaussian mixtures ([Tuch, 2002]) and Wisharts Mixtures ([Jian and Vemuri, 2007]).

Some of the model-based techniques will be developed in Chapter 5, in the context of inference of microstructure parameters modeling the diffusion propagator. Next sections will expose a selection of these models, which are used in this thesis : the DTI, the analytical QBall and the SDT.

3.4.3.3 DTI

As previously explained, in white matter fibers, the diffusion parallel to the direction of the axon is not restricted but the diffusion phenomenon perpendicularly to this direction

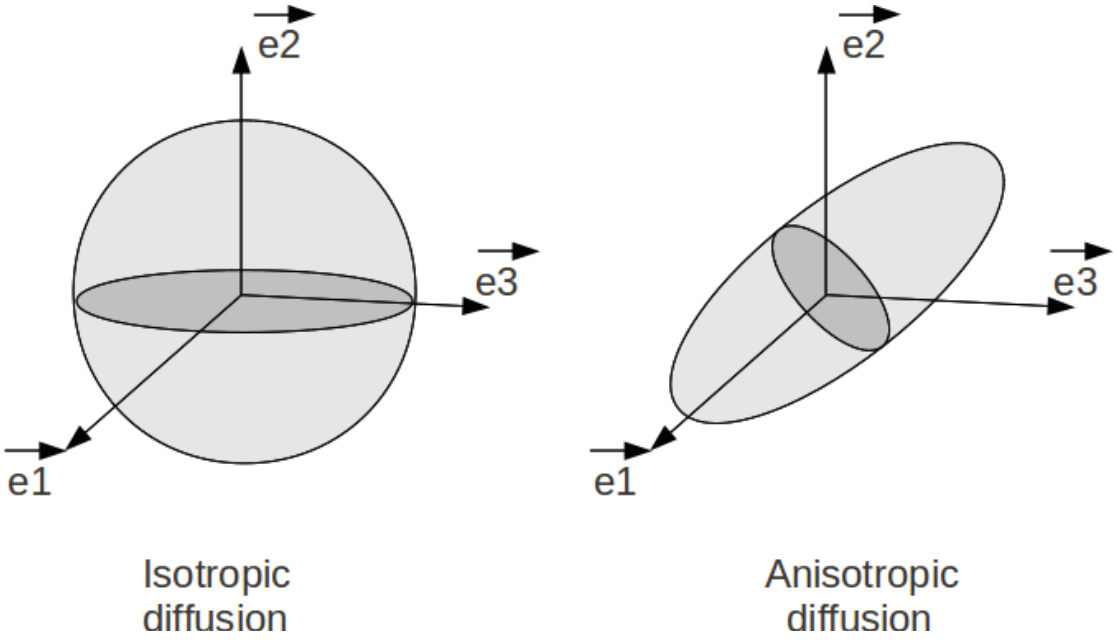

FIGURE 3.24: Reprenstation of the diffusion tensor D in the cases of isotropic and anisotropic diffusion

is contrained by membranes. This anisotropic behavior is described by the diffusion tensor model ([Basser et al., 1994]). This model is based on the observation that in tissues, the water molecules' motion can be approximated by a Gaussian distribution depending on a principal direction of diffusion assumed to be aligned with the direction of the fibers within the white matter. Therefore the propagator of (3.20) is adapted to take the different directions into account. The diffusion is not only characterized by a single D coefficient but by a matrix, the diffusion tensor $\mathbf{D}$ (Figure 3.24), corresponding to the covariance matrix of diffusion displacements. Finally the propagator has the form of a multivariate gaussian model :

$$P(r_0, r_1, t) = \frac{\exp(-\frac{(r_1-r_0)^T \mathbf{D}^{-1}(r_1-r_0)}{4t})}{\sqrt{4\pi t^3 |\mathbf{D}|}}, \tag{3.33}$$

with

$$\mathbf{D} = \begin{pmatrix} D_{xx} & D_{xy} & D_{xz} \\ D_{yx} & D_{yy} & D_{yz} \\ D_{zx} & D_{zy} & D_{zz} \end{pmatrix}.$$

The final signal equation using a PGSE sequence is given by :

$$E(q, \tau) = \exp(-\frac{TE}{T_2}) \exp(-\tau q^T \mathbf{D} q).$$

Diagonalization of this matrix provides three eigenvectors : $\mathbf{e_1}, \mathbf{e_2}, \mathbf{e_3}$ corresponding to the eigenvalues $\lambda_1, \lambda_2, \lambda_3$ (in decreasing order), being the apparent diffusivities along the

three principal directions of the tensor, the highest one corresponding to the apparent diffusivity along the main direction (along the fibers in white matter). When all the eigenvalues are equals, the diffusion is isotropic (see Figure 3.24). By measuring the signal attenuation in six directions, we can construct the tensor in each voxel and get the main axis of diffusion. This local model provides several measures such as fractional anisotropy (FA) (see Figure 3.25, right), apparent diffusion coefficient(ADC), the radial diffusivity $\lambda_\perp$, the axial diffusivity $\lambda_\parallel$:

$$\lambda_\parallel = \lambda_1$$

$$\lambda_\perp = \frac{\lambda_2 + \lambda_3}{2}$$

$$FA = \frac{\sqrt{(\lambda_1 - \lambda_2)^2 + (\lambda_2 - \lambda_3)^2 + (\lambda_1 - \lambda_3)^2)}}{\sqrt{2(\lambda_1^2 + \lambda_2^2 + \lambda_3^2)}}$$

$$ADC = \frac{\lambda_1 + \lambda_2 + \lambda_3}{3}.$$

From these data one can also infer the principal direction of motion of water molecules. A common manner to represent it is the colour-encoded orientation map (RGB map), encoding the direction using RGB representations : the red, green and blue colors indicate respectively the x, y and z directions (see Figure 3.25). This technique, widely used

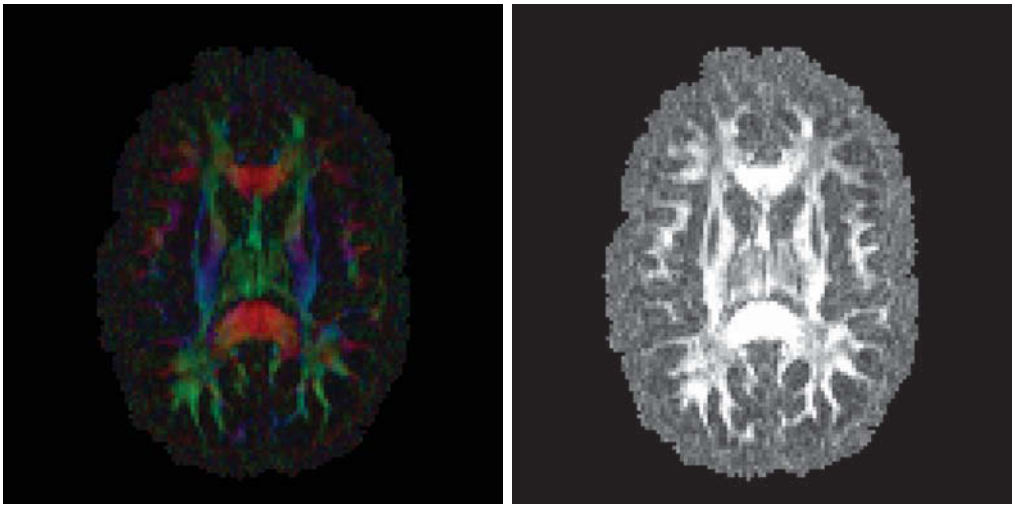

FIGURE 3.25: RGB and FA maps

by the physicians because of the simplicity of the model (very few parameters) and its acceptable acquisition duration, relies on the strong hypothesis of a Gaussian probability of displacement, which is not always valid, and moreover, it allows to only model one population of fibers within a single voxel and cannot resolve fiber crossings. To overcome this limitation, a multi-tensor model using a Gaussian mixture has been developed by

[Tuch et al., 2002], before moving to high angular resolution diffusion imaging or HARDI models.

3.4.3.4 Numerical and analytical Qball imaging

New acquisition schemes were developed, using the relation (3.30), relying on the sampling of the Q-space to characterize the diffusion propagator. Indeed, to overcome the limitations of the DTI, and therefore access to the non-gaussianity of the diffusion process, more measurements were required. Alternative imaging such as High Angular Resolution Diffusion Imaging including the QBall ([Tuch, 2004]) and the analytical QBall ([Descoteaux et al., 2007]) arose. QBall imaging includes an acquisition scheme sampling the Q-space on a sphere (of radius corresponding to a high b-value $\geq 3000 s/mm^2$) to provide the angular information of the propagator, and therefore to obtain the dODF at each voxel. To reach sufficient precision, this technique requires a high number of diffusion orientation (> 60). In QBI, the diffusion orientation distribution function of the diffusion process (dODF) can be approximated from the signal measurements by the Funk-Radon Transform :

$$FRT(S(o, q_0)) = 2\pi q_0 \int_{S^2} P(r, \theta, z) J_0(2\pi q_0 r) r dr d\theta dz. \tag{3.34}$$

$$dODF(o) = \int_{S^2} P(r, \theta, z) \delta(r) \delta(\theta) r dr d\theta dz. \tag{3.35}$$

The Funk Radon Transform of a function at a given point on a sphere is in fact the integral over the equator of the sphere perpendicular to the orientation corresponding to this point and passing by the origin. The first step of QBI is to interpolate the values along these great circles from the set of measurements. From these interpolated values, the Funk Radon Transform can be computed and it then provides the dODF at each point. This technique overcomes the DTI problem by solving fiber crossings. The analytical QBI ([Descoteaux et al., 2007]) differs from the previous technique by changing the interpolation step along the equators. Indeed, the Funk Radon Transform is already a first approximation of the dODF, and the additional approximation brought by the interpolation step leads to a decrease in accuracy of the estimation of the orientation distribution function. In order to solve this problem ([Descoteaux et al., 2007]) uses the fact that any function on the sphere can be decomposed on a set of orthogonal functions, defined as spherical harmonics. In this model, the spherical harmonics have been modified to take into account the positiveness and the symmetry of the signal :

$$S(o) = \sum_{k=1}^{K} C_k^{DWI} Y_k(\theta(o), \phi(o)),$$

with C^{DWI} the coefficients obtained from the least square solution and using a Thikonov regularization :

$$C^{DWI} = (B^T B + \lambda L)^{-1} B^T S/S_0$$

with L the Laplace-Beltrami matrix and B the matrix of modified spherical harmonics :

$$Y_k(\theta,\phi) = \begin{cases} \sqrt{2} Re(\sqrt{\frac{(2l+1)(l-|m|)!}{4\pi(l+|m|)!}} P_l^{|}m|(cos\theta) \exp i|m|\phi & -l \leq m < 0 \\ (\sqrt{\frac{(2l+1)(l-m)!}{4\pi(l+m)!}} P_l^m(cos\theta) \exp im\phi & m = 0 \\ (-1)^{m+1}\sqrt{2} Im((\sqrt{\frac{(2l+1)(l-|m|)!}{4\pi(l+|m|)!}} P_l^{|}m|(cos\theta) \exp i|m|\phi) & 0 < m \leq l \end{cases}$$

The Funk-Hecke theorem shows that the decomposition of the signal in spherical harmonics can be linked to the dODF :

$$dODF(o) = \sum_{k=1}^{K} C_k^{dODF} Y_k(\theta(o), \phi(o))$$

with $C_k^{dODF} = PC^{DWI}$ and P the Funk-Hecke matrix (where the diagonal element are $2\pi P_{l(j)}(0)$ with $P_{l(j)}$ the Legendre Polynomial of order l(j). An example using the analytical QBall model is presented in Figure 3.26. This technique provides improved

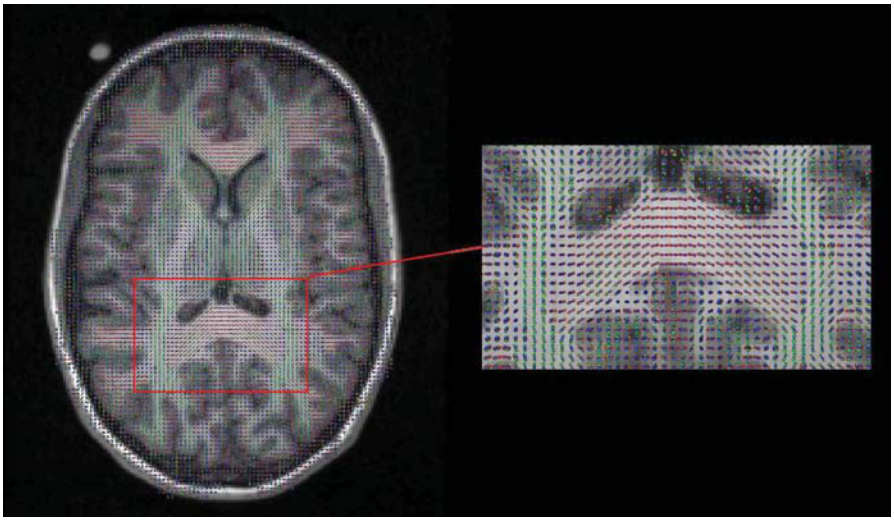

FIGURE 3.26: Analytical QBall field (computed using CONNECTOMIST 2.0).

information in comparison to DTI. First, we can derive here more than one principal diffusion direction : observing the peaks of the dODF or fODF provides the directions with the highest probabilities. The plurality of principal directions gives the opportunity of resolving fiber crossings. Second, we can extract a General Fractional Anisotropy :

$$GFA = \sqrt{\frac{n \sum_{i=1}^{n} (dODF(o_i) - 1/n)^2}{(n-1) \sum_{i=1}^{n} dODF(o_i)^2}}, \tag{3.36}$$

with n the number of orientations o_i.

3.4.3.5 Spherical Deconvolution Techniques

The Spherical Deconvolution model introduced by [Tournier et al., 2004] relies on the hypothesis that during the diffusion time, no exchange occurs between fibers and the final signal can then be decomposed as the sum of the response of all the different populations of fibers. Furthermore it assumes that the individual response of each fiber population are the same, except their orientations. This method can provide the fODF for which the signal is expressed as the convolution of the response of a single fiber R and the fODF :

$$S(q) = \int \text{fODF}(x)R(q,x)dx, \tag{3.37}$$

This approach has been improved in [Tournier et al., 2007], who proposed a Constrained Spherical Deconvolution (CSD) approach, to optimize the resolution of the system when few sample points are acquired.
[Descoteaux, 2008] introduced the Spherical Deconvolution Transform (SDT) where the fODF can be obtained from a spherical deconvolution of the dODF. The dODF is expressed as the convolution of the fODF with the impulse response of a single fiber R to the diffusion process :

$$dODF(o) = \int R(o,o')fODF(o')do' \tag{3.38}$$

where R is expressed as a prolate tensor and, as we already presented before, this convolution can be performed analytically using a decomposition of the dODF in spherical harmonics (c_j being the coefficients of this decomposition) and therefore obtain the coefficients d_j of the decomposition of the fODF using:

$$fODF(o) \approx \sum_{j=1}^{R} 2 * \pi * P_{l(j)}(0)\frac{c_j}{f_j}Y_j(o), \tag{3.39}$$

with $d_j = \frac{c_j}{f_j}$, $f_j = 2\pi \int_{-1}^{1} P_{l(j)}(t)R(t)$. This technique will be used in the next chapter. We have just developed the major local modelings of the diffusion process. The next subsection will then present the applications of the diffusion weighted MRI.

3.4.4 Application of the diffusion weighted imaging

Through all these models, diffusion weighting imaging is now a powerful tool to infer structural information studying the displacement of water molecules in the tissue, particularly in white matter tissues where this displacement is highly constrained, due to

the presence of the myelin sheath, considered impermeable regarding the diffusion time of the PGSE experiments. We already mentionned the use of DTI to characterize ischemia, only by exploiting the ADC maps coming from the diffusion data. One major application of diffusion weighted imaging in the white matter is the *in vivo* inference of the brain connectivity, by following the major pathways defined by the mobility of the molecules. These major paths reflect the actual fiber bundles, made of axons, in the brain but we can only define them by "numerical" fibers, since they are not real. The second application of diffusion weighted imaging is the microscopic diffusion MRI, going further in the study of brain microstructure, modeling the diffusion propagator to extract structural parameters such as axon diameter and density in the white matter using models as the CHARMED ([Assaf et al., 2004]) model presented in the previous subsection. We only present here the tractography application, since the microstructure by diffusion MRI will be developed in the Chapter 5.

3.4.4.1 Inference of structural connectivity using tractography

The various local models of the diffusion process give in each voxel the angular probability of the displacements of water molecules. Following the direction(s) with the highest probability(ies) can provide the principal pathways of water motion, corresponding to the paths where the motion of water molecules is less restricted. In white matter, the direction where the molecules are less constrained corresponds to the parallel direction to fibers. That is the idea of tractography introduced by [Basser]. Tractography is still the unique tool to provide access to the anatomical connectivity of the brain *in vivo* and non invasively. Tractography techniques vary in their way to manage the reconstruction of the fiber paths.

The first and widely used technique is the streamline deterministic tractography. This technique was used in [Basser et al., 2000] to compute the tractogram from DTI data. The streamline is a 3D curve characterized by the fact that, at each point, the tangent at this streamline is always parallel to the main vector field represented, for the DTI example, by the principal direction of the tensor. At each step of the algorithm, a line is propagated, following the orientation having the highest probability according to the given local orientation field. In each voxel, several lines are drawn from different "seeds", where the dODF or fODF is interpolated. Taking into account the low curvature of fibers, streamling algorithms generally consider at each step of the propagator an aperture cone forwards or backwards restricting the domain of propagation within the cone thus speeding up the streamlining process (see Figure 3.28). Only the voxels belonging to a brain mask are considered, giving then a stopping criterion, usually defined using a FA or GFA threshold. More robust T_1-based masks were also proposed

by [Guevara et al., 2011a] to define the domain of propagation of streamlines without depending on an arbitrary FA threshold that quite often misses some pieces of white matter. Streamline tractography is very fast but, even if it is not limited to the tensor model, it cannot always resolve fiber configurations such as crossings or kissings and is sensitive to noise and potentially creates false positive fibers (noise can produce an artificial peak in the dODF) or miss fibers. An example of a deterministic streamline tractography is shown in Figure 3.27. The streamline probabilistic tractography algo-

FIGURE 3.27: Streamline deterministic tractography (from one subject of the Archi Database).

rithms([Parker and Alexander, 2003], [Perrin et al., 2005b], [Chao et al., 2008], [Berman et al., 2008], [Descoteaux et al., 2009b]) are an alternative, keeping a degree of uncertainty at each voxel. In such algorithms, the highest probability is not systematically followed. For example, a random orientation can be randomly chosen within the angular cone, centered on the highest probability given by the local model. Several particles are drawned randomly for each voxel, each of them following a process where the principal direction provided by the ODF field is not systematically followed. Probabilistic streamline algorithms can better handle fiber crossings and are more robust to noise as they can overcome propagation of errors. However, they take a longer time to reconstruct the whole tractrogram. Other algorithms were proposed such as Bayesian probabilistic tractography ([Behrens et al., 2003], [Friman et al., 2006], [Jbabdi et al., 2007], [Morris et al., 2008]), providing maps of probabilistic connectivity maps between regions using a Bayesian Framework, and Monte Carlo Markov Chain process to infer the probability of connection. Geodesic tractography ([Jbabdi et al., 2004], [Jbabdi et al., 2008])aims at finding for the shortest path linking two points in a specific space, corresponding to the diffusion space with a specific metric of the dODFs. Finally global gractography techniques ([Poupon, 1999], [Cointepas et al., 2002], [Kreher et al., 2008], [Fillard et al., 2009], [Reisert et al., 2011]) were developed to infer the whole set of brain connections

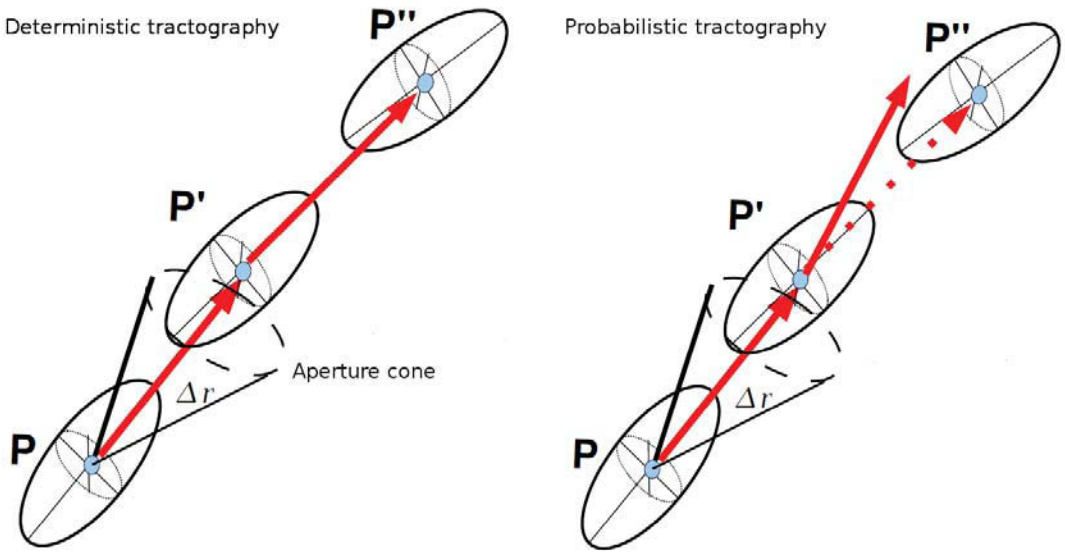

FIGURE 3.28: Deterministic versus Probabilistic tractography.

globally rather than locally like the other techniques where each pathway is built independently of the other. [Fillard et al., 2009] introduced the use of "spin-glass" approach to infer white matter tracts. These spin-glasses are considered as pieces of tracts, and the idea is to optimize their configuration minimizing a global energy, attracting the spins to be oriented along the main fiber directions, and to form long chains with low curvature. If the number of spins is not enough to solve the local configuration (such as crossings), the algorithm allows them to be replicated. These global techniques are efficient since they are less blind than others but take longer computation time requiring strong optimization of the code and the use of high performance computing hardware.

3.5 Conclusion

We summarized the main knowledge about MRI we need to develop the contributions of this thesis work. Quantitative MRI and diffusion MRI are clearly two complementary modalities to investigate the cytoarchitecture. Before presenting the use of diffusion MRI to infer microstructural information, we will move to the first main contribution : the use of relaxometry data to extract information about microstructure and the interest of combining it with diffusion MRI in order to better characterize the white matter.

Chapter 4

Brain white matter relaxometry atlases

4.1 Introduction

The previous chapter introduced the basis of relaxometry and diffusion MRI. We have shown that both of them can provide information about tissue microstructure. On one hand, T_1 and T_2 relaxation times are generally used to characterize specific water compartments within tissues, such as water trapped in the myelin thus providing the associated myelin water fraction, which is an accurate biomarker for diseases inducing a demyelination of axons. On the other hand, diffusion MRI uses the interaction of water molecules with the surrounding tissue membranes to reveal the tissue organization and to provide for example the orientation of fibers within white matter, useful to study the anatomical connectivity of the brain *in vivo*. Therefore, relaxometry and diffusion MRI provide similar and complementary information on tissue microstructure, and it could be of great interest to combine them in order to study how they both characterize the white matter structure.

Relaxometry data have been used to study grey matter microstructure of the healthy brain (cortex or deep structures) providing mean values of T_1 and T_2 in predefined regions of interest ([Lee et al., 2006], [Wansapura et al., 1999]) or using T_1 and T_2 mapping to delineate substructures ([Deoni et al., 2005b]). However, these studies didn't involve the use of diffusion MRI data. Moreover, several studies have combined relaxometry and diffusion MRI data in the study of white matter to explore the structural variations along white matter bundles or the maturation of the infant brain ([Dubois et al., 2010]) and better understand the link between these relaxation times and the underlying microstructure ([Cherubini et al., 2009],[Herve et al., 2011], [Russell-Schulz et al., 2013]).

To our knowledge, all studies were performed at the individual level and group analysis were generally performed directly from the average T_1 and T_2 values measured at the individual scale on specific ROIs. A more comprehensive analysis should include diffusion or relaxation parameters computed along the bundles, using the projection of scalar values onto a streamline or a surface representing the bundles [Corouge et al., 2006], [Goodlett et al., 2009], [O'Donnell et al., 2009], [Zhang et al., 2010], [Jones and Deoni, 2006]. Concerning DTI parameters, [Yeatman et al., 2012] explored the FA variation along several bundles and [Mårtensson et al., 2013] built a FA profile along the Inferior-Fronto Occipital fasciculus in progressive supranuclear palsy. [Reich et al., 2006], added to the DTI parameters the T_1 & T_2 values investigation along the corticospinal tract. Only recently, [De Santis et al., 2014] addressed the variation of combined diffusion parameters and relaxation times along several white matter bundles.
The first contribution of this thesis was to combine diffusion parameters and relaxation times along major white matter bundles in a large population of healthy subjects. To attain this goal, we first constructed reference quantitative atlases of profiles of the T_1 and T_2 relaxation times along white matter bundles and second studied their variability across the subjects, as well as the asymmetry of the profiles between the two hemispheres. These profiles were then compared to the profiles of diffusion parameters such as ADC, FA, $\lambda_{\parallel}$ and $\lambda_{\perp}$. Therefore the ultimate goal is to provide a normative atlas of quantitative features along white matter bundles against which to compare pathological cases. In this chapter, we first briefly describe the CONNECT/Archi database used in the frame of this study, and we detail the processing pipeline developed to construct the two super-resolved quantitative atlases of T_1 and T_2 relaxation times. Then we develop the construction of the T_1 and T_2 profiles along long white matter tracts. From these profiles, we compute an asymmetry index useful to compare profiles between the right and left hemispheres. Finally we analyze the correlation between T_1 and T_2 values with diffusion parameters along the bundles.

4.2 The ARCHI database

The CONNECT/ARCHI database is a large human brain MRI database acquired in the frame of the European CONNECT project [Assaf et al., 2013] which aimed at inferring the connectome atlas of the human brain from functional and anatomical MRI data at 3T. Data were collected on a population of 79 healthy young subjects on a Tim Trio 3T MRI system equipped with a 12-channel head coil (Siemens, Erlangen), and the part of the MRI protocol used to investigate diffusion MRI includes acquisition of the following datasets :

- a high resolution T_1-weighted dataset using a MPRAGE sequence (160 slices; FOV 256mm, Phase FOV 93.8 % ; TH 1.10mm; TE/TR=2.98/2300ms; TI=900ms; FA=9deg; matrix 256x240; RBW=240Hz/pixel),
- a B0 fieldmap using a double echo gradient echo sequence for *a posteriori* correction of susceptibility artefacts,
- a single-shell HARDI dataset along 60 optimized diffusion directions [Dubois et al., 2006] using a twice-refocused single-shot EPI sequence at a b-value of 1500s/mm^2 (70 slices; FOV 220mm, Phase FOV 100%; Slice thickness 1.7mm; TE=93ms; TR=14s; flip angle FA=90deg; matrix 128x128; read bandwidth RBW=1502Hz/pixel; echo-spacing ES=0.75ms; 1 excitation; partial Fourier factor PF=6/8; parallel acceleration factor GRAPPA=2; total scan time 16min46s).

The ARCHI database was originally dedicated to perform HARDI imaging, thus constraining the amount of time remaining to perform relaxometry. Taking into account this constrain, spin echo EPI sequences were developped specifically and to perform T_1 and T_2 mapping respectively, allowing to scan 10 values for the inversion times and the echo times in a very short duration ($<$ 5 minutes) :

- T_1 mapping dataset : spin echo EPI single-shot sequence (FOV 220mm ; TH=1.7mm ; 70 slices ; TE/TR=30ms/20.6s ; flip angle FA=90deg; 128x128 ; GRAPPA2 ; PF=5/8 ; RBW=1502Hz/Pixel ; 10 uniformly distributed inversion times TI between 300ms-3000ms),
- T_2 mapping dataset : a spin echo EPI single-shot sequence (FOV 220mm ; TH=1.7mm ; 70 slices ; TR=23.2s ; flip angle FA=90deg; 128x128 ; GRAPPA2 ;PF=6/8 ; RBW=1502Hz/Pixel ; 10 uniformly distributed echo times TE between 30ms-200ms).

Usually, the T_2 relaxation time is computed from several spin echo sequences with varying echo times and T_1 relaxation time is computed from several inversion times from gradient spin echo sequences. But an accurate estimation of T_1 and T_2 in each voxel requires a sufficient sampling of echo times and inversion times, and therefore a too long scan duration for a clinical application. [Deoni et al., 2005a] proposed alternative approaches to historical spin echo and inversion recovery spin echo sequences to efficiently map the T_1 and T_2 relaxation times on the entire brain in a clinical acceptable time (on the order of half an hour for both). But these sequences require additional mapping of B_1 and of the inhomogeneties of B_0 since the model depends on varying flip angles. Another alternative is to use EPI sequences [Poupon et al., 2010], allowing to acquire several inversion

and echo times in a reasonable time (5 minutes for each T_1 & T_2 map). These short acquisitions can even be used for the study of myelin formation on newborns or children where the scan time is even more limited [Dubois et al., 2010]. However, the use of EPI echo train reduces the achievable spatial resolution. Since the spatial resolution of the present study is obviously limited by the resolution of the diffusion data, the resolution provided by EPI sequences is therefore acceptable. Another consequence of the use of EPI sequence is the additional geometrical distorsions, which are also found in diffusion weighted data. Consequently, diffusion and relaxometry dataset will share a similar preprocessing step to correct for geometrical distorsions, thus yielding similar residual errors, before going to the main processing pipelines. First, a connectivity atlas was built from the diffusion data, providing well-known white matter bundles for each subject in a common space and scalar atlases of diffusion parameters. Second, relaxometry data were analyzed to built two super-resolved atlas of T_1 and T_2 relaxation times. Third, the relaxation times were projected on each bundle and hemisphere asymmetry as well as correlation between T_1 and T_2 and diffusion parameters were studied. The next sections will present in details these three steps.

4.3 Inference of an atlas of the structural connectivity

Using the method of [Guevara et al., 2011b], a probabilistic atlas of the human brain connectivity was built from the HARDI dataset as well as probabilistic atlases of several diffusion-based features such as FA and mean/transverse/parallel diffusivities [Duclap et al., 2013b], [Assaf et al., 2013] . This probabilistic atlas includes 38 well-known long WM bundles : 15 in each hemisphere and 4 interhemispheric (the Anterior Arcuate fasciculus (AArc), the Posterior Arcuate fasciculus (PArc), the Arcuate (Arc), the Short Cingulum fasciculus (SCing), the Temporal Cingulum fasciculus (TCing), the Long Cingulum fasciculus (LCing), the Inferior-FrontoOccipital fasciculus (IFO), the Inferior-Longitudinal fasciculus (IL), the Fornix (Fx), the Uncinate (Unc), the Anterior, Inferior, Motor, Parietal and Posterior Thalamic Radiations(ATR, ITR, MTR, PaTR, PoTR), the Corpus Callosum divided into four parts (Rostrum, Genu, Body, Splenium)) as well as for 94 short white matter bundles found in all subjects of the database. This atlas is the fundamental referential to study quantitative information on brain tissue of healthy subjects and therefore to go further into the study of brain microstructure, combining different modalities. We describe here the different steps required to build the connectivity atlas. All the processing was done using BrainVISA and Connectomist 2.0 softwares ([Duclap et al., 2012]) and are summarized in Figure 4.1. Let's now focus on the description of the details of the processing of diffusion MR data yielding such bundle maps at the individual scale.

FIGURE 4.1: Connectomist pipeline leading to the fiber bundle labelling

4.3.1 Quality check and correction of imaging artefacts

Because the diffusion MRI data were acquired using an echoplanar imaging technique, it is sensitive to any local field inhomogeneities that are integrated (and consequently "amplified" during the long acquisition echotrain). As we described in chapter 3, artefacts can be classified in two categories: those due to hardware imperfections, and those due to the subject itself. The first class of artefacts includes eddy currents stemming from the commutation of strong diffusion gradients that can take longer to be switched off thus adding residual gradients at the same time of the application of the gradients along phase and read directions yielding geometrical distorsions. Post-processing techniques exist to correct *a posteriori* the distorsion that can be approximated to a combination of a translation, a scaling and a shearing along the phase encoding axis when the eddy currents are assumed short ([Mangin et al., 2001]). An alternative is to use assymetric bipolar gradients with two refocusing pulses as proposed by [Reese et al., 2003] that compensate eddy currents to the first order. Spikes or vibration effects are also part of the first class. Spikes are due to RF contamination of the signal by a frequency generally equal to 50 Hz for instance due to an external device present in the magnet room but with a poorly filtered supplier. They can also be due to failing coil antennas (typically with dysfunctionning preamplifiers). They correspond to a strip pattern on the image that can be easily detected. Vibrations are a typical phenomenon present in dMRI due to the commutation of very strong gradients. They result from a mechanical coupling between the gradient coil, the patient bed and the subject itself. They lead to loss of signal in large areas and can also be detected quite easily ([Gallichan et al., 2010]). Last for this first class of artefacts is the non Gaussian noise, being either Rician or χ-non centered depending on the parallel reconstruction algorithm. Siemens systems provides the GRAPPA reconstruction algorithm delivering reconstructed data characterized by a χ-non centered noise (see [Brion, 2013]). The quality check pipeline of Connectomist 2.0 proposes automatic corrections for eddy currents, spikes and vibration effects, non Gaussian noise that was used to preprocess the diffusion MR data of the CONNECT/Archi database. The second class of artefacts is linked to the subject itself. First, susceptibility effects at the place of air-tissue interfaces like for instance close to the sinus or the bones induce field inhomogeneities leading to non linear distorsions and distorsions

of the grey level intensity. Two solutions exist to correct for them : the first solution relies on the acquisition of a field map calibration scan from which the correction field can be inferred ([Jezzard and Balaban, 1995]) and the second solution consists of non linear registration of the distorted data to a T_1-weighted anatomical reference free of susceptibility artefacts ([Bhushan et al., 2012]). The two techniques are also available in Connectomist 2.0, but since B_0 field maps were acquired, the first solution was used to correct for susceptibility artefacts. Motion of the subject must also be dealt. Each diffusion weighting volume can be corrected to a b=0 s/mm^2 reference volume using a rigid transformation but the diffusion directions have also to be corrected by the rotation matrix stemming from the rigid transformation. Connectomist 2.0 also provides such a motion correction.

4.3.2 Local modeling and tractography

After the correction of artefacts, we computed a field of local diffusion models, providing the Orientation Distribution Function for each voxel. Several local models described in the previous chapter were applied in the Archi database and for the present study, Spherical Deconvolution Transform (SDT,[Descoteaux et al., 2009a]) was used. The SDT model was computed using a spherical harmonic order SH=6, a regularization factor $\lambda = 0.0006$. The Gaussian deconvolution kernel was estimated using the 300 most anisotropic (of FA at least equal to 0.65) voxels within the corpus callosum, assuming a cylindrical symmetry of the kernel ($\lambda_2 = \lambda_3$). A regularized streamline deterministic tractography [Perrin et al., 2005a] was performed with a propagation domain computed from the associated T_1-weighted data ([Guevara et al., 2011a]) using BrainVisa [Cointepas et al., 2003] / Morphologist [Rivière et al., 2002]. The regularized streamline deterministic tractography algorithm was chosen over the probabilistic algorithm in order to be compatible with the use of the bundle atlas of Guevara et al. [2011b]. Contrary to most existing tractography tools using a simple thresholded FA map where the choice of the threshold can be debated, our tractography domain is computed from the robust brain mask resulting from the Morphologist pipeline. An homotic erosion was applied using a skeleton of the sulci, in order to prevent any connection between the two sides of each sulcus, (this can happen at the millimeter resolution of the T_1-weighted MRI). We added to this mask a mesh of the deep nuclei to ensure a good delineation of the deep structures (see Figure 4.2). The parameters were as follows : aperture angle of 30 degrees, forward step of 0.2mm (corresponding to a eigth of the diffusion weighting spatial resolution), one seed per voxel of the propagation domain uniformly sampled. It provided an average of 30 millions of fibers per subject.

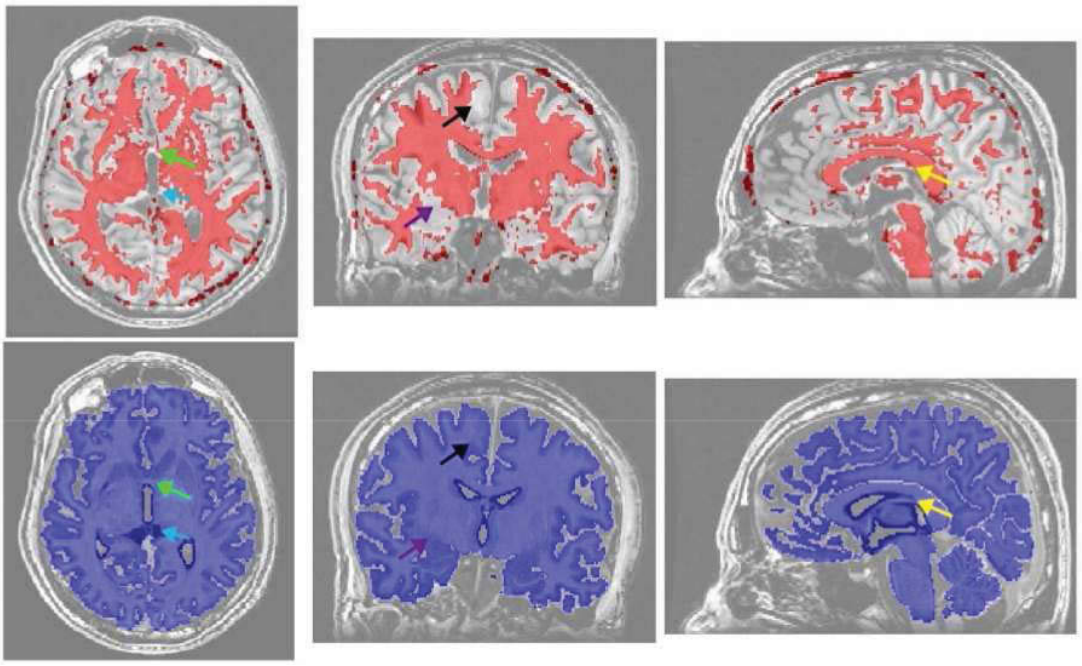

FIGURE 4.2: Robust Tractography mask (figure from [Guevara et al., 2011a]).First line: mask with a simple FA threshold, second line: T_1-based mask. many important areas of white matter are missed when using FA based masks

4.3.3 Intra-subject and inter-subjects clustering

The fibers of each subject were clustered into small fascicles using the automatic technique of [Guevara et al., 2011b]. All the details about the algorithm are provided in [Guevara et al., 2011b] and [Guevara et al., 2012] but to summarize, the tractogram is first divided into four parts, fibers in the right hemisphere, fibers in the left hemisphere, fibers partly in each hemisphere, and fibers passing through the cerebellum. Secondly, these groups are again splitted in ten groups of different lengths (20-35mm, 35-50mm, 50-65mm, 65-80mm, 80-95mm, 95-110mm, 110-130mm, 130-150mm, 150-175mm, 175-200mm) and a hierarchical clustering is performed on white matter parcels using a connectivity-based segmentation. Fascicles are then differentiated using another clustering based on their extremities. Centroids of the obtained fascicles are computed and used in a second level clustering to provide the final bundles. The clustering step is illustrated in Figure 4.3.

4.3.4 Labelling

Centroids of the bundles of each subject obtained during the previous step are computed and compared, using a specific distance (corresponding to the maximum of the Euclidian distance between two points of the two centroids normalized by the difference between

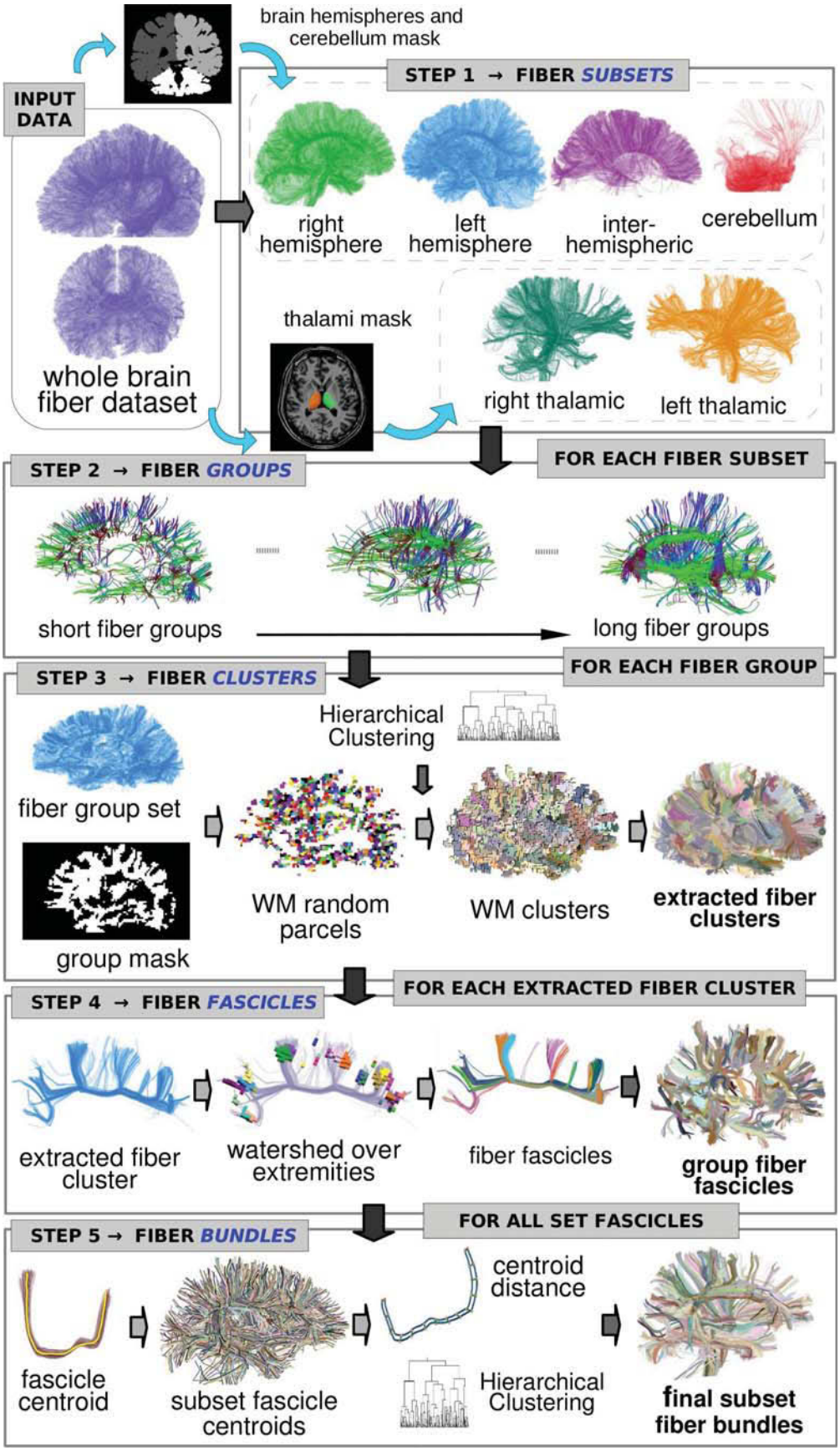

FIGURE 4.3: Clustering. Step 1 : hierarchical decomposition, Step 2: length-based segmentation, Step 3: voxel-based clustering, Step 4: extremity-based clustering, and Step 5: fascicle merge. From [Guevara et al., 2012].

FIGURE 4.4: Major white matter bundles of the 79 subjects of the ARCHI database: corpus callosum (rostrum: dark pink, genu: dark blue, body: dark green, splenium : brown), arcuate tracts (arcuate: red, anterior arcuate: green, posterior arcuate: yellow), uncinate tract: cyan, Inferior Fronto Occipital tract: pink, Inferior Longitudinal Tract: purple, Cingulum: brown

their lengths) to the centroids of all bundles of bundle atlas previously built by [Guevara et al., 2011b]. Each centroid of each subject receives the label corresponding to the closest bundle centroid of the atlas. In this way, we obtain all the well-known long white matter bundles for each subject. Figure 4.4 depicts the long white matter bundles combining the labelling bundles of the 79 subjects of the CONNECT/Archi database.

4.3.5 Diffeomorphic registration of subjects using DTI-TK

A common space is needed to build quantitative and probabilistic atlases. A simple affine transformation is not sufficient to register diffusion data because of the inter-subject variability. Because our work focuses explicitly on white matter connectivity, the orientation information embedded in the orignal DTI or HARDI data have to be preserved. Different techniques have been proposed using either DTI or HARDI data. [Alexander et al., 2001] described a method allowing to register DTI data keeping the original orientations of the tensor and DTI-TK proposed in [Zhang et al., 2006] provided a diffeomorphic tensor-based coregistration optimized for aligning white matter anatomy. With the emergence of HARDI-models going beyond DTI, new techniques were developped that took benefit of the high angular resolution of the ODFs or fODFs. In [Raffelt et al., 2011], diffusion weighted data were registered using a diffeomorphic transformation based on the decomposition of the fiber orientation distribution on a modified spherical harmonics basis. Another alternative was proposed by [Yap et al., 2011] using an elastic registration of HARDI data based on the spherical harmonics decomposition of the diffusion orientation distribution function.

In our study, we chose the available DTI-TK software ([Zhang et al., 2006], `dti-tk.sourceforge.net`) which has been validated and used in several studies ([Wang et al., 2011], [Keihaninejad et al., 2012], [Liu et al., 2014],...) (in future analysis it could be useful to compare

the results obtained with the DTI-TK software and the recent HARDI-based coregistration techniques). All the subjects' data were first coregistered to the IXI template (http://biomedic.doc.ic.ac.uk). Then, a new template was built from the DTI maps of all subjects. All subjects' data were then coregistered to this new template using the DTI-TK approach. In their approach, the authors first define a new distance between two tensors $\mathbf{D_1}$ and $\mathbf{D_2}$ in the space of diffusion tensor, defined as follows :

$$||\mathbf{D_1} - \mathbf{D_2}||_D = \sqrt{\frac{8\pi}{15}(||\mathbf{D_1} - \mathbf{D_2}||_C^2 - \frac{1}{3}Tr(\mathbf{D_1} - \mathbf{D_2})^2)} \tag{4.1}$$

with $||\mathbf{D_1} - \mathbf{D_2}||_C = \sqrt{Tr((\mathbf{D_1} - \mathbf{D_2})^2)}$, Tr being the trace of the tensor. This new metric is used in the optimization scheme. The registration is defined as an optimization problem expressed in the form :

$$\underset{v \in V}{\arg\min}(\phi(I_t, I_s, v) + \psi(v)) \tag{4.2}$$

with I_t the template image, I_s the subject image, v the transformation, ϕ the similarity measure between the two images, ψ a regularization term. The optimization scheme includes the problem of reorientation of the tensors. Global transformation (if smooth) between the images can be expressed locally by an affine transformation. The rotation matrix required for tensor reorientation can be extracted from the Jacobian of the tranformation. The Jacobian matrix can be decomposed as the product of an orthogonal matrix Q, corresponding to the rotation part and a symmetric and a positive-definite matrix S. The local affine tranformation F is expressed as $F = (\mathbf{QS})x + \mathbf{T}$, $\mathbf{Q}$ being the rotation matrix, S the deformation matrix, and T the translation vector and the similarity measure is defined by

$$\phi(p) = \int_\Omega ||I_s((\mathbf{QS})\mathbf{x} + \mathbf{T}) - QI_t(\mathbf{x})\mathbf{Q}^T||^2 dx \tag{4.3}$$

for a region Ω and for p the parameters of the affine transform. Using this similarity measure allows to take into account the reorientation of the tensor during the optimization. The template is then divided hierarchically into several regions with a multi-scales approach (dividing each dimension by 4, 8, 16 and 32), and the optimization algorithm researches the best affine transformation between this region and the subject image. The following regularization term is imposed on the borders of each region :

$$\psi(p_i, p_j) = \int_{\Omega_i \cap \Omega_j} ||F_i(x) - F_j(x)||dx, \tag{4.4}$$

with F_i the affine transformation corresponding to the region i. The final deformation vector field is computed by interpolating the deformation on borders to smooth the

discontinuities between the obtained transformations of the regions separated by these borders.

4.3.6 Super resolved quantitative atlases

While still controversal, super-resolution techniques can efficiently improve the spatial resolution of diffusion-based quantitative maps such as FA or color-encoded maps [Calamante et al., 2012]. This technique consists in projecting any quantitative information onto dense streamline-based tractograms constructed at a high spatial resolution (for instance corresponding to the forward step during the fiber tracking) and secondly projecting the information back to a Cartesian grid of a higher spatial resolution compared to the acquisition resolution (see Figure 4.5). Working at the resolution offered by the tractogram allows thus to preserve fine anatomical details naturally embedded in the diffusion-weighted signal that are lost when staying at the acquisition resolution [Duclap et al., 2013c]. We extended this approach originally developed at the individual scale to the group level. It was then applied to the coregistered maps of the Archi database subjects to create a 500μm isotropic resolution (a higher resolution would not provide additional information since it is limited by the initial tractography density) atlas of the white matter connectivity (Figure 4.6 shows the results the FA atlas from an original resolution of 1.7mm isotropic to 1mm, 0.75mm and 0.5mm). The super-resolved maps using the tractograms of the subjects, obtained using 27 seeds per voxels, an aperture angle of 30 degrees and a forward step of 0.2mm.

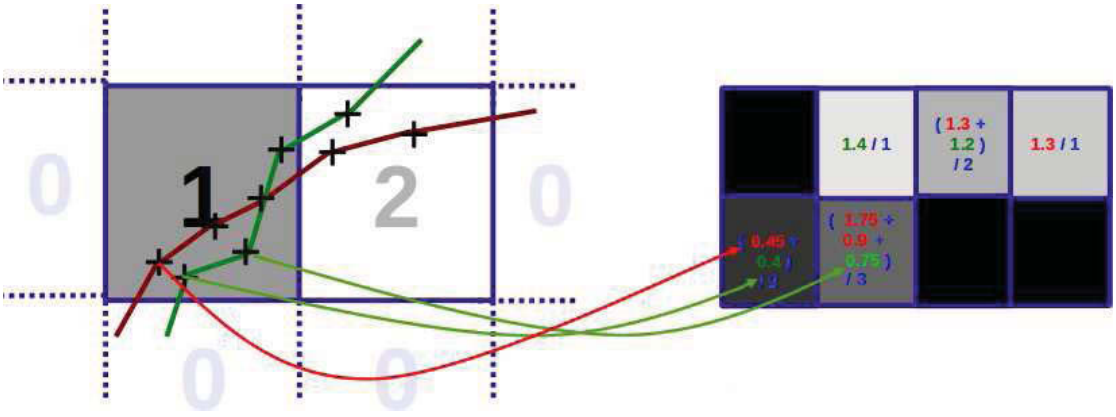

FIGURE 4.5: Super resolution technique

4.3.7 Connectivity Atlas

Finally, several probabilistic atlases were computed from the 79 individual maps using the super-resolution technique, thus providing atlases at the initial resolution of 1.7mm

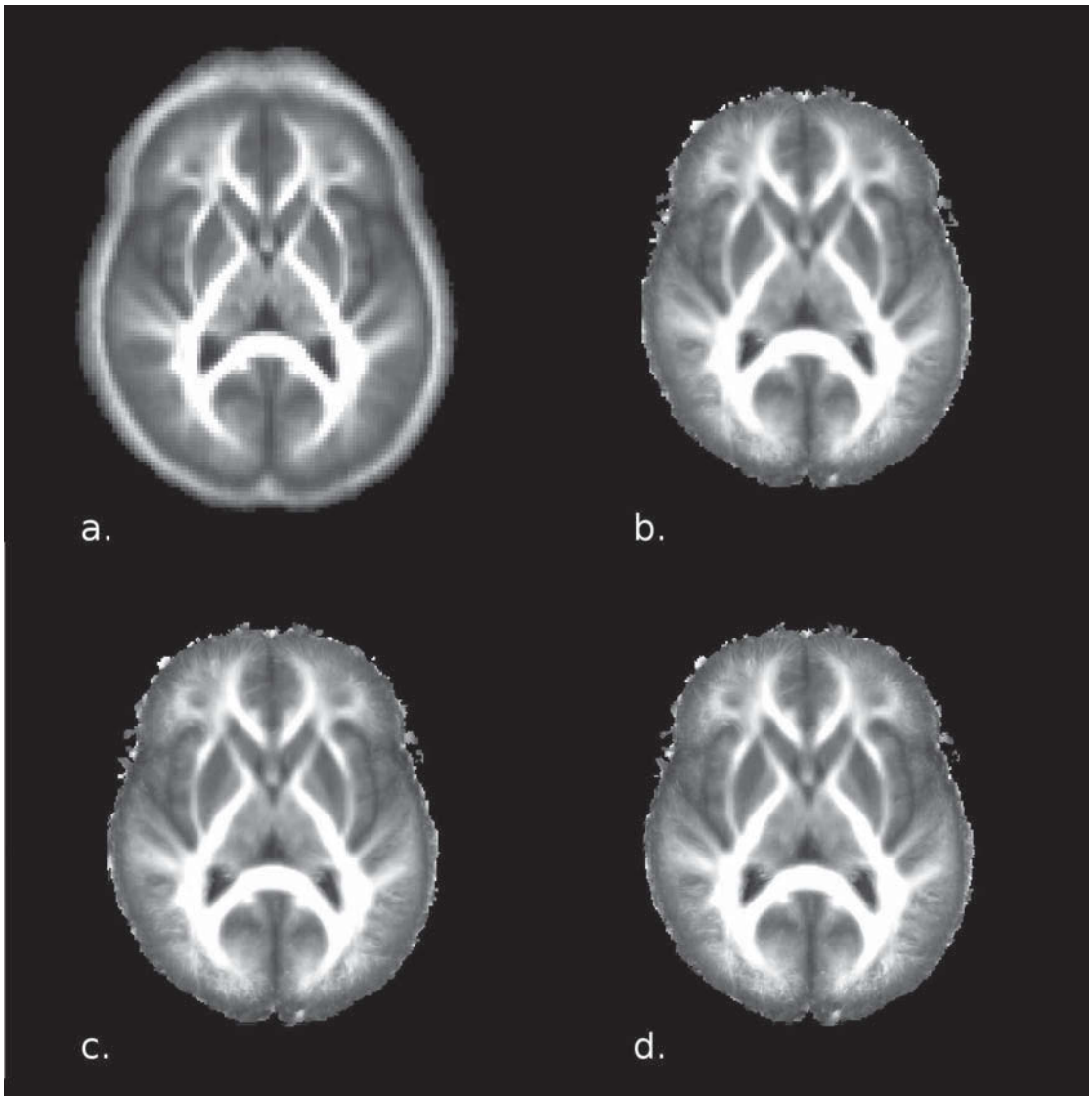

FIGURE 4.6: Super resolution technique : FA maps obtained from the combination of the 79 subjects' maps from the initial resolution 1.7mm isotropic (a) to 1mm (b), 0.75mm (c) and 0.5mm (d)

isotropic and at the high resolution of $500\mu m$. Figure 4.7 depicts the FA, ADC, axial and radial diffusivities maps at the 500 μm isotropic resolution. These maps show good anatomical contrast and the super resolution method provides an unique way to look at fine anatomical details along white matter bundles.

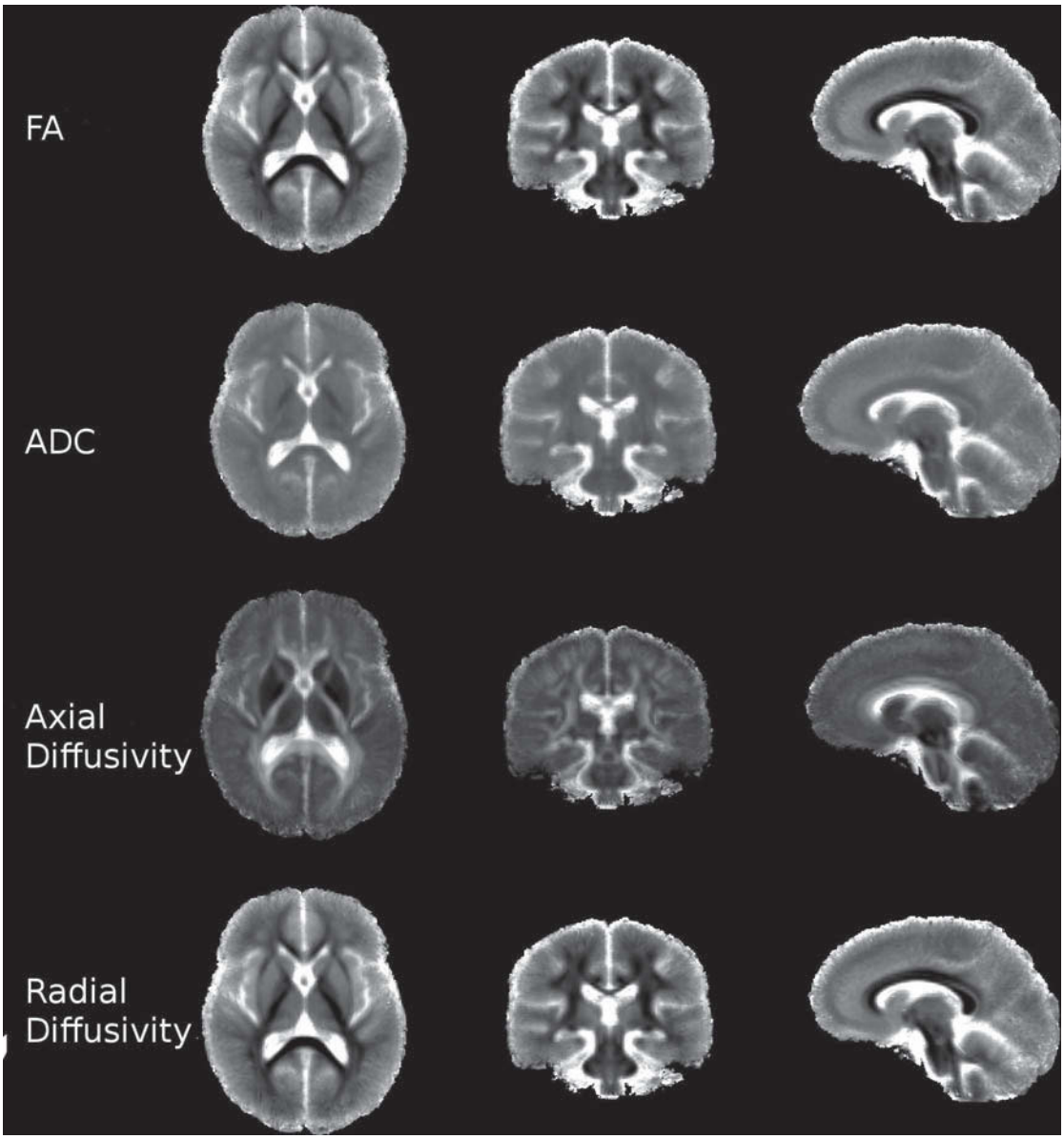

FIGURE 4.7: Super-resolved (0.5mm isotropic) FA map (top line), ADC map (second line), Axial Diffusivity (third line), Radial Diffusivity (bottom line)

4.4 High resolution relaxometric 3D atlases

4.4.1 Inference of individual relaxometry maps

As mentioned previously, echoplanar sequences were used to acquire the T_1 and T_2 datasets in order to significantly decrease the acquisition time to less than 5 minutes per dataset. Thus, the datasets suffer from the same geometric distortions as for the HARDI dataset, and were corrected for geometric distortions induced from susceptibility effects using the same approach based on the use of B0 field maps. Then, the corrected dataset was matched to the T_1-weighted anatomy using a rigid 3D transformation and masked

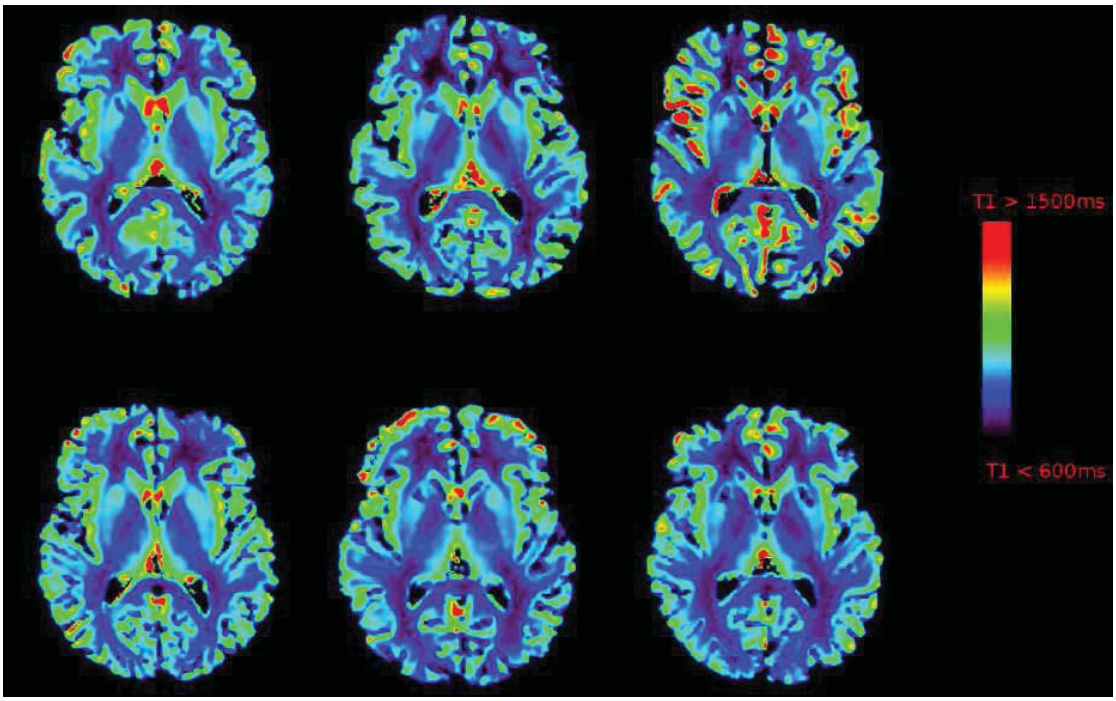

FIGURE 4.8: Individual T_1 maps of 6 subjects from the Archi database using a T1-based mask

with the same T_1-based mask used as tractography mask of the diffusion data. The T_1 & T_2 quantitative maps of each subject were computed by fitting the following two equations to the T_1 and T_2 datasets, respectively:

$$S = \rho\,|1 - 2\exp(-TI/T_1)| \text{ and } S = \rho\exp(-TE/T_2),$$

ρ being the proton density, TI the inversion time and TE the echo time. A Levenberg-Marquardt non-linear fit algorithm was used to obtain the optimum parameters at the voxel level. The initial parameters were chosen carefully in order to take into account the high sensitivity of the algorithm to its initialization. We initialized T_1 & T_2 close to the mean values for grey and white matter found in the litterature at 3T ([Wansapura et al., 1999]): T_1=1000ms, T_2=90ms. Figure 4.8 and 4.9 show the obtained individual T_1 and T_2 maps of 6 subjects, showing good contrast between grey and white matters and a good delineation of the nuclei, especially in T_2 maps.

4.4.2 Inference of high resolution atlases

From the 79 individual T_1 and T_2 maps, high-resolution T_1 and T_2 atlases were built using the same approach as for the connectivity atlas. The individual T_1 and T_2 quantitative maps were coregistered to the diffusion-weighted data and were then transformed using the same diffeomorphic transformation in order to create a novel relaxometry atlas.

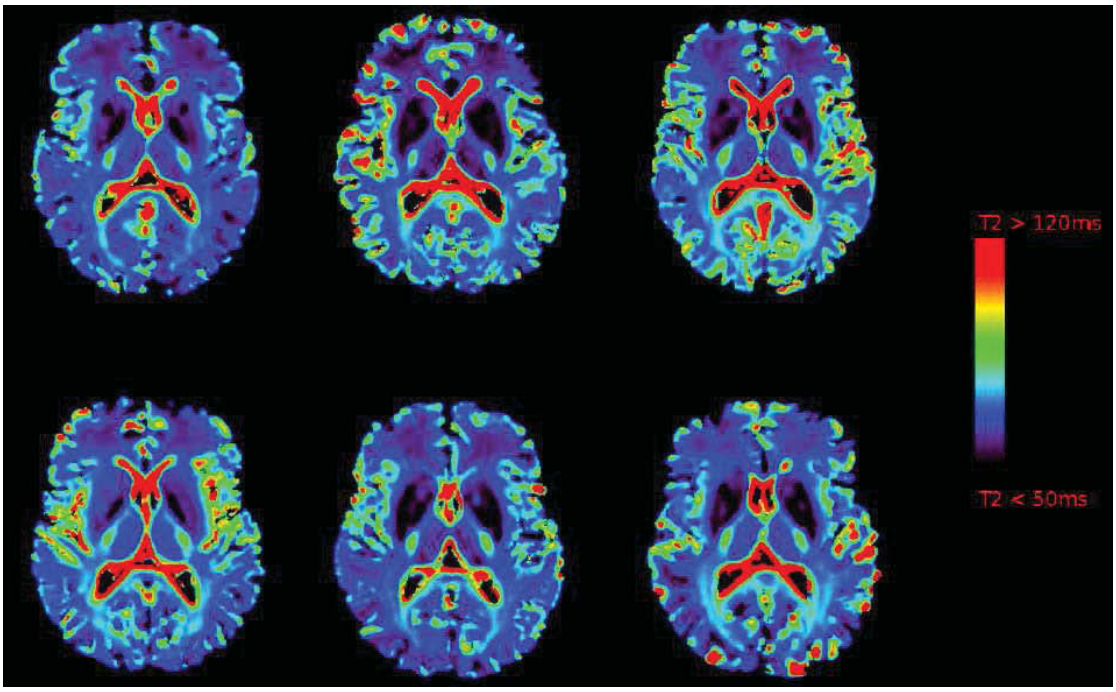

FIGURE 4.9: Individual T_2 maps of 6 subjects from the Archi database using a T1-based mask

Therefore, the bundle maps, the scalar diffusion maps and the T_1 and T_2 maps of all the subjects are all coregistered to a common space, defined by the Archi template built from the DTI maps of the 79 subjects. The super-resolution technique was also applied to reach a $500\mu m$ resolution. Figure 4.10 depicts the half-millimeter resolution quantitative atlases of T_1 and T_2 relaxation times.

The maps clearly show a good contrast between the various brain structures, such as the cortex, the deep nuclei and the white matter anatomy. The T_1 values are between 600ms and 1200ms, and the T_2 values are between 50 and 120ms, corresponding to the expected values at 3T.

4.5 T_1 and T_2 profiles along white matter bundles

4.5.1 Profile Computation

Our analysis relies on the combination of white matter and relaxometry atlases. Here, we present the mean profiles of T_1, T_2, ADC, FA, $\lambda_\perp$ and $\lambda_\parallel$ along 8 well-known bundles (arcuate, anterior arcuate, posterior arcuate, long cingulum, corticospinal, inferior fronto-occipital, inferior longitudinal and uncinate bundles) computed for the subjects of the CONNECT/Archi database. The thalamic radiations originally included in the

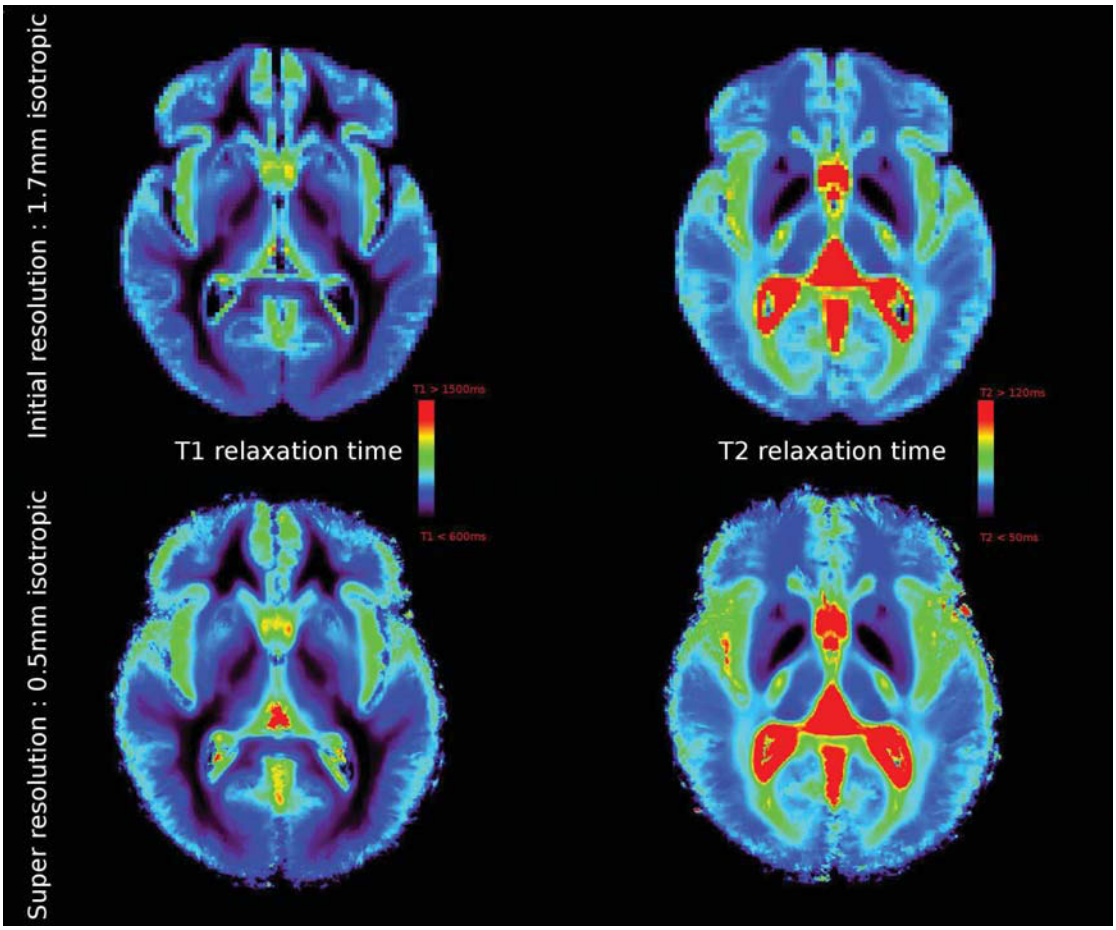

FIGURE 4.10: First line: 1.7 mm isotropic resolution atlases of quantitative T_1(left) and T_2(right) relaxation times obtained from the 79 subjects of the CONNECT/Archi database, second line : 500μm isotropic resolution atlases using the super resolution technique

extracted bundles from the clustering were excluded because of the difficulty to represent the fasciculus by a centroid due to its fanning configuration.

To get the final profile for each bundle, there were several steps to be followed. First, a centroid was obtained from the merged bundles of all subjects. The centroid of each bundle was divided into 1mm length sections using a curvilinear coordinate system and a distance map was computed, assigning to each voxel the label of the nearest section. The scalar values from relaxometry and diffusion data analysis of the high resolution atlases were computed along each fiber of each subject's bundle (each fiber is defined by a set of consecutive points and was resampled to get a regular distance of 0.1 mm between two consecutive points). The values obtained along each fiber of each subject's bundle were then projected onto the centroid providing an individual profile based on a group centroid. The average scalar value attributed to a section is obtained by integrating the interpolated values along the pieces of fibers intersecting the corresponding labelled region (see Figure 4.11). Finally, an average bundle profile was computed merging all individual profiles per bundle. One of the goals of this study was to be able to compare

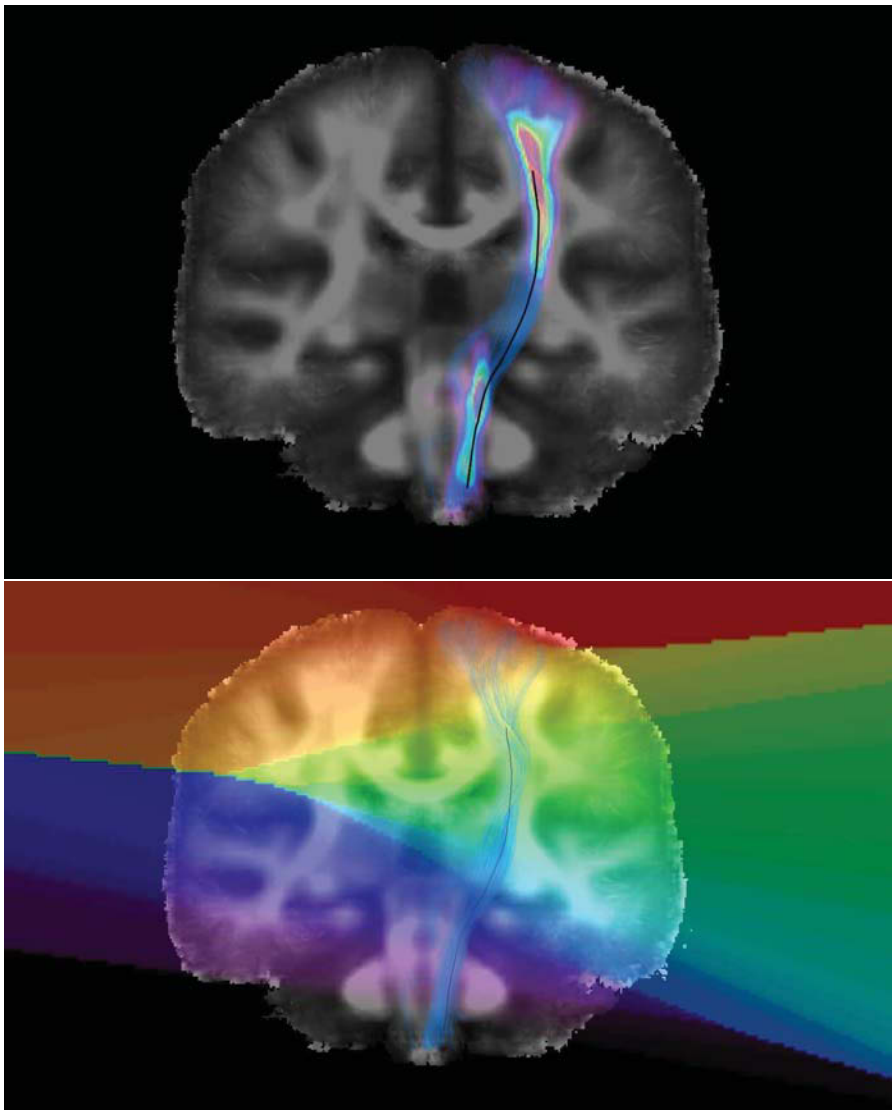

FIGURE 4.11: Profile computation. Top : Computed centroid of left corticospinal tract and corresponding density map. Bottom : sections computed from the centroid defining the domain of integration

right and left hemispheres and to do so, the centroid sections have to be comparable. Matching the profiles is a challenging task.[Mårtensson et al., 2013] proposed a technique to register left and right profiles using anatomical landmarks (such as anterior and posterior commissures, internal capsule...). But this approach is limited and require manual delineation of these anatomical structures.[Durrleman et al., 2011] offered an alternative modeling bundles as currents. We here used a simpler technique. At the group level, we projected the left bundle onto the right hemisphere, using the symmetry with respect to the midplane between the two hemispheres of the brain. The right and left bundles were then merged and a common centroid was computed. Finally, the left centroid was obtained projecting the computed centroid back to the left hemisphere which allowed the comparison between the profiles of each hemisphere.

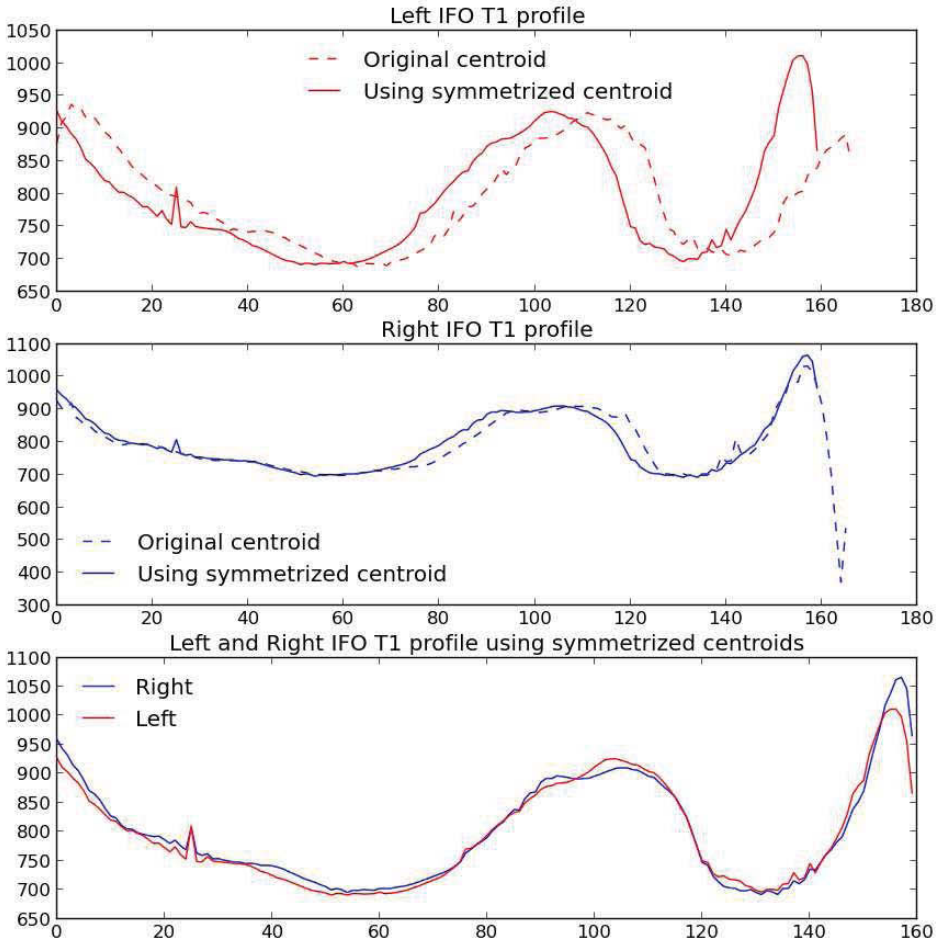

FIGURE 4.12: Differences between profiles using orignal centroids and symmetrized centroids

4.5.2 Validation of the symmetrized centroids

Figure 4.12 shows the accuracy of the registration of the profiles using the symmetrized left and right centroids computed from the merged bundles of both hemispheres. The first two graphs depict the difference between the T_1 profile of the IFO tract using the centroids computed from left and right bundles separately and using the centroids computed originally from the merged bundles obtained by projection of the left bundles onto the right hemisphere. The last graph shows the final left and right profiles computed from the symmetrized centroids. This technique clearly preserves the shape of the profiles to accurately match right and left profiles.

4.5.3 Profiles of T_1 and T_2 along WM bundles

Main results are given in figures 4.13-4.18, showing the average group profiles for T_1 & T_2 as well as FA, ADC, $\lambda_\perp$,$\lambda_\parallel$ profiles (obtained from the SDT analysis of the diffusion data) of eight chosen white matter bundles and out of the 19 long available bundles in the high resolution atlas: the corticospinal tract, the group of the arcuate tract and anterior/posterior arcuate, the uncinate, the inferior longitudinal, the cingulum and the fronto-occipital fasciculi. Right hemisphere profiles are plotted in green and left profiles in blue.

4.5.4 Anatomical analysis of the profiles

As it was already exposed in section 3.3, for the white matter, the pool of water located inside the myelin sheath is caracterized by short T_1 and T_2 and the pool of water located outside the myelin sheath, including intra and extra axonal water is characterized by longer T_1 and T_2 relaxation times. Variations of T_1 and T_2 could then partially be explained by the degree of myelination with respect to free water. But other complicated chemical exchanges could also affect these relaxation times. Fiber configurations could also affect the T_1 and T_2 values such as highly packed fibers or crossings. The comparison with diffusion parameters profile can potentially help us to understand fluctuations of values in T_1 and T_2 profiles. In this section, we discuss the obtained profiles from an anatomical point of view.

4.5.4.1 General observations

T_1 profiles exhibit a similar pattern for all the bundles. The middle section relies on an area with packed and highly myelinated fibers for the chosen bundles, leading to low values for the T_1 relaxation times. When the fibers reach the cortex (at both extremities of the profiles), the fanning configuration, the partial volume effect with grey matter as well as potential crossings with U-fibers lead to higher values of T_1. T_2 profiles generally follow the variations of the corresponding T_1 profiles, but the differences between the extremities and the middle of the bundles are not always as clear as for T_1. Beyond these general considerations, we can notice some differences between the profiles of the different fasciculus, and for some of them we can correlate the variations along the profiles with the underlying anatomy along the bundles.

4.5.4.2 Arcuate Group (Figures 4.13-4.15)

T_1 and T_2 profiles for three bundles of the arcuate group generally exhibit a simple pattern with low values in the middle of the fasciculus (corresponding to the deep white matter, without partial volume effect from grey matter). T_2 profiles have a larger variation across the subjects than T_1 profiles for these bundles. For the posterior arcuate bundle, T_2 values are still high in the middle of the tract while the FA remains high in this region.

4.5.4.3 Cingulum Tract (Figure 4.16)

T_1 and T_2 profiles show a little decrease from the anterior part to the posterior pregion, revealing microstructural differences between these regions, suggesting different fiber configurations, such as variation in the density or in the orientation dispersion. This differences are also indicated by a similar pattern of the radial diffusivity.

4.5.4.4 CorticoSpinal fasciculus (Figure 4.17)

The first consideration about the corticospinal tract concerns T_2 values significantly higher (between 80ms-105ms) than for all the other bundles (between 65ms-80ms), this has been reported previously in [Reich et al., 2006], [Herve et al., 2011], [Russell-Schulz et al., 2013], that could be explained by the presence of large and sparsly distributed axons. T_1 and T_2 profiles of the corticospinal tract exhibits two peaks of hyperintensities (around the 25th and 60th sections) corresponding to the crus cerebri and the internal capsule respectively(small peak but in concordance with [Russell-Schulz et al., 2013] and [Herve et al., 2011]). One hypothesis for the internal capsule peak is related to the presence of higher radii and sparsity of fibers in this region ([Russell-Schulz et al., 2013]). An additional characteristic of CST profiles is that T_1 and T_2 profiles don't exhibit a clear variation at the level of Corpus Callosum fibers (around the 80th section), while FA and $\lambda_{\parallel}$ profiles clearly do, being sensitive to crossings.

4.5.4.5 Inferior Fronto Occipital fasciculus (Figure 4.18)

One particularity of the IFO profiles is the presence of a peak around the 100th section for both relaxation times, corresponding to the beginning of the external capsule which may be due to partial volume effect with nuclei surrounding this region. T_2 profile follows the trend of FA and $\lambda_{\parallel}$ from the 40th section, with a decrease from the posterior part to the anterior part of the fascicle ; T_1, ADC and $\lambda_{\perp}$ exhibits a similar behaviour.

4.5.4.6 Inferior Longitudinal Fasciculus (Figure 4.19)

All the profiles of the inferior longitudinal fasciculus follow the same trend (except the T_2 profiles more stable), with a high-low-high pattern for T_1, T_2, ADC, $\lambda_\perp$ and low-high-low for the other parameters (that may be explained by the contamination of the signal by partial volume effect with gray matter at the extremities).

4.5.4.7 Uncinate fasciculus (Figure 4.20)

T_1 and T_2 profiles globally decrease along the bundles from the temporal lobe to the orbitofrontal cortex. The observed peaks in FA and $\lambda_\parallel$ profiles around the 40th section, where the fibers of the inferior fronto occipital fasciculus join the fibers of the uncinate, are less visible in T_1 and T_2 profiles.

4.5.4.8 Corpus Callosum

The profiles obtained for the corpus callosum (see Appendix C) depict spurious peaks probably stemming from partial volume effects due to the presence of neighborhing ventricles characterized by much higher T_1 and T_2 values. This indicates that partial volume effect should be considered in the future to improve profiling of quantitative parameters.

4.6 Study of inter-hemispheric asymmetries

For each measurement m, an asymmetry index was computed for each section of the centroid :

$$A(s) = (m(s)_{left} - m(s)_{right})/(m(s)_{right} + m(s)_{left}).$$

To compare the differences between right and left hemispheres, we performed a Wilcoxon test on each section of the profiles to compare the difference between right and left profiles of white matter tracts. Differences are considered significant for $p\text{-}value < 0.01$. Results have been corrected for multiple comparisons using the False Discovery Rate. Finally, we only considered series of at least four significantly consecutive sections. The second column of figures 4.13 - 4.18 shows the median asymmetry index profiles for each bundle. The observed asymmetries are mostly small, inferior to 10% as already reported in [Reich et al., 2006] for the Corticospinal tract. In the figures, in red are depicted the

asymmetries that were significantly different from 0. The higher asymmetry values are found for FA profiles.

4.6.1 Arcuate asymmetries (Figure 4.13-4.15)

The anterior part of the arcuate group doesn't depict any global asymmetry, but locally in the middle, a right lateralization is shown for FA and $\lambda_{\parallel}$, corresponding to the left lateralization of T_2 and $\lambda_{\perp}$ in this region. The T_1 and T_2 values for the posterior part exhibit a lateralization mainly close to the extremities, corresponding to regions corrupted by high partial volume effect. The arcuate tract is the only tract of the group that clearly shows an asymmetry between the two hemispheres. FA values are clearly higher on the left part, while ADC, T_1 and T_2 values are higher on the right. The difference of lateralization of the three segments of the arcuate has already been discussed in [Hugdahl and Westerhausen, 2010], in terms of size. The long segment has a larger tract on the left side, the anterior segment has larger right tract and the posterior part is rather symmetrical. These observations are consistent with our findings, indicating more fibers (and then more myelin fraction, as T_1 and T_2 profiles suggest) on the left side for the long segment and on the right side for the anterior segment.

4.6.2 Cingulum asymmetries (Figure 4.16)

Differences have also been detected for the cingulum bundle with higher anisotropy of the left side that may indicate a higher myelination or fiber density in this hemisphere, confirmed by higher T_1, ADC, $\lambda_{\parallel}$, $\lambda_{\perp}$ on the right side. T_2 values seem to be slightly higher on the left side, but the asymmetry values are very low in comparison to the other parameters. Another interesting observation is that the asymmetry is clearly higher on the anterior part of the cingulum. This is interesting since anterior and posterior cingulum are implicated differently in different cognitive functions. This specificity was already found in other studies [Gong et al., 2005], and the decrease of this asymmetry has been reported in schizophrenic subjects in [Wang et al., 2004].

4.6.3 CorticoSpinal asymmetries (Figure 4.17)

The asymmetry profiles along the corticospinal tract indicate a higher anisotropy for the left side for most sections, confirmed by a higher right ADC, $\lambda_{\parallel}$, $\lambda_{\perp}$ and T_2. Surprisingly, T_1 exhibits higher values on the left side. But for both T_1 and T_2 values the asymmetry values remain low in comparison to FA. This left domination could be explained by the handedness, since the Archi database is almost entirely composed of right-handed

subjects (only three left-handed subjects). Several studies focus on this topic such as [Seizeur et al., 2013] and [Westerhausen et al., 2007], discussing the uncertainty about the origin of this asymmetry.

4.6.4 Inferior Fronto Occipital asymmetries (Figure 4.18)

No specific pattern was found for this tract. The T_1 and T_2 values seem to be higher in the right hemisphere in the posterior part, and higher in the left hemisphere for the anterior part. This trend is not the one followed by diffusion parameters, showing higher right values for ADC and $\lambda_\perp$ in the middle of the tract and higher left values for the rest of the tract.

4.6.5 Inferior Longitudinal asymmetries (Figure 4.19)

We cannot observe any global asymmetry for T_1 and T_2 profiles, while for diffusion parameters, the asymmetry profiles show a right lateralization (reported in [De Santis et al., 2014]) for the region between the 20th and 60th sections (but only significant for ADC and $\lambda_\perp$) and higher values in the left hemispheres for the rest of the tract.

4.6.6 Uncinate asymmetries (Figure 4.20)

T_1,T_2, $\lambda_\parallel$, $\lambda_\perp$ and ADC values shows higher values on the left side while FA shows greater values on the right side. A right lateralization for the numbers of fibers was already found in healthy subjects in a comparison study with schizophrenic patients [Highley et al., 2002], indicating a greater right-sided fronto-temporal connectivity.

4.7 Comparison with the profiles of diffusion structural parameters

We computed the Pearson correlation coefficient of each section for each pair of diffusion parameter (ADC,FA,$\lambda_\perp$,$\lambda_\parallel$) & T_1 relaxation time and diffusion parameter & T_2 relaxation time. Figures 4.21-4.24 represent the correlations between each diffusion parameters and T_1 or T_2 relaxation times, along the bundles. From a global point of view, for all the bundles, positive correlations have been found between ADC and T_2/T_1 relaxation times. FA shows strong negative correlation with T_1. The relationship between

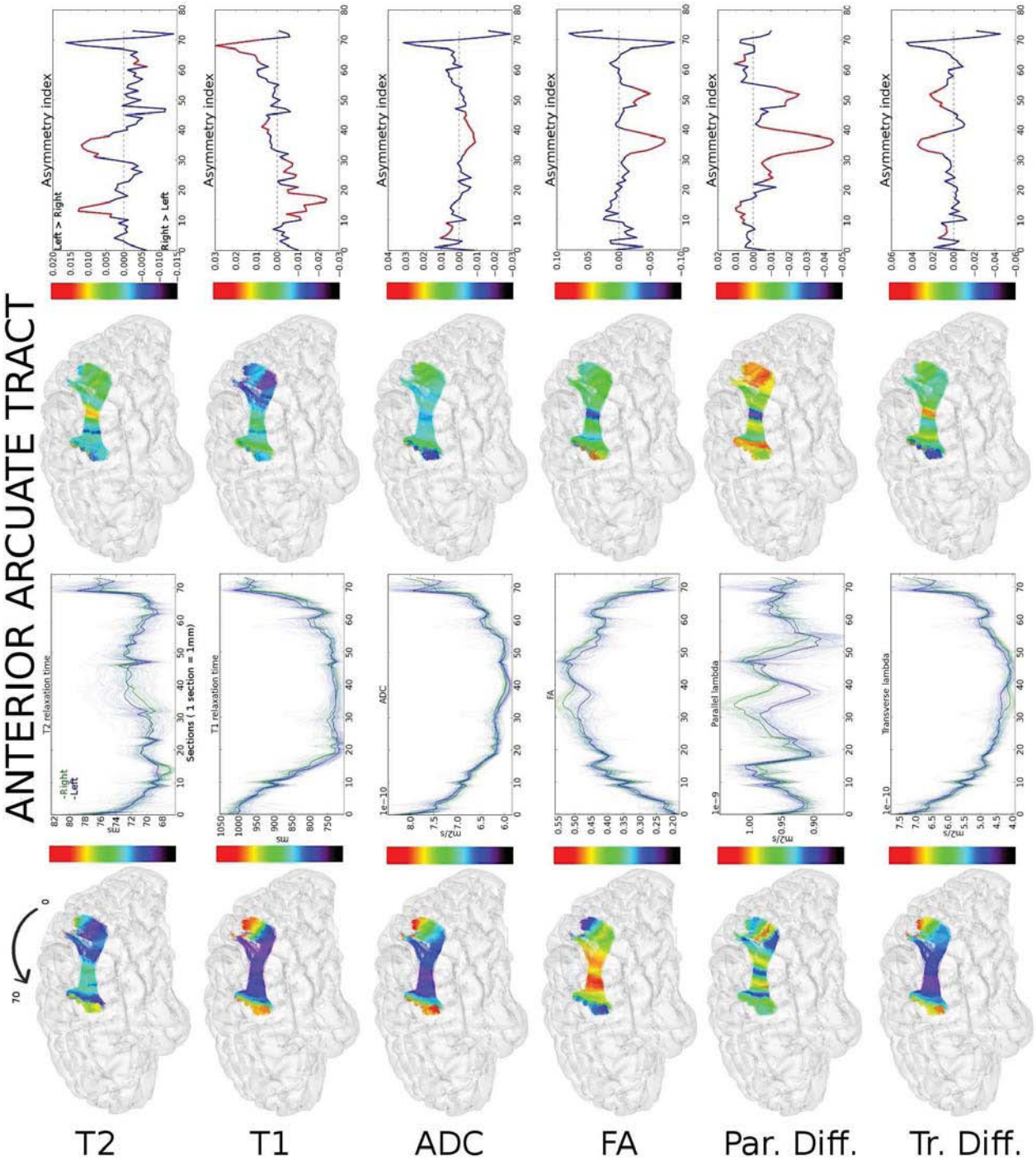

FIGURE 4.13: Left Columns : Average T_1, T_2, FA, ADC, $\lambda_{\|}$ and $\lambda_{\perp}$ profiles of the anterior arcuate tracts (In green : right bundle profiles, in blue left bundle profiles). Individual profiles are also plotted. Right Columns : Interhemispheric asymmetries (red lines correspond to regions with at least 4 significantly asymmetric sections)

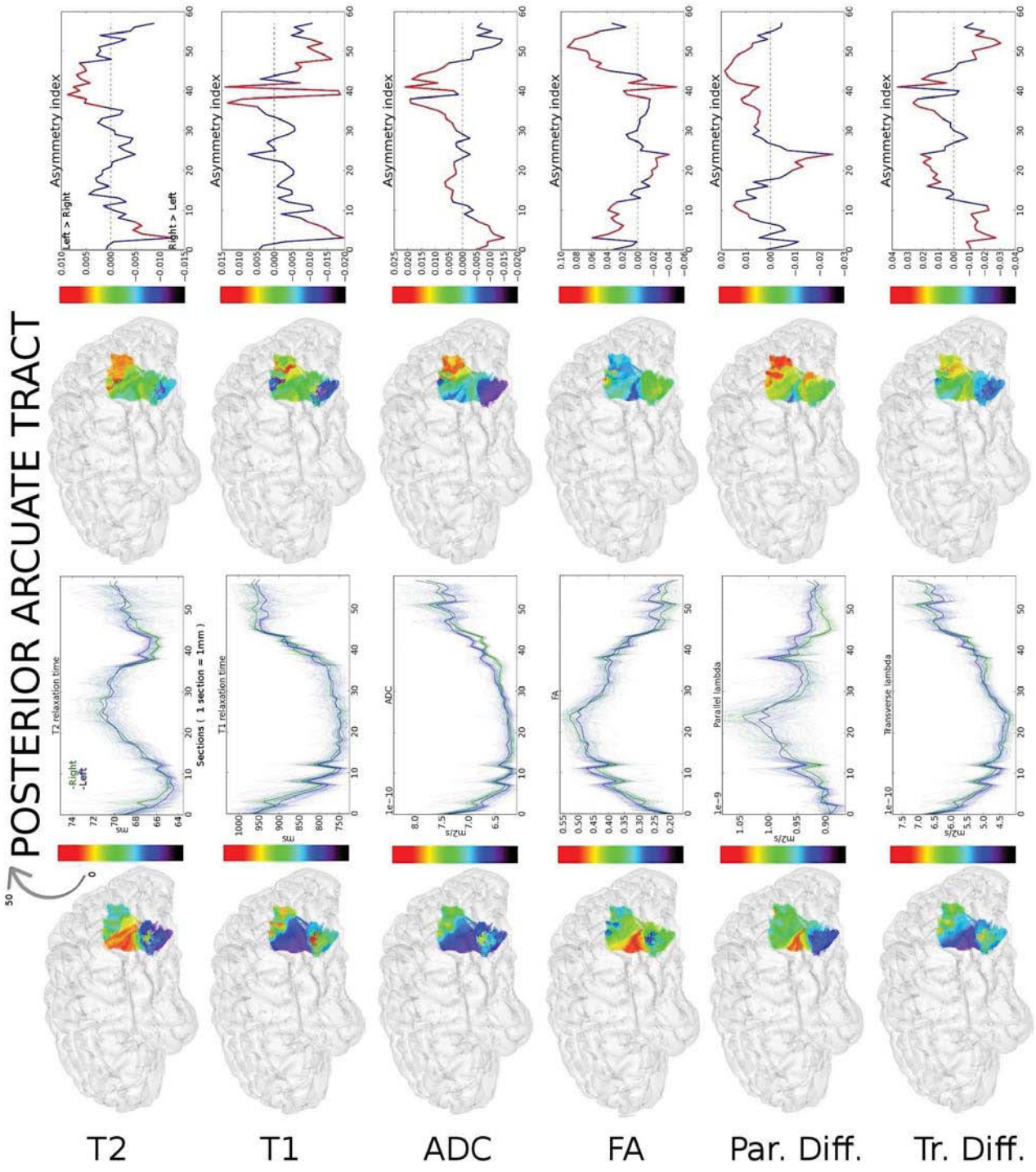

FIGURE 4.14: Left Columns : Average T_1, T_2, FA, ADC, $\lambda_{\|}$ and $\lambda_{\perp}$ profiles of the posterior arcuate tracts In green : right bundle profiles, in blue left bundle profiles. Individual profiles are also plotted. Right Columns : Interhemispheric asymmetries (red lines correspond to regions with at least 4 significantly asymmetric sections)

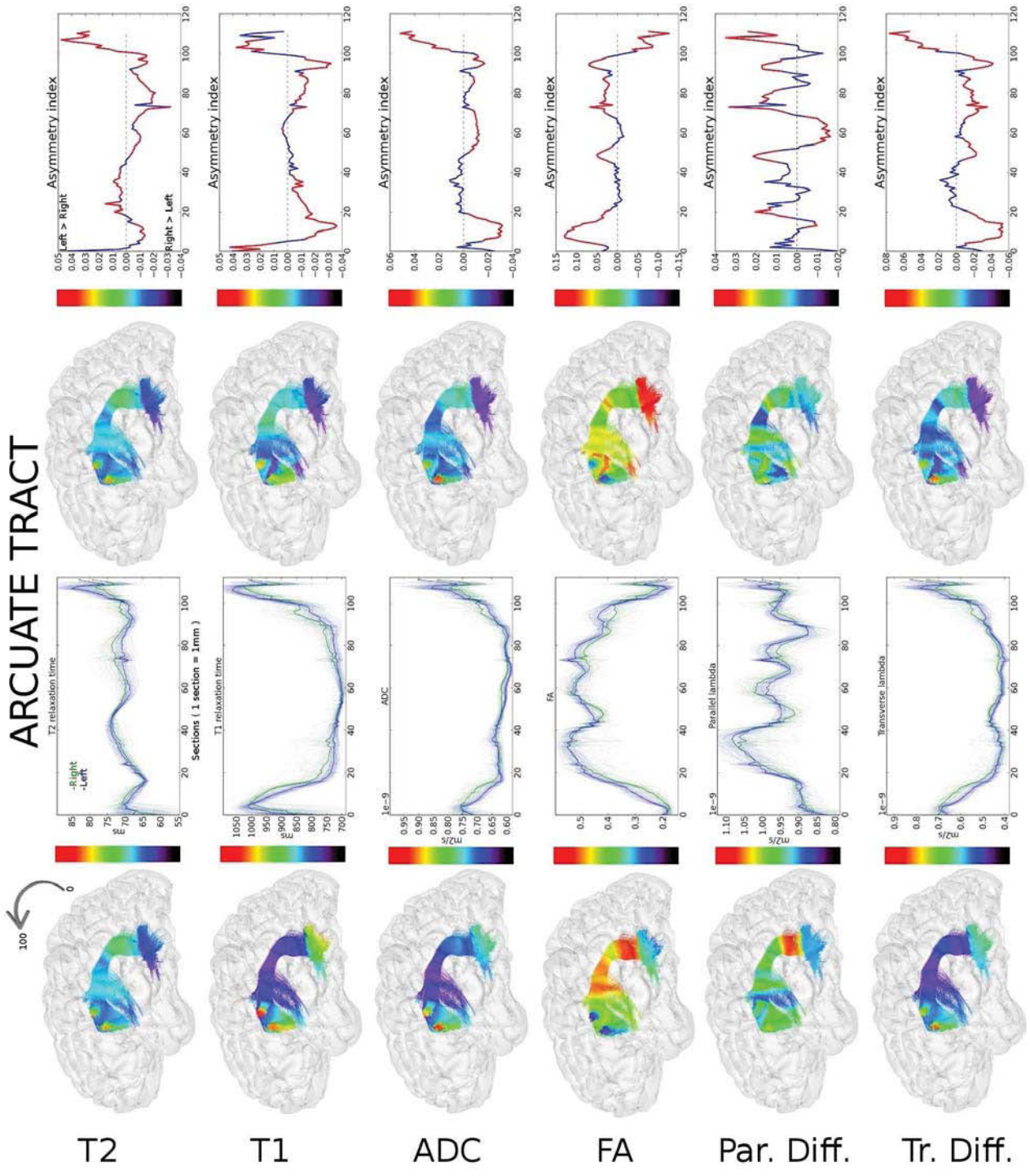

FIGURE 4.15: Left Columns : Average T_1, T_2, FA, ADC, $\lambda_{\|}$ and $\lambda_{\perp}$ profiles of the arcuate tracts In green : right bundle profiles, in blue left bundle profiles. Individual profiles are also plotted. Right Columns : Interhemispheric asymmetries (red lines correspond to regions with at least 4 significantly asymmetric sections)

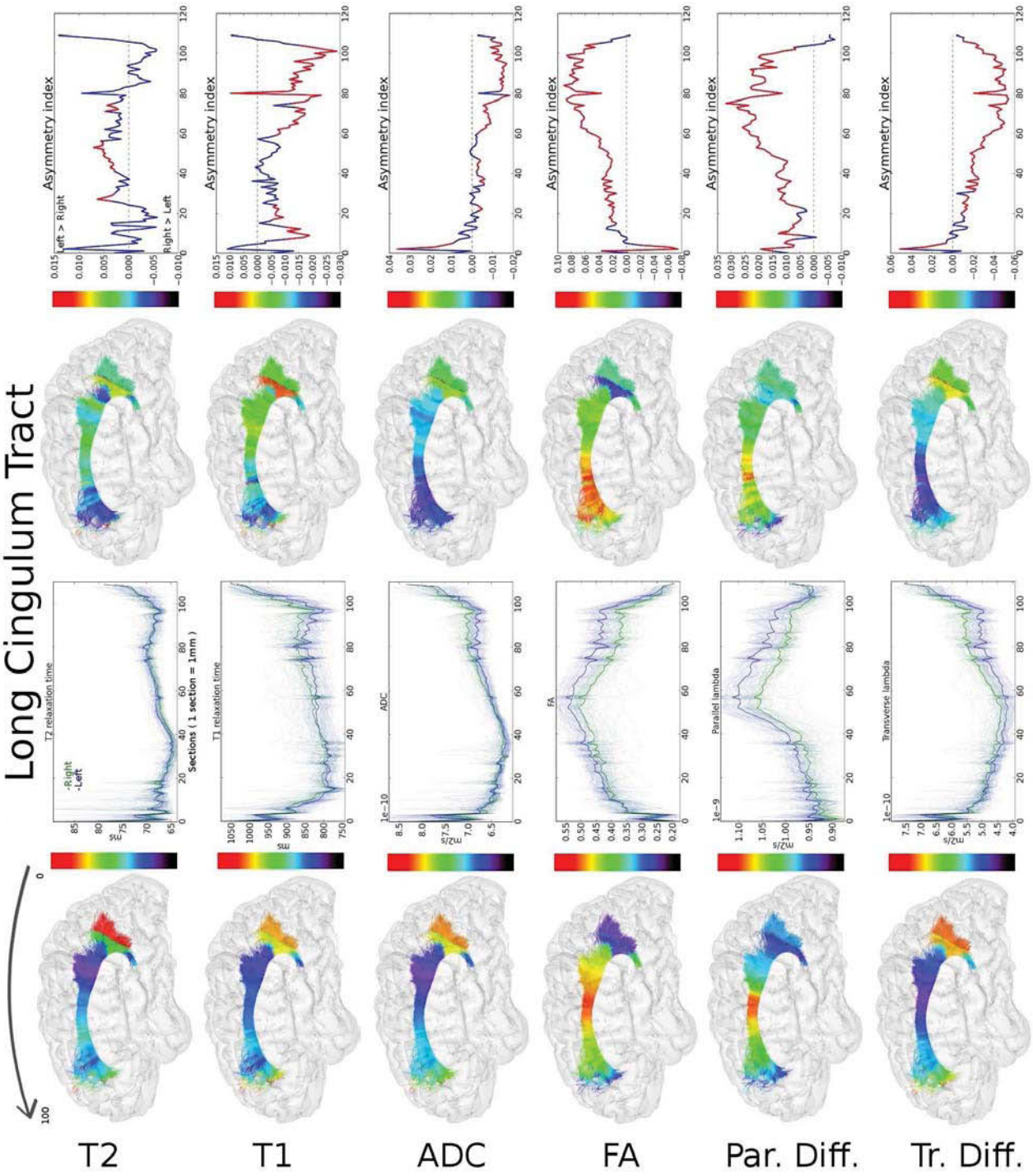

FIGURE 4.16: Left Columns : Average T_1, T_2, FA, ADC, $\lambda_{\|}$ and $\lambda_{\perp}$ profiles of the cingulum tracts In green : right bundle profiles, in blue left bundle profiles. Individual profiles are also plotted. Right Columns : Interhemispheric asymmetries (red lines correspond to regions with at least 4 significantly asymmetric sections)

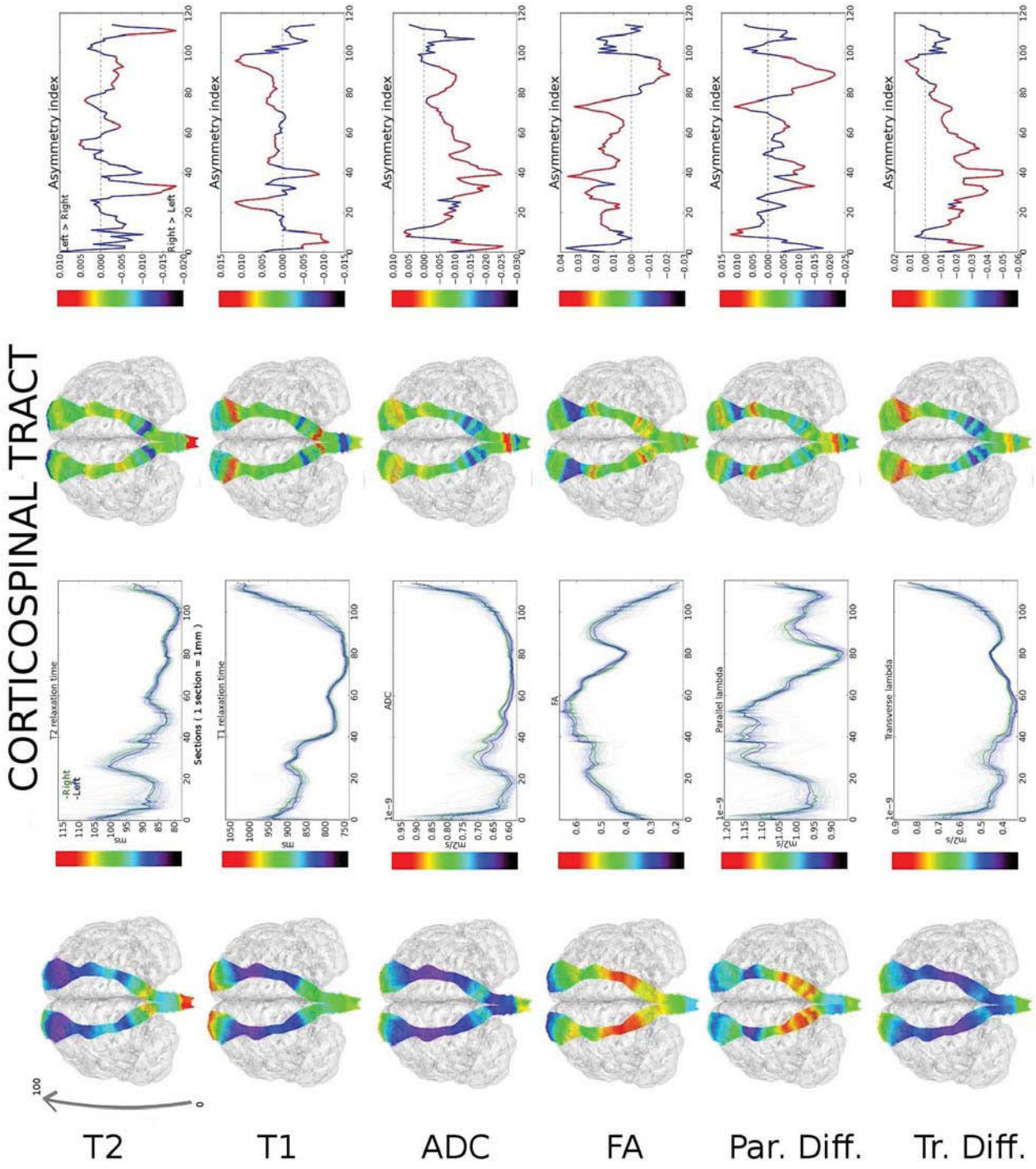

FIGURE 4.17: Left Columns : Average T_1, T_2, FA, ADC, $\lambda_{\|}$ and $\lambda_{\perp}$ profiles of the right/left corticospinal tracts. In green : right bundle profiles, in blue left bundle profiles. Individual profiles are also plotted. Right Columns : Interhemispheric asymmetries (red lines correspond to regions with at least 4 significantly asymmetric sections)

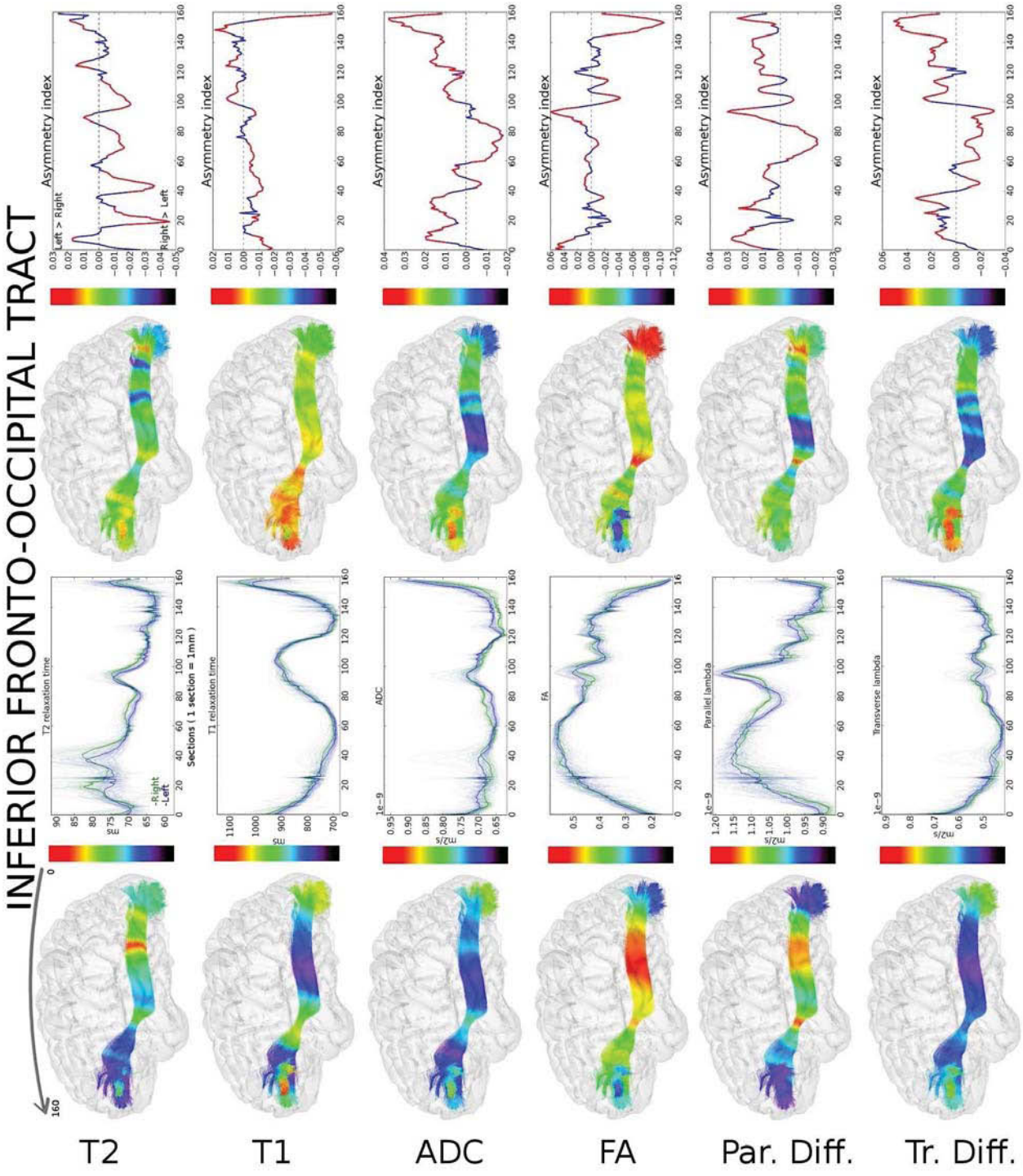

FIGURE 4.18: Left Columns : Average T_1, T_2, FA, ADC, $\lambda_{\|}$ and $\lambda_{\perp}$ profiles of the right/left inferior fronto occipital tracts. In green : right bundle profiles, in blue left bundle profiles Right Columns : Interhemispheric asymmetries (red lines correspond to regions with at least 4 significantly asymmetric sections)

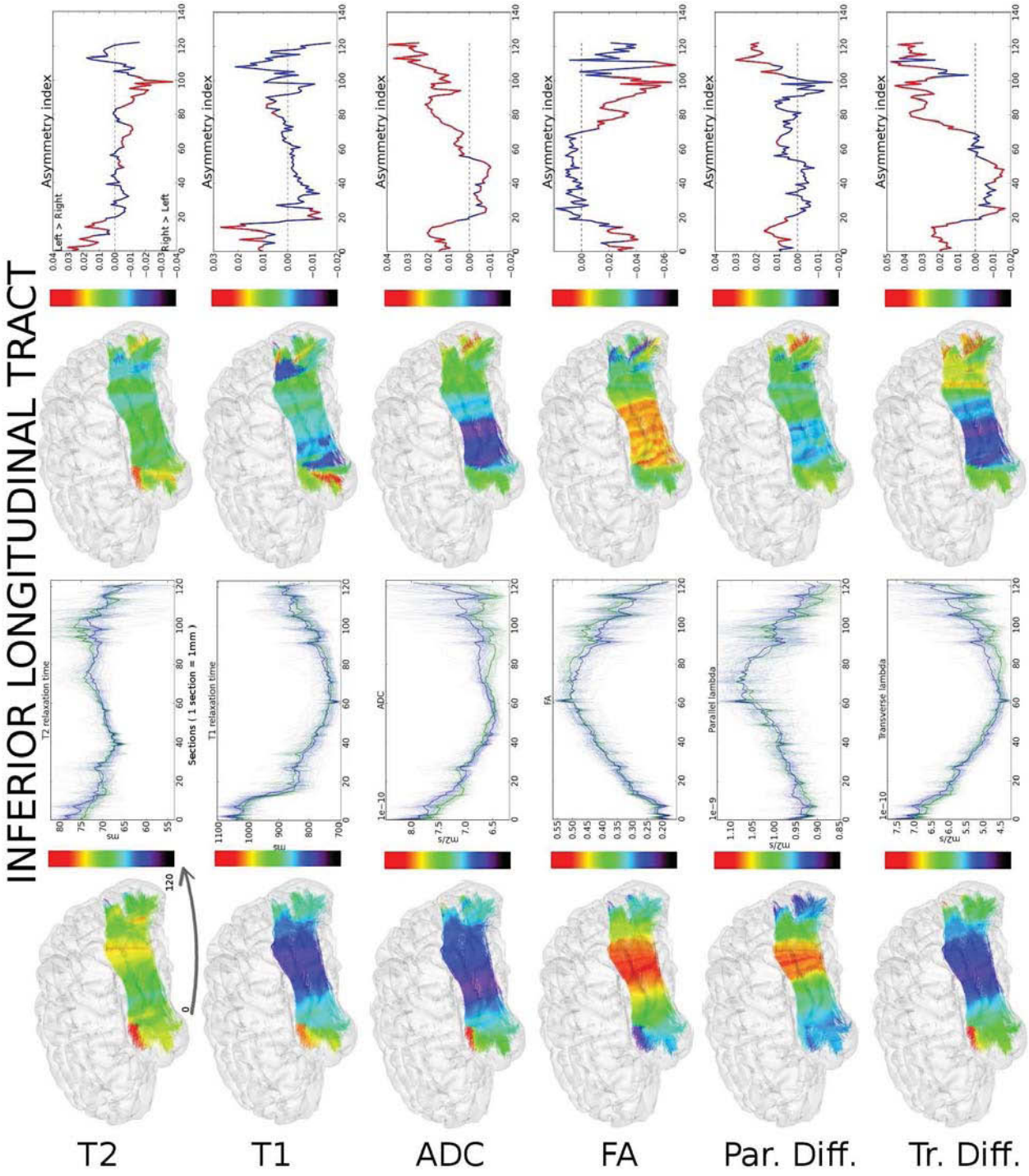

FIGURE 4.19: Left Columns : Average T_1, T_2, FA, ADC, $\lambda_{\|}$ and $\lambda_{\perp}$ profiles of the right/left inferior longitudinal tracts. In green : right bundle profiles, in blue left bundle profiles. Individual profiles are also plotted. Right Columns : Interhemispheric asymmetries (red lines correspond to regions with at least 4 significantly asymmetric sections)

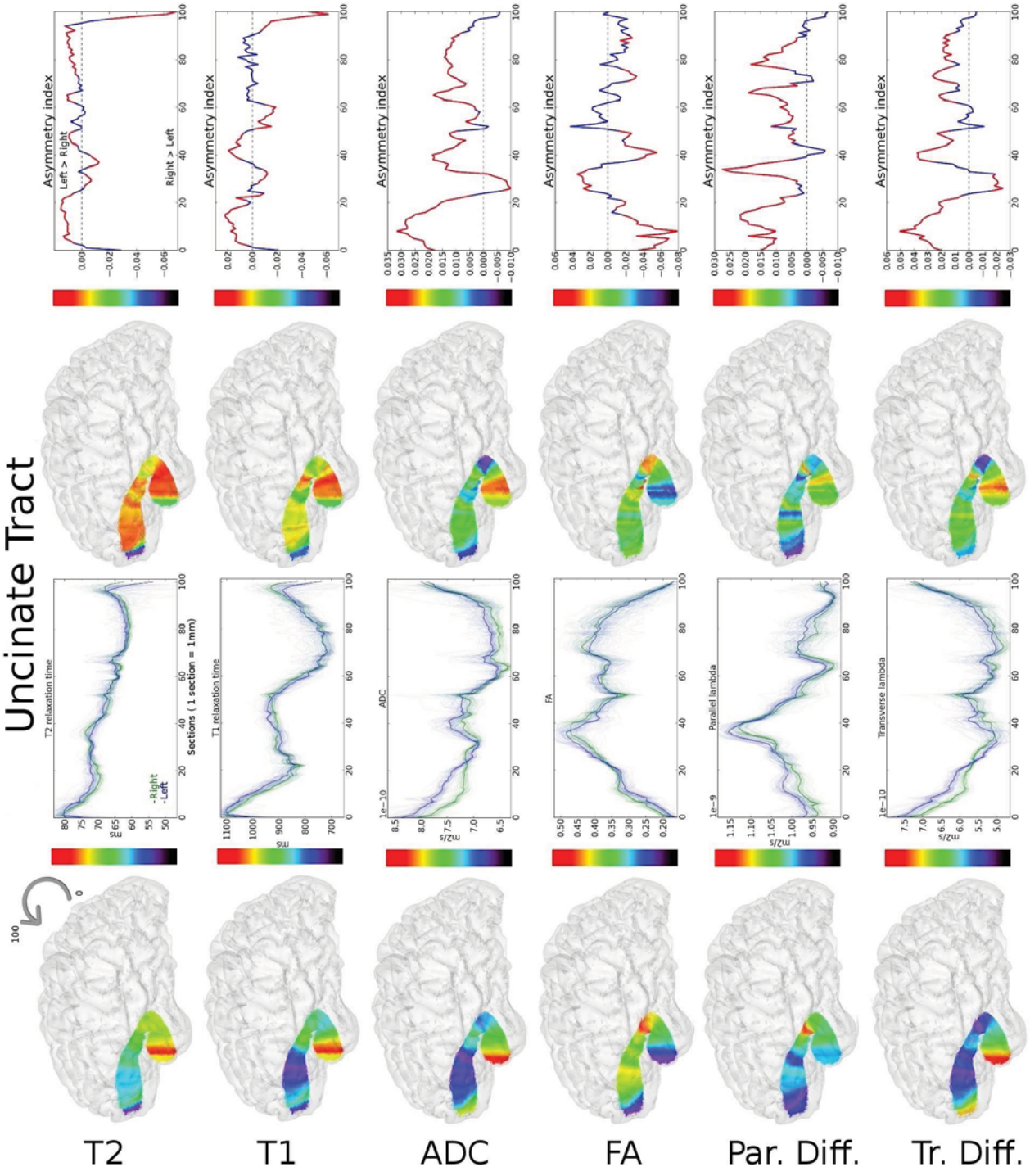

FIGURE 4.20: Left Columns : Average T_1, T_2, FA, ADC, $\lambda_{\|}$ and $\lambda_{\perp}$ profiles of the right/left uncinate tracts. In green : right bundle profiles, in blue left bundle profiles. Individual profiles are also plotted. Right Columns : Interhemispheric asymmetries (red lines correspond to regions with at least 4 significantly asymmetric sections)

FA and T_2 is less evident, since sometimes there is a positive correlation and sometimes a weak negative correlation between the two. $\lambda_{\parallel}$ seems to be negatively correlated with T_1 but sometimes positively correlated with both T_1 and T_2. Finally, $\lambda_{\perp}$ is globally positively correlated with T_1, but T_2 has both positive and negative correlation with this parameter. These observations are consistent with the known existing link between T_1 & T_2 and the water compartments within white matter tissues. Both parameters are sensitive to myelination: in highly myelinated regions, relaxation time is shorten and the fractional anisotropy would be naturally higher, because myelination highly constrains the directionality of the water molecules. In this configuration, $\lambda_{\perp}$ is reduced, explaining the positive correlation with T_1 and T_2 values. Finally, when there is more free water and less myelin, the ADC increases as well as T_1 or T_2 relaxation times. We also noticed that generally, T_1 values show greater correlation with diffusion parameters than T_2 values, which could indicate that T_1 and diffusion parameters share a similar sensitivity to the microstructure variations.

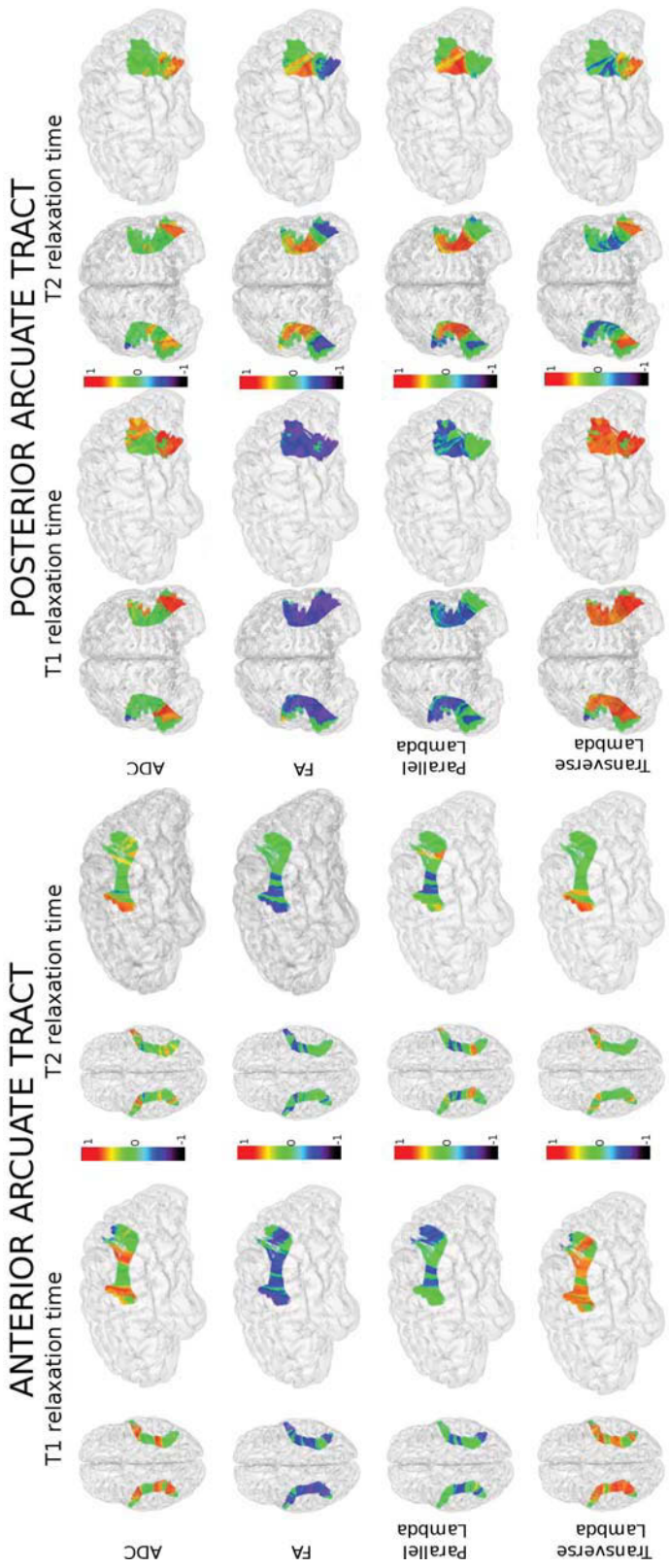

FIGURE 4.21: Correlation between T_1/T_2 relaxation times and diffusion parameters : Anterior/Posterior Arcuate tracts

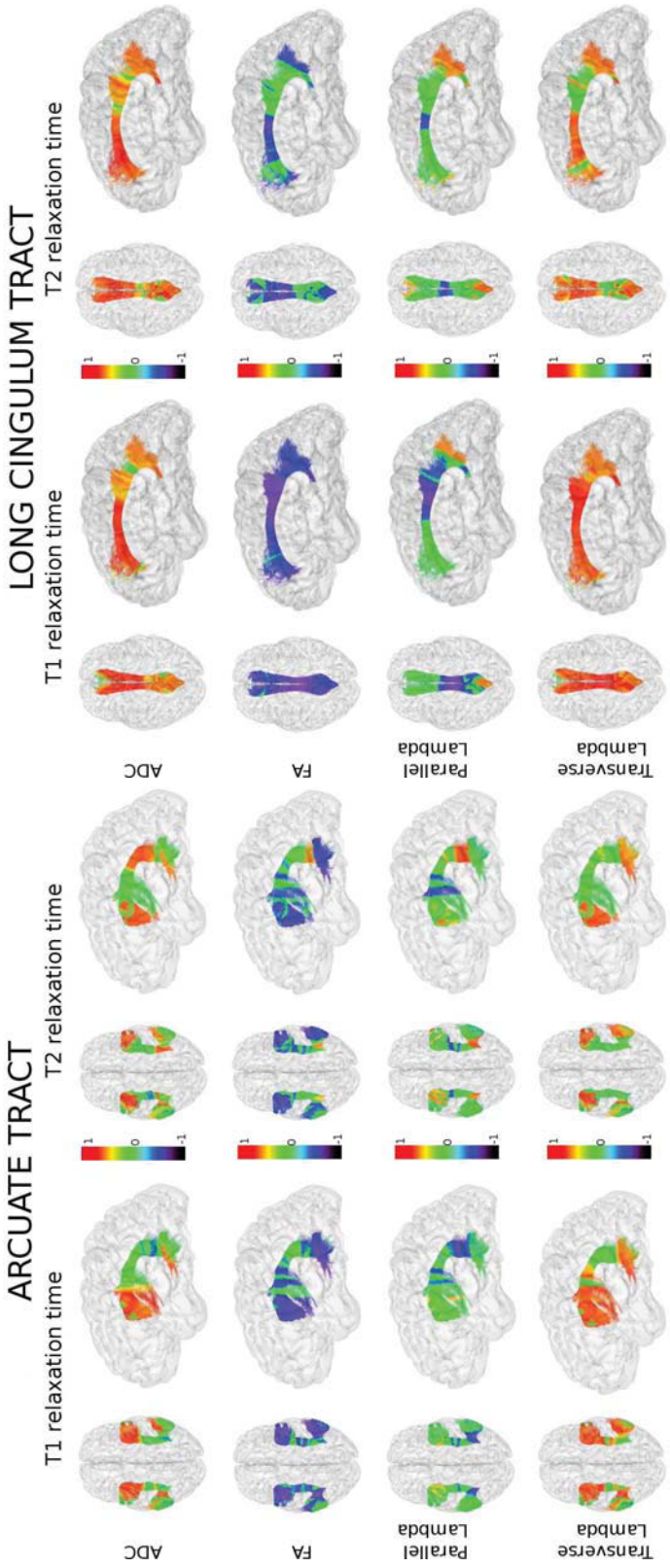

FIGURE 4.22: Correlation between T_1/T_2 relaxation times and diffusion parameters : arcuate and cingulum tracts

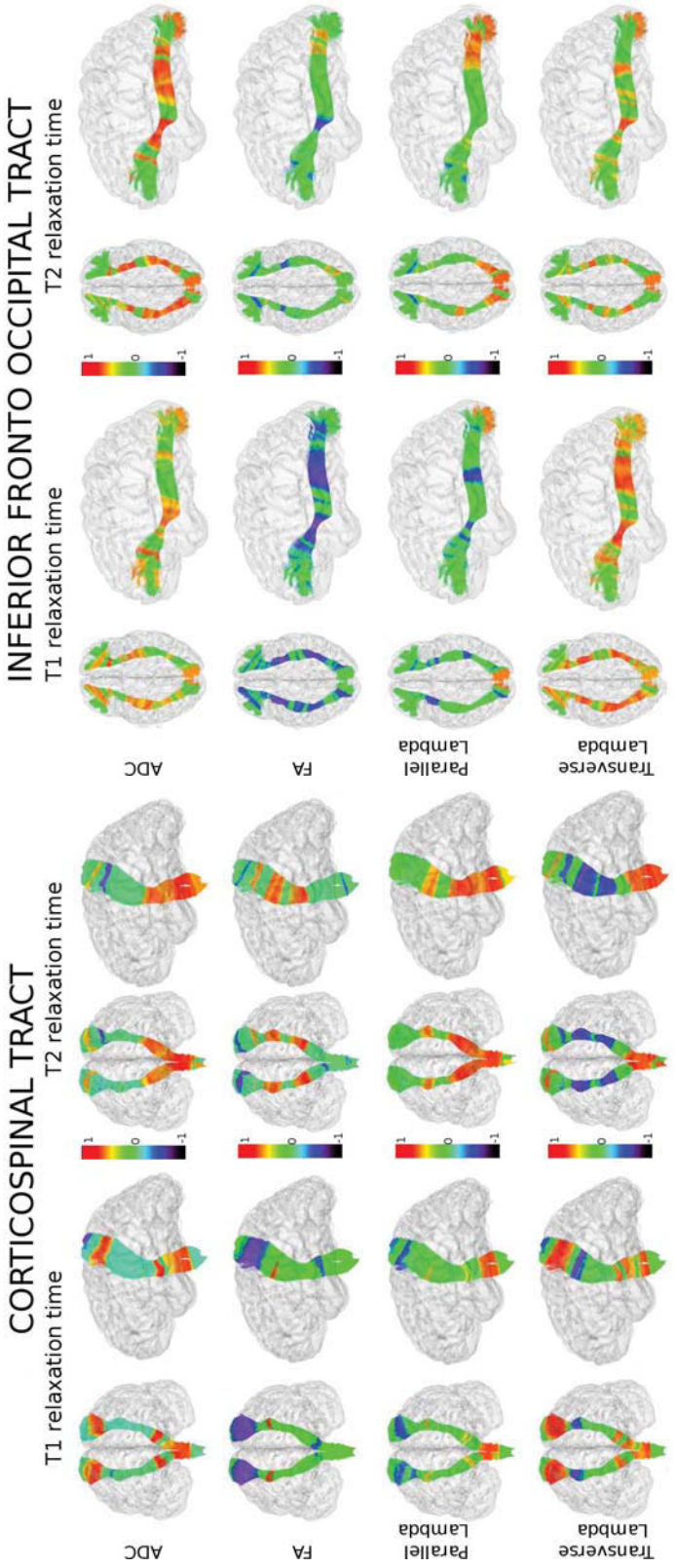

FIGURE 4.23: Correlation between T_1/T_2 relaxation times and diffusion parameters :corticospinal and inferior occipital tracts

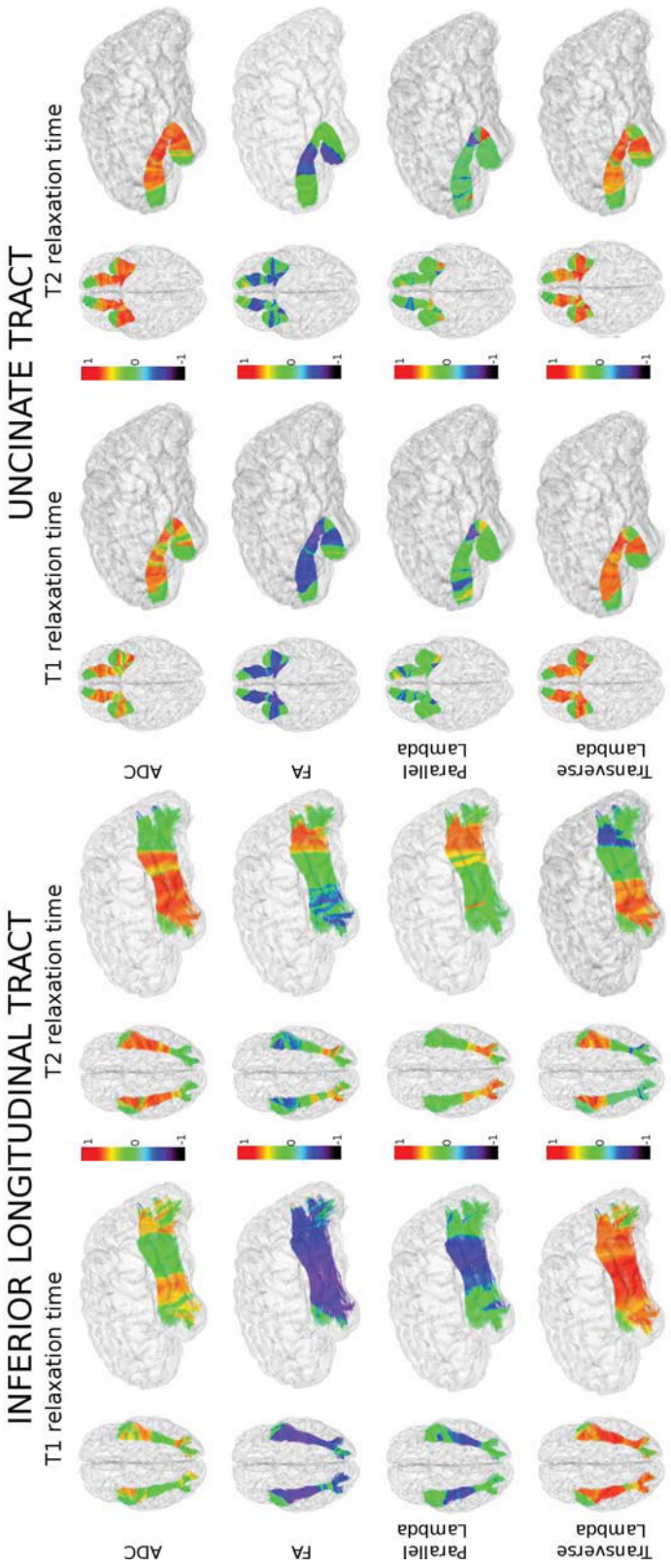

FIGURE 4.24: Correlation between T_1/T_2 relaxation times and diffusion parameters : inferior longitudinal and uncinate tracts

Interestingly, the observed correlations are not always homogeneously distributed along the bundles, some regions being more correlated than others. This observation can be related to the presence of one or more fiber populations as discussed in [De Santis et al., 2014], since the impact of different fiber organizations is not the same for all parameters (FA is, for example, reduced in the presence of multiple fiber populations). We also observed positive and negative correlations between the same couple of parameters along the same bundle. This singularity confirms the complementarity of relaxation times and diffusion parameters to characterize the microstructure of white matter bundles. We list here some specificities of several bundles.

We observed positive correlation between ADC, T_1, $\lambda_\perp$ and T_1 but not with T_2 in the fanning part of the corticospinal tract (Figure 4.23), while a negative correlation occurs between FA and T_1. In this region, where a high partial volume effect is present, T_2 values don't seem to exhibit the same trend than the other parameters, pointing out a difference of sensitivity, maybe to free water fraction of T_1 in comparison to T_2. We further obeserved positivie correlation between FA and T_1 and T_2 at the level of crossing with callosal fibers. It can be explained by the fact that crossing fibers lead to a decrease in FA values which are sensitive to the orientation dispersion and on the other hand lead to larger concentration of myelin, which is characterized by the domination of the shortest T_1 and T_2 component.

Arcuate group (Figure 4.21-4.22) exhibits a high negative correlation between T_1 and FA profiles for most of the bundles. This is less evident for T_2 relaxation times. Some regions exhibit negative correlation between T_1 and $\lambda_\parallel$ but whereas the T_2 and $\lambda_\parallel$ correlation is sometimes positive (for the posterior arcuate tract). Finally, positive correlation exists between T_1 and $\lambda_\parallel$.

The correlations observed in the cingulum tract (Figure 4.22) show differences between the anterior and posterior parts, differences that we already noticed in the asymmetry analysis. ADC and $\lambda_\perp$ have positive correlation with both T_1 and T_2 values while this correlation is negative with FA and $\lambda_\parallel$. In this tract, where the profile is stable, we can see that T_1 and T_2 are strongly correlated to diffusion parameters and therefore sensitive to the anisotropy of the tissue. The inferior-fronto-occipital (Figure 4.23), inferior longitudinal and uncinate tracts (Figure 4.24) show the same trend. This study confirms the T_1 & T_2 link with the different water compartments but also that their combination with diffusion parameters can help to reveal particular structural organization, fiber packing, density and orientation dispersion for example. Furthermore, the T_2 profiles seem to be less related to the diffusion parameters' profiles. Relaxometry and diffusion measures provide individually important information about the underlying microstructure, but more importantly the relationship between them can improve our understanding about the structural variations within the white matter.

4.8 Conclusion

The quantitative mapping of T_1 and T_2 relaxation times may be complementary to diffusion MRI and bring new insights about the cellular organization of white matter. In this chapter, we have developed two novel high ($500\mu m$ isotropic) resolution quantitative atlases of T_1 and T_2 relaxation times within white matter from a large sample of healthy subjects. We combined the atlas of long white matter bundles stemming from the CONNECT/Archi database with our relaxometry atlases to propose a first atlas of mean T_1 and T_2 profiles along white matter bundles. Our results demonstrate that T_1 and T_2 values are clearly sensitive to the microstructure and can be related to other structural parameters such as the anisotropy or the ADC. The differences we could observe between T_1 and T_2 profiles and profiles stemming from diffusion parameters indicate that they don't exactly provide the same information, but complementary information. The analysis of asymmetries between right and left hemispheres shows that some differences that remain moderate (<10%) for both T_1 and T_2 exist. Even if the level of asymmetry is often low, it appears significant for several bundles such as the corticospinal, the arcuate or the cingulum tracts. Moreover, the noticed asymmetry has been previously reported from a morphological point of view (volume asymmetry, differences of fiber numbers, etc...). Finally the correlations between T_1 and T_2 relaxation times and the diffusion parameters show again the clear relationship between the variation of the relaxation times and the variations in the microstructure. The findings of this work complete the observations made in [De Santis et al., 2014].

The current analysis pipeline is reliable but it could be improved in the future. For instance, the profiles are computed using a centroid which is highly dependent on the obtained bundle relying itself on the tract clustering step. Moreover, it could also not be accurately representative of the bundle. For example, in the corpus callosum where it is not in the antero-posterior direction or in the case of fanning configuration. This part could be improved using surface modeling of bundles as introduced in [Zhang et al., 2010]. HARDI-based registration technique could also improve the accuracy of the profile computation. As we already explained, the relaxometry data were acquired with a very limited scan duration with the aim of allowing such a protocol to be used in clinical routine. The T_1 and T_2 mappings could then be improved using different acquisition strategies, but the results we obtained already give the opportunity to get structural information on the scanned population. The computation of the profiles along the bundles extracted and labelled from the tractography of each subject allowed to access to more local information along bundles.

This is a further step towards the understanding of the white matter microstructure, and future work will consist in correlating the T_1 & T_2 information with the axon density and radii maps available today with diffusion-based axon calibration techniques. In the

same manner, we can build atlases from patients suffering from different pathologies such as Alzheimer's or Parkinson's diseases, and compare the profiles to the healthy average profiles provided by our atlas now considered as a normative atlas. The profiles of these parameters could also be used to study variations of the white matter microstructure with respect to the age as well as white matter maturation during early brain development. This work has been presented at the ISMRM conference in 2013 ([Lebois et al., 2013a]) and recently submitted to the NeuroImage Journal. This work focused on different parameters such as T_1, T_2, FA, ADC, $\lambda_{\parallel}$ or $\lambda_{\perp}$. We have shown that they can provide different contrasts depending on the underlying microstructure. But all these parameters suffer from a lack of specificity, and it is often difficult to understand which modification in the cytoarchitecture can explain the differences we observed for these parameters. The following chapter proposes to address the problem of this specificity, trying to get closer to an *in vivo* microscopy of the tissue. Diffusion MRI could provide a unique tool to reach this ultimate goal. We will describe how it is now possible to probe the cytoarchitecture using specific diffusion MRI schemes and how this thesis contributes to these new techniques.

Chapter 5

Microstructure mapping using diffusion MRI

In the previous chapter, we used the combination of diffusion MRI and relaxometry to build an atlas of profiles of relevant related features along the white matter bundles, showing the ability of these modalities to give complementary information and help to characterize part of their microstructure. T1, T2, FA, ADC, $\lambda_{\parallel}$, $\lambda_{\perp}$ are all sensitive to the microstrucure but they suffer from a lack of specificity: a variation in fractional anisotropy reveals change in the tissue, but we can't clearly assess whether this variation comes from a variation of the axonal compartment or of the extracellular compartment. This part looks even further in the microstructure study at the cell level. Here, we intend to access to specific parameters such as cell sizes and densities to come closer to an *in vivo* microscopic scale, using diffusion MRI. Diffusion ensemble average propagator (EAP), the holy grail of the dMRI, can be obtained from multiple-shell spherical sampling of the Q-space (see [Assemlal et al., 2009], [Descoteaux et al., 2011]) or cartesian sampling of the Q-space (see DSI [Wedeen et al., 2000]). But astonishingly, few information about tissue microstructure can be computed from EAPs, as of today. An alternative to EAP imaging relies on the modeling of the restriction effects occuring in cells, using models of the diffusion attenuation within simple (quite often oversimplistic) models of the geometry of cells. In the case of white matter, the signal attenuation depends on structural parameters such as axon radius or distribution and on sequence parameters. By measuring the diffusion attenuation with an adequate sampling of the Q-space (typically, in a PGSE experiment, the gradient strength, the pulse width and the diffusion time), the signal expression can be fitted to derive microstructure features. The first difficult task is the tissue modeling, because of the complexity of the brain cytoarchitecture. In diffusion MRI, the model must remain not too complicated, for several reasons. The first reason is that the diffusion propagator expression is well

known for geometry such as spheres or cylinders, but is far more difficult to find for more complex geometries. Secondly, a complicated model induces a high number of parameters, and therefore a higher number of measurements is required to be able to estimate them accurately. For clinical application, the acquisition time is limited to 1h30, and doesn't allow to obtain the sufficient number of measurements for complex model. In addition, clinical MRI systems are limited in terms of gradient magnitude and slew rate, such that the sampling of the diffusion time can remain strongly limited to a short range of values to preserve SNR and sufficient diffusion sensitivity. However, even a simple model can already provide useful insights on tissue microstructure and help to differentate tissues, putatively offering nice imaging biomarkers of atrophiated tissues in many disease inducing microstructure alterations. The second problem of diffusion MRI is to choose the adequate sequence and protocol to map microstructure features accurately : PGSE is the most common sequence in diffusion MRI and diffusion MRI microscopy, but other sequences have appeared dedicated to cytoarchitecture imaging, such as double PGSE, Oscillating gradient Spin Echo or Arbitrary Gradient Spin Echo. In this chapter, we describe the different models and sequence schemes of the literature focused on this new field of dMRI : diffusion MR microscopy (μdMRI). We also expose the contributions of this thesis on the subject : first, the derivation of a novel model of axon and cells, taking into account the biphasic behavior of the water in the cells and second the development of a novel Arbitrary Gradient Spin Echo sequence able to run on any 3T and 7T Siemens MRI system.

5.1 Microstructure modeling of the brain tissue

Inferring microstructure parameters such as cell sizes or density using diffusion MRI requires to develop mathematical models of the diffusion process in the tissue. The diffusion signal is in fact the result of a composition of signals coming from different compartments of the tissue, usually corresponding to the main cell species of the tissue, such as neuron bodies, axons, dendrites, glial cells, oligodendrocytes and astrocytes. These different components have to be modelled, and since dMRI is sensitive to the movement of water molecules, the issue of exchange between these different compartments has to be addressed. Natural barriers such as membranes are indeed not impermeable and allows the water molecules to go from one compartment to the other. These different aspects of tissue modeling will be discussed before reviewing the current white and grey matter models. Principles of diffusion MR microscopy and the associated sequences will also be presented as well as contributions of this thesis on this topic.

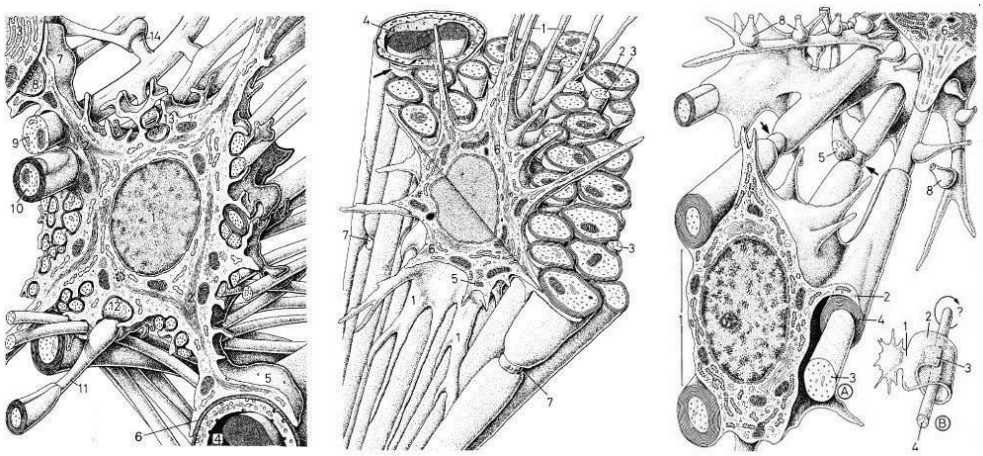

FIGURE 5.1: Tissue microstructure (astrocyte and oligodendrocytes) (from http://www.db-gersite.com)

5.1.1 Compartmentalization and exchange

5.1.2 Compartmentalization of the brain tissue

In the early years of diffusion MRI, the diffusion in white matter was principally considered as a Gaussian process, depending on the b value and an apparent diffusion coefficient, averaging the complexity of the tissue. Microstructure modeling of the brain tissue aims at describing the diffusion signal not only by one monoexponential component but by the combination of the signals arising from distinct compartments of the tissue. The chosen model has to be sufficiently simple in order to enable the computation of its corresponding propagator in a simple way, but it must reflect the behavior of the various diffusion processes occuring in the complex environment of the brain tissue (see Figure 5.1).

All the models introduced in the literature rely on natural compartimentalization of the tissue. Each main component of the tissue can be a compartment, with a given volume fraction in the voxel and characterized by different diffusion processes. In white matter, the natural compartments are the axons, the glial cells and the extra-cellular space. In grey matter, the extra-cellular space, neural cells, astrocytes and dendrites are considered. Once these comparments are defined, we have to take into account the exchange of water between these compartments. In addition, CSF compartment is generally added to take into account any partial volume effect due to the limited spatial resolution of dMRI data.

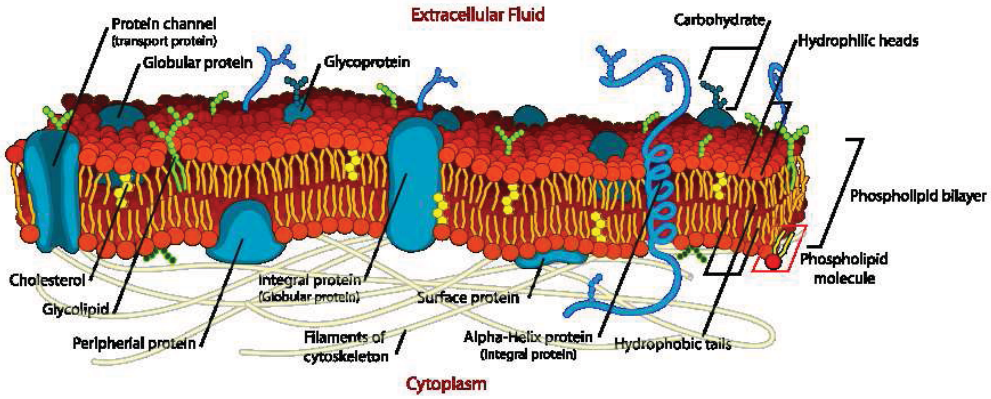

FIGURE 5.2: Cell membrane structure adapted from wikipedia

5.1.3 Exchange between compartments

As it was presented in the previous section, modeling the diffusion process in brain tissues requires the definition of different compartments of the tissue. But a very difficult task is to take into account the fact that in the human brain, the water compartments are not fully isolated but are in permanent exchange. This exchange process comes from the nature of cell membranes. Cell structure is depicted in Figure 5.2. It is made of two layers of phospholipids with embedded proteins. It is surrounded in the extra cellular space by the glycocalix made up of glycoproteins and by the cytoskeleton in the intra cellular space. The membrane has a key role in the transport of different substances between the intra and extracellular spaces. The membrane is selectively permeable, and only specific substances can cross this natural barrier. Pumps, carriers and proteins channels allow for those substances to travel between the two spaces. The pumps are responsible for the transport of ions and small molecules. A specific channel called aquaporin (see Figure 5.3) is responsible for water molecule transport. The main aquaporin existing in the human brain is the AQP4, found in the membranes of the astrocytes. The presence of myelin will slow down the water exchange, therefore the exchange is higher in astrocytes than in axon. In diffusion modeling, the permeability is characterized by the p parameter, (in $cm\ s^{-1}$) directly linked to an exchange rate $k = \frac{pS}{V}$ with S the surface of the membrane and V the volume of the structure. The exchange rate is the inverse of the residence time τ. In [Stanisz, 2003] this question is addressed. The permeability has a variable impact on the diffusion signal strongly depending on the diffusion sequence parameters , especially the diffusion time of the experiment. Depending on the type of exchange we consider, the model has to be adapted. We can distinguish slow, fast and intermediate exchanges. The notions of slow/fast is of course relative to the diffusion time of the observation.

In the case of slow exchange between the intra and extra-cellular water for example, the

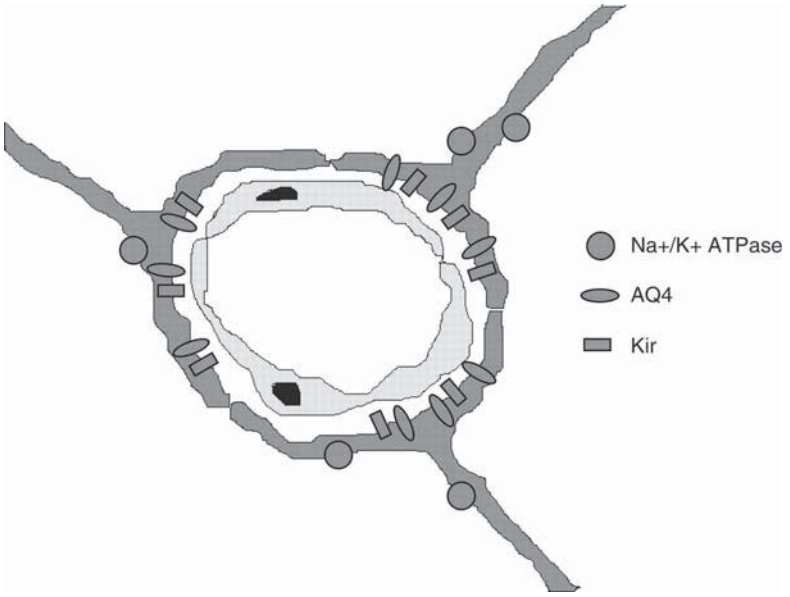

FIGURE 5.3: Cell membrane and molecules transfers from [Ayus et al., 2008]

PGSE signal can be described as the weighted sum of the two compartments :

$$\frac{S}{S_0} = f \exp(-bADC_i) + (1-f)\exp(-bADC_e) \tag{5.1}$$

where f is the volume fraction of the first compartment and ADC_k are the apparent diffusion coefficients of the two compartments. Intermediate and fast regimes can be solved using Karger equations. The residence time varies between 12 ms and 600ms in the human tissue, and axon has a residence time of about 500ms [Quirk et al., 2003]. The residence time for glial cells is significantly shorter. Therefore, if the diffusion time of the experiment is short enough, the axon membrane can be considered as impermeable and the glial cells are just barriers hindering the water molecules. Grey and white matter models have been developed taking the multi-comparment aspect of the tissue and the exchange issue into consideration. We will now list the major models developed in the field of diffusion MRI in the past up to now.

5.2 State of the art of tissue modeling

5.2.1 Current white matter models

White matter composition has been described in Chapter 2. It contains mainly myelinated axons, surrounded by glial cells and CSF. Various models have been proposed to describe white matter tissues, starting from the simple biexponential model to the CHARMED model ([Assaf et al., 2004]). In these models, axons are often modeled as

packed cylinders whose diameters correspond to the inner diameter, not taking into account the myelin layers. The main differences between the various models consist of the number of compartments that are chosen, the possibility to deal with the orientation dispersion of the axons and to take into account the membrane permeability. Most models were developed assuming that the acquisitions are performed using PGSE sequences. However, they can be used with alternative sequences that we will describe later.

5.2.1.1 Beyond monoexponential model : biexponential model of white matter

The monoexponential model defined using a Gaussian propagator has been shown to not perfectly describe the signal. A biexponential model, with slow and fast ADC was found to be more accurate, especially for high b-values. This very simple model is described as follows :

$$\boxed{S = S_0(f_{slow}\exp(-bD_{slow}) + f_{fast}\exp(-bD_{fast}))} \tag{5.2}$$

The expected volume fractions would correspond to the extra and intra cellular fractions, since the diffusion in the extra-cellular (20%) is much faster than in the restricted part (80%). But in several studies, it has been shown that the fractions don't match with the extra and intra cellular fractions : $f_{slow} \approx 20\%$. This model is therefore not very descriptive of the tissue microstructure and it doesn't well fit the signal at very high b-values. This model will be discussed in the next section, where we see that slow and fast pools can be used to extend the current axon model.

5.2.1.2 First analytical model with cell geometrical model

In 1997, Stanisz et al. [1997] developed an analytical model of the ex-vivo bovine optic nerve from PGSE experiment. From a transmission electron microscope study, a model for the optic nerve was developed. In this first study, cylinders were not used to represent the axons but prolate ellipsoids instead. They are characterized by short perpendicular direction and longer parallel direction. The glial cells are modeled as spheres with a unique diameter. The cell membranes are considered permeable with different values of permeability used for axons and other cells. Stanisz et al specified two different diffusion coefficients, one for the water molecules inside the intracellular space, the other for those in the extracellular space. The model is therefore a three compartment model: the prolate ellipsoid modeling the axons, the spheres modeling the glial cells and the extracellular space (see Figure 5.4). Each compartment follows a monoexponential decay, each characterized by a specific diffusion coefficient, and permeability has been included in the differential equations of the magnetization. The extracellular ADC was defined as

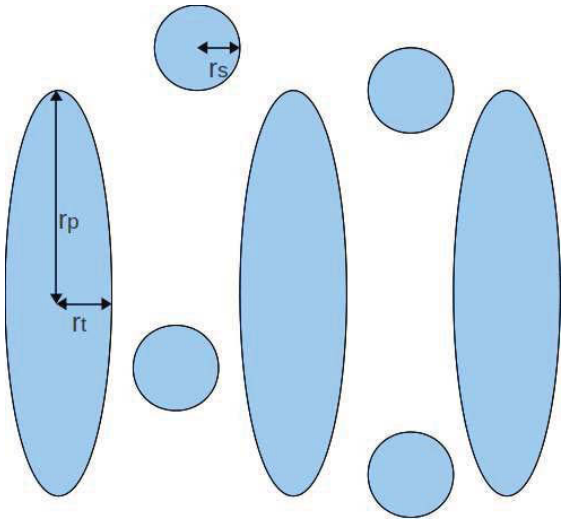

FIGURE 5.4: Optic nerve model : axons are modelled as prolate ellipsoid with a axial radius r_p and the transverse radius r_t, glial cells are modeled as spheres of radius r_s and an additional compartment corresponds to the extra-cellular space

the ratio between the free diffusion coefficient and a tortuosity factor λ, since the water molecules move almost freely but are hindered by several barriers (the representation is valid if the mean-squared displacement of the molecules during the diffusion time exceeds the cell dimensions), creating tortuosity : $ADC_E = \frac{D}{\lambda}$. The diffusion coefficient for the ellipsoid and spheres is defined as the diffusion coefficient of water molecules between two flat and impermeable barriers of spacing corresponding to the cell diameters. This model shows the ability of the PGSE sequence to provide structural information through tissue modeling. But this experiment was performed in *ex vivo* conditions, and the model has to be adapted for *in vivo* application.

5.2.1.3 Ball and Stick model

In ([Behrens et al., 2003]), the ball and stick model has been introduced defining the signal in the white matter as the sum of one isotropic compartment (corresponding to the extra-cellular space) and one completely anisotropic compartment, corresponding to axons, represented by one stick. The signal model is then expressed, in a PGSE framework, as follows :

$$S = S_0((1-f)\exp(-bD) + f\exp(-bD(\mathbf{g}^T\mathbf{n})^2)) \tag{5.3}$$

with b the b-value, D the mean diffusivity, $\mathbf{g}$ the gradient orientation, $\mathbf{n}$ the fiber orientation. This model can be extended to several fiber populations. Different models were derived from this kind of model : the extra-cellular part is either modeled as a complete isotropic ball or as a zeppelin (a tensor with cylindrical symmetry) or a full tensor; the

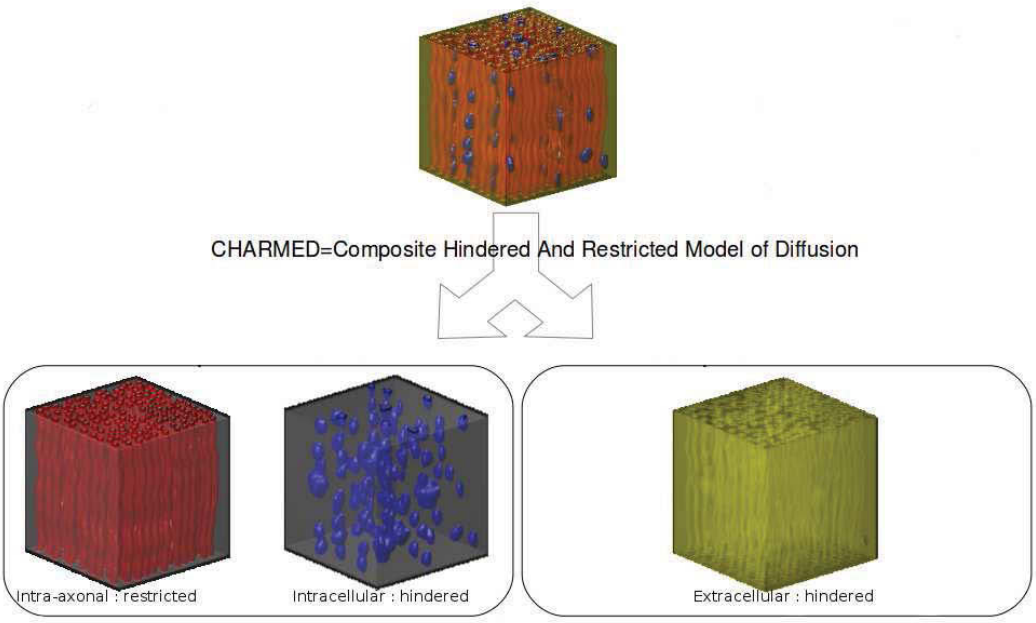

FIGURE 5.5: CHARMED model of white matter [Assaf et al., 2004]

intra-cellular cellular part is modeled using sticks or cylinders. Advanced models of this type, such as the ball and racket model adds a support for fanning configuration of the fibers [Sotiropoulos et al., 2012].

5.2.1.4 The composite hindered and restricted model of diffusion (CHARMED)

A major model has been introduced in [Assaf et al., 2004] decomposing the signal in white matter into two different compartments : an hindered compartment corresponding to the signal coming from the extra-axonal space and a restricted compartment coming from molecules trapped in the axon (see Figure 5.5). This model considers the myelin sheath as impermeable, considering the diffusion time used in the experiment. The signal equation is then expressed as follows :

$$\boxed{E(q) = f_{hindered}E_{hindered} + f_{restricted}E_{restricted}} \tag{5.4}$$

with f_h and f_r the volume fraction of the hindered and restricted compartment. The hindered compartment is following a Gaussian distribution and the restricted compartment is modelled using the diffusion propagator of a population of parallel cylinders, representing the axons. Diffusion in cylinders with different boundary conditions was introduced in [Callaghan, 1995]. The CHARMED model have been used in two major frameworks : the AxCaliber framework developed by [Assaf et al., 2008] and the

ActiveAx framework developed by [Alexander, 2008]. These frameworks define specific protocols to infer white matter microstructure, and were used to study in particular in the corpus callosum. The protocols will be detailed in the section 5.5. In the AxCaliber framework model, the restricted part of the CHARMED model corresponds to a whole distribution of axon diameters (using a gamma Γ distribution, chosen for its consistency with axon diameter distribution observed in the corpus callosum using electron microscopy). Axons are represented as packed parallel and impermeable cylinders. In the ActiveAx framework, white matter is defined as a collection of axons with the same diameter (corresponding to the average diameter of the real distribution). In the recent work derived from ActiveAx [Alexander et al., 2010], two other compartments were added : the signal from the CSF (considered as gaussian and isotropic) existing because of partial volume effects and the signal stemming from the resident water, trapped in glial cells.

5.2.1.5 Extension of CHARMED model for orientation dispersion

But in these models only one fiber orientation was considered, which is acceptable in the corpus callosum configuration, where all the fibers are strongly structured with few orientation dispersion but which fails in other part of the white matter. For this reason, the model used in ActiveAx has been extended by [Zhang et al., 2011b], introducing in the model the possibility to characterize the dispersion of the orientations of the axons by the use of an axonal orientation distribution, modeled as a Watson's distribution.

5.2.1.6 Models including myelin sheaths

All the models such as the CHARMED model, do not include myelin sheath in their model, and only consider its effect on the permeability of the axons. Several studies extended the cylinder model using a thick layer arount the inner cylinder corresponding to the axon. [Sen and Basser, 2005] studied the apparent diffusion coefficients of different configuration of arrays of cylinders having a thick layer corresponding to the myelin sheath. Inner core, membrane and myelin sheath were considered as distinct compartments. This model has the advantage of being closer to the real tissue structure of white matter but necessarily adds additional parameters to characterize the tissue, making the inference more complex from a computational point of view.

5.2.1.7 Comparison of the white matter models

In [Panagiotaki et al., 2012] all the existing white matter models were compared and it is shown that the model including the restricted part corresponding to the axons better explains the data than the others. Considering the actual size of axons and the diffusion process in the extracellular space as described in CHARMED model improves the fitting process, and the results using a whole distribution of axon diameter (AxCaliber) is less stable than with an average axon diameter (ActiveAx) when targetting clinical applications.

5.2.2 Grey matter models and mixed models

Modelling grey matter is a difficult task in comparison to white matter. The tissue is not well structured, with random orientations and a high permeability. It is common to reduce the geometry of neuron bodies to a sphere. In grey matter models, the permeability must to be taken into account. The experiments on grey matter to infer the cell diameter are constrained by the presence of high membrane permeability of cells. Indeed, the sensitivity of the signal to the cell membranes are therefore reduced in comparison to the highly restricted compartment of the axons. Adding the permeability parameters in the model increases the complexity of the model and consequently also increases the instability of the fitting procedure. However some studies focussed on grey matter trying to map the density of dendrites. [Jespersen et al., 2007] and [Jespersen et al., 2010] introduced a two-compartment model: one characterizing the diffusion inside axons and dendrites (neurites) using cylinders, and the other corresponding to the diffusion component coming from the other compartments. An orientation distribution function was also used to extract neurite orientations. This approach showed good agreement with electron microscopy data and allowed to characterize both white and grey matter tissues. [Zhang et al., 2012] extended this neurite model to map the density and orientation dispersion of the neurites. In this model, the cylinder model is replaced by a stick model and the orientation distribution function follows a Watson's distribution. This study differs from the previous one by the will of the authors to map neurite density in clinical routine, relying on the same protocol optimization as ActiveAx, that will be develop in the next section.
Figure 5.6 summarizes the geometrical models for white and grey matter.

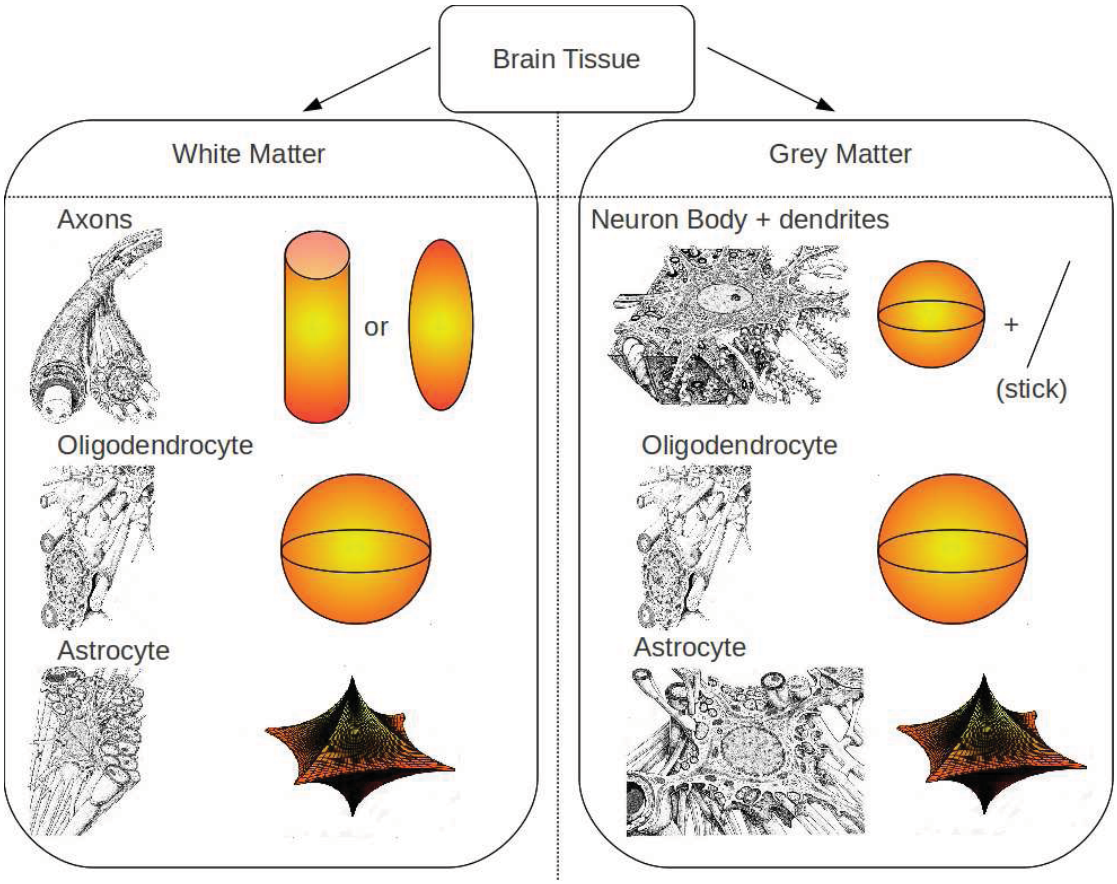

FIGURE 5.6: Geometrical models of brain tissue components

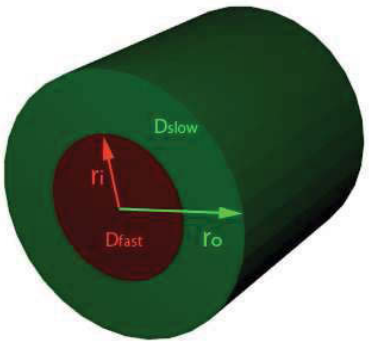

FIGURE 5.7: Two-pool cylinder model

5.3 Beyond the CHARMED model : axon model using a two-pool model cylinder

Several studies ([Niendorf et al., 1996], [Assaf and Cohen, 1998], [Clark and Le Bihan, 2000]) revealed the fact that the behavior of diffusion inside the cell is not mono-exponential, thus revealing the existence of fast and slow pools inside the cell. This approach was mainly used in the study of the decrease of ADC in the case of stroke. Several hypothesis were introduced to explain this phenomenon : the cellular swelling, the changes in membrane permeability or the decrease of water mobility in the cell. But in fact, ADC doesn't depend on permeability, so the explanation could be either in swelling or decrease of water mobility in the cell. However, the biological effects are still debated and controversy.

5.3.1 Do the fast and slow pools correspond to extra and intra-cellular space ?

The first idea to explain this biexponenital behaviour is to match the fast pool to the extra-cellular space (since the diffusion is only hindered, the ADC has to be relatively high) and the slow pool the intra-cellular space (because of the restriction). If this configuration is the right one, we should find $f_{fast} = f_{extra}$ and $f_{slow} = f_{intra}$. But [Niendorf et al., 1996] found in the rat that the volume fractions corresponding to a fast/slow two pool model don't correspond to the extra and intra cellular volume fractions with $f_{slow} \approx 0.2\%$ and $f_{fast} \approx 0.8$, while $f_{extra} \approx 0.3$ and $f_{intra} \approx 0.7$. Similar results were presented in [Clark and Le Bihan, 2000] in the human brain, suggesting that the two pools don't match the extra and intra cellular spaces.

5.3.2 A biexponential diffusion behaviour inside the cell

[Assaf and Cohen, 1998] and [Sehy et al., 2002] showed that this biexponential behaviour is also found in the cell itself, revealing the presence of two compartments inside the cell. But it can't be directly applied to the human brain. [Le Bihan, 2007] suggested that the signal coming from the axon is in fact stemming from two different pools : one near the membranes, characterized by a slow diffusivity coefficient and one far from the membranes, characterized by a higher diffusivity. This model suggests that water in cell could have a different organization than in simple bulks of water. In the cell, the cytoplasm contains many molecules and proteins and membrane itself is made up of two layers of phospholipids with proteins. It has been shown that by their negative charges, the proteins will naturally attract dipolar water molecules. This attraction will

then induce a particular organization of the water molecules around the proteins, giving "structured water". If in the litterature this organization has been found uniquely in the range of one or two layers of molecules [Clegg, 1984], [Stiopkin et al., 2011], representing a distance from the proteins of 0.3nm, other studies [Rorschach et al., 1991] extended this behaviour to several layers, suggesting that a high proportion of the cell would contain structured water. More recenlty [Xu and Yeung, 1998] and [Shelton, 2000] studies support the idea of a long range of the cooperative effect of the proteins, up to 200nm around the protein. This effect would be reinforced near the membrane, because of the thick matrix around the membranes containing proteins (glycocalyse and cytoskeleton). In the presence of highly structured water, the diffusion coefficient is strongly reduced, leading to the formation of a "slow pool". In this configuration, the two-pool model can be defined as follows : the fast pool contains water molecules interacting with the water hydration shell around macromolecules. The slow pool corresponds to structured water molecules with reduced mobility, explained by the spatial distribution of charges at the membrane surface, leading to an increase of structural order [Francesco Sciortino, 1991]. The slow pool will also include the water molecule around the macromolecules in the cell, but the molecules near the membranes are in much greater proportions. This model can be used assuming a slow exchange between the two pools but it can be modified using the Karger equations to take into account an intermediate exchange. This hypothesis is supported by the findings of [Buckley et al., 1999] and more recently of [Jelescu et al., 2014], where ouabain was used to cause cell swelling. It has been found that in this case, the slow pool fraction increase but neither the fast or slow diffusion coefficient change. One plausible explanation is therefore that the membrane surface increasing during the swelling, the slow pool fraction will therefore increase too. This model could explain the ADC drop in the case of a stroke, and findings using simulation of [Yeh et al., 2013] confirms that this ADC drops could be explained by the increase of the surface of the membranes, leading to an increase of slow pool volume fraction, finally giving a drop in the ADC. For a cell with a 1 μm radius, [Le Bihan, 2007] computes a slow layer of 50nm around the membranes. We here propose this new model for a new application in axon calibration to maybe overcome the recurrent overestimation of the smallest axon diameters using the CHARMED model.

5.4 Cytoarchitectural modeling of the grey matter : beyond the sphere model

The same assumption can be used in grey matter. We can apply the two-pool model on the sphere to model biphasic cell in grey matter.

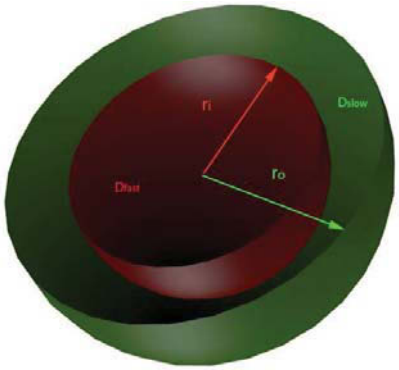

FIGURE 5.8: Two-pool sphere model

5.5 Diffusion MR microscopy

This section presents the different approaches in diffusion MRI microscopy. Diffusion MRI microscopy aims at extracting microstructural features by modeling the tissue and measuring the diffusion signal to fit the model parameters. We already listed the different models for white and grey matter. This part introduces the various frameworks differing in the sequence they use. If the PGSE remains the commonly used sequence in diffusion MRI microscopy, alternative sequences have been shown to be efficient such as double PGSE or Oscillating Gradient Spin Echo. The main idea governing all these studies is the exploitation of the parameters of the sequence to be sensitive to restrictions induced by the membranes. By tuning these sequences, it is possible to create the adequate constrast to extract cytoarchitectural parameters.

5.5.1 Principles of diffusion MRI microscopy

5.5.1.1 Using varying diffusion time to probe tissue microstructure

Let us remind that the PGSE sequence is characterized by the following parameters : δ, the diffusion gradient duration; Δ, the duration between the two gradients and G, the gradient magnitude. The behaviour of the signal will strongly depend on δ and Δ in comparison to the dimensions of the structure. On one hand, δ and Δ defines the effective diffusion time. We have seen before that for PGSE experiment, the effective diffusion time is given by $t_{diff} = \Delta - \delta/3$. From the mean-square displacement expression, the typical length water molecules will travel during the diffusion time is $a \approx \sqrt{t_{diff} \times D}$ with D the diffusion coefficient. Therefore, for a size pore r longer than this typical length, the spins won't feel the restrictions induced by membranes. If we increase the diffusion time, then the spins will encounter the membranes and their

displacement will be restricted. Varying the effective diffusion time thus creates a contrast between the different population of axons, depending on their specific size. From a collection of measurements using different diffusion times, it is possible to extract tissue characteristics such as axon diameter, white matter fraction, ... computing the signal associated to the combination of the tissue model with the used diffusion sequence. We define in the next part the mathematical framework for the computation of this signal.

5.5.1.2 Diffusion MRI simulation

Diffusion MRI microscopy aims at allowing to measure microstructure parameters thanks to MRI experiments. But to understand the complexity of the diffusion process, the Monte Carlo simulation experiments, simulating the diffusion signal from the brownian motion of particles in the geometrical environment of the model can be very helpful. Tools such as the diffusion simulator provided in the Camino [Cook et al., 2006] toolkit or the Diffusion Microscopist Simulator introduced in [Yeh et al., 2013] provides new insights on how diffusion works in complex tissues. From various 3D tissue models and sequences schemes, the simulator provides the resulting synthetic dMRI signal. This approach can also help when there is not analytical expression for the considered tissue model. This approach was often used to validate analytical expression of the models we have presented before and study the deviation between them. As we will see in the next subsection, approximations are used to compute signal in the different geometries, and simulation experiments give the possibility to assess the validity of these approximations. Even if simulation experiments are not the main topic of this thesis, it is important to know that all the models coud be validated using simulations and simulation tools are very useful to test a model in all of its aspects.

5.5.1.3 Mathematical framework of signal attenuation computation : Short Pulse Gradient and Gaussian Phase Distribution approximations

Diffusion MRI microscopy relies on the establishment of an analytical signal attenuation equation depending on the tissue model and the type of the diffusion sequence. Let's first discuss the effect of the gradient duration δ. In chapter 3, it was shown that a Fourier relationship exists between the signal attenuation measured in the Q-space and the propagator of the diffusion process of water molecules. But this relationship remains available only if δ is infinitely short, ideally corresponding to a Dirac pulse. Unfortunately, MRI systems (in particular clinical scanners) cannot always provide inifinitely short gradient pulses, and under the condition $\delta << \Delta$, the signal will be computed using the Short Gradient Pulse approximation (SGP). When the δ duration is sufficiently

short, it is possible to neglect the motion of the spins during δ : this is the short gradient pulse approximation. The phase change of the spin at the initial position r_0 during the first gradient and moving to r_1 during the second gradient is then directly given by :

$$\Delta\phi = \gamma G\delta(r_1 - r_0), \tag{5.5}$$

with G the gradient magnitude and γ the gyromagnetic ratio.
The signal attenuation is then expressed as follows :

$$E(q,\Delta) = \int\int \rho(r_0)P(r_0,r_1,\Delta)\exp i\gamma\delta G(r_1 - r_0)dr_0dr_1. \tag{5.6}$$

If we set $R = r_1 - r_0$, then we can define $P(R,\Delta) = \rho(r_0)P(R|r_0,\Delta)$ as the average propagator. But we will see tha the b-value is also a key point to be sensitive to small pore sizes. Clinical MR scanners have very limited gradient strength so to have a high enough b-value, the δ and Δ parameters are increased. But increasing Δ will lead to longer echo time and therefore lower SNR due to the combination of diffusion decay and T2 decay. This is why the clinical conditions are often $\delta \approx \Delta$. In this condition, we must take into account the spin movement during the gradient pulse. If δ is not sufficiently low in comparison to Δ, the water molecule motion during the gradient duration δ. has to be taken into account. Under certain conditions, a Gaussian probability of the gradient phase distribution during the gradient application can be assumed, leading to the Gaussian Phase Distribution approximation (GPD). Before the refocusing pulse of the spin echo sequence (at t=TE/2), during the application of the first diffusion gradient (applied, for example along the x axis, at time t_1), the phase shifting induced can be expressed as :

$$\phi(TE/2) = \gamma B_0(TE/2) + \gamma G\int_{t_1}^{t_1+\delta} x(t)dt, \tag{5.7}$$

TE being the echo time. At the end of the sequence, the total phase shift for each spin is then expressed as :

$$\phi(TE) = \gamma G\left(\int_{t_1}^{t_1+\delta} x(t)dt - \int_{t_1+\Delta}^{\Delta+\delta+t1} x(t')dt'\right) \tag{5.8}$$

We can then expressed the signal as follows :

$$S(TE) = S_0(TE)\int_{-\infty}^{\infty} P(\phi,TE)e^{i\phi}d\phi \tag{5.9}$$

with ϕ the phase. [Douglass and McCall, 1958] demonstrated that for free water, the phase distribution function can be expressed as a Gaussian distribution function :

$$P(\phi, TE) = \frac{\exp \frac{-\phi^2}{2<\phi^2>}}{\sqrt{2\pi < \phi^2 >}} \tag{5.10}$$

with $< \phi^2 >$ the mean-squared phase change :

$$< \phi^2 >= \gamma^2 G^2 < \{\int_{t1}^{t1+\delta} x_i(t)dt - \int_{t1+\Delta}^{t1+\Delta+\delta} x_i(t)dt\}^2 > \tag{5.11}$$

$$\begin{aligned} < \phi^2 >= \gamma^2 G^2 \{ & \int_{t1}^{t1+\delta} \int_{t1}^{t1+\delta} dt_a dt_b \\ & -2 \int_{t1}^{t1+\delta} \int_{t1+\Delta}^{t1+\delta+\Delta} dt_a dt_b + \\ & \int_{t1+\Delta}^{t1+\delta+\Delta} \int_{t1+\Delta}^{t1+\delta+\Delta} dt_a dt_b \} \\ & < x(t_a)x(t_b) > \end{aligned}$$

and

$$< x(t_a)x(t_b) >= \int_{-\infty}^{\infty} \int_{-\infty}^{\infty} \int_{-\infty}^{\infty} (r_1 - r_0)_x (r_2 - r_0)_x \rho(r_0) P(r_0, r_1, t_a) P(r_1, r_2, t_b - t_a) dr_0 dr_1 dr_2 \tag{5.12}$$

the mean-squared displacement. This is valid for free water, but when the water motion is restricted, this distribution is theoritically non Gaussian. But in some cases, the phase distribution can be *approximated* by a Gaussian distribution function. This approximation is valid for short gradient duration, when spins don't encounter the restrictions. At long diffusion times, the position of a spin will be independent of its initial position, so the phase distribution can also be considered as a Gaussian. But it has been shown that even for δ of the order of the pore size, for simple geometries, the distribution can be well approximated using Gaussian distribution (Neuman [1974], Balinov et al. [1993]). After computing the diffusion propagator for the geometry of the tissue (for example a cylinder), it is straightforward to compute the mean-squared displacement in the direction of the gradient, and finally the mean-squared phase change and the attenuation. For free diffusion, the signal from the PGSE is expressed as follows :

$$E(q) = S(q)/S_0 = \exp(-q^2(\Delta - \frac{\delta}{3})D) \tag{5.13}$$

with D being the diffusion coefficient.

5.5.1.4 Equation of the diffusion propagator

The computation of the signal attenuation requires the definition of the diffusion propagator of the tissue. The models we described in the previous part, often relies on the combination of one hindered compartment, described by a Gaussian diffusion behaviour and one restricted compartment, modeled as a sphere or cylinder. For restriced compartments, the simplest way to get the propagator is to compute its eigen mode expansion (Neuman [1974], Callaghan [1995]). The problem is posed as follows :

$$P(r|r',t) = \sum_{n=0}^{\infty} exp(-\alpha_n t) u_n(r) u_n^*(r'), \tag{5.14}$$

$$\text{The initial condition : } P(r|r',0) = \delta(r-r'), \tag{5.15}$$

$$\text{The boundary conditions (M is the permeability): } D\mathbf{n}\nabla P + MP = 0. \tag{5.16}$$

Diffusion propagator expression for the axon : cylinder geometry

In the case of the axon, the majority of the models assume M = 0, since they are considered as impermeable in the diffusion time scale. The diffusion propagator of the cylinder of radius a is given by :

$$u_n(r) = A_{nn'} J_n(\frac{\beta_{nn'} r}{a}) \exp(in\theta)$$

with

$$A_{nn'} = \sqrt{\frac{\frac{2\beta_{nn'}}{\pi a^2 J_n(\beta_{nn'})^2}}{(\frac{Ma}{D})^2 + \beta_{nn'}^2 - n^2}}$$

,

$$A_{0n'} = \sqrt{\frac{\frac{\beta_{nn'}}{\pi a^2 J_0(\beta_{nn'})^2}}{(\frac{Ma}{D})^2 + \beta_{0n'}^2}}$$

and $\beta_{nn'}$ are the zeros of the equations :

$$\beta_{nn'} \frac{J_n(\beta_{nn'})'}{J_n(\beta_{nn'})} + \frac{Ma}{D} = 0$$

.

Diffusion propagator expression for neural cells : sphere geometry

For a sphere of radius a :

$$u_n(r) = A_{nn'} Jn(\frac{\beta_{nn'} r}{a}) P_n(cos\theta)$$

with

$$A_{nn'} = 1/\sqrt{\frac{2\pi}{2n+1}a^3(j_n(\beta_{nn'})^2) - j_{n-1}(\beta_{nn'})j_{n+1}(\beta_{nn'})},$$

and $\beta_{nn'}$ are the zeros of the equations :

$$\beta_{nn'}\frac{j_n(\beta_{nn'})'}{j_n(\beta_{nn'})} + \frac{Ma}{D} = 0.$$

These zeros can be computed using interlacing properties of bessel function roots and using Newton-Raphson's or/and bisection methods.

Once the propagator is found, the signal attenuation is obtained using either the GPD or the SGP approximations. We established here the context of diffusion MRI microscopy and the constrains imposed by the sequence parameters. The following sections describes the different sequences used to infer microstructural features and the signal attenuation associated to them, following either the SGP or GPD approximations.

5.5.2 Diffusion MRI microscopy using Pulse Gradient Spin Echo

Several studies attempted to extract microstructural features using Pulse Gradient Spin Echo. Two major frameworks were developed to address the inference of axon radii and density: AxCaliber developed by Assaf et al. [2008] and ActiveAx Alexander [2008]. Both of them establishes a particular protocol dedicated to the inference of microstructure parameters from several measurements using PGSE sequence under SGP or GPD conditions, varying the sequence parameters in order to sample the signal efficiently to fit the tissue model from the experimental measurements. Another less common approach, is the exploitation of diffraction pattern occuring for the long time limit of the PGSE signal, giving a signature of the underlying microstructure. We first explain AxCaliber and ActiveAx framework, before introducing the long time limit PGSE framework.

5.5.2.1 AxCaliber Framework

The AxCaliber Framework introduced by [Assaf et al., 2008] aims at measuring a distribution of axon diameters using PGSE experiments and remains limited to preclinical studies (requiring huge sampling and SGP assumption).

Tissue model :

This framework uses the CHARMED model to describe the tissue, where the restricted part integrates the contributions of several fiber populations, each of them being characterized by a specific diameter. From the observation of tissues by electron microscopy, a gamma Γ distribution has been chosen to model the actual axon diameter distribution.

Acquisition schemes :

This technique requires to know the orientation of the axon in the observed region. This is why this framework is primarely applied in the study of the corpus callosum, where most of the fibers are in the left-right direction. Knowing this orientation, the different diffusion measurements are performed applying the diffusion gradients perpendicularly to the axon direction, in order to be sensitive to the restricted part of the signal attenuation induced by the cylinder membrane. The gradient duration δ is fixed and kept short ($\delta \approx 3/4ms$) in comparison with Δ. The protocol is made of several measurements corresponding to a large sampling of Δ : typically from 10ms to 150 ms in order to get the appropriate contrast between the different axon diameters. For each Δ, the gradient strength is incremented several times (sixteen in [Assaf et al., 2008] with a high maximum gradient strength ($G_{max} \approx 300T/m$)).

Signal Attenuation :

Under these conditions, the signal attenuation is computed from the CHARMED model assuming a contribution corresponding to and hindered compartment (the extra-axonal space) and to a restricted compartment (the intra-axonal space) :

$$E(q) = f_h E_h(q) + f_r E_r(q), \tag{5.17}$$

$$E_r(q) = E_\perp E_{\|}, \tag{5.18}$$

In the case of the AxCaliber protocol, the measurements are only performed perpendicularly to the fiber direction. The hindered part is therefore expressed as a 1D Gaussian diffusion problem:

$$E_h(q) = \exp\left(-(\Delta - \delta/3)q^2 D_h\right) \tag{5.19}$$

with D_h the hindered diffusion coefficient. The restricted part, corresponding to the diffusion process in the packed impermeable cylinders representing axons, is expressed from Callaghan [1995] with no relaxation (the membrane is considered impermeable) :

$$E_\perp = \sum_k 4\exp(-\beta_{0k}^2 * D * \Delta/a^2)\frac{2\pi q a J_0'(2\pi q a)}{((2\pi q a)^2 - \beta_{0k}^2)^2} + \sum_{nk} 8\exp(-\beta_{nk}^2 * D * \Delta/a^2)\frac{\beta_{nk}^2}{\beta_{nk}^2 - n^2}\frac{2\pi q a J_n'(2\pi q a)}{((2\pi q a)^2 - \beta_{nk}^2)^2} \tag{5.20}$$

Assuming the existence of different fiber populations, we obtain :

$$E_\perp = \sum_i \frac{f_i}{\pi a_i^2}\left(\sum_k 4\exp(-\beta_{0k}^2 * D * \Delta/a_i^2)\frac{2\pi q a_i J_0'(2\pi q a_i)}{((2\pi q a_i)^2 - \beta_{0k}^2)^2} + \sum_{nk} 8\exp(-\beta_{nk}^2 * D * \Delta/a_i^2)\frac{\beta_{nk}^2}{\beta_{nk}^2 - n^2}\frac{2\pi q a_i J_n'(2\pi q a_i)}{((2\pi q a_i)^2 - \beta_{nk}^2)^2}\right) \tag{5.21}$$

with f_i and a_i the volume fraction and the radius corresponding to the fiber population i. The different axon radii are weighted using a Γ distribution defined as : $w_i(a_i, \alpha, \beta) = \frac{a_i^{\alpha-1} \exp(-a_i/\beta)}{\beta^\alpha \Gamma(\alpha)}$.

Results and limits :

This framework has been shown to be efficient, for example in the original paper [Assaf et al., 2008] in ex-vivo porcine optic and sciatic nerves or in the corpus callosum of rodents [Barazany et al., 2009], where an additional isotropic Gaussian compartment was added to deal with the contamination of the signal by the Cerebro Spinal Fluid component. Results from [Assaf et al., 2008] (Figure 5.9) assessed the ability of this technique to recover the axon diameter distribution using electron microscopy as ground truth. The limitation of this work is that these protocols cannot be used in clinical applications, since the scan duration is too long, the required gradient strength is high and the short δ condition is difficult to obtain with clinical gradient coils, because of the finite duration of the gradients. Moreover, it requires the knowledge of the fiber orientation and it relies on the assumption of the Γ distribution of the axon diameter, that cannot be assumed anymore when moving from healthy tissues to diseased tissues.

5.5.2.2 ActiveAx Framework : optimization of acquisition scheme for clinical routine

The ActiveAx framework was first proposed in Alexander [2008] to perform axon calibration *in vivo*, and the major constrain of being usable for clinical applications. This framework relies on a first step of optimization to obtain the best set of sequence parameters and measurements given hardware and safety constraints to perform axon calibration with the highest accuracy in a limited scan duration. The protocol is thus reduced to only M PGSE profiles, each of them being applied along N diffusion directions (4 combinations of $G/\delta/\Delta$ and 30 directions for example), by optimizing it to reduce the variance of the parameter estimates given a geometrical model. The different steps are :

- Definition of a tissue model : for white matter model application, the CHARMED model is used with a restricted part corresponding to packed and impermeable cylinders that can be correlated to an average diameter over the fiber populations, but any kind of model can be used.

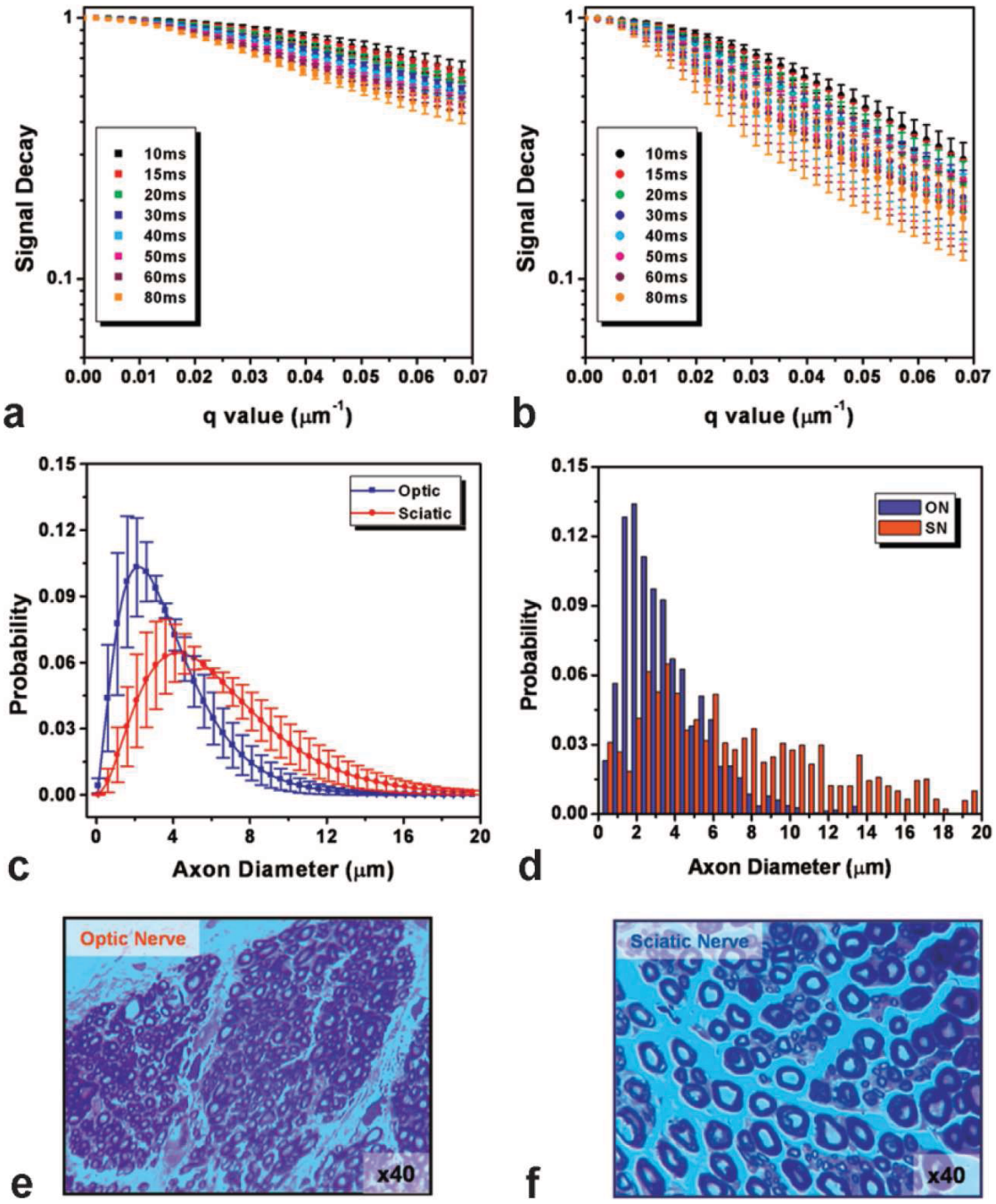

FIGURE 5.9: AxCaliber Framework results from [Assaf et al., 2008] for ex-vivo porcine optic and sciatic nerves : a. Multi diffusion time diffusion spectroscopy signal decay of an optic nerve sample. b. Multi diffusion time diffusion spectroscopy signal decay of a sciatic nerve sample. c. Extracted AxCaliber axon diameter distribution based on the signal decays given in (a) and (b). d. Axon diameter distribution derived from electron microscopy section of the two nerve samples. e,f. Electron microscope section of one optic nerve (e) and one sciatic nerve samples upon which the data in (a– d) is based.

- Protocol optimization : find M PGSE profiles to acquire along N directions over a single shell chosen to minimize the variance of the estimates of the model parameters using the Cramer-Rao lower bound criterion and a noise model (typically the Rician noise).

- Acquisition of measurements using the optimized protocol
- Inference of the axon diameter using a Monte Carlo Markov Chain procedure to draw the posterior distributions of the parameters (see Appendix B).

The optimization process is constrained by several requirements : the scan duration (leading to a small M of measurements), the hardware constraints (the maximum gradient strength of the system, the static field, leading to a limited echo time and therefore a limited diffusion time), the safety constraints for the human volunteer, and the possibility to be orientationnaly invariant, contrary to AxCaliber protocols. The latter naturally leads to single shell Q-space samplings. The objective function to minimize is built from the Cramer-Rao lower bounds of the tissue model parameters, providing the lower bound of the variance of the estimates using the Fisher matrix :

$$f_{obj} = \sum_{i=1}^{P} CRLB_i / p_i^2$$

with f_{obj} the objective function, $CRLB_i$ the Cramer-Rao lower bound of the parameter i p_i. $CRLB_i = (J)_{ii}^{-1}$ with J the Fisher matrix defined as $J_{ij} = E(\frac{\partial L}{\partial p_i \partial p_j})$ where L is the likelihood of the measurement. The likelihood of the measurements depends on the tissue model parameters but moreover on a noise model. As we have seen before, the Rician noise is often considered for MRI experiments, and therefore the Rician probability distribution is used to compute the likelihood. This optimization framework then provides M sets of G,δ,Δ parameters allowing to obtain a minimum variance of the estimates of the model parameters. The computation of the objective function also depends on prior knowledge of the parameters, such as the intra-axonal and extra axonal diffusivities. Measurements obtained using this acquisition scheme can then be analyzed using a MCMC procedure to obtain posterior distribution of each parameter. The decoding part of this technique relies on the expression of the signal using GPD approximation. In clinical applications, the SGP approximation cannot be used because the gradient strength being limited, it is not possible to reduce the δ parameter sufficiently. The signal model in this condition is therefore :

Signal model :

- Hindered Compartment for the GPD approximation :

$$E_h(q) = \exp -(\Delta - \delta/3) q^T D q \tag{5.22}$$

Restricted Compartment for the GPD approximation :
The restricted component is the signal coming from the intra-axonal water molecules. Using the cylinder model, the restricted part is the product of the signal perpendicular to the axon and parallel to the axon. The parallel restricted part is modeled as a 1D Gaussian diffusion process :

$$E_{\parallel}(q) = \exp(-(\Delta - \delta/3)|q_{\parallel}|^2 D_{\parallel}) \tag{5.23}$$

The perpendicular part is the diffusion process perpendicular to a cylinder, expressed by Van Gelderen [Van Gelderen et al., 1994] :

$$ln(E_{\perp}) = -2\gamma^2 g_{\perp}^2 \sum_{m=1} \frac{2D\alpha_m^2\delta - 2 + 2e^{-D\alpha_m^2\delta} + 2e^{-D\alpha_m^2 * \Delta}}{D^2\alpha_m^6\left(r_i^2\alpha_m^2 - 1\right)} + \frac{-e^{-D\alpha_m^2(\Delta-\delta)} - e^{-D\alpha_m^2(\Delta+\delta)}}{D^2\alpha_m^6\left(r_i^2\alpha_m^2 - 1\right)} \tag{5.24}$$

with $\alpha_m J_1(\alpha_m r_i)' = 0$

Results and Limits :
This framework was applied in [Alexander et al., 2010] using the CHARMED model but the restricted part was simplified to consider only one axon diameter, not a distribution. This framework aims at providing an orientationnaly invariant axon index, the signal is therefore not measured along the unique perpendicular direction. The hindered part is represented by a tensor. Additional compartments were included in the model : an isotropic compartement following a Gaussian diffusion to characterize the contamination by Cerebro Spinal Fluid and a compartment for the bulk of stationnary water molecules. This work proved the accuracy of the optimized protocols to recover axon diameter in both fixed monkey brains and *in vivo* human brain, using a 3T clinical scanner, with a maximum gradient strength of 60 mT/m, N = 90 orientations of four multiple shell PGSE profiles. Figure 5.10 shows the optimized protocol for the human study. This protocol shows that a combination of low and high b-values are useful. In this study, only one radius is extracted, expecting to correlate with the mean diameter of the axon distribution. This parameter, called "axon diameter index", a', is suggested to in fact correlate with the mean axon diameter weighted by volume : $\alpha = \frac{\int p(a)a^3 da}{\int p(a)a^2 da}$, p being the actual distribution of axons. In the same way, an index of axon density is characterized as $\frac{4\nu'}{\pi a'^2}$, ν' being the extracted ratio between the intra-axonal fraction and the sum of the intra and extra cellular spaces. Results of this study are shown in Figure 5.11, where we can see that this model allows to find a low-high-low profile of the axon radius estimate and the high-low-high behavior of the axon density along the corpus callosum,

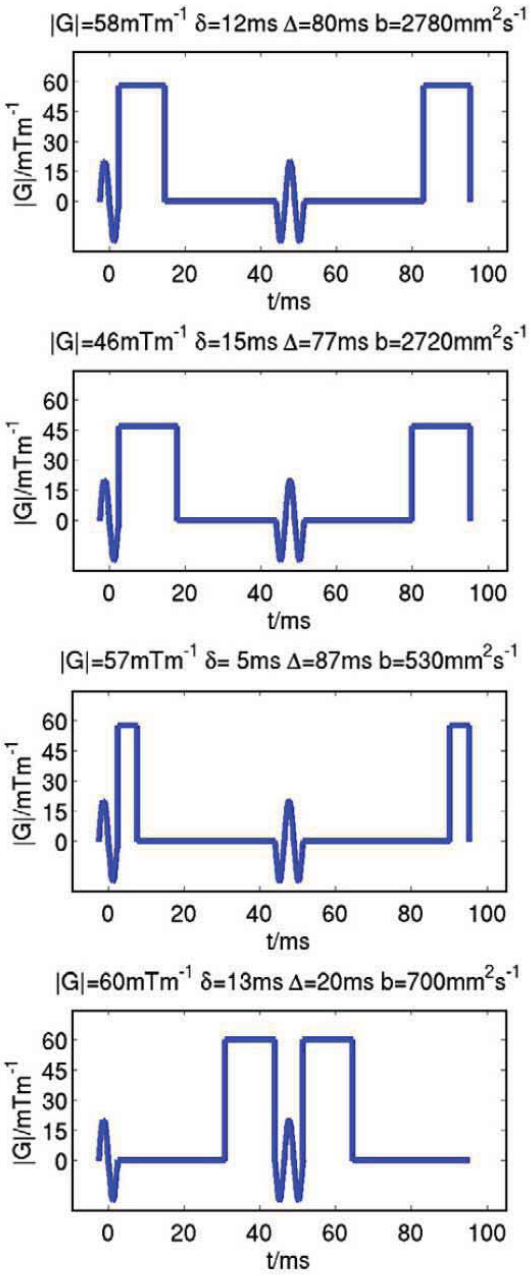

FIGURE 5.10: Human optimized protocol extracted from [Alexander et al., 2010] (RF pulses are also shown)

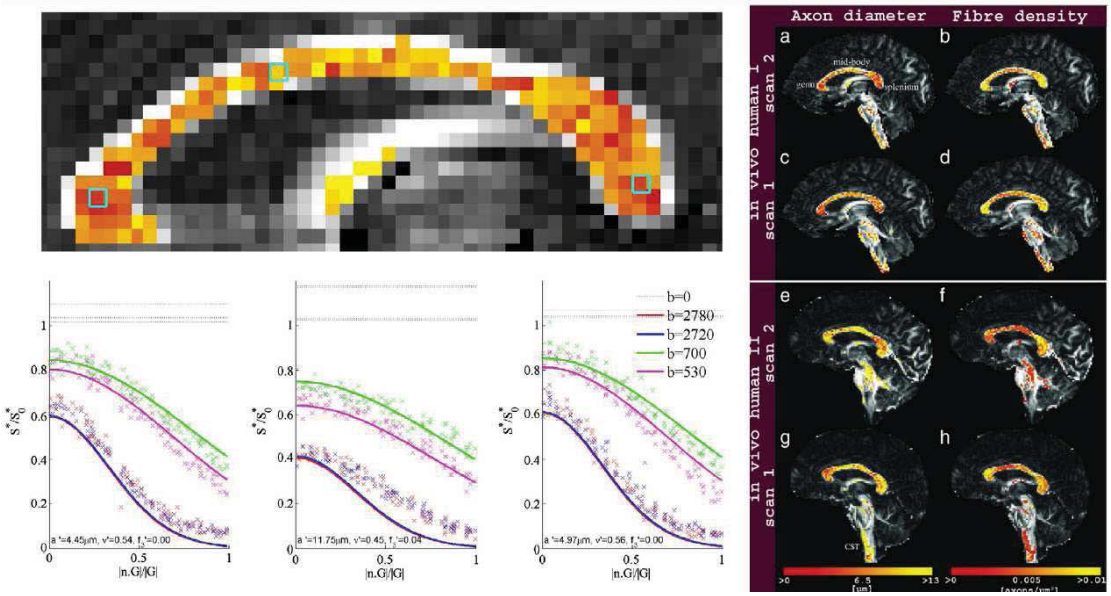

FIGURE 5.11: Results of ActiveAx framework on the corpus callosum of human subjects from [Alexander et al., 2010]

expected from the results of histology. In [Alexander, 2008], different aspects of the axon calibration were adressed using simulated data. The range of axon radii that can be well estimated is limited by the sequence parameters. High gradient strength for example allows a better accuracy of the estimation (partly because of the reducing echo time, increasing the Signal-to-noise ratio). Since δ cannot be reduced, this limits the smallest radii that can be accurately extracted. But simulations in this study shows that even if it is not possible to distinguish small radii ($\leq 2\mu m$), it is possible to define them as "small".

This question of accuracy and stability of the estimation was also adressed in [Dyrby et al., 2013]. Several ActiveAx protocols were tested on a 4.7T Varian Imaging system on a fixed monkey brain and simulated data, varying the gradient strength from $60mT/m$ to $300mT/m$, and the δ and Δ parameters. The authors simulated data assuming different axon diameter distribution and compared the estimated radius from 100 repeated fitting of the data to the idealized axon diameter α of the distribution for the different gradient strength and for different SNR conditions (see Figure 5.12). It is shown that the gradient strength has a strong influence on variance of axon diameter index and smallest axons cannot be well estimated since the diffusion gradient duration cannot be sufficiently reduced. The actual distribution of axons also strongly influences the deviation between the index and α. This study confirms the existence of a lower and upper bounds of radii that can be identified using ActiveAx imaging. The presence of lower bound is explained by the minimum achievable diffusion time coming from the limited gradient strength (limiting its sensitivity to the smaller radii) and the upper bound by the insufficient diffusion time of the experiment (limited by the echo time to preserve a high SNR).

The conclusion of this work is that using high gradient strength provides more accurate estimates and higher SNR could also help to reduce the variability of the mean axon diameter index (but its impact is less pronounced than for higher gradient strength). In this thesis, we will address the the lower bound issue using two different approaches: the development of an arbitrary gradient waveform diffusion sequence, allowing to reduce the diffusion time in comparison with PGSE and the development of the two pool model that may help to reduce this overestimation.

This framework allowed to perform for the first time *in vivo* axon calibration on humans and to study the sensitivity of the ActiveAx protocol to the microstructure parameters and the influence of the different sequence parameters. Even if the estimation is better for higher gradient strengths, this protocol obviously provides contrast allowing to distinguish different regions based on its microstructure. Moreover, it is not constrained by the knowledge of the orientation of the axons. This work has been extended [Zhang et al., 2011a] to tackle the problem of fiber dispersions using the same model but adding a Watson's distribution to model the orientation dispersion. This gives the opportunity to get extra structural parameters in regions where the configuration is not as simple as one fiber population with one direction. This model is expressed as the sum of the intra and extra cellular compartments, such as CHARMED model but includes the orientation dispersion function. The intra axonal part is thus expressed as

$$E_{restricted} = \int \rho(\mathbf{n}) E_{cylinder}(\mathbf{n}) d\mathbf{n}, \tag{5.25}$$

with $\rho(\mathbf{n})$ the axonal orientation distribution, $E_{cylinder}(\mathbf{n})$ the attenuation of the population of axons oriented along $\mathbf{n}$. The extra-cellular part is modelled using an Gaussian anisotropic process, with the diffusion tensor D_{ec} depending on both the volume fraction of the intra-cellular part and the orientation distribution. Its signal is expressed as:

$$\mathbf{D_{ec}}(\rho, f_{restricted}) = \int \rho(\mathbf{n}) \mathbf{D_h}(\mathbf{n}, f_{restricted}) d\mathbf{n} \tag{5.26}$$

with D_h the tensor of population characterized by the direction $\mathbf{n}$. $\rho(\mathbf{n})$ is expressed as a Watson distribution :

$$\rho(\mathbf{n}) = M(\frac{1}{2}, \frac{3}{2}, \kappa)^{-1} \exp((\kappa(\mu - \mathbf{n}))^2), \tag{5.27}$$

where M is a confluent hypergeometric function (see Appendix A), μ the unit vector about which the distribution is cylindrically symmetric and κ controling the extent of the orientation dispersion. [Zhang et al., 2012] uses the same model to map neurite density, replacing the cylinder model by a stick and therefore proposing to study density in white and grey matter.

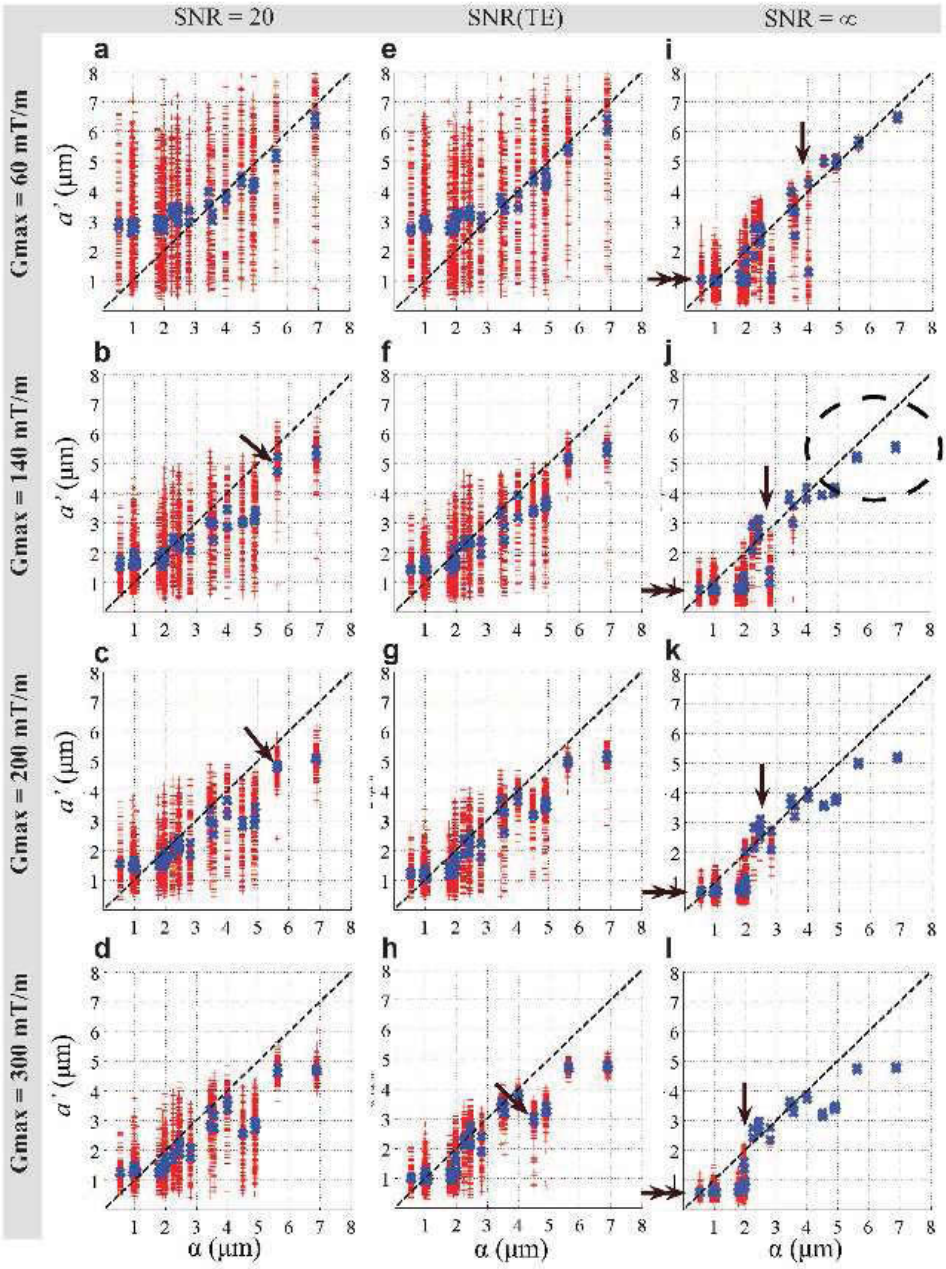

FIGURE 5.12: Comparison of the estimated axon radius a' versus the ideal axon diameter index α from simulated data at different gradient strength (60mT/m, 140 mT/m, 200 mT/m, 300mT/m) and with various SNR (from [Dyrby et al., 2013]). In blue: the mean of the repetitions of the fitting, in red: the estimates for each repetition

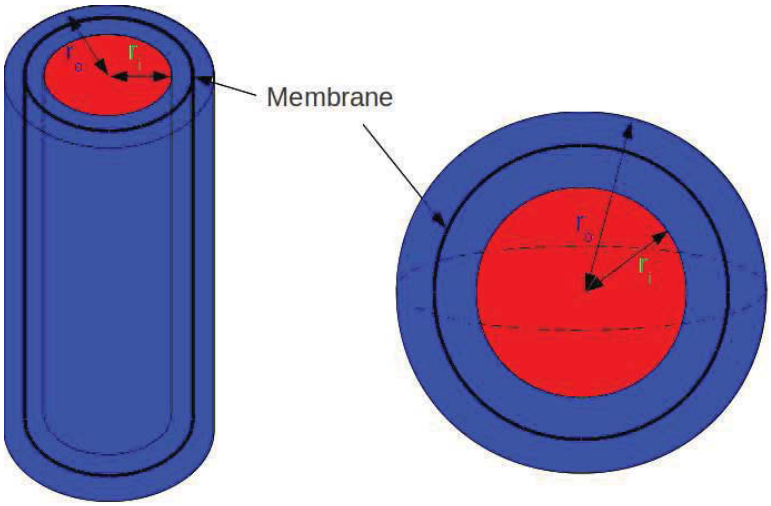

FIGURE 5.13: Two-pool cylinder and sphere model : in blue the slow pool, in red the fast pool

5.5.2.3 Second contribution : signal attenuation for the two-pool model

All the various studies dealing with axon calibration stress the fact that the estimates of axon small radii often overestimates the actual axon radii in comparison with histology. One possible explanation is the limited gradient strength, allowing to only distinguish radii higher than 2μm. However, it is not the only explanation and it could also come from the tissue model itself (orientation dispersion, exchange between compartments, nature of the compartments...). We here propose an alternative model to the cylinder, to partly explain this overestimation. As we described in section 5.7, a two-pool model was proposed by [Assaf and Cohen, 1998] and [Sehy et al., 2002] to explain the biexponential behavior of the diffusion leading to consider one pool, near the membranes and characterized by a slow diffusion coefficient and another pool of water molecules, far from the membranes and characterized by a fast diffusion coefficient. The slow behavior has been explained by the structural organization of the water near the layer of lipids and proteins of the membrane. In this thesis, we extended the cylinder model to a thick cylinder with two different diffusivities in the layer and around. This model has been integrated in ActiveAx-like protocols using PGSE sequences. We here expose the computation of the signal attenuation for this model and sequence, under clinical conditions leading to the use of GPD approximation. The attenuation signal coming from a circular layer under SGP approximation was derived in [Ghadirian et al., 2013].

Development of the PGSE signal attenuation for the two-pool cylinder model:

Let's consider E_{fast} the echo attenuation for the fast pool within the cylinder (between

0 and r_i), and E_{slow} the echo attenuation within the thick layer of the cylinder (between radius r_i and r_o, see Figure 5.13), the total attenuation is given by the following mixture:

$$E = f_{fast}E_{fast} + f_{slow}E_{slow} = f_{fast}E_{fast\perp}E_{fast\parallel} + f_{slow}E_{slow\perp}E_{slow\parallel},$$

with $f_{fast} + f_{slow} = 1$. separating the diffusion attenuation perpendicular and parallel to the cylinder. Both slow and fast parallel attenuations can be modeled using Gaussian propagators. D_{fast} and D_{slow} are the diffusivity of each compartment.

1. *Fast pool perpendicular attenuation*

   Within the cylinder, the signal attenuation is given by the GPD approximation on a simple cylinder model of radius r_i (the inner radius). The attenuation perpendicular to the fiber assuming a PGSE scheme is given by [Van Gelderen et al., 1994].

$$ln(E_{fast\perp}) = -2\gamma^2 g_\perp^2 \sum_{m=1} \frac{2D_{fast}\alpha_m^2\delta - 2 + 2e^{-D_{fast}\alpha_m^2\delta} + 2e^{-D_{fast}\alpha_m^2 * \Delta}}{D_{fast}^2\alpha_m^6\left(r_i^2\alpha_m^2 - 1\right)} + \frac{-e^{-D_{fast}\alpha_m^2(\Delta-\delta)} - e^{-D_{fast}\alpha_m^2(\Delta+\delta)}}{D_{fast}^2\alpha_m^6\left(r_i^2\alpha_m^2 - 1\right)} \quad (5.28)$$

   with $\alpha_m J_1\left(\alpha_m r_i\right)' = 0$ The α_m are computed numerically using Newton and bisection method.

2. *Slow pool perpendicular attenuation*

   Propagator in cylindrical coordinates :
   (J_n and Y_n are respectively first and second kind Bessel's functions (see Appendix A for definition)

$$P_s\left(r, r', \theta, \theta', t' - t\right)_\perp = A_{00} + \frac{1}{\pi}\sum_{mn} A_{nm}\left(J_n\left(\frac{\beta_{mn}r}{r_i}\right)J_n\left(\frac{\beta_{mn}r'}{r_i}\right) - \frac{J_n\left(\beta_{mn}\right)'}{Y_n\left(\beta_{mn}\right)'}Y_n\left(\frac{\beta_{mn}r}{r_i}\right)Y_n\left(\frac{\beta_{mn}r'}{r_i}\right)\right) \left(\cos\left(n\theta\right)\cos\left(n\theta'\right) + \sin\left(n\theta\right)\sin\left(n\theta'\right)\right) e^{\frac{-\beta_{mn}^2 D}{r_i^2}(t'-t)} \quad (5.29)$$

$$A_{00} = \frac{1}{\pi\left(r_o^2 - r_i^2\right)} \tag{5.30}$$

$$\text{and } A'^{-1}_{nm} = \frac{Y_n\left(\beta_{mn}\right)'}{A_{nm}} = \int_{r_i}^{r_o} r\left[R(r)\right]^2 dr \tag{5.31}$$

$$\text{with } R(r) = J_n\left(\frac{\beta_{mn} r}{r_i}\right) Y_n\left(\beta_{mn}\right)' - Y_n\left(\frac{\beta_{mn} r}{r_i}\right) J_n\left(\beta_{mn}\right)' \tag{5.32}$$

Boundary conditions : $R'(a) = 0$ and $R'(b) = 0$ so β_{mn} are the roots of $J_n\left(\frac{\beta_{mn} r_o}{r_i}\right)' Y_n\left(\beta_{mn}\right)' - Y_n\left(\frac{\beta_{mn} r_o}{r_i}\right)' J_n\left(\beta_{mn}\right)' = 0$, θ is the angle between the gradient and r.

$$\left\langle r(t) r(t') \right\rangle = \frac{1}{\pi\left(r_o^2 - r_i^2\right)} \int_0^{2\pi} d\theta \int_0^{2\pi} d\theta_0 \int_0^{2\pi} d\theta' \int_{r_i}^{r_o} dr \int_{r_i}^{r_o} dr_0 \int_{r_i}^{r_o} dr' r_0 r r'$$
$$P_{slow}\left(r, r_0, \theta, \theta_0, t\right) P_{slow}\left(r', r, \theta', \theta, t' - t\right) \left[r cos\left(\theta\right) - r_0 cos\left(\theta_0\right)\right] \left[r' cos\left(\theta'\right) - r_0 cos\left(\theta_0\right)\right] \tag{5.33}$$

After some simplifications we get :

$$\pi\left(r_o^2 - r_i^2\right)\left\langle r(t) r(t') \right\rangle = \frac{\pi\left(r_o^4 - r_i^4\right)}{4} - \sum_{m=1} A'_{1m} I \left[\pi e^{\frac{-\beta_{1m}^2 D_{slow}}{r_i^2} t} - \pi e^{\frac{-\beta_{1m}^2 D_{slow}}{r_i^2}(t'-t)} + \pi e^{\frac{-\beta_{1m}^2 D_{slow}}{r_i^2} t'}\right] \tag{5.34}$$

$$I = \frac{r_i^6}{\beta_{1m}^2} \times \left(Y_1\left(\beta_{1m}\right)' \left[\frac{J_2\left(\frac{\beta_{1m} r_o}{r_i}\right) r_o^2}{r_i^2} - J_2\left(\beta_{1m}\right)\right] - J_1\left(\beta_{1m}\right)' \left[\frac{Y_2\left(\frac{\beta_{1m} r_o}{r_i}\right) r_o^2}{r_i^2} - Y_2\left(\beta_{1m}\right)\right]\right)^2$$

$$A'^{-1}_{1m} = \frac{r_i^2}{2\beta_{1m}^2} [\left(\frac{\beta_{1m}^2 r_o^2}{r_i^2} - 1\right)\left(J_1\left(\frac{\beta_{1m} r_o}{r_i}\right) Y_1\left(\beta_{1m}\right)' - Y_1\left(\frac{\beta_{1m} r_o}{r_i}\right) J_1\left(\beta_{1m}\right)'\right)^2 - \left(\beta_{1m}^2 - 1\right)\left(J_1\left(\beta_{1m}\right) Y_1\left(\beta_{1m}\right)' - Y_1\left(\beta_{1m}\right) J_1\left(\beta_{1m}\right)'\right)^2]$$

Mean-squared phase change: (δ is the pulse duration and Δ the separation time of the PGSE)

$$< \phi^2 >= \gamma^2 g^2 \left[\int_0^\delta dt \int_0^\delta dt' - 2\int_0^\delta dt \int_\Delta^{\Delta+\delta} dt' + \int_\Delta^{\Delta+\delta} dt \int_\Delta^{\Delta+\delta} dt' < r(t) r(t') >\right]$$

$$< \phi^2 >= 2\gamma^2 g^2 \frac{1}{\left(r_o^2 - r_i^2\right)} \sum_{m=1} A'_{1m} I$$
$$[\frac{2D_{slow}\frac{\beta_{1m}^2}{r_i^2}\delta - 2 + 2e^{-\frac{\beta_{1m}^2}{r_i^2}D_{slow}\delta} + 2e^{-\frac{\beta_{1m}^2}{r_i^2}D_{slow}\Delta} - e^{-\frac{\beta_{1m}^2}{r_i^2}D_{slow}(\Delta+\delta)} - e^{-\frac{\beta_{1m}^2}{r_i^2}D_{slow}(\Delta-\delta)}}{D_{slow}^2\frac{\beta_{1m}^6}{r_i^6}}] \tag{5.35}$$

Signal attenuation : $E_{slow\perp} = \exp\left(- < \phi^2 > /2\right)$

Signal attenuation for the thick layer sphere using PGSE:

We can also extend the two-pool model for a sphere model, useful to model spherical cells for instance. This part exposes the result assuming an impermeable membrane, but one needs to keep in mind that for cell modeling, permeability has to be introduced and therefore leading to different boundary conditions.

If E_{fast} is the echo attenuation for the fast pool, inside the sphere (between 0 and r_i), and E_{slow} the echo attenuation inside the thick layer of the sphere (between radius r_i and r_o), the total attenuation is given by: $E = E_{fast} + E_{slow}$ with D_{fast} and D_{slow} the diffusivity of each compartment.

1. *Fast pool attenuation*

   Inside the sphere, the signal attenuation is given by the GPD approximation on a simple sphere model of radius r_i (the inner radius).

$$\ln(E_{fast}) = -\frac{2\gamma^2 g^2}{D_{fast}} \sum_{m=1}^{\infty} \frac{\alpha_m^{-4}}{\alpha_m^2 r_i^2 - 2}[2\delta - \frac{2 + \exp\left(-\frac{\alpha_m^2 D_{fast}(\Delta-\delta)}{r_i^2}\right) - 2\exp\left(-\frac{\alpha_m^2 D_{fast}\delta}{r_i^2}\right)}{\alpha_m^2 D_{fast}} + \frac{-2\exp\left(-\frac{\alpha_m^2 D_{fast}\Delta}{r_i^2}\right) + \exp\left(-\frac{\alpha_m^2 D_{fast}(\Delta+\delta)}{r_i^2}\right)}{\alpha_m^2 D_{fast}}] \tag{5.36}$$

   with $\alpha_m j_1 \left(\alpha_m r_i\right)' = 0$

2. *Slow pool attenuation*

Propagator in spherical coordinates: (j_n and y_n are respectively first and second kind spherical bessel functions)

$$P_s\left(r,r',\theta,\theta',\phi,\phi',t'-t\right)_\perp = A_{00} + \frac{2n+1}{2\pi}\sum_{mn} A_{nm} \left(j_n\left(\frac{\beta_{mn}r}{r_i}\right) j_n\left(\frac{\beta_{mn}r'}{r_i}\right) - \frac{j_n\left(\beta_{mn}\right)'}{y_n\left(\beta_{mn}\right)'} y_n\left(\frac{\beta_{mn}r}{r_i}\right) y_n\left(\frac{\beta_{mn}r'}{r_i}\right)\right) P_n\left(\cos\left(\theta\right) P_n\left(\cos\left(\theta'\right)\right)\right) e^{\frac{-\beta_{mn}^2 D_{slow}}{r_i^2}(t'-t)} \quad (5.37)$$

$$A_{00} = \frac{3}{4\pi\left(r_o^3 - r_i^3\right)}$$

$$\text{and } A_{nm}'^{-1} = \frac{y_n\left(\beta_{mn}\right)'}{A_{nm}} = \int_{r_i}^{r_o} r^2\left[R(r)\right]^2 dr$$

$$\text{with } R(r) = j_n\left(\frac{\beta_{mn}r}{r_i}\right) y_n\left(\beta_{mn}\right)' - y_n\left(\frac{\beta_{mn}r}{r_i}\right) j_n\left(\beta_{mn}\right)' \text{ and no } \phi \text{ dependence}$$

Boundary conditions : $R'(a) = 0$ and $R'(b) = 0$ so $\beta_{mn}$are the roots of $j_n\left(\frac{\beta_{mn}r_o}{r_i}\right)' y_n\left(\beta_{mn}\right)' - y_n\left(\frac{\beta_{mn}r_o}{r_i}\right)' j_n\left(\beta_{mn}\right)' = 0$

Initial condition : $P(r',r,t=0) = \delta\left[r-r'\right]$

Mean-squared displacement :(δ *is the pulse duration and* Δ *the separation time of the PGSE)*

$$\left\langle r(t)r(t')\right\rangle = \frac{3\times 8\pi^3}{4\pi\left(r_o^3 - r_i^3\right)} \int_0^\pi d\theta \int_0^\pi d\theta_0 \int_0^\pi d\theta' \int_{r_i}^{r_o} dr \int_{r_i}^{r_o} dr_0 \int_{r_i}^{r_o} dr' r_0^2 r^2 r'^2 P_{slow}\left(r,r_0,\theta,\theta_0,t\right) P_{slow}\left(r',r,\theta',\theta,t'-t\right)\left[r cos\left(\theta\right) - r_0 cos\left(\theta_0\right)\right]\left[r' cos\left(\theta'\right) - r_0 cos\left(\theta_0\right)\right] \quad (5.38)$$

θ is the angle between the gradient and r.

After some simplifications we get :

$$\left(r_o^3 - r_i^3\right)\left\langle r(t)r(t')\right\rangle = \frac{\left(r_o^5 - r_i^5\right)}{20} - 2\sum_{m=1} A_{1m}' I\left[e^{\frac{-\beta_{1m}^2 D_{slow}}{r_i^2}t} - e^{\frac{-\beta_{1m}^2 D_{slow}}{r_i^2}(t'-t)} + e^{\frac{-\beta_{1m}^2 D_{slow}}{r_i^2}t'}\right]$$

with

$$I = \frac{r_i^8}{\beta_{1m}^2} \times \left(y_1\left(\beta_{1m}\right)'\left[\frac{j_2\left(\frac{\beta_{1m}r_o}{r_i}\right) r_o^3}{r_i^3} - j_2\left(\beta_{1m}\right)\right] - j_1\left(\beta_{1m}\right)'\left[\frac{y_2\left(\frac{\beta_{1m}r_o}{r_i}\right) r_o^3}{r_i^3} - y_2\left(\beta_{1m}\right)\right]\right)^2$$

$$A'^{-1}_{1m} = \frac{r_i^3}{2\beta_{1m}^2}[\left(\frac{\beta_{1m}^2 r_o^2}{r_i^2} - 2\right)\left(j_1\left(\frac{\beta_{1m} r_o}{r_i}\right) y_1\left(\beta_{1m}\right)' - y_1\left(\frac{\beta_{1m} r_o}{r_i}\right) j_1\left(\beta_{1m}\right)'\right)^2 - \left(\beta_{1m}^2 - 2\right)\left(j_1\left(\beta_{1m}\right) y_1\left(\beta_{1m}\right)' - y_1\left(\beta_{1m}\right) j_1\left(\beta_{1m}\right)'\right)^2]$$

Mean-squared phase change:

$$< \phi^2 >= \gamma^2 g^2 \left[\int_0^\delta dt \int_0^\delta dt' - 2\int_0^\delta dt \int_\Delta^{\Delta+\delta} dt' + \int_\Delta^{\Delta+\delta} dt \int_\Delta^{\Delta+\delta} dt' < r(t) r(t') >\right]$$

$$< \phi^2 >= 4\gamma^2 g^2 \frac{1}{\left(r_o^3 - r_i^3\right)} \sum_{m=1} A'_{1m} I[\frac{2D_{slow}\frac{\beta_{1m}^2}{r_i^2}\delta - 2 + 2e^{-\frac{\beta_{1m}^2}{r_i^2}D_{slow}\delta} + 2e^{-\frac{\beta_{1m}^2}{r_i^2}D_{slow}\Delta}}{D_{slow}^2 \frac{\beta_{1m}^4}{r_i^4}} - \frac{e^{-\frac{\beta_{1m}^2}{r_i^2}D_{slow}(\Delta+\delta)} - e^{-\frac{\beta_{1m}^2}{r_i^2}D_{slow}(\Delta-\delta)}}{D_{slow}^2 \frac{\beta_{1m}^4}{r_i^4}}] \quad (5.39)$$

Signal attenuation : $E_{slow} = \exp\left(- < \phi^2 > /2\right)$

The obtained signal attenuations are consistent with those found in [Grebenkov, 2008]. This new model was implemented in the PTK toolbox of the UNIRS lab of NeuroSpin and the roots β_{nk} were computed using the iterative algorithm [Sorolla et al., 2013]. This work has been presented ar the ISMRM Workshop on diffusion MRI as a probe of microstructure in 2013([Lebois et al., 2013b] and [Lebois et al., 2013c]). Next chapters will present how these models can be used to putatively explain the overestimation of smaller radii. We have presented here the two major frameworks using PGSE sequence to map axon diameters introducing the context of contributions of this thesis. We presented the second contribution of this work, the development of a novel two-pool model for the axon and cell modeling taking into account the biphasic behaviour of the water in the neural cells. We now move to the long time limit application of diffusion MRI using PGSE before introducing alternative diffusion sequences.

5.5.2.4 Long time limit : diffusive-diffraction experiments

For the case of a long Δ, the diffusion propagator doesn't depend on the initial starting positions of the spins and becomes equal to the spin density. The signal attenuation is then expressed as follows :

$$\boxed{E(q,\infty) = \int \rho(r_0)\exp(-i2\pi q r_0)dr_0 \int \rho(r_1)\exp(i2\pi q r_1)dr_1 = |S(q)|^2} \quad (5.40)$$

S being the Fourier Transform of the spin density : $S(q) = \int dr \rho(r)\exp(i2\pi q r)$ In the case of ordered and regularly packed cylindrical or spherical pores, the signal will exhibit a diffraction pattern, with several minima occuring, which can be directly used to extract

the characteristic length of the geometries. The typical geometries in tissue modeling are the parallel planes, the cylinder and the sphere. For these three geometries, the FT of the spin density is given in the following table :

Parallel planes separated by R	$S(q) = \frac{sin(\pi qR)\exp(i\pi qR)}{\pi qR}$
Cylinder (radius=R)	$S(q) = \frac{J_1(2\pi qR)}{\pi qR}$
Sphere (radius=R)	$S(q) = \frac{3[2\pi qR\cos(2\pi qR) - sin(2\pi qR)]}{(2\pi qR)^3}$

FIGURE 5.14: PGSE signal expression in long time limit for several geometries

From table 5.14, the minima will occur when $|S(q)|^2 = 0$: at q = n/R for parallel planes with n an integer. This pattern is of course very sensitive to the gradient direction and can be observable when the gradient is perpendicular to the main axis of the structure (for example, in the cylidner, perpendicular the main axis).. The diffraction pattern is shown in figure 5.15 for the case of diffusion between parallel planes at a distance of 2R (left) and in a sphere of radius R (right). The equation 5.14 underlines an important requirement for diffusion diffraction experiment : to infer a pore size R, we need $q \approx 1/R$. This means that the smaller the pore, the higher the required q value. The gradients strength are usually limited, in particular on clinical systems. Usually, a longer gradient duration is used but all the theory developed in the long time limit relies on the Short Gradient Pulse approximation. Using longer δ in the PGSE experiment will therefore lead to a violation of the SGP approximation, and the dips of the pattern will occur at even higher q value, decreasing the estimation accuracy (leading to an underestimation of the actual pore size). PGSE diffusive diffractions is also limited by the fact that in the presence of a distribution of diameters, the diffraction pattern won't be visible.

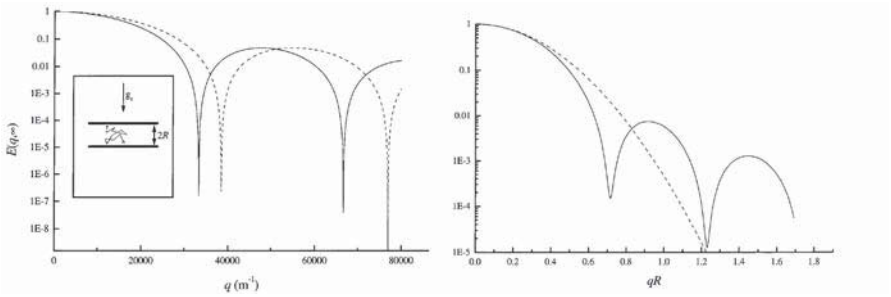

FIGURE 5.15: Diffraction pattern for parallel planes separated by a 2R distance (left) and in a sphere of radius R (right). Figures extracted from [Price, 1997]

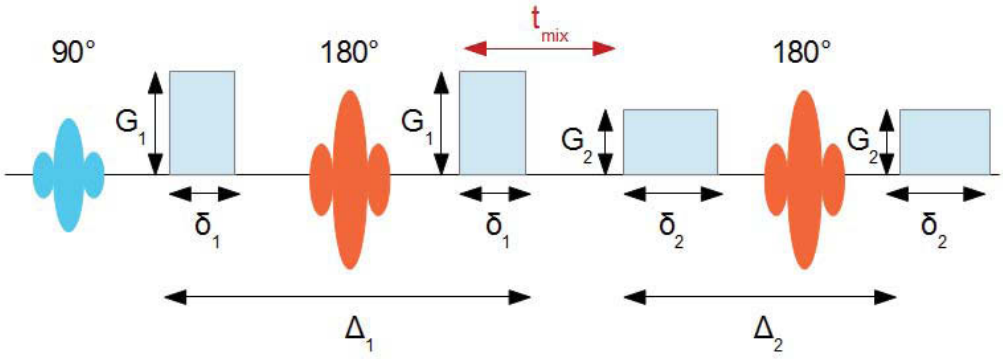

FIGURE 5.16: Double PGSE diagram

5.5.3 Diffusion MRI microscopy using double PGSE

The double PGSE, introduced by [Cory, 1990] is an alternative of the Pulse Gradient Spin Echo. The sequence diagram is exposed in Figure 5.16, characterized by two consecutives PGSE schemes with (G_1,Δ_1,δ_1) the parameters of the first PGSE scheme and (G_2, Δ_2, δ_2) the parameters of the second PGSE scheme. The two PGSE are separated by a mixing time t_m. The two pairs of gradients can be applied in different directions. More thant two PGSEs can be used, leading to multi-PGSE experiments. We focus here on double PGSE.

5.5.3.1 Extracting microstructure features from diffraction patterns

In 1995, [Mitra, 1995] investigated multi-PGSE experiments, showing the dependence of the signal on the angle between the two pairs of diffusion gradients, indicating a high sensitivity to microscopic anisotropy, even higher than PGSE [Özarslan, 2009]. This sequence allows to study the correlation of the net displacement of the spins, revealing information on the microstructure of tissues, especially in ordered configuration. As for PGSE experiments, the signal attenuation strongly depends on the different sequence parameters, in particular on the angle between the two gradient sets, the gradient duration and strength and the mixing time. Main applications of dPGSE use the conditions where the gradient duration $\delta \to 0$, $\Delta \to \infty$ and either the mixing time $t_{mixing} = 0$ or $t_{mixing} \to \infty$. The first kind of application is an extension of the diffusive diffraction experiment for a single PGSE. In [Özarslan and Basser, 2007], the diffraction patterns were studied for different numbers of PGSE-like experiments applied using the same gradient strength, the same separation duration and the same angle of application of the diffusion gradients. As for the single PGSE experiment, the signal in the case of long diffusion times can be expressed as a function of the FT of the spin density. For double PGSE experiment, the mixing time will introduce some differences :

- For $t_{mixing} \to \infty : E(q) = \|S(q)\|^4$
- For $t_{mixing} = 0 : E(q) = S(q)^2 S(-2q)$

From these equations, it appears that for a infinite mixing time, the pattern for the double PGSE experiment won't drastically differs from the one obtained with single PGSE, in fact the signal will be more attenuated with higher number of PGSE in comparison with single PGSE, but the minima will occur at the same places. But when null mixing time is used, the minima appear at half the q-value in comparison to the single PGSE diffaction pattern, allowing to reduce the required q values and therefore to probe small pore sizes. It has also been shown that for an even number of PGSE experiments, like for instance the double PGSE, the signal is less sensitive to the decrease of Δ and even if the mixing time is not strictly reduced to zero, the first lobes of the pattern are preserved. Finally, they are also preserved in the case of a broad distribution of the pore sizes, allowing to compute an average size. But, even if this approach leads to better results than using sPGSE diffusive diffraction, those experiments still require high q-values. This sequence is widely used in high q value domain, using the diffraction pattern to infer microstructure parameters thus limiting its use to preclinical MRI systems. If quasi-null mixing times is required to probe pore sizes, long mixing time can be used to reveal local anisotropy ([Callaghan and Komlosh, 2002]).

5.5.3.2 Signal angular dependency

Another approach is then to use the dependence of the attenuation on the angle between the two pairs of gradients. In [Shemesh et al., 2009], using the dependency at low q-value on the angle (previously described by [Mitra, 1995] between the two pair of gradients expressed in [Ozarslan and Basser, 2008], it is shown that for moderate q-value, the signal will exhibit a dependence on the angle. Choosing a pair of gradients applied perpendicularly to the pore and varying the angle between them can provide an estimation of the pore size and reveal the underlying anisotropy of the samples.

Application to white matter structure

Protocols including variation of the angle between the two gradients with null mixing times have been employed to map structural parameters. This sequence has been used to extract axon sizes in Zhou and Laidlaw [2011]. This study extends the AxCaliber framework to double PGSE experiments using the angular dependence of the signal, adapting the CHARMED model to double PGSE. It shows that using this angular dependence, axon diameter can be estimated in a limited scan duration, with limited

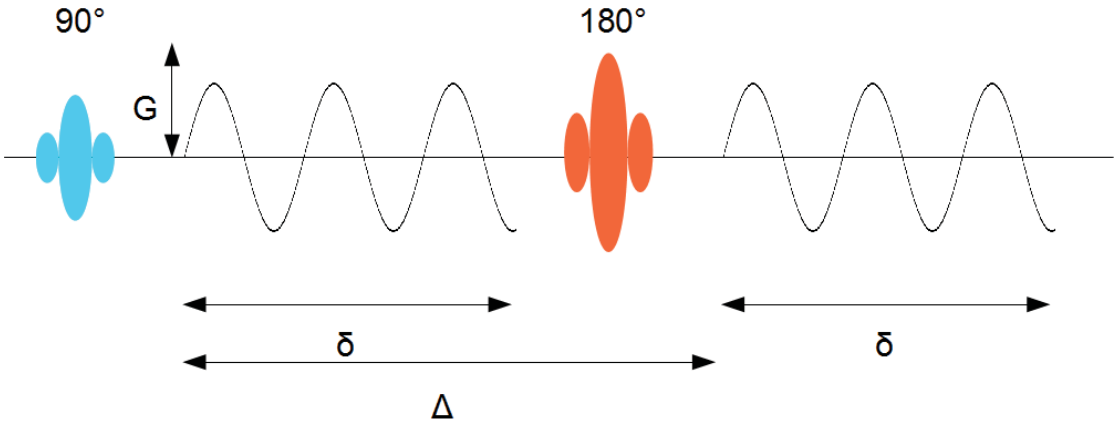

FIGURE 5.17: OGSE diagram

gradient strength (70mT/m). [Koch and Finsterbusch, 2011] also used double PGSE signal angular dependency to extract pore sizes along the corticospinal tract of human volunteers at 3T. [Komlosh et al., 2011] validated the ability of using double PGSE to infer pore sizes using a phantom made of capillaries.

5.5.4 Oscillating gradient sequences : OGSE and SW-OGSE

In PGSE and double PGSE experiment, the size of the pores we can extract is limited by the gradient strength and to probe very small pores, the gradient magnitude needs to be very high. To reach smaller diffusion times, the trapezoidal gradient waveform of the Pulse Gradient Spin Echo could be replaced by an oscillating gradient waveform : a sine, a cosine or oscillating trapezoids, the frequency of the waveform defining the diffusion time. This kind of sequence is depicted in 5.17. These sequences are commonly used on preclinical systems, since they require high gradient strength and gradient slewrate. Indeed, when the frequency is increased, the diffusion time reduces but one needs to have sufficient gradient strength to keep a high diffusion sensitivity. This sequence could be a way to be more sensitive to axon radii, in particular to smaller ones in axon calibration studies. OGSE sequences can be both used in temporal diffusion spectroscopy experiments or in replacement of PGSE in Q-space experiments. We describe these two applications in the following subsections.

5.5.4.1 OGSE and temporal diffusion spectroscopy

This kind of sequence allows to have a complete different approach, using the analysis of a diffusion spectrum. This application of diffusion is called temporal diffusion spectroscopy, different from the q-space approach. For this purpose, we define a frequency-dependent diffusion tensor $D(\omega)$.

$$D_{i,j} = \int_0^\infty dt' exp(i\omega t') < v_i(t')v_j(0) > \tag{5.41}$$

This is the Fourier transform of the autocorrelation of the particles' velocity (v_i). If the molecule moves in a restricted environment, the velocity will exhibit a correlation with itself, leading to a characteristic shape of the autocorrelation function and therefore of the frequency diffusion tensor. In the presence of a diffusion gradient g(t), the signal is given by :

$$S = S_0 exp(-\frac{1}{\pi}\int_0^\infty F(\omega)D(\omega)F(-\omega)d\omega) \tag{5.42}$$

with F the fourier transform of the time integral of the gradient. Thus, the OGSE allows to vary the gradient frequencies ω, sampling the frequency space and therefore providing the frequency diffusion tensor. [Gore et al., 2010] sums up the use of the OGSE in temporal diffusion spectroscopy to probe microstructure. In [Xu et al., 2009], the expression of OGSE signal is expressed for parallel planes, cylindrical array and a three-compartment model distinguishing the cytoplasm, the nucleus of the cell and the extracellular cell. The employed gradient waveforms were a cosine and sine profiles and several b-values and gradient frequencies were used to fit the simulated data in these structures. This study shows that it is possible to use OGSE to discriminate different tissues. Widely used on the rat brain, OGSE signal can also provide a surface to volume (S/V) ratio of the studied pores. By analyzing the behaviour of the diffusion coefficient in function of the diffusion time, in particular for the short and long diffusion time limits, the S/V ratio can be inferred as described in [Sen, 2004]. As explained in [Novikov and Kiselev, 2011], at very short diffusion time ($t << \frac{r^2}{D}$, with D the intrinsic diffusion coefficient and r the characteristing length of the pores), the molecules don't have the time to encounter the membranes of the tissue and the diffusion coefficient depends on the diffusion time in a linear way :

$$D(t) = D_0(1 - \frac{4S}{9\sqrt{\pi}V}\sqrt{D_0 t}), \tag{5.43}$$

where $D_0 = D(0)$. At very long diffusion times, all the molecules have already interacted with the membranes, and the diffusion coefficient is then linear linked to the frequency

of the gradient and to the inverse of the diffusion time :

$$D(\omega) = D_0(1 - C_d\frac{S}{V}\sqrt{\frac{D_0}{\omega}}), \tag{5.44}$$

where C_d is a factor depending on the sequence. Therefore, assuming for example that the tissue can be considered as random arrangement of flat, permeable and thin membranes (these conditions come from the very short diffusion time that is considered, the molecules cannot feel the "curvature" effect of the membrane) the ratio s/V can provide a useful information on average density of the membranes and average distance between them. But this analysis relies on very strong gradient strength to reach short enough diffusion time.

5.5.4.2 OGSE for cell calibration

The OGSE can be used in classical Q-space approach, instead of PGSE or double PGSE. GPD approximation can be used to express the signal attenuation using oscillating gradient. Only the temporal part of the signal expression will change, since the radial part contained in the diffusion propagator is not dependent on the used sequence. [Ianuş et al., 2013] lists the expression of signal for OGSE using the GPD approximation, especially for trapezoidal waveforms. In the case of restricted diffusion in a cylinder, the signal expression is given by :

$$S = \exp(-\frac{2\gamma^2}{D^2}\sum_{n=0}\frac{B_n}{\lambda_n^2}\Gamma_n), \tag{5.45}$$

with Γ_n depending on the used sequence. $B_n = \frac{2(R/\mu_n)^2}{\mu_n^2-1}$ with $\lambda_n = \frac{\mu_n^2}{R^2}$ and μ_n is the root of equation $J_1'(x) = 0$, J being the Bessel's function of order 1. For sine waveforms of frequency ω :

$$\Gamma_n = \frac{G^2\omega^2/(\lambda_n D)^2}{(1+\omega^2/(\lambda_n D)^2)^2}\times \\ (\frac{\lambda_n D\delta(\lambda_n^2D^2+\omega^2)}{2\omega^2} + 1 - \exp(-\lambda_n D\delta) - \exp(-\lambda_n D\Delta)(1 - cosh(\lambda_n D\delta)))) \tag{5.46}$$

For cosine waveforms of frequency ω:

$$\Gamma_n = \frac{G^2}{(1+\omega^2/(\lambda_n D)^2)^2}\times \\ (\frac{(\lambda_n^2D^2+\omega^2)}{\lambda_n D}(\delta/2 + \frac{sin(2\omega\delta)}{4\omega}) - 1 + \exp(-\lambda_n D\delta) + \exp(-\lambda_n D\Delta)(1 - cosh(\lambda_n D\delta)))) \tag{5.47}$$

Trapezoidal expression can be also derived, but results in a more complicated expression. [Siow et al., 2013] explored the differences between several sequences using the ActiveAx protocol to infer axon diameters in the corpus callosum. They compared the results of PGSE and OGSE sequences, showing that oscillating trapezoid gradient (SW-OGSE) gives a higher accuracy on the estimation. Moreover, in comparison with sine oscillations, trapezoidal waveforms allow to obtain higher diffusion sensitivity for short diffusion times, and then could be more sensitive to small diameters.

5.5.5 Beyond the PGSE : spin echo sequence diffusion weighted with arbitrary gradient waveforms (AGWSE)

We just described the common sequences used in diffusion MRI, starting from the PGSE. We saw that each of them presents drawbacks and advantages, and also that modifying the waveform of the diffusion gradients could help us to reach smaller diffusion times and thus smaller structures. But the requirement of high gradient strength and often long scan duration limits their applications in clinical routine. We cited above the work introduced in [Alexander, 2008], addressing this problem, proposing a framework optimizing PGSE sequence parameters to guarantee a limited variance of the estimates of the tissue model parameters (the CHARMED model). This technique showed great results in [Alexander et al., 2010] allowing to recover the axon diameter in the corpus callosum. Keeping the idea of optimization of the sequence, why not including the all waveform of the gradient in the optimization scheme ? This is the idea of Arbitrary Gradient Waveform Spin Echo (AGWSE). Since the waveform seems to have an impact of the accuracy of axon diameter estimation, optimizing it with respect the tissue model and hardware constraints could help to reach better estimation. This idea was developed by [Drobnjak et al., 2010], proposing to optimize the all gradient waveform, points by points, covering all kind of waveforms from the PGSE to the OGSE. In [Drobnjak and Alexander, 2011], the authors go even further, allowing to also varying the orientation at each time points. An example of these kind of waveforms are depicted in Figure 5.18.

The optimization follows exactly the framework of [Alexander, 2008]. Signal expression can be obtained using the matrix framework introduced in [Callaghan, 1997]. A simple matrix formalism is proposed to compute the expression of restricted diffusion signal for any kind of waveforms. In fact, the gradient are decomposed into several narrow pulses, separated by a time step τ. We recall that for the case of two narrow pulses separated by a 180∘ pulse, as it is the case for the SGP approximation of the PGSE, :

$$E(q) = \int\int \rho(r)P(r,r',\Delta)\exp(i2\pi qr)\exp(-i2\pi qr')drdr' \tag{5.48}$$

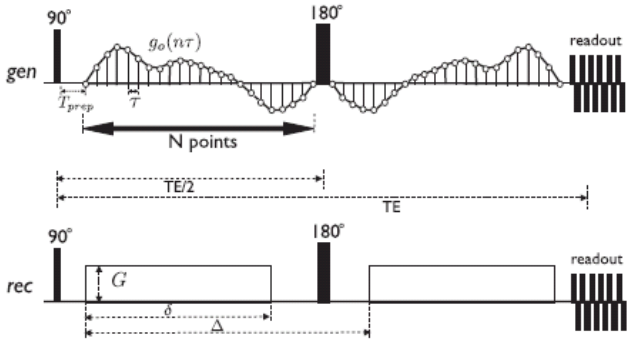

FIGURE 5.18: AGWSE diagram from [Drobnjak et al., 2010]

For a general gradient waveform decomposed into N narrow pulses, we have :

$$E(q) = \int dr_1 \int dr_2 ... \int dr_N \rho(r_1) \exp(i2\pi q_1 r_1) P(r_1, r_2, \tau) \exp(i2\pi q_2 r_2)$$
$$P(r_2, r_3, \tau) ... \exp(i2\pi q_{N-1} r_{N-1}) P(r_{N-1}, r_N, \tau) \exp(i2\pi q_N r_N) \quad (5.49)$$

With $q_n = m_n \gamma \delta g_{step}$, g_{step} being the unit of the gradient amplitude. m_n could be either positive or negative. Using the decomposition in eigenfunctions of the propagator, we can express (5.49) as a matrix product :

$$E = S(q) R[A(q)]^{m_1} ... R[A(q)]^{m_N} R\overline{S(q)} \quad (5.50)$$

with

$$S_k(q) = V^{-1/2} \int dr u_k(r) exp(i2\pi qr) \quad (5.51)$$
$$R_{kk} = \exp(-\lambda_k \tau) \quad (5.52)$$
$$A_{kk}(q) = \int dr u_k^*(r) u_{k'}(r) \exp(i2\pi qr) \quad (5.53)$$

with V the volume of the pore, and u_k the eigenfunctions of the propagator expansion. This matrix framework has been extended by [Drobnjak and Alexander, 2011] for varying gradient orientation. Experiments of [Drobnjak and Alexander, 2011] were focused on the study of the generated waveform for a cylinder model varying the a priori radii from $1\mu m$ to 5 μm and allowing different orientations of the gradients in the three directions. They tested it on simulated data. This study provides several insights : optimizing the direction of the gradients in the plane parallel to cylinder increase the accuracy of the estimation, confirming that the sampling of directions all over the sphere of the ActiveAx protocol could provide better results that in a single perpendicular direction as it is done in [Assaf et al., 2008]. Moreover it shows that the typical waveform obtained in

the perpendicular plane to the cylinder with a complete arbitrary waveform seems to approximate a trapezoidal oscillating gradient spin echo. The waveform oscillates between -G_{max} and G_{max} with variable frequency, frequency increasing while radius decreases. In [Siow et al., 2012], applications of the generalized gradient waveforms were applied for the estimation of pore size in a microstructure phantoms, made of capillaries with an unique radius per phantom. Optimized protocols using PGSE and AGWSE sequences were computed with different prior pore radii and for different gradient strengths. The measurements made perpendicularly to the phantoms on a 9.4T Varian scanner with a gradient of 1T.m^{-1} were then compared. This experiment shows that variance of estimates are reduced using the generalized waveforms in comparison to PGSE optimized protocol. The lower bound of radii we can estimate is reduced using AGWSE, being then around 2.5μm at 40mT/m. The AGWSE gives better estimates when the protocol is optimzed using the true value of the radius, but still provides good estimates for the other protocols. The following part will expose the contributions of this thesis on AGWSE sequences and its use to probe microstructure parameters.

5.5.5.1 Developpment and implementation of an AGSWE sequence in a clinical routine at 3 Teslas and 7 Teslas

AGWSE seems to be a promising way to probe microstructural parameters in clinical routine. For now, this kind of protocol have been used on preclinical scanners, proving their ability to provide information on microstructure. This thesis aims at characterizing the tissue microstructure of the human brain *in vivo*. This part of this work aims at setting the methodology to perfom axon calibration *in vivo*. To this purpose we developed a new diffusion gradient weighted sequence on the 3T and 7T clinical Siemens systems of NeuroSpin (VB17-IDEA Toolkit). The implementation on the 7T scanner is of great interest since this system provides higher SNR than the 3T scanner and the actual maximum gradient strength of the 7T is 80mT/m. With this new sequence, any kind of waveform can be played, from the usual PGSE sequence to the OGSE and to the fully arbitrary sequences, respecting the gradient slewrate and maximum strength of the systems (see Figure 5.19). The use only need to provide a file describing the waveform indicating first the number of time points followed by the profile of the gradient waveforms on each axis. Since this sequence was developed to perform axon calibration, this file can contain the gradient waveforms for several profiles. The other parameter of the sequence can be tuned in a panel dedicated to this special sequence in the Siemens interface (see Figure 5.20). From this panel it is possible to select the kind of wanted sequence: a simple Spin-Echo, a PGSE (it is then possible to directly set *delta*, *Delta* and G_{max} on the panel) or an AGWSE. In this last case, it is possible to set

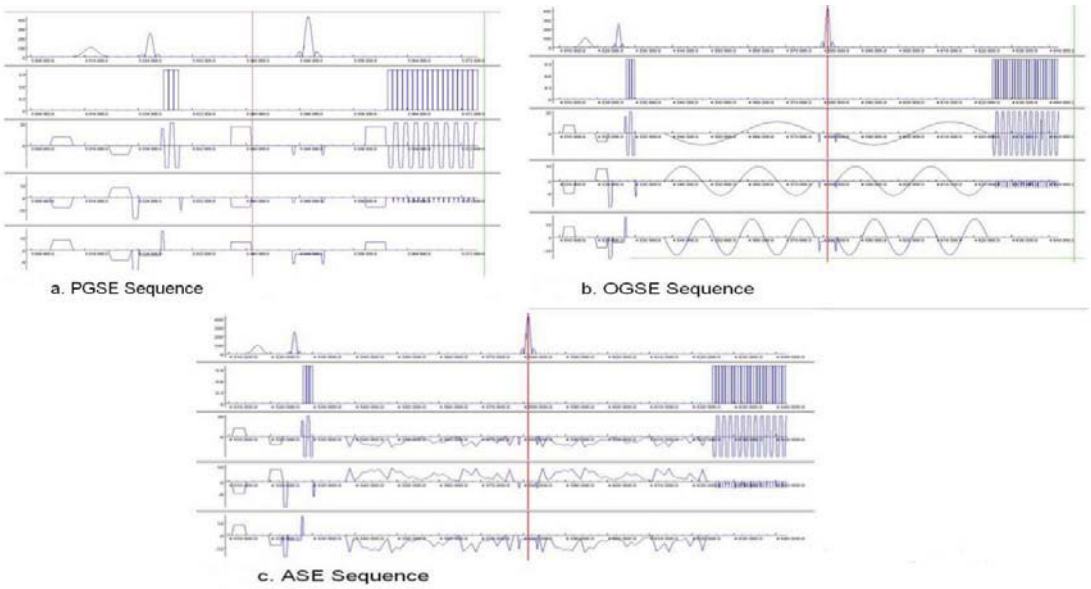

FIGURE 5.19: PGSE, OGSE and totally arbitrary gradient waveform from the AGWSE sequence

the gradient amplitude along the three axis, to define the time duration between each time point of the waveform, the number of desired T2-weighted images to acquired, the orientation count (the corresponding orientations are then extracted from a file where optimized diffusion orientations are stored). It is also possible to specify if the sequence is a sine, cosine or trapezoidal Oscillating Gradient Spin Echo. This allows to define only the gradient frequency instead of the whole waveform. Finally, it possible to segment the aquisition of the different orientations in blocks in order to decrease the scan time of each individual scan. The profile counter button allows to select the wanter profile if several profiles were described in the waveform file.

Figure 5.22 shows the validation of our sequence on the fiberCup phantom ([Poupon et al., 2008], [Fillard et al., 2011])using a totally arbitrary gradient waveform (sequence c) in 5.19 on the 3T clinical MR system of NeuroSpin. The fiberCup phantom has been developed to the study and the validation of HARDI models. This phantom is made of acrylic fibers with a diameter d=17μm. Fibers were disposed in bundles following the scheme (Figure 5.21) in order to mimick different configurations and crossings of the fiber bundles of the human brain. The finaly density of fibers was 1900 fibers/mm^2. The container was filled using pure distilled water. We compared the RGB maps and ODF fields obtained from a standard PGSE sequence and with the totally arbitrary gradient waveform for a common b-value = $480 s/mm^2$. For both protocols, FOV=240mm, TH=10mm, Matrix = 128x128, PF=6/8, TR = 4s. For the PGSE protocol, δ=25ms and Δ =35ms, TE = 84ms and $G_{max} = 20mT/m$. For the AGWSE protocol, the gradient duration was 49ms, TE = 110ms and $G_{max} = 22mT/m$. The signal was measured along 10 optimized directions. Figures 5.22 and 5.23 show the results on the fiberCup

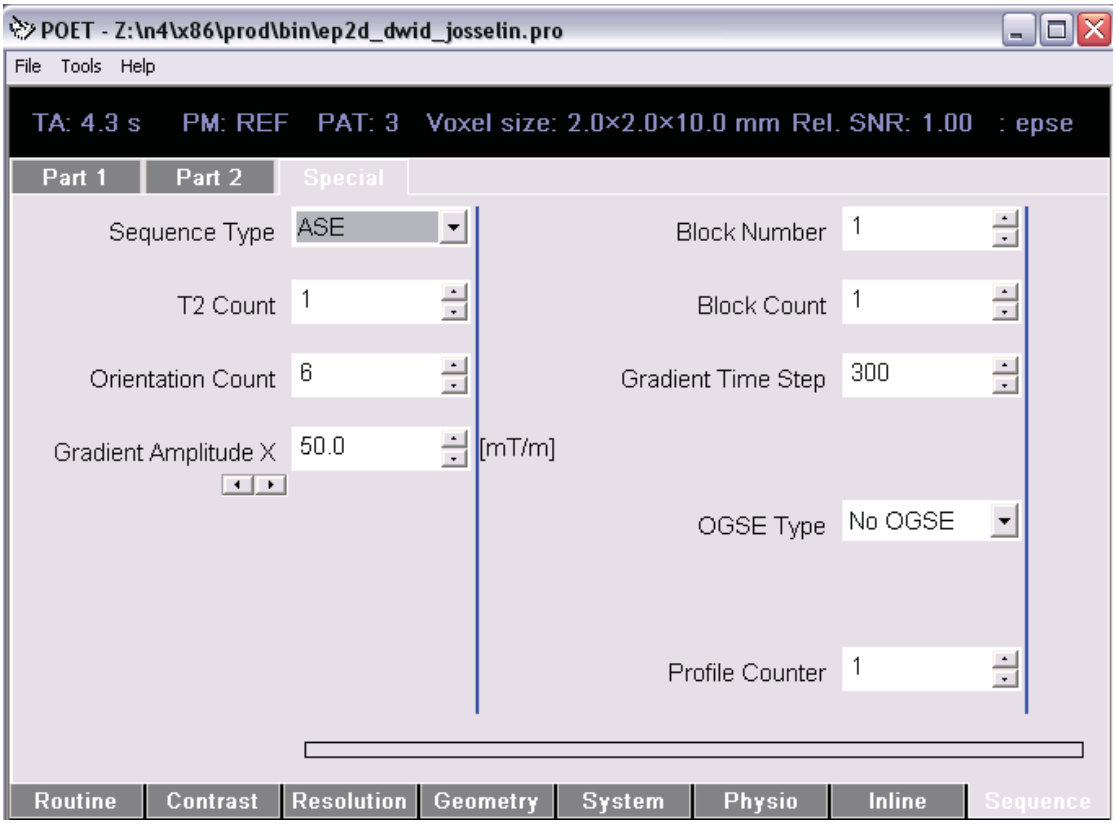

FIGURE 5.20: Panel dedicated to our novel diffusion sequence. For an AGWSE sequence, it is possible to set the time duration between each time point, the maximum gradient strength along each axis, the number of T2-weighted images, the number of diffusion orientations, the number of profiles, the number of orientation blocks and finally the kind of sequence

phantom, showing the RGB and GFA maps as well as ODF fields computed from a Q-ball local model. This experiment shows that this novel sequence with arbitrary gradient waveform is valid and provides angular information stemming from the anisotropy of the diffusion process. The comparison between the PGSE and AGWSE sequence in figure 5.23 depicts the ODF fields obtained in both cases, showing that the arbitrary gradient waveform allows to reconstruct accurate ODF fields. We also performed the first clinical test of AGWSE on a human subject, using the same arbitrary sequence. The parameters of the sequence was FOV=256mm, TH=2mm, matrix = 128x128, Partial Fourier = 6/8, TR=4s, TE=110ms. Figure 5.24 shows the obtained RGB map and ODF fields. This first experiment of arbitrary gradient waveform on an healthy subject shows again the validity of the sequence and the possibility to use it to be more sensitive to microstructural features. This novel sequence has been presented at the ESMRMB 2012 conference ([Lebois et al., 2012]). The idea is first to test ActiveAx-like protocols, using several PGSE profiles and after to compare with optimized AGWSE sequence on human volunteers (see next chapter).

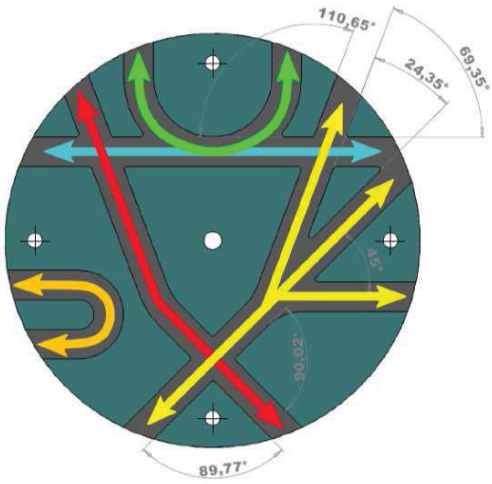

FIGURE 5.21: FiberCup phantom. Fiber pathways are highlighted in colors. Arrows indicate the directions of the synthetic fiber bundles.

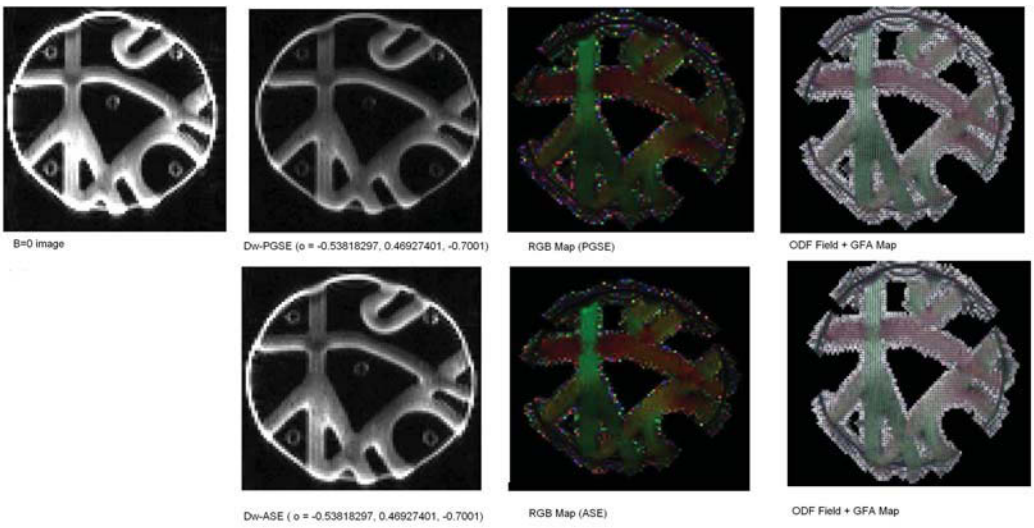

FIGURE 5.22: AGWSE tests at 3T on the fibercup phantom : comparison between the PGSE and the AGWSE protocol

5.6 Conclusion of this chapter

We have described how diffusion MRI can be used, through tissue modeling to obtain micrsotructural information. Diffusion MRI microscopy allows to go further in comparison to model such as DTI or QBall, giving not only angular but also radial information locally. Several models of white and grey matter have been derived, often based on simple geometries such as cylinders and spheres, for which it is relatively simple to derive the diffusion propagator. Differences between the approach differs from the different compartments that are considered and the exchange between them. We also listed the

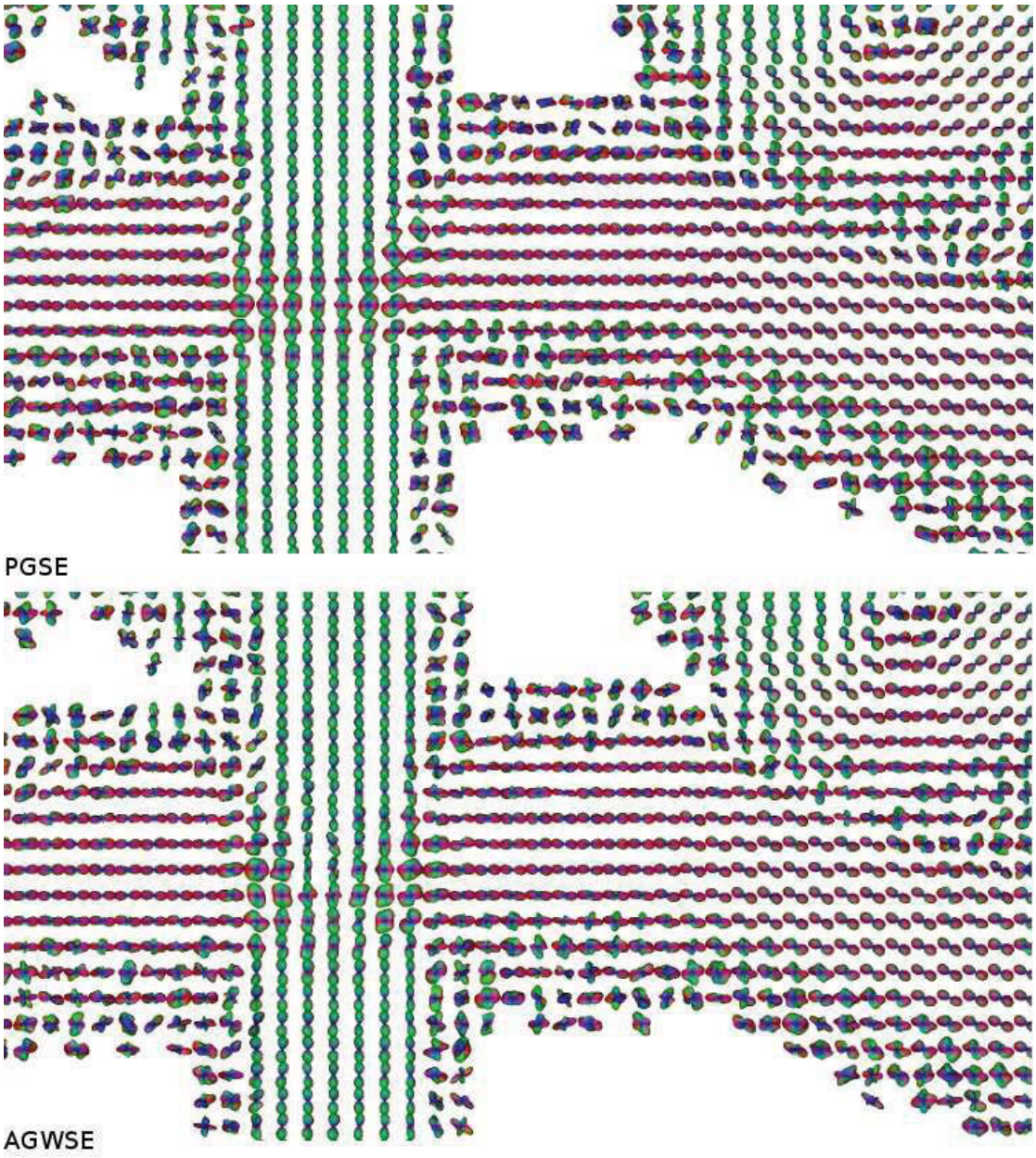

FIGURE 5.23: AGWSE tests at 3T on the fibercup phantom : zoom on the odf field

different sequences that are used in diffusion MRI microscopy, each of them providing useful insights on microstructure of the tissue. A part of the community focused on the necessity to perform these kind of experiments on human subjects. But clinical experiments are constraining, imposing a limited scan duration, hardware and safety constraints. The challenge is to obtain the best estimates of microstructure parameters taking into account those constraints. The Active Imaging, represented by the ActiveAx protocols have shown, optimizing the acquisition schemes, to be able to provide contrast based on microstructure in clinical routine. A new kind of sequence, with arbitrary gradient waveform allows to obtain even more accurate estimation of parameters and

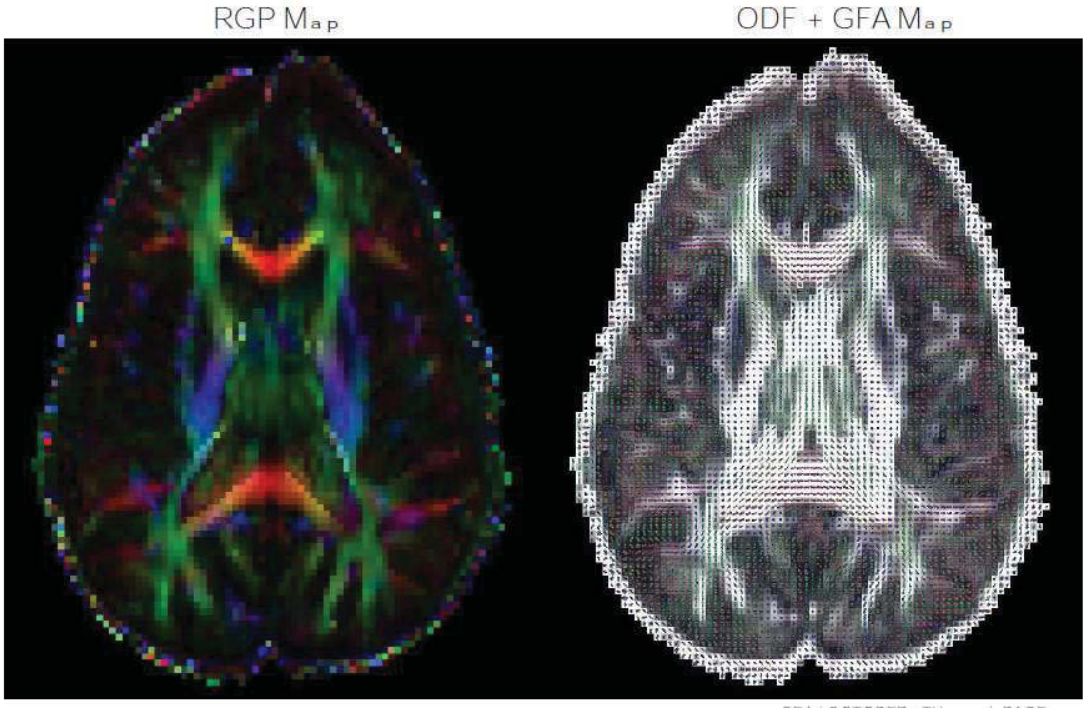

FIGURE 5.24: AGWSE tests at 3T on a human subject : RGB map and ODF fields

reduces the minimal radius that can be estimated. This kind of sequence could provide additional degree of freedom in comparison with PGSE or OGSE, allowing to be more sensitive to the microstructure. The contributions of this thesis on this topic is two-fold : we have implemented AGWSE sequences to perform the first human *in vivo* experiments on a 3T and 7T Siemens scanners and we also propose a new model for axon and cell, including a layer around the membrane with lower diffusivity than the core water. Next chapter presents the experiments performed on the 7T scanner on a dozen of human subjects to map the axon radii of their corpus callosum and we will demonstrate how the two-pool model can help to reduce the overestimation of the smaller radii.

Chapter 6

White Matter Microstructure Mapping

We previously exposed how diffusion MRI can be used to infer structural information at a resolution much higher than the image resolution, thus allowing to characterize the cytoarchitecture. Modeling the tissue and matching the diffusion signal to this model provides then parameters such as cell sizes or density. Diseases such as Alzheimer's, Parkinson's or Autism, are known to induce modifications of the tissue microstructure but that could only be revealed using dMRI by a drop in fractional anisotropy (FA), or an increased apparent diffusion coefficient (ADC), but for now it is difficult to know precisely what causes these differences from these tensor invariants. Diffusion microscopy tries to answer this question and to make the link between differences in non-specific parameters such as FA and differences in microstructure organization, that can be revealed by cell radii and density mapping for example. This task is difficult to achieve, in particular because of the limitations that clinical routine implies : limited scan duration, limited gradient strength, limited static field... But active imaging, represented by ActiveAx protocols, has shown that with a reduced set of diffusion experiments, it is possible to obtain good contrast in terms of cytoarchitectural parameters, providing an average axon radius and density in white matter, for example. These experiments have to use a tissue model describing the actual cytoarchitecture but remaining sufficiently simple to preserve a limited amount of required measurements. Few studies of brain microstructure mapping using ActiveAx protocols have been perfomed on 3T scanners with a maximum gradient strength of 60mT/m using four optimized PGSE measurements, sampling along 90 directions.

Our approach completes these previous works. Our study proposes to take advantage of high-field MRI, scanning the subjects on a 7T equipped with a 80mT/m gradient coil but

the actual achievable gradient strength was until now limited to 50mT/m (but this limitation will be raised in future work). We focused on the Corpus Callosum microstructure mapping, scanning 14 healthy subjects and extending the initial four measurements to ten along 60 directions. Higher number of measurements allows to improve complexity of the model of axons, including for example the two-pool model we presented in the previous section. We also scanned an healthy subject using the Arbitrary Gradient Waveform Spin Echo (AGWSE) sequence and we here propose to compare the results with PGSE experiments. Finally, the protocol was adapted and used to scan autistic patients and controls in the frame of a clinical study performed on the 3T scanner of the NeuroSpin center.

6.1 Mapping the white matter using the PGSE sequence

6.1.1 Methods

One of the major goal of this work is the construction of the first atlas of axon radii and density of the corpus callosum on a clinical 7T MRI system on healthy subjects.

6.1.1.1 MRI data acquisition

To this purpose, fourteen healthy subjects (3 females and 11 males between 23 and 45 years old) underwent the same protocol, composed of ten different PGSE profiles, along 60 directions on a Tim Trio 7T Siemens scanner, equipped with a 80mT/m gradient coil (but limited to 50mT/m) using a 32-channel head coil. The idea was to extend the initial ActiveAx protocol using a higher number of profiles (initially set to 4 profiles), in order to reduce the variability of the axon mean radius observed when using only 4 profiles by increasing the range of diffusion times and b-values, mase possible because of the increased SNR obtained at ultra high field. This choice was motivated by a previous work [Duclap et al., 2013a] aiming at building an atlas of the axon radii, white matter fraction and orientation dispersion along major white matter bundles, including the corpus callosum for 10 subjects of the Archi database. This former work was performed on a 3T Philips Achieva MRI system, equipped with a 80mT/m gradient (but the maximum gradient strength was actually limited to 60mT/m), using 4 PGSE shells along 60 directions. This study provided profiles along white matter bundles such as the corticospinal, arcuate and corpus callosum tracts using the CHARMED model including orientation dispersion modeling. Interesting information were extracted, in particular in orientation dispersion along the different bundles but some limitations arose on the reproducibility of the axon diameter parameter, in particular in the corpus callosum.

For this reason and since our scanner couldn't deliver higher gradient strength than 50mT/m at the time of the scans, we considered to increase the number of shells. This protocol respects the time constraint of a clinical application : the scan duration remains limited to 1h20. Our protocol is therefore a mixture of ActiveAx and AxCaliber protocol : the number of profiles is limited in order to be applied in clinical conditions, and we sample not only along the direction perpendicular to the axons, but along 60 optimized diffusion directions (plus three b=0 s/mm^2 images). 24 slices were acquired centered on the corpus callosum. For each profile, the acquisition was divided into three blocks of 20 directions to limit individual scans to a few minutes thus improving the subject comfort. The sequences parameters were : TR = 5.2s, TE = 95 ms, FOV = 256mm, TH=2mm, Matrix = 128x128, Gmax=50mT/m, SlewRate = 333T/m/s. The different profiles are plotted in the figure 6.1. They allow to cover a range of diffusion times from 19ms to 61ms. This protocol also covers a range of b-value from 700 s/mm^2 to 6000 s/mm^2. Varying the diffusion times increases the sensitivity to cell populations of different sizes. Comparison between the protocol used in [Duclap et al., 2013a] and our protocol is described in table 6.2.It also important to have low and high b-value to better distinguish the restricted from the hindered compartments.

6.1.1.2 White matter model

The model we used in this part was the CHARMED model. We delibarately kept the model simple, to further investigate the new two-pool in the subsequent section. The signal attenuation is therefore assumed to follow equation 6.1.

$$E = f_r E_r + f_h E_h + f_i E_i \tag{6.1}$$

The restricted part E_r is expressed following the equation (5.24). The hindered part follows (5.22) and an additional isotropic part was added to deal with partial volume effect with CSF. f_r, f_h and f_i are the respective volume fractions of the compartments. The model parameters were consequently: the perpendicular diffusivity corresponding to the diffusivity perpendicular to the axons in the Diffusion Tensor Model($D_\perp$), the parallel diffusivity, corresponding to the diffusivity parallel to the axons($D_\parallel$), the main direction of the fibers ($\mathbf{n}$), the radius (r), the signal without diffusion (S_0), the restricted fraction (f_r) and the isotropic volume fraction (f_i).

6.1.1.3 Axon Calibration Algorithm

A toolbox was developped in the PTK toolbox to perform axon calibration. The estimation follows the algorithm described in [Alexander et al., 2010].

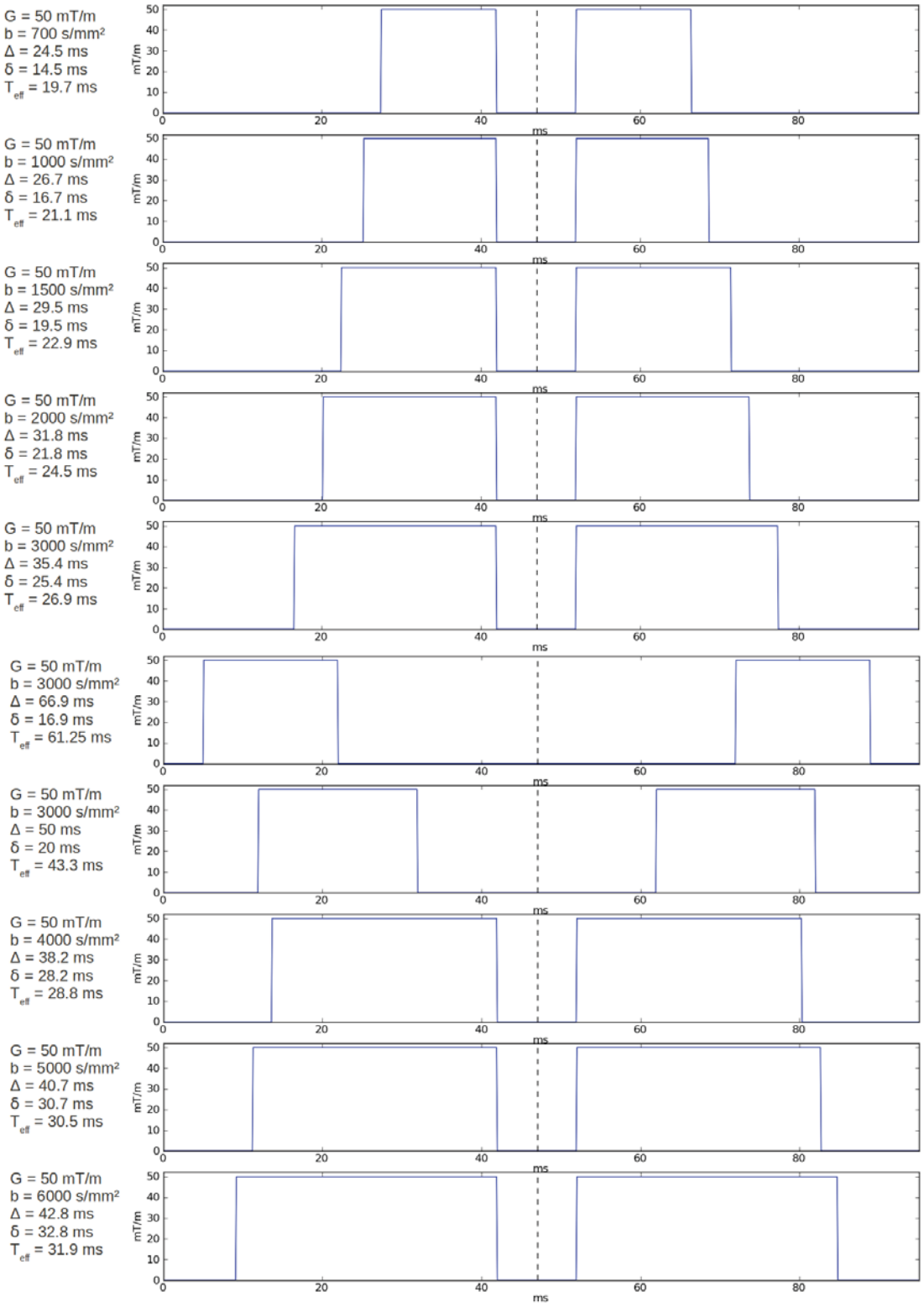

FIGURE 6.1: Diffusion PGSE protocol

Protocols	Protocol of [Duclap et al., 2013a]	Our protocol
Number of profiles	4	10
Orientation count	61	60
Diffusion time range	$74.5ms/81ms/74ms/18ms$	$19.7ms/21.1ms/22.9ms/24.5ms/26.9ms$ $28.8ms/30.5ms/31.9ms/43.3ms/61.3ms$
b-values	$2625s.mm^{-2}/858s.mm^{-2}$ $2710s.mm^{-2}/668s.mm^{-2}$	$700s.mm^{-2}/1000s.mm^{-2}/1500s.mm^{-2}$ $2000s.mm^{-2}/3000s.mm^{-2}(\times 3)$ $4000s.mm^{-2}/5000s.mm^{-2}/6000s.mm^{-2}$
Echo time	88.5ms	95ms
Magnetic field	3T	7T
G_{max}	70mT/m	50mT/m
Voxel size	2mm × 2mm × 3.9mm	2mm × 2mm × 2mm

FIGURE 6.2: Comparison between the protocol of [Duclap et al., 2013a] and our protocol

- We extracted DTI data for each profile of each subject
- We set the principal direction to the direction obtained from one of the profile at b= 3000 s/mm^2 (avoiding to deconvoluate but it could also be done using $b = 1500s/mm^2$). It will remain fixed during the optimization process.
- We set the intrinsic diffusivity of water to $1.7\times10^{-9}m^2/s$, the transverse diffusivity as follows $D_\perp = (1 - \frac{f_r}{f_r+f_h})D_\parallel$
- We set the initial value of the radius by default to $4\mu m$ and the initial S_0 to the average of the values extracted from the b=0 images.
- An Monte Carlo Markov Chain (MCMC, see Appendix B) optimizer, taking into account the Rician noise model was applied to obtain the posterior distributions of the non fixed parameters : S_0, the radius, the volume fractions of the compartment, the transverse diffusivity. 10000 burn-in steps were used as well as 100 samples with 1000 intervals. The authorized range of values for each parameter were : $0\mu m <$ radius $< 20\mu m$ and $0 < S_0 < 10000$. The volume fractions were forced to be between 0 and 1 and their sum equals to 1. The radial diffusivity was computed at each step : $D_\perp = (1 - \frac{f_r}{f_r+f_h})D_\parallel$ (corresponding to a tortuosity model).
- Each output parameter was chosen as the mean of the posterior distribution

6.1.1.4 Post-processing

First, the data were corrected for motion. This step is essential to guarantee a good match between the different profiles. All the images were registered to the images of the first block of the first profile using a 3D rigid transform. The diffusion orientations were

then also corrected using the rotation matrix of the transform. Second, we extracted the diffusion tensor for each profile in each voxel and the derived parameters : FA, ADC, $\lambda_{\parallel}$ and $\lambda_{\perp}$. This part provides the principal direction in each voxel and will allow to compare the diffusion parameters to the microstructure paramters. The DTI model can be assumed for the orientation detection as the corpus callosum is highly anisotropic and characterized by an unique direction. But it could have been infered from HARDI or HYDI more elaborated models, which is mandatory for more complex white matter bundles. In order to reduce the computation time, the corpus callosum was delineated in each volunteer using FA maps, and three slices were selected, one in the mid-sagittal plane, the two other on each side of the first one. The axon calibration algorithm was run on these three slices. We derived the fourteen maps of radii, white matter fraction and axon density computing following the relation : $\rho = \frac{f_r}{\pi r^2}$ (axon density index of [Alexander et al., 2010]). A profile was computed for each parameter of each subject projecting the values onto a centroid created from the skeleton of the mask. This centroid was splitted into sections every 2mm. Each point of the mask was then projected onto the nearest section of the centroid. Finally, average profiles of microstructure parameters were computed from the profiles of the fourteen subjects. We extracted the maximum number of sections over the profiles of each subject and redefined new profiles using this maximum number of sections in order to be able to compare and average them. This approach allows to observe the local variations of the parameters along the corpus callosum and to compare them with local variations of DTI-based parameters. The detailed steps of the data processing are depicted in Figure 6.3.

6.1.2 Results

6.1.2.1 Microstructure mapping

Figure 6.4 and 6.5 present the results on the midsagittal plane from the fitting procedure using the ten profiles on 14 healthy subjects. First column depicts the axon radii, the second column the white matter fraction and the third the axon density.

6.1.2.2 Average profile

Figure 6.6 shows the average profile computed from the 14 profiles of each subject of white matter fraction, radius and the derived axon density as well as the standard deviation across the subjects.

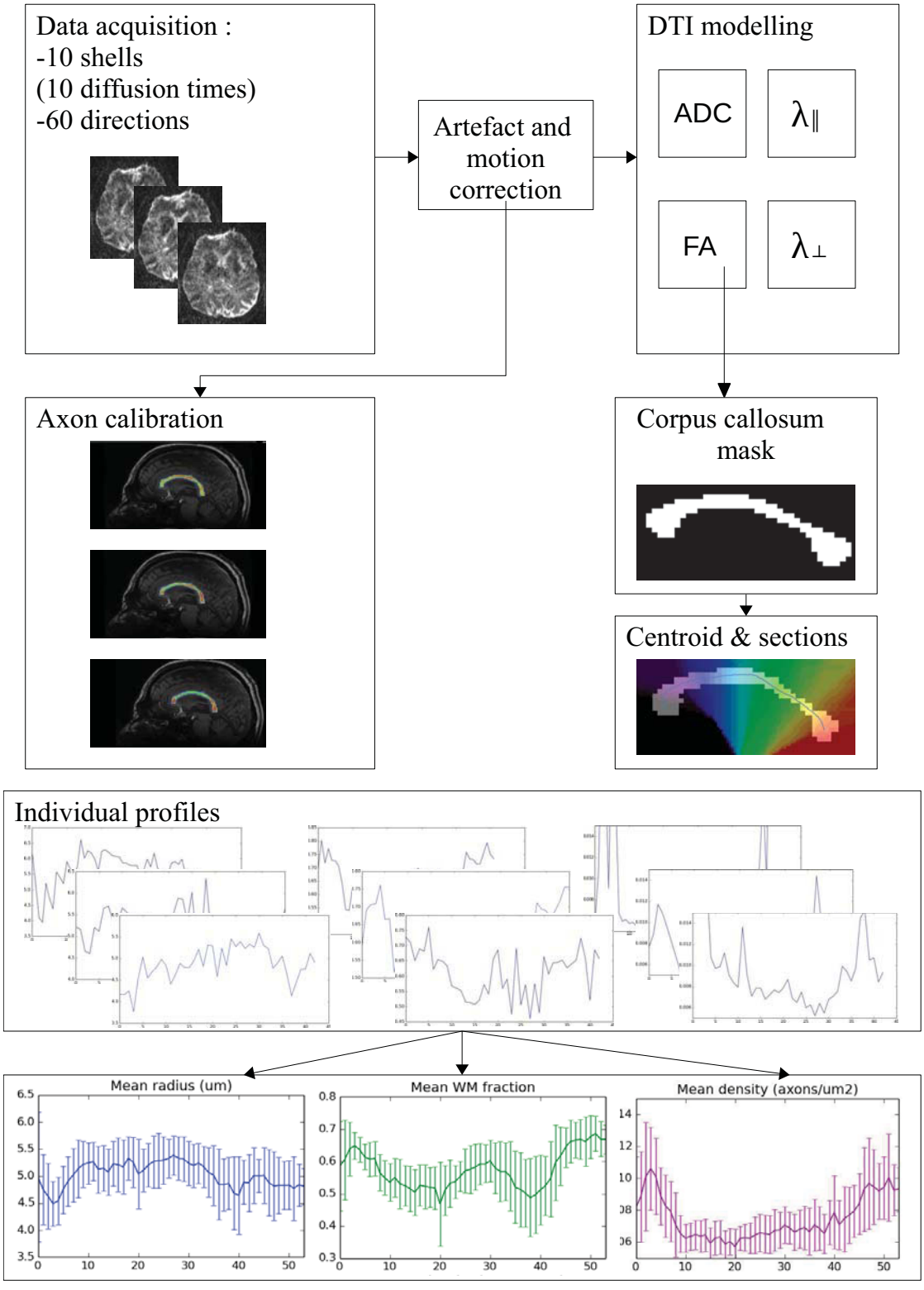

FIGURE 6.3: Processing steps from the data acquisition to the computation of the average profiles

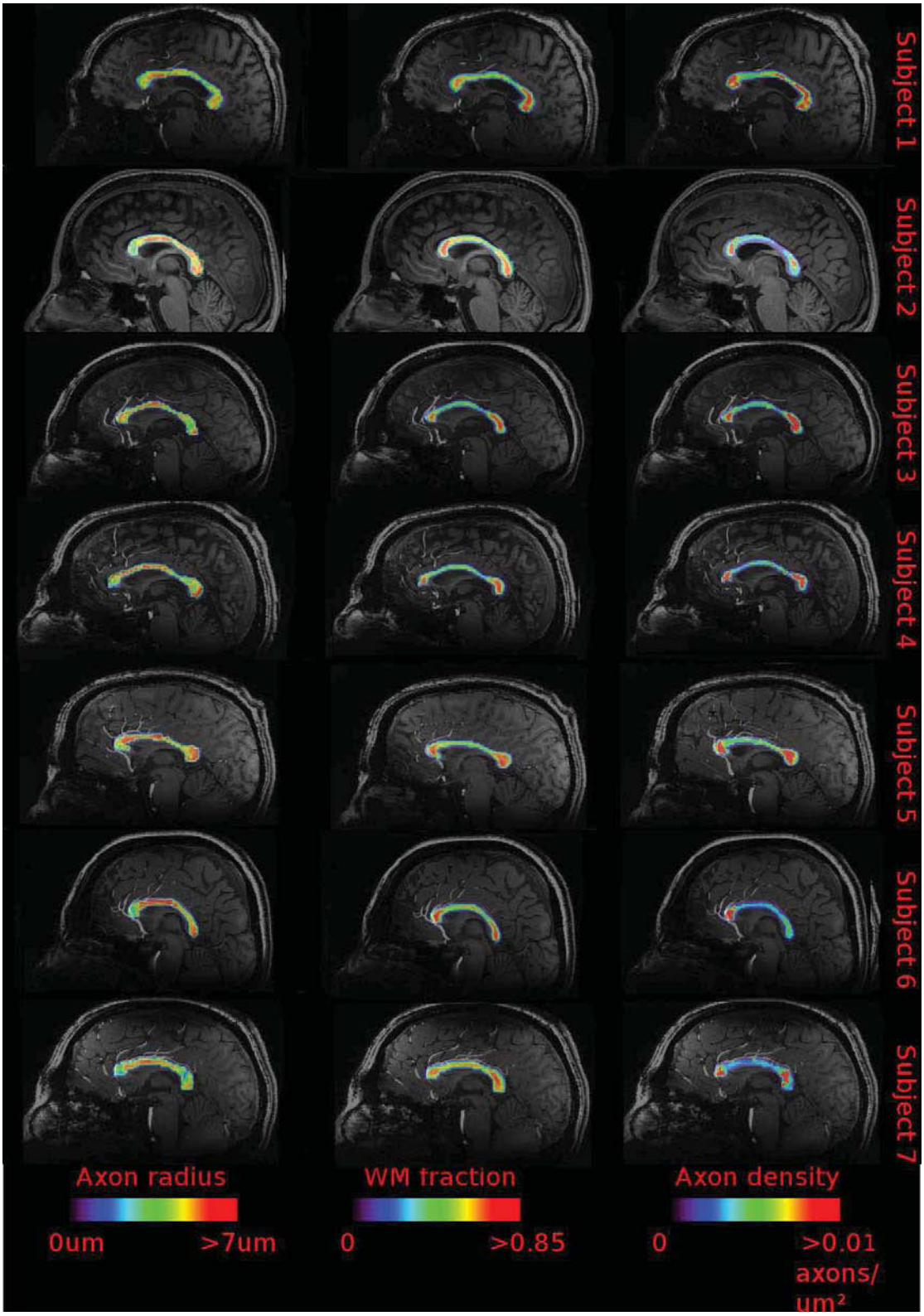

FIGURE 6.4: Individual axon calibration obtained on 7 of 14 healthy subjects using the protocol described in section 6.1.1.1 at 7T (50mT/m, SR=333mT/m) including 10 different diffusion times and b-values. On the right : axon radius maps, in the middle : white matter fraction, on the left : density index.

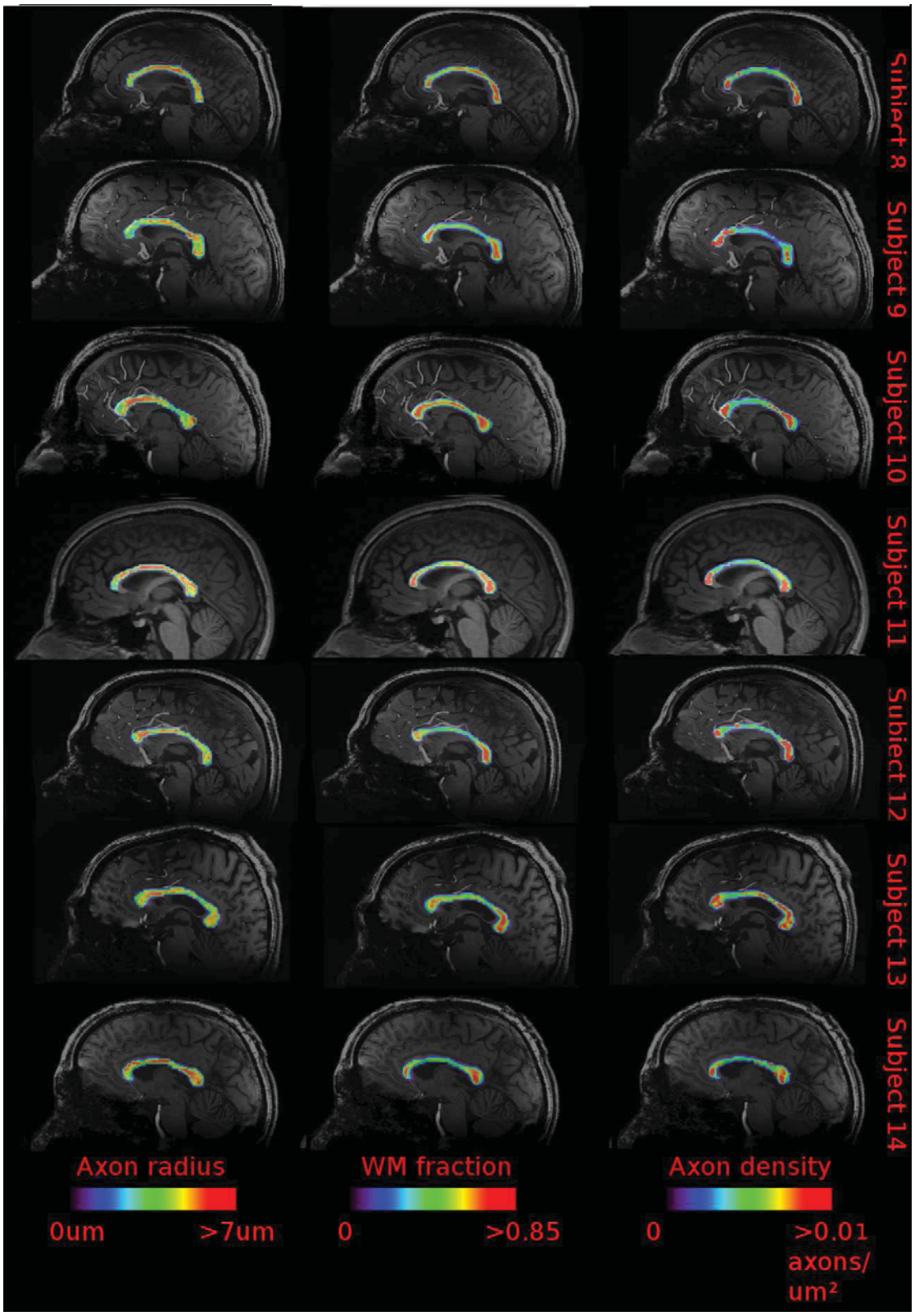

FIGURE 6.5: Individual axon calibration obtained on 7 of 14 healthy subjects using the protocol described in section 6.1.1.1 at 7T (50mT/m, SR=333mT/m) including 10 different diffusion times and b-values. On the right : axon radius maps, in the middle : white matter fraction, on the left : density index.

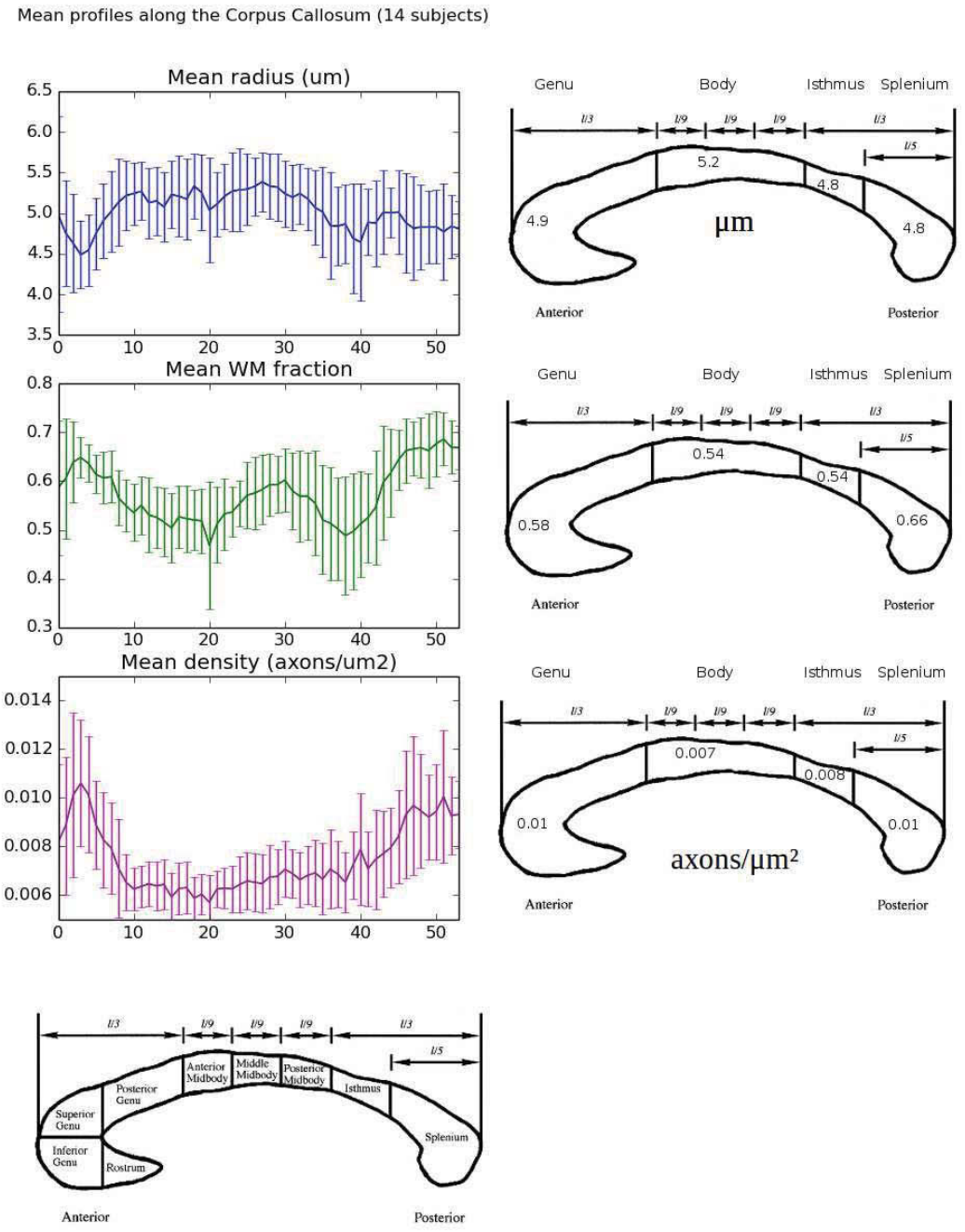

FIGURE 6.6: Average profile of white matter fraction and radius estimates and the derived axon density along the Corpus Callosum from 14 subjects

6.1.3 Discussion

6.1.3.1 Results versus histology

[Aboitiz et al., 1992] described the fiber composition of the corpus callosum using light microscopy. Small fiber diameters were found in a greater amount in the genu and the splenium while larger fiber diameters ($> 3\mu m$) are mainly found in the body. Moreover, the fiber density is higher on both genu and splenium regions than in the body. The authors explain the differences of density not only by the presence of large axon diameter but also by an increase of the extra-cellular volume (inter-fiber distance). Our results are thus in good agreement with histological data, since we observe a high-low-high density profile and a low-high-low average radius profile (consistent with previous *in vivo* studies : [Alexander et al., 2010],[McNab et al.]). The white matter fraction globally follows the trend of the density. These observations were mainly made on the midsagittal plane. The mean profiles confirm these observations but shows a local increase of the white matter fraction in the posterior body, just before the isthmus. It could be explained by the presence of larger axon radii in these regions.The obtained radii remain high in comparison with histological data, highlighting the overestimation already mentioned in the last chapter (probably stemming from the limited gradient strength combined to the simplicity of the model). This phenomenon of overestimation reduces the actual amplitudes between the genu, the body and the splenium.

6.1.3.2 Intra and Inter-subject variability

Figure 6.7 and 6.8 shows the standard deviation map of each posterior distribution of radius and white matter fraction estimates of one subject obtained from the MCMC procedure. The standard deviation of the radius is lower in the body region (around 0.3um for the axon radius) than at the extremities of the corpus callosum especially(around 0.8um), maybe explained by a higher angular dispersion on the extremities of the corpus callosum or the partial volume effect. The standard deviation of the white matter fraction doesn't change much along the corpus callosum (around 0.03 on average).

From figure 6.6, the inter-subject variability seems to be quite low, in particular for the radius parameter. This can be explained by the fact that with 10 profiles the MCMC procedure converges more easily to a global minima, but also that the 7T static field provides higher SNR, allowing to reduce the noise contamination of the measurement.

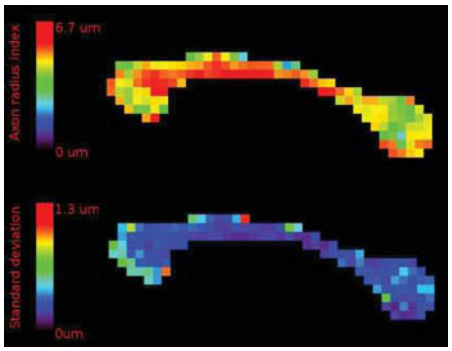

FIGURE 6.7: Standard deviations of the radius posterior distribution from the MCMC fitting on the mid-sagittal plane of one subject. Top : radius estimates, bottom: radius standard deviation

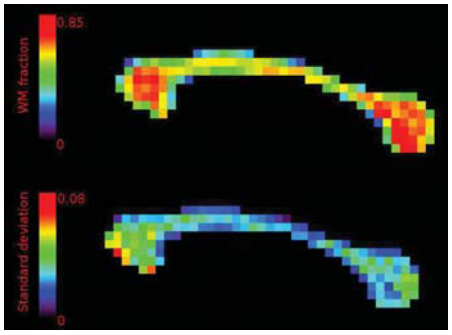

FIGURE 6.8: Standard deviations of the radius posterior distribution from the MCMC fitting on the mid-sagittal plane of one subject. Top : white matter fraction estimates, bottom: white matter fraction standard deviation

6.1.3.3 Stability of the results

We compared the results for one subject from different initializations of the axon radius with $R_{ini} = 2\mu m, 3\mu m, 4\mu m, 6\mu m$ and $8\mu m$ as well as the results using a white matter fraction initialization of $f = 0.5$. Figure 6.10 depicts the maps obtained from the different initial values. We observe that the MCMC procedure is not strongly affected by the initial value when initial radius is set in the range of $3 - 8\mu$m or $f = 0.5$, leading to a reasonable differences and a similar global pattern. The higher differences in radius estimates are located in the genu and the splenium, maybe coming from the limited sensitivity of our protocol to the smaller radii, inducing higher variability and therefore higher depedency on the initial values in these regions. But these differences are very limited (5 %). However, starting from a smaller value (2μm) shows more differences and a slight increase of the standard deviation of the estimates. The differences are however limited to 12% for the radius and 4% for the white matter fraction.

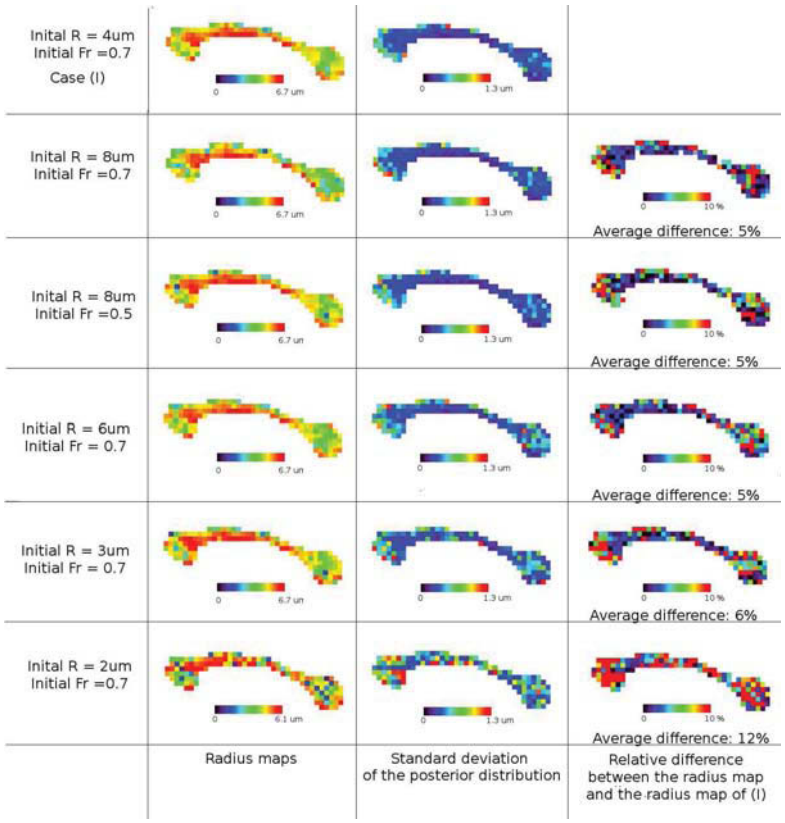

FIGURE 6.9: Comparison of the radius estimates with different initial values (on one subject)

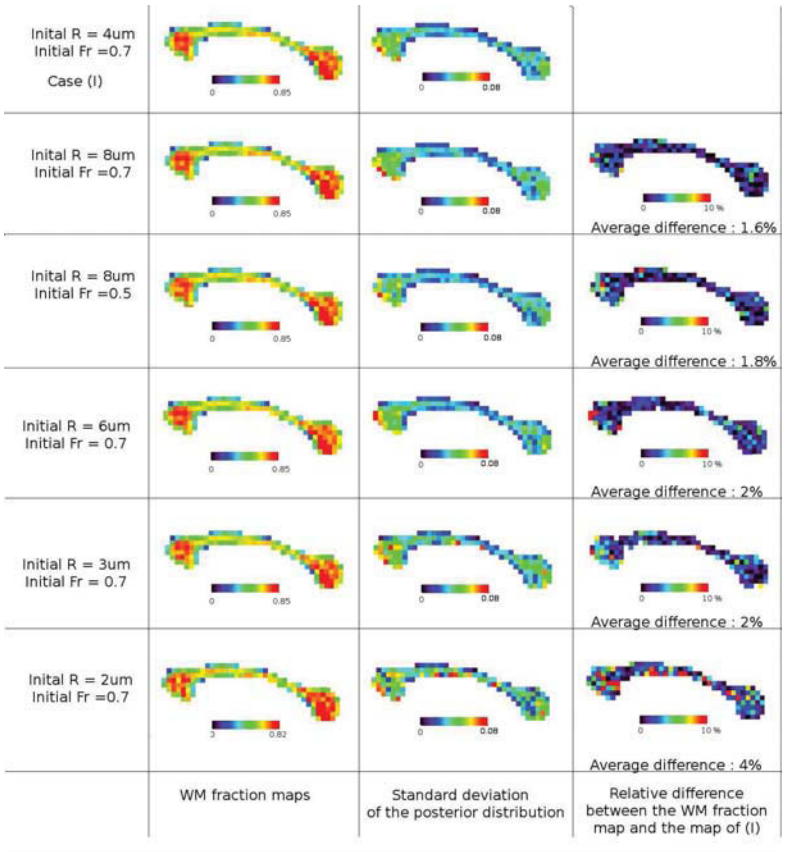

FIGURE 6.10: Comparison of the white matter fraction estimates with different initial values (on one subject)

6.1.3.4 Comparison with 4 profiles

Figures 6.11 and 6.12 show the comparison of the white matter and radius estimates using only 4 selected profiles using a mix of low and high-bvalue as well as short and long diffusion times : $\delta = 14.5ms/\Delta = 24.5ms/G = 50mT/m/bvalue = 700s/mm^2$, $\delta = 21ms/\Delta = 31ms/G = 50mT/m/bvalue = 2000s/mm^2$, $\delta = 16.9ms/\Delta = 66.9ms/G = 50mT/m/bvalue = 3000s/mm^2$, $\delta = 32.8ms/\Delta = 42.8ms/G = 50mT/m/bvalue = 6000s/mm^2$ against the results obtained from 10 profiles. As expected, the standard deviation of the MCMC posterior distributions is significantly reduced for both axon and white matter fraction estimates using 10 profiles. Moreover, using 10 profiles increases the contrast between the different regions, thus assessing the protocol we developped.

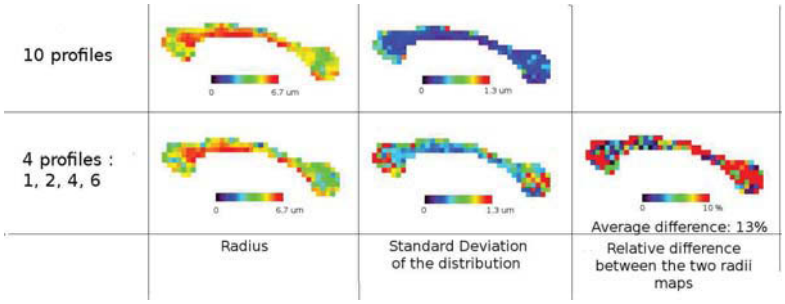

FIGURE 6.11: Comparison of the radius estimates using 4 and 10 PGSE profiles

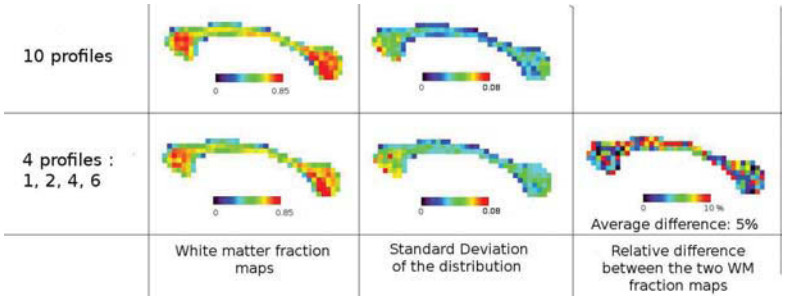

FIGURE 6.12: Comparison of the white matter fraction estimates using 4 and 10 PGSE profiles

6.1.3.5 Comparison with our previous study

Figure 6.13 shows the results extracted from our previous study [Duclap et al., 2013a] along the corpus callosum. This study provided profiles characterized by lower mean values of the radii (maybe due to the higher used gradient strength) but an increased standard deviation in both white matter fraction and radius profile in comparison with our results. Moreover, the profiles obtained from the 10 profiles protocol are more consistent with histological observations. These differences may come from the protocol differences but also from the highest SNR provided by the 7T.

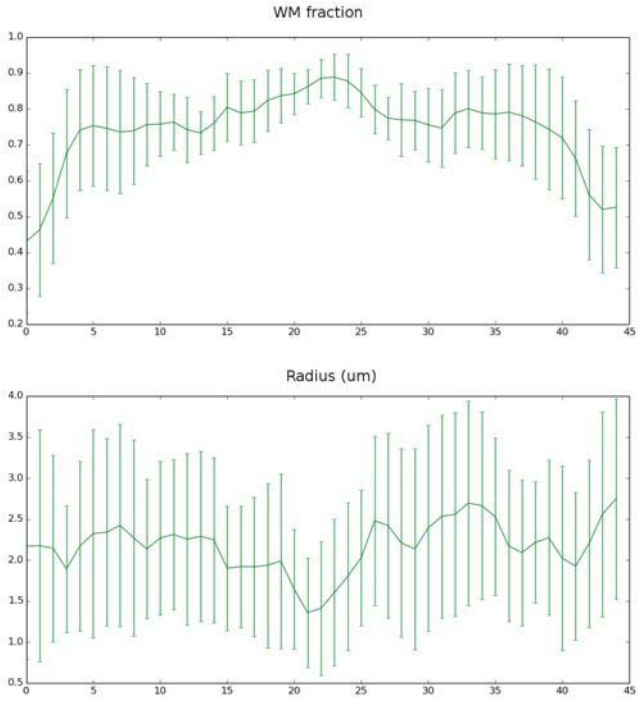

FIGURE 6.13: Wm fraction and radius profiles from the 10 subjects of the Archi database using the protocol of [Duclap et al., 2013a]

6.1.3.6 Correlations between microstructure parameters and dti parameters

Figure 6.14 shows the Pearson's correlation coefficient computed between microstructure parameters (radius, fraction and density) and DTI parameters (FA, ADC, $\lambda_{\parallel}$, $\lambda_{\perp}$). The correlation coefficients were computed from the combined values of all the sections of all the subjects, but restricting the analysis to the voxel presenting limited contamination from CSF (e.g. CSF fraction < 0.2). FA values show negative correlation with the radius (r=-0.4), white matter fraction (r=0.73) and density (r=0.61). In regions were radii are large, the radial diffusivity increases (the correlation between the radius and $D_{\perp}$ is r= 0.35), leading to a decrease of the anisotropy. Similarly, a high white matter fraction or density indicates more restriction effects (the water molecules are more constrained in the perpendicular direction), leading to a decrease of the perpendicular diffusivity (also indicated by the negative correlation coefficient between $D_{\perp}$ and the density or white matter fraction) inducing a higher global anisotropy. Axial diffusivity shows relatively poor correlations with the three parameters in comparison with the other correlation coefficient. Corresponding to the diffusivity along the fibers, it is not surprising that change in radius does not affect its values. However, white matter fraction and density seem to have greater negative correlations with it. This results may come from the increasing hindrance of the extra-cellular water molecules in regions with high axon

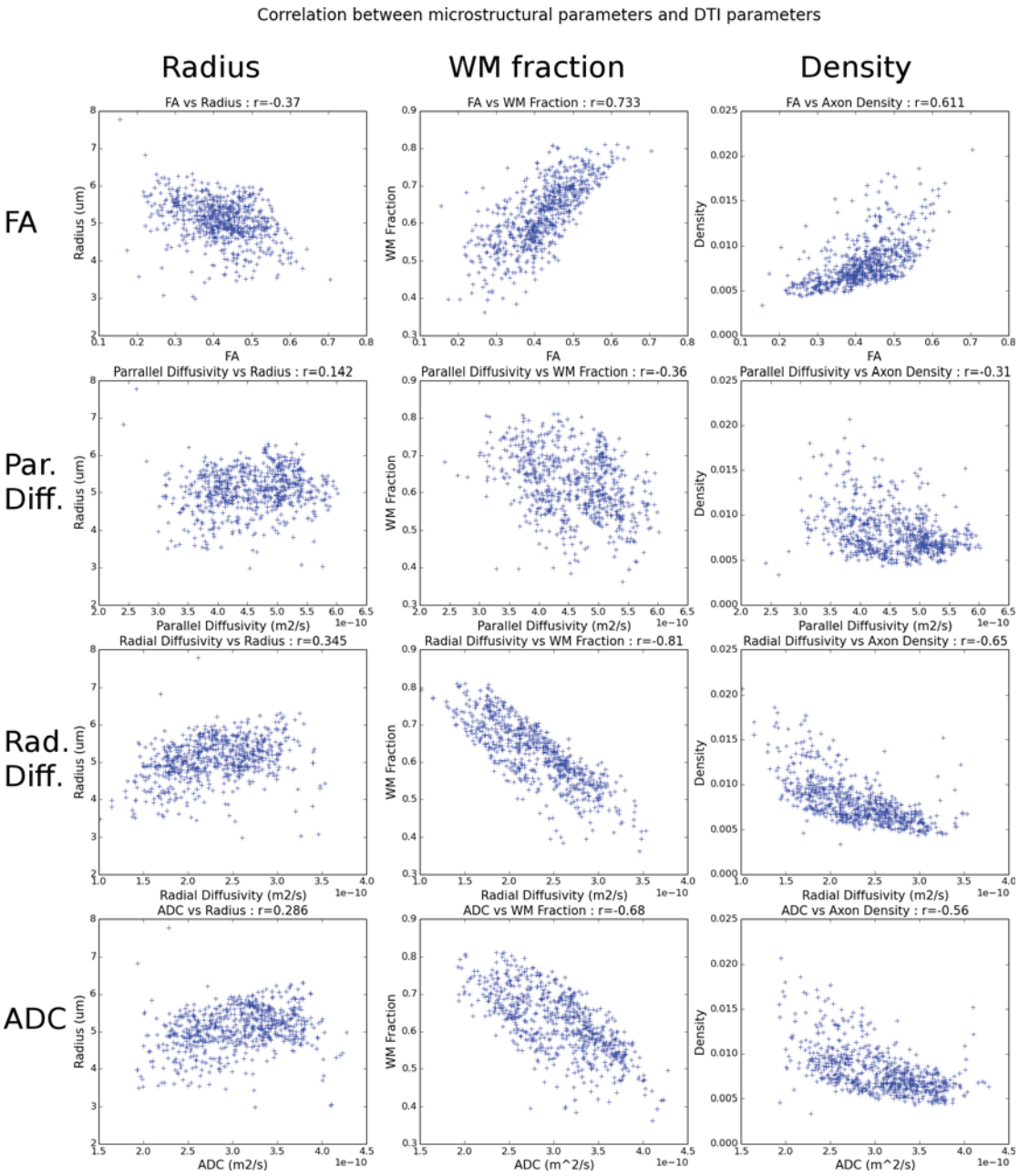

FIGURE 6.14: Correlations between microstructure parameters derived from the model and dti parameters (pvalue<0.05). First row : FA vs radius/WM fraction/ Axon density, second row : $\lambda_{\parallel}$ vs radius/WM fraction/ Axon density, third row : $\lambda_{\perp}$ vs radius/WM fraction/ Axon density, fourth row : *ADC* vs radius/WM fraction/ Axon density.

density, therefore reducing the axial diffusivity. It may also come from the limitations of the model (orientation dispersion of the fibers for example). Finally, ADC values show similar behaviour (for the same reasons) exhibiting a positive correlation with the radius and negative correlations with the white matter fraction and the axon density. Figure 6.15 shows the correlations between the microstructure parameters. Radius shows negative correlation with white matter fraction. It can be explained by the higher density

of the smallest radii in the corpus callosum, that could lead to a higher white matter volume fraction. This is confirmed by the strong correlation (r=-0.85) of the radius with the axon density (coming from the definition of the axon density, being inversely proportionnal to the squared radius). These correlations are similar that those found in

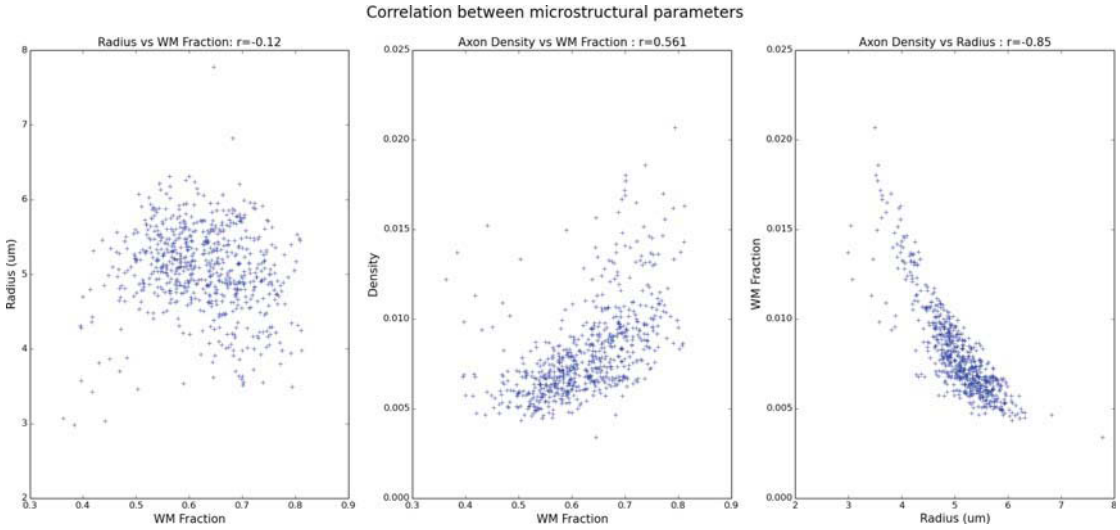

FIGURE 6.15: Correlations between microstructure parameters (pvalue<0.05).

previous works ([Alexander et al., 2010], [Barazany et al., 2009]) except the positive (but very small) correlation of the axial diffusion coefficient with the radius and the negative correlation of the axial diffusion coefficient with the white matter fraction and density.

6.1.3.7 Conclusion and discussion

We here demonstrated the feasibility of axon radii and density mapping of 14 healthy subjects at 7T. Our results are consistent with previous studies and histology. The inter and intra subject variability indicate a good reproducibility of the results, probably coming from the use of ultra high static field (7T). Nonetheless, the estimated axon radii shows an overestimation of the smaller radii we reported previously. First, the axon radius index is correlated with an averaged radius weighted by the cross-section area, therefore larger radii will contribute more to this value. We propose now to investigate the use of the two-pool model presented in the previous chapter to tackle this overestimation. To conclude, we have shown that *in vivo* axon calibration is feasible and increased gradient strength as well as increased SNR could help us to estimate microstructure features more accurately. We have established a new protocol including ten PGSE schemes, allowing a larger sampling of the diffusion time, and therefore opening the way to the study of more elaborated models of white matter to go beyond the CHARMED model, such as our two-pool cylinder model.

6.2 Theoretical study of the two-pool model to improve axon calibration

The previous section showed that increasing the SNR using a higher static magnetic field improves the reproducibility of the axon calibration and reduces the variability of the results. But we have shown that small radii are still overestimated. As we described before, the limited gradient strength is one of the reason of the limited access to small radii : smaller radii can be detected as "small" but cannot be distinguished. In this thesis, we presented a new model for the restricted part corresponding to the axons. We added a thin layer around the membrane of the axon, corresponding to a pool of water molecules with slower diffusivity than inside the axon, represented by a cylinder. We present a purely theoretical study of the behavior of the signal attenuation in clinical conditions ($\delta \approx \Delta$).

6.2.1 Single-pool vs the two-pool model

Assuming a PGSE experiment with $\delta = 29ms$ and $\Delta = 35ms$ leading to an effective diffusion time of $T_{diff} = 25ms$, the signal attenuation using the two-pool model with the assumed slow and fast diffusivity : $D_{slow} = 10^{-10}mm^2/s$ and $D_{fast} = 10^{-9}mm2/s$ ([Le Bihan, 2007]) was computed for 100 bvalues from 0 to 10000 s/mm^2 increasing the gradient strength from 0 to $80mT/m$ (corresponding to the achievable gradient strength on the advanced MRI systems). We computed the signal attenuation for three axon radii: R=1μm, R=2μm and R=3μm. We assumed that the signal is measured perpendicularly to the axons (like in AxCaliber studies). The signal was then fitted using this time a one-pool model. Figures 6.16, 6.17 and 6.18 shows the signal attenuation with respect to the b-value for the three chosen radii. First column depicts the attenuation obtained using a two-pool model, second column the attenuation obtained using a single pool model fitting (where the diffusivity is equal to D_{fast} the two-pool attenuation and the third column shows the surimposed signal attenuations. For small radii, here R=1μm and R=2μm the signal attenuation coming from a two-pool cylinder model with a thin layer (e.g. $100nm$) can perfectly match the signal attenuation using a single-pool model, but with a larger radius. For example, for an axon radius equals to 1μm and a layer thickness of 100nm, the single-pool model estimates the radius to be 1.69μm and for an axon radius equals to 2μm, the radius is estimated at 2.28μm. This overestimation disappears with larger radii and for 3μm, the difference becomes negligible.

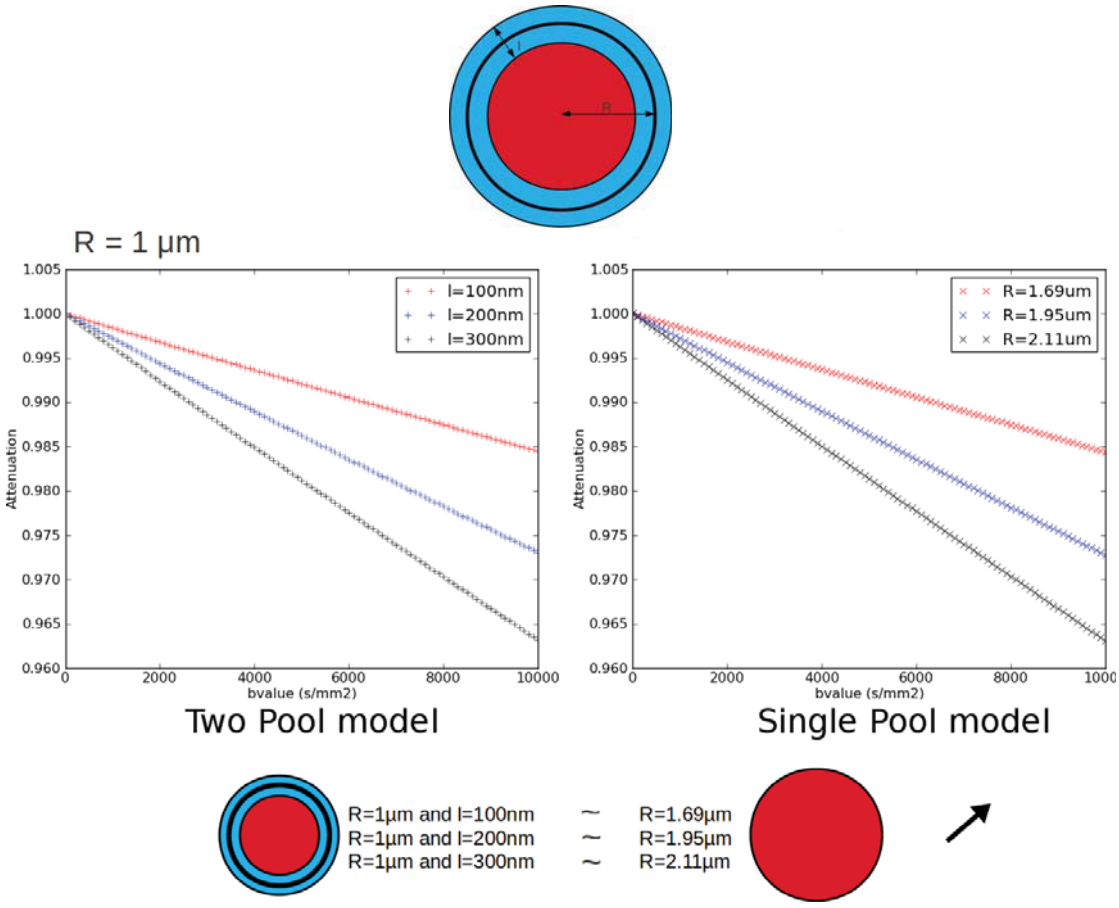

FIGURE 6.16: Signal attenuation for an axon of radius of 1μm; Left: using the two-pool model and right: using the simple cylinder model

6.2.2 Origin of the overestimation

For small radii, a layer of 100nm corresponds to a significant fraction of the restricted compartment. The attenuation in the layer is the combination of the attenuation along the radial coordinates and along the angular coordinates. For thin layers (see [Grebenkov, 2008]), the attenuation is mainly driven by the attenuation along the boundaries, assimilated thefore to diffusion in the interval [0, π L], L being the outer radius of the cylinder (see Figure 6.19). Since the diffusion coefficient is lower in the layer, the motion of the molecules is less constrained than in the core cylinder, where the diffusion coefficient is ten times higher. Therefore, the signal is more attenuated in the layer than inside the cylinder (along the boundaries, the mean-squared displacement corresponding to the slow diffusivity (L_{slow}=1.6×10^{-6}μm) is inferior to the perimeter, while inside the cylinder the mean squared displacement corresponding to the fast diffusivity (L_{fast}=5×10^{-6}μm) is lower than the inner radius). The combination of both of the compartments therefore corresponding to a simple cylinder with larger radius. For larger axon radii, the signal in the layer becomes less attenuated than in the inner cylinder and moreover, the volume fraction corresponding to the layer becomes negligible.

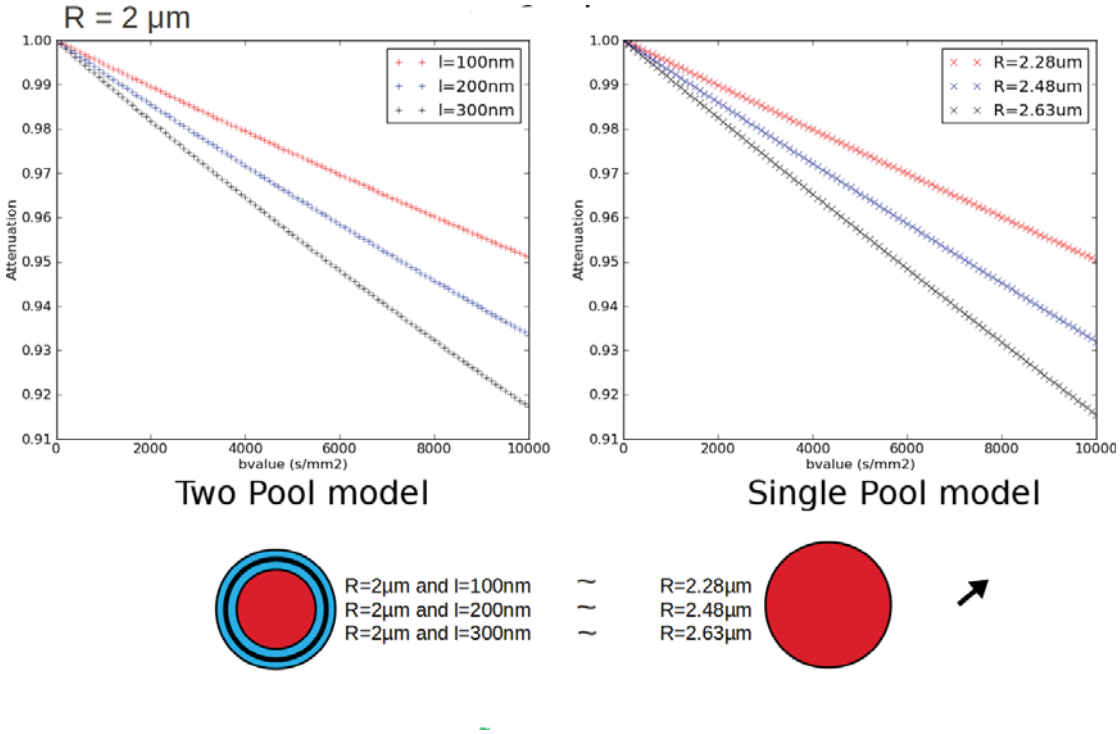

FIGURE 6.17: Signal attenuation for an axon of radius of 2μm; Left: using the two-pool model and right: using the simple cylinder model

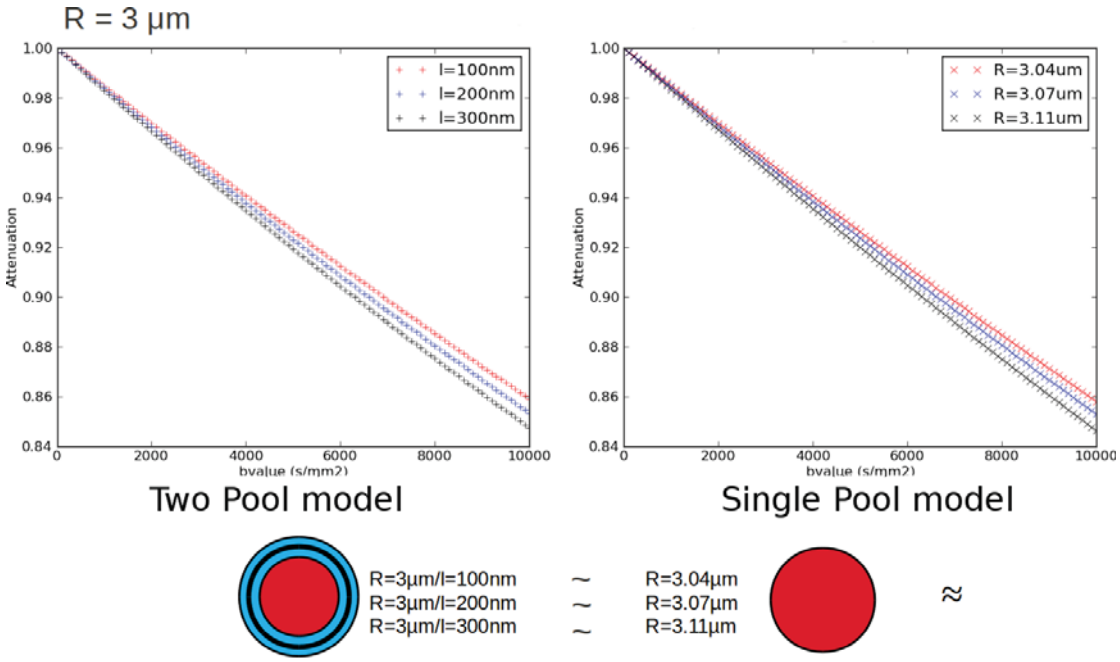

FIGURE 6.18: Signal attenuation for an axon of radius of 3μm; Left: using the two-pool model and right: using the simple cylinder model

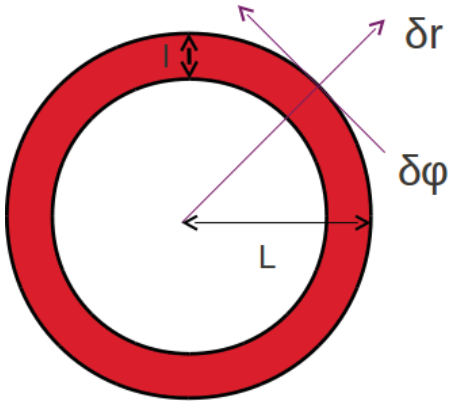

FIGURE 6.19: Diffusion in a circular layer : the attenuation comes from the attenuation along the boundaries and perpendicular to them

6.2.3 Limitations of the model

This model relies on several assumptions that needs to be verified. First, the ratio between the two diffusion coefficients will change the minimum radii for which the overestimation can be observed. Second, the diffusion time also influences this minimum radius (for example, for a longer diffusion time $T_{diff} = 76ms$ even at 3μm, the radii is overestimated using the single pool model at 4.6 μm assuming a 100nm layer thickness). The model assumes slow exchange between the two compartments considering the diffusion time achievable on clinical MRI systems. It will be more realistic to consider intermediate exchange. Including exchange complicates the model (the Neuman's conditions simplifies the computation of the analytical expression of the signal) and introduces a new parameter to estimate. For now, we did not apply this new model to our 14 subjects, since the signal computation is very long due to the computation of the roots defined by the boundary conditions). Optimization of the algorithm will be part of our future work, in order to test the model on healthy subjects and compare with the actual model. This study is the beginning of more investigations on the biophysical reality of the two-pool model and the possibility to improve the accuracy of axon calibration algorithms. This work has been presented at the ISMRM conference in 2014 ([Lebois et al., 2014]).

6.3 Ongoing studies

6.3.1 Arbitrary Gradient Waveform Spin Echo versus PGSE : *in vivo* comparison

We presented in the previous chapter the development of a diffusion sequence allowing to play any kind of waveform. The optimized AGWSE sequence has been proven to

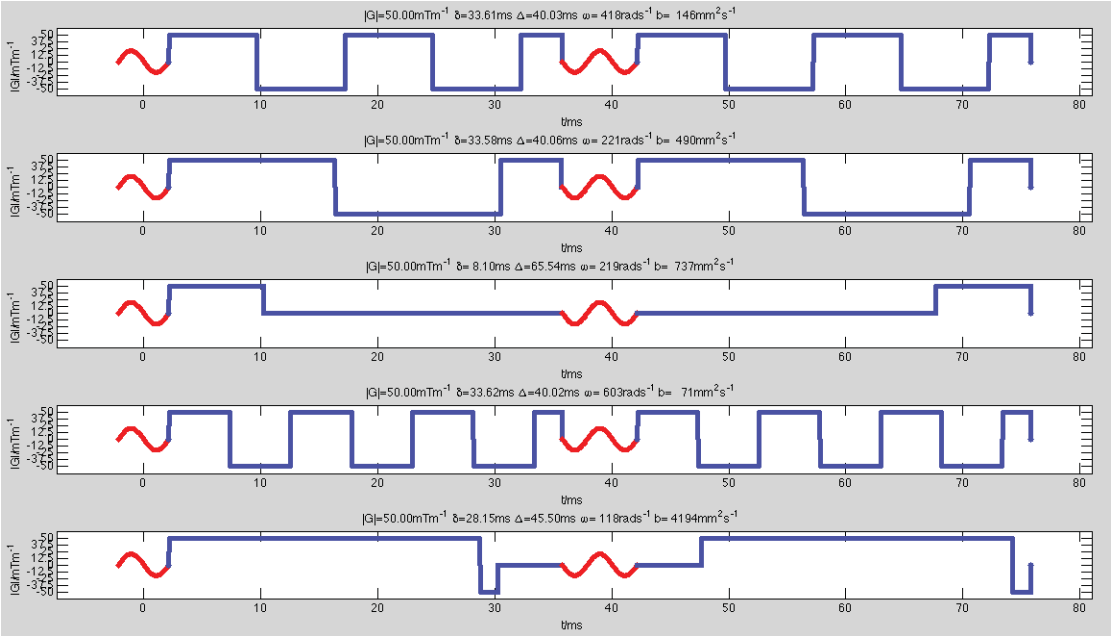

FIGURE 6.20: Optimized protocol using trapezoidal oscillating gradients (courtesy of Dr. I. Drobnjak)

improve the accuracy of axon calibration ([Siow et al., 2012],[Siow et al., 2013]). In order to compare AGWSE to PGSE protocol on human subjects at 7T, two volunteers have been scanned using an optimized AGWSE-based protocol (provided by Dr. Ivana Drobnjak from the CMIC, University College of London). This protocol was optimized considering the CHARMED model as tissue model, characterized by *a priori* parameters $f_r = 0.7$,$D_{\|} = 1.7 \times 10^{-9} mm^2/s$ and $r = 5\mu$m. The characteristics of the 7T Siemens scanner was also included in the constraints of the optimization algorithm. Since a completely arbitrary gradient waveform could be computationly intensive, the waveform was contrained to be oscillating trapezoids with varying frequencies (see Figure 6.20). The signal was measured along 60 optimized directions. An ongoing project thus focuses on the comparison of optimized PGSE and AGWSE in clinical conditions from several subjects.

6.3.2 Towards characterization of diseases through axon calibration : application to a cohort of autistic patients

Axon diameter mapping could provide interesting biomarkers of diseases and microstructural information on region where a decrease of connectivity or fractional anisotropy for example is observed in patients. Clinical systems are constrained by their limited gradient strength and static field but it could be of interest to apply an ActiveAx-like protocol to study if it is possible to observe differences between controls and patients, even if the parameter estimates cannot be as accurate as those obtained using higher

gradient strength. In a feasibility study, we included 4 PGSE profiles along 30 directions (plus 2 b=0s/mm^2 images) into an imaging protocol dedicated to the study of autistic patients suffering from Asperger's syndrome (in collaboration with the team of Dr Marion Leboyer and Dr Josselin Houenou of the Albert Chenevier center of the Mondor Institute in the Fondamental Institute). This study (approved by the local ethical commitee C07-33, INSERM) focuses on the biomarkers of autism under a multimodal approach : MRI, clinical evaluation, eye-tracking (cognitive and social tasks), immunoinflammatory dosage, neuropsychological test. The imaging protocol includes T1, T2 flair, T2 mapping, resting-state fMRI and diffusion weighted MRI. The acquisition takes approximately 70 minutes including our protocol. The study is actually conducted on a Tim Trio 3T MRI system equipped with a 12-channel head coil on 40 autistic patients and 30 controls. It is important to stress that the number of profiles and orientations was imposed by the remaining scan time of the imaging protocol for our study.

6.3.2.1 MRI protocol and methods

10 autistics patients and 10 controls have already been included in this preliminary study at the time of the writing of this manuscript. The parameters of the PGSE profiles were : $\delta = 12ms/\Delta = 56.8ms/G = 26mT/m/bvalue = 368s/mm^2$, $\delta = 24ms/\Delta = 28.8ms/G = 26mT/m/bvalue = 580s/mm^2$, $\delta = 28ms/\Delta = 72.8ms/G = 26mT/m/bvalue = 2400s/mm^2$, $\delta = 23ms/\Delta = 77.8ms/G = 26mT/m/bvalue = 1795s/mm^2$. The acquisition parameters were : FOV = 210mm, TH=2mm, TR=6s, TE=130ms, SlewRate = 150T/m/s, matrix=102x102. 30 slices were acquired centered on the corpus callosum of each volunteer. Since the 3T is equipped with a 40mT/m gradient but limited to 26mT/m, we don't expect to have the accuracy we obtained at 7T but we wanted to test whether it was possible to find differences between the two populations, even at low gradient strength. The axon calibration procedure was run on the corpus callosum at the level of the midsagittal plane. The burnin steps of the MCMC procedure was increased up to 50000, the intervals were fixed to 1000 and the number of samples was extended to 300. A profile along the corpus callosum was computed following the same method described before. We also extracted the fractional anisotropy along the corpus callosum from the computation of the diffusion tensor from the profile with the highest b-value.

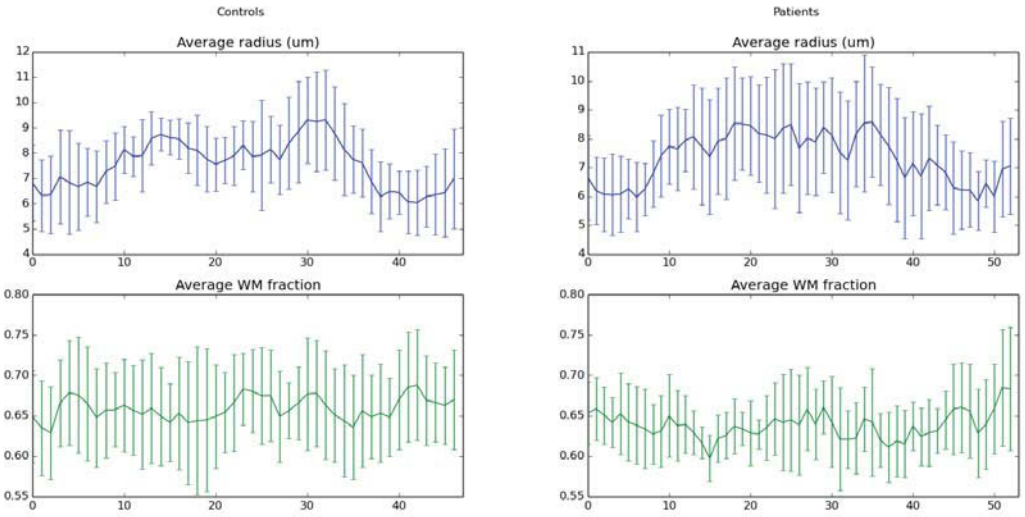

FIGURE 6.21: Average profiles of axon radii and white matter fraction. On the left : autistic patients. On the right : controls

6.3.2.2 Preliminary results

Figure 6.22 depicts respectively the average profile of axon radii and white matter fraction of autistic patients and controls. As expected the inter and intra-subject variance of the parameters is quite high (up to 0.1 for white matter fraction and 2.5 μm for axon radius). If the radius seems to be higher in the body of the corpus callosum, the white matter fraction doesn't change much along the corpus callosum for controls. We computed the differences across the subjects on each section using a Mann-Whitney test. Significative section (see Figure 6.22) are located in the posterior part of the genu and at the level of the isthmus, it indicates lower white matter fraction, radius and FA for the population of autists at the level of the posterior part of the genu and a lower white matter fraction in the isthmus. Previous studies ([Alexander et al., 2007],[Barnea-Goraly et al., 2004],[Chen et al.]) reported a reduced volume of the corpus callosum as well as a reduced fractional anisotropy in the genu and the splenium and at the global level of the corpus callosum and an increased mean diffusivity in all regions except the splenium. Both FA and mean diffusivity differences were explained by the increase of the radial diffusivity. Here, we don't observe a global difference. Lower FA can be explained by a lower white matter fraction (and lower average radii) as suggested by our results. These results have to be taken with caution, considering the variability of the results. The number of subjects included in our study will be increased in the future (to 40 autistic subjects and 30 healthy subjects). And results could be improved using a similar protocol, with more orientations and profiles. The relaxometry data acquired in the same imaging protocol could be used to characterize a potential difference in myelination.

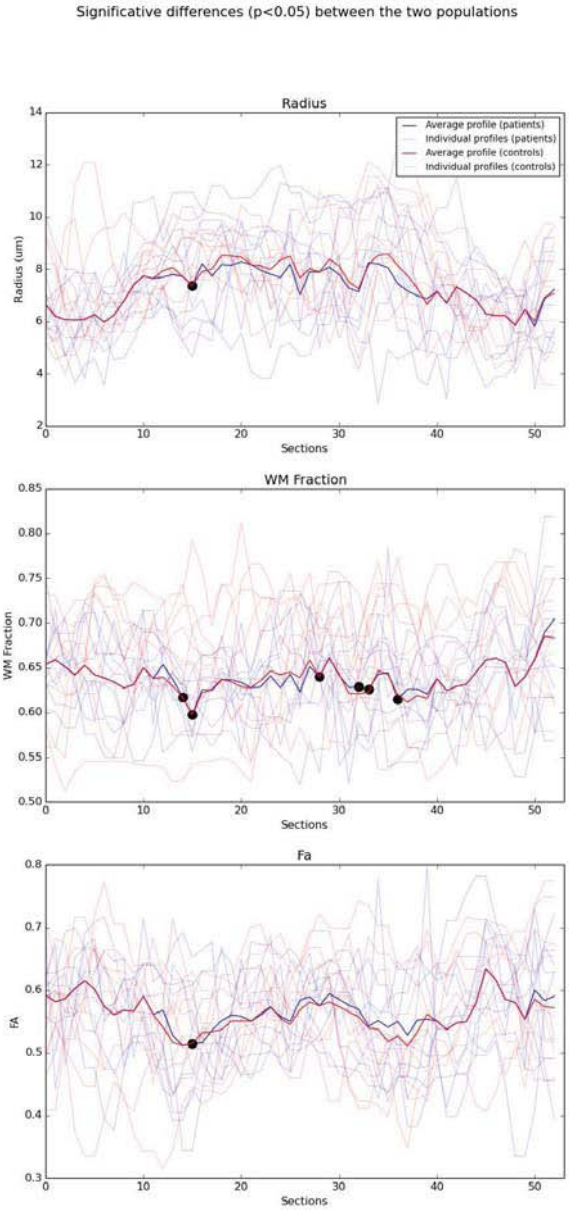

FIGURE 6.22: Significative regions ($p < 0.05$) for radius, white matter fraction and FA along the corpus callosum

6.4 Conclusion

In this chapter, we first presented axon radii and density maps obtained for 14 subjects using a new protocol dedicated to axon calibration with ten PGSE profiles along 60 directions on a 7T clinical scanner. A previous work ([Duclap et al., 2013a]) based on only 4 profiles showing some limitations mainly on the reproducibility of the results, we have chosen to extend our protocol to ten profiles, to obtain a larger sampling of the diffusion times and low, medium and strong b-values (strong b-values allowing to be more sensitive to the restricted part of the signal). The tissue model was kept simple, corresponding to a CHARMED model with an additional isotropic compartment to deal with CSF contaminations. Results were in good agreement with histological observations, despite an overestimation of the smallest radii partly explained by the limited gradient strength (50mT/m) and by the too simple CHARMED model. However, the inter and intra-subject variability of the estimates were reasonable and thanks to the 10 profiles and the higher SNR provided by the 7T scanner, the results were reproducible and their sensitivity to the initial parameters are limited. We also observed significant correlations between the microstructural parameters and the DTI-based parameters, proving that such a method could provide insights at the microstructure scale of increase or decrease of DTI parameters such as FA, ADC, $\lambda_\perp$ and $\lambda_\parallel$ in patients in comparison with controls. This work could be improved using the achievable gradient strength of the 7T (80mT/m, limited to 50mT/m at the time of our study) and also using an improved model, since the sampling provided by the ten profiles allows to add model parameters. The two-pool axon model described in the previous chapter from a mathematical point of view could be an interesting extension of the present model. We have shown through a theoretical study in clinical conditions that using a single-pool cylinder model instead of the two-pool model for the axon could lead to an overestimation of the actual axon radius when the measurement are made perpendicularly to the fiber. The reality of this model is still discussed and it will be of great interest to run the axon calibration procedure on our data using this new model (for now, the computation of the signal being too long due to the algorithm computing the roots of the boundary equations, the axon radii mapping using the two-pool model couldn't be done at the end of this thesis, but optimization of the algorithm is ongoing and will allow us to include this model in our toolbox and compare the results with the single pool model). Finally, improvement of our methodology can also be done using an optimized Arbitrary Gradient Waveform Spin Echo sequence to improve the accuracy of the radius and density estimates. This chapter ends with a clinical application on a autistic cohort at 3T. Our results showed significantly differences in regions of the corpus callosum between patients and controls but due to the limited gradient strength of ou 3T MRI system and the choice of the orientations that could be improved by using a set of directions in the midsagital plane,

the variability of the estimates remains high but an increase of the number of profiles and orientations as well as the gradient strength (like for the 7T, we are able now to push the gradient strength to 40mT/m instead of 26mT/m) could help to be more discriminant between the two populations and therefore provide reliable biomarkers of autism.

Chapter 7

Conclusion and Future Work

7.1 General conclusion and contributions

This thesis aimed at developing methodological tools to map brain microstructure using both quantitative and diffusion MRI. This work was driven by the need to be able to map microstructure under clinical conditions, inducing limited scan duration, limited gradient strength and static field as well as safety constraints. Because of the complexity of the brain microstrcture and given these constraints, measuring microstructural parameters is a real challenge. The main idea of this thesis was to provide maps of parameters characterizing the microstructure of white matter (T1, T2, diffusion parameters, axon radii and density...) and study their variations across healthy subjects in order provide a normative atlas of these features along white matter bundles, useful then to address pathological cases. We summarize here the major contributions of this work.

7.1.1 Atlas of T1 and T2 relaxation times from the 79 subjects of the CONNECT/Archi database

The first contribution of our work was focused on the construction of high resolution atlases of relaxation times combined with a connectivity atlas, providing profiles of T1, T2 and diffusion parameters along major white matter bundles of the 79 subjects of the CONNECT/Archi database, that will be open to the scientific community. These atlases could be used as normative atlases of quantitative features to be compared to pathological cases. This work has been presented at the ISMRM conference ([Lebois et al., 2013a]) and submitted to the NeuroImage journal.

7.1.2 Contributions to axon calibration methods

The common axon calibration methods are now able to provide axon radii and density consistent with histology but they are still limited by hardware constraints and scan duration imposed by clinical applications. This leads to a reduced accuracy of the estimates and a difficulty to distinguish small radii from each other (which are therefore overestimated). Optimization methods of the sequence parameters could improve the accuracy of the estimates. The other contributions of this thesis deal with this problem.

7.1.2.1 Implementation and validation of an Arbitrary Gradient Waveform Spin Echo sequence

We developed a new diffusion weighted sequence on the 3T and 7T Siemens clinical MRI systems of NeuroSpin ([Lebois et al., 2012]), able to play any kind of diffusion gradient waveforms. This sequence was validated on a phantom using a totally arbitrary gradient waveform. Optimizing the gradient waveform using hardware and safety constraints and according to a prior model of the tissues have been shown to increase the accuracy of measures of microstructural parameters([Drobnjak et al., 2010]).

7.1.2.2 A novel geometrical model of the axon

Our third contribution was the proposition of a new geometrical model of the axon, taking into account the biphasic behaviour of the water in the living tissue and relying on a thick cylinder model of axons with fast and slow pools of water([Lebois et al., 2013b],[Lebois et al., 2013c]). This may help to reduce the overestimation of the smallest radii observed when using the conventional CHARMED model.

7.1.2.3 Axon radii and density mapping of the corpus callosum at 7T

We proposed a new protocol, made of ten PGSE profiles sampling several diffusion times with increasing b-values to perform axon calibration in the corpus callosum of 14 healthy subjects to take advantage of the high static field provided by the 7T in comparison with previous studies performed at 3T. We showed that this protocol provide an acceptable intra and inter subjects variability, but we still observed an overestimation of the smallest radii. Our results showed correlations with usual DTI parameters indicating that they provide real insights to explain the observed variations of these parameters (as a FA drop for example) from a microstructural point of view at a cellular scale.

7.1.3 Software contribution

A toolbox dedicated to axon calibration, integrating tissue and sequence models was developped in the PTK library and is about to be integrated into the BrainVisa/Connectomist toolbox.

7.2 Future Work

7.2.1 Construction of further atlases based on the CONNECT/Archi MRI database

The diversity of the data acquired in the Archi database allows to build other atlases to improve our knowledge about white matter microstructure. We could for example extract the myelin white matter fraction from the relaxometry data that would increase the understanding of the variability of the microstructure along the bundles and their relationship to variation of myelination.

7.2.2 *In vivo* axon calibration at 7T

The experiments using the ten PGSE profiles on the 7T scanner showed improved compared to 3T results and we still have the opportunity to improve this study by increasing the gradient strength up to the maximum gradient strength (80mT/m). The two-pool model we introduced in this thesis has also to be validated *in vivo* and compared to the single pool model to study the potential improvement it could bring. The axon calibration procedure we developed will be thus optimized and parallelized to be able to map the axon radius and density using this novel model on the same subjects. A model of orientation dispersion will also be included in our model to allow axon calibration in other regions of the brain exhibiting a higher dispersion than in the corpus callosum. Finally, maps of microstructure parameters will be derived scanning the subjects of the Archi databse using a similar protocol in order to go further in the comparison with other quantitative parameters of the microstructure such as T1 and T2 relaxation times.

7.2.3 *In vivo* comparative study of AGWSE vs PGSE

Acquisitions are currently conducted on human subjects on the 7T scanner using an AGWSE sequence. The protocol was optimized using a CHARMED model as a tissue model

and including hardware constraintes of the scanner. The waveform was constrained to be trapezoidal, the optimization process provided 5 protocols with oscillating trapezoidal gradients at different frequencies. The subjects will also undergo an optimized PGSE protocol. Oscillating gradients were proven to provide more accurate estimates ([Siow et al., 2013]) and we would like to compare the results obtained with AGWSE and PGSE protocols on the 7T scanner.

7.2.4 Towards clinical applications

We presented in the last chapter the beginning of a study on a cohort of autistic patients at 3T. The obtained results on the midsagittal plane shows high variability, due to the limited gradient strength and number of orientations. The first improvement is to increase the maximum gradient strength (since in our study it was limited to 26mT/m but it is possible to reach the 40mT/m) but also to optimize the orientations, in order to be more sensitive to the restricted compartment. The preliminary analysis showed decrease white matter fraction in the posterior part of the genu in the autistic population in comparison with the controls. More patients and controls will be included to increase the statistical power of the study. We will also improve the profile computation, projecting the values on the centroid obtained from the corpus callosum tract extracted from the tractogram of each subject. We are also implicated in the DYSBRAIN project initiated by F. Ramus (Laboratory of cognitive sciences and pyscholinguistics, ENS Paris) to study the hypothesis of abnormal microstructure in cortical areas in dyslexia (dyslexic brains show neural migration anomalies). This study will required to develop a novel model to characterize the grey matter cells integrating permeability effects.

7.2.5 Real-time axon calibration

Finally, a real time project, conducted by F. Poupon of NeuroSpin (PediART) aims at estimating microstructure parameters in real time during the acquisition. This project could offer the possibility to control the accuracy of the estimation during the ongoing acquisition and to modify sequence parameters in real time to improve the accuracy. Our sequence and MCMC procedure will be included in this work involving high performance computing. The first application of this project will be the study of microstructure in a pediatric population of patients suffering from metachromatic leukodistrophy and focal epilepsy.

7.2.6 Extension of the study to grey matter

It is far more difficult to extract cell sizes and density in grey matter. One of the biggest limitation is the permeability of their membranes, makes the model more complex. An interesting extension would be therefore to adapt our two-pool model to grey matter to provide biomarkers of diseases affecting the grey matter.

7.2.7 Human Brain Project

Last this work will be continued in the frame of the Human Brain Project, a large project unifying scientific resources with the ultimate goal of mimicking the human brain.

7.2.8 Publications

We list here the different publications arising from this work.

7.2.8.1 Journal Papers

A. Lebois , D. Duclap , P. Guevara , C. Santos , D. LeBihan , J.F. Mangin , C. Poupon. A novel quantitative atlas of T1, T2 relaxation times along white matter bundles : asymmetry study and comparison with diffusion MRI. *Submitted to NeuroImage.*

Y. Assaf, D. C. Alexander, D. K. Jones, A. Bizzi, T. E. Behrens, C. A. Clark, Y. Cohen, T. B. Dyrby, P. S. Huppi, T. R. Knoesche, D. LeBihan, G. J. Parker, and C. Poupon. The CONNECT project: Combining macro- and micro-structure. *NeuroImage*, 80 (0):273 – 282, 2013. ISSN 1053-8119. doi: http://dx.doi.org/10.1016/j.neuroimage. 2013.05.055

7.2.8.2 Conference Papers

A. Lebois, C.H. Yeh, D. Le Bihan, J.F. Mangin, C.P Lin, C. Poupon. On the use of the two pool model to improve axon radius estimation. In *Proceedings of the International Society Magnetic Resonance in Medicine*, 2014.

A. Lebois, C.H. Yeh, , D. Le Bihan, J.F. Mangin, C.P. Lin, and C. Poupon. Axon diameter mapping : Gaussian phase distribution approximation of the diffusion signal attenuation using a two pool thick layer cylinder model. In *Proceedings of the International Society Magnetic Resonance in Medicine Workshop : Diffusion as a probe of*

neural tissue microstructure, 2013

A. Lebois, C.H. Yeh, , D. Le Bihan, J.F. Mangin, C..P. Lin, and C. Poupon. Cell diameter mapping : Gaussian phase distribution approximation of the diffusion signal attenuation using a two pool thick layer sphere model. In *Proceedings of the International Society Magnetic Resonance in Medicine Workshop : Diffusion as a probe of neural tissue microstructure*, 2013.

D. Duclap, P. Hubbard, H. Zhang, P. Guevara, A. Lebois, D. Le Bihan, J.F. Mangin, D. Alexander, G. Parker, and C. Poupon. A novel microstructural atlas of the white matter bundles. In *Proceedings of the International Society Magnetic Resonance in Medicine Workshop : Diffusion as a probe of neural tissue microstructure*, 2013

A. Lebois, D. Duclap, B. Schmitt, C. Dos Santos, P. Guevara, H. Zhang, D. Le Bihan, J.F. Mangin, and C. Poupon. Towards probabilistic atlases of the t1/t2 relaxation times from the connect/archi database. In *Proceedings of the International Society Magnetic Resonance in Medicine*, 2013

D. Duclap, B. Schmitt, A. Lebois, P. Guevara, H. Zhang, Y. Assaf, P. F, R. Denis, Y. Cointepas, D. Le Bihan, J.F. Mangin, and C. Poupon. A novel probabilistic connectivity atlas for the human connectome: the connect/archi atlas. In *Proceedings of the International Society Magnetic Resonance in Medicine*, 2013

D. Duclap, B. Schmitt, A. Lebois, P. Guevara, H. Zhang, C. Dos Santos, D. Le Bihan, J.F. Mangin, and C. Poupon. Towards a super-resolution connect/archi atlas of the white matter connectivity. In *Proceedings of the International Society Magnetic Resonance in Medicine*, 2013

A. Lebois, B. Schmitt, D. Duclap, F. Poupon, and C. Poupon. A novel diffusion weighted arbitrary spin echo pulse sequence to customize diffusion gradient shapes. In *Proceed. ings of the European Society Magnetic Resonance in Medicine and Biology*, 2012

D. Duclap, A. Lebois, B. Schmitt, O. Riff, P. Guevara, L. Marrakchi, V. Brion, F. Poupon, J.F Mangin, C. Poupon, Connectomist.2.0: a novel diffusion analysis toolbox for brainvisa. In *Proceedings of the European Society Magnetic Resonance in Medicine and Biology*, 2012.

A. Lebois, C. Poupon, L. Ciobanu, D. Le Bihan, B. Djemai, N. Pyatigorskaya, J.F Mangin, I. Kezele, Short.time diffusion analysis at ultra-high field (17T) to infer surface-to-volume ratio in the grey matter of rat brain in vivo and ex vivo. In *Proceedings of the European Society Magnetic Resonance in Medicine and Biology*, 2011.

Appendix A

Mathematical Functions used in this thesis

A.1 Bessel Functions

A.1.1 Bessel Functions of the first kind

$$J_n(x) = \sum_{p=0}^{\infty} \frac{(-1)^p}{p!(n+p)!}(\frac{x}{2})^{2p+n}$$

(n integer)

A.1.2 Neuman Functions (second kind)

$$Y_n(x) = \lim_{\lambda \to +n} \frac{J_\lambda(x)cos(\lambda\pi) - J_{-\lambda}(x)}{sin(\lambda\pi)}$$

A.2 Modified Bessel Functions of the first kind

$$I_n(x) = (\frac{1}{2}x)^n \sum_{k=0}^{\infty} \frac{(\frac{1}{4}x^2)^k}{k!\Gamma(n+k+1)}$$

(n integer)

A.3 Spherical Bessel Functions

A.3.1 Spherical Bessel Functions of the first kind

$$j_n(x) = \sqrt{\frac{\pi}{2x}} J_{n+1/2}(x)$$

(n integer)

A.3.2 Spherical Bessel Functions of the second kind

$$y_n(x) = \sqrt{\frac{\pi}{2x}} Y_{n+1/2}(x)$$

A.4 Legendre Polynomials

The Legendre Polynomials can be defined in several ways, we here describe them through the Rodrigues formula :

$$P_n(x) = \frac{1}{2^n n!} \frac{d^n}{dx^n}((x^2-1)^n)$$

A.5 Confluent hypergeometric function

$$M(a,b,c) = \sum_{n=0}^{\infty} \frac{a^{(n)} z^n}{b^{(n)} n!},$$

where $a^{(0)} = 1$ and $a^{(n)} = a(a+1)(a+2)...(a+n-1)$

Appendix B

MCMC Procedure

We here describe the MCMC procedure used to draw samples of posterior distribution of each parameter of the model from the measurements. This procedure does not require the knowledge of partial derivatives of the signal to optimize with respect to the parameters.

1. Computation of the signal using current parameters (initial values)
2. New parameters are computed, perturbating the current parameters using a Gaussian perturbation.
3. New parameters are accepted if they respect the prior conditions (typically, if the value belongs to the range of authorized values)
4. Computation of the signal with new parameters.
5. Computation of the likelihood ratio (LR) between the new signal using the perturbed parameters and the old signal with current parameters using, in the case of Rician noise :

$$LR_{rician}(S_{measured}) = \frac{S_{measured} \times I_0(\frac{S_{measured}S_{new}}{\sigma^2}) \exp(\frac{-S^2_{measured}-S^2_{new}}{2\sigma^2})}{S_{measured} \times I_0(\frac{S_{measured}S_{old}}{\sigma^2}) \exp(\frac{-S^2_{measured}-S^2_{old}}{2\sigma^2})}$$

6. The new parameters are kept if the likelihood ratio is greater than one or greater than a random value (drawned from a uniform probability)
7. The procedure returns to step 2

This procedure is first repeated a large number of times, to let the Markov Chain become stable: this is the burnin period. The final samples of the posterior distribution are kept

every n draws, called intervals to guarantee the independance of the draws. At the end, the algorithm provides samples of the posterior distribution of each parameter. The estimates of the model can for example be computed from the average value of this distribution.

Appendix C

Corpus Callosum T1 and T2 profiles

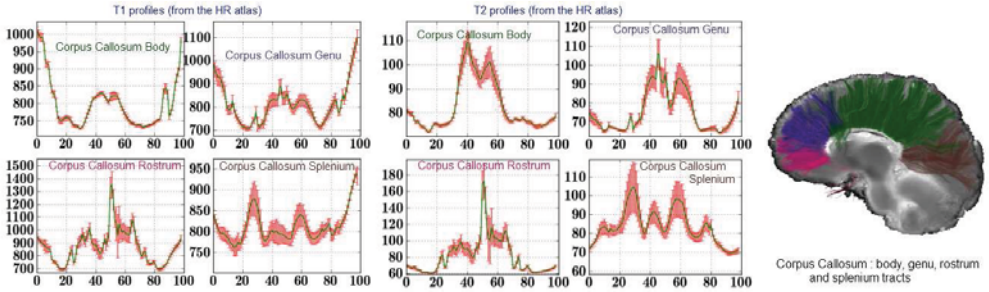

We here provide the profile of T1 and T2 relation times along the corpus callosum.

Bibliography

F. Aboitiz, A. B. Scheibel, R. S. Fisher, and E. Zaidel. Fiber composition of the human corpus callosum. *Brain Research*, 598(1–2):143 – 153, 1992. ISSN 0006-8993. doi: http://dx.doi.org/10.1016/0006-8993(92)90178-C. URL http://www.sciencedirect.com/science/article/pii/000689939290178C.

A. Alexander, Y.-C. Wu, and P. Venkat. Hybrid diffusion imaging (hydi). In *Engineering in Medicine and Biology Society, 2006. EMBS '06. 28th Annual International Conference of the IEEE*, pages 2245–2248, Aug 2006. doi: 10.1109/IEMBS.2006.259453.

A. L. Alexander, J. E. Lee, M. Lazar, R. Boudos, M. B. DuBray, T. R. Oakes, J. N. Miller, J. Lu, E.-K. Jeong, W. M. McMahon, E. D. Bigler, and J. E. Lainhart. Diffusion tensor imaging of the corpus callosum in autism. *NeuroImage*, 34(1):61 – 73, 2007. ISSN 1053-8119. doi: http://dx.doi.org/10.1016/j.neuroimage.2006.08.032. URL http://www.sciencedirect.com/science/article/pii/S1053811906008901.

D. C. Alexander. A general framework for experiment design in diffusion mri and its application in measuring direct tissue-microstructure features. *Magnetic Resonance in Medicine*, 60(2):439–448, 2008. ISSN 1522-2594. doi: 10.1002/mrm.21646. URL http://dx.doi.org/10.1002/mrm.21646.

D. C. Alexander, C. Pierpaoli, P. J. Basser, and J. C. Gee. Spatial transformations of diffusion tensor magnetic resonance images. *IEEE Transactions On Medical Imaging*, 20(11), 2001.

D. C. Alexander, P. L. Hubbard, M. G. Hall, E. A. Moore, M. Ptito, G. J. Parker, and T. B. Dyrby. Orientationally invariant indices of axon diameter and density from diffusion {MRI}. *NeuroImage*, 52(4):1374 – 1389, 2010. ISSN 1053-8119. doi: http://dx.doi.org/10.1016/j.neuroimage.2010.05.043. URL http://www.sciencedirect.com/science/article/pii/S1053811910007755.

Y. Assaf and P. J. Basser. Composite hindered and restricted model of diffusion (charmed) {MR} imaging of the human brain. *NeuroImage*, 27(1):48 – 58, 2005.

ISSN 1053-8119. doi: http://dx.doi.org/10.1016/j.neuroimage.2005.03.042. URL http://www.sciencedirect.com/science/article/pii/S1053811905002259.

Y. Assaf and Y. Cohen. Non-mono-exponential attenuation of water andn-acetyl aspartate signals due to diffusion in brain tissue. *Journal of Magnetic Resonance*, 131(1): 69 – 85, 1998. ISSN 1090-7807. doi: http://dx.doi.org/10.1006/jmre.1997.1313. URL http://www.sciencedirect.com/science/article/pii/S1090780797913136.

Y. Assaf, R. Z. Freidlin, G. K. Rohde, and P. J. Basser. New modeling and experimental framework to characterize hindered and restricted water diffusion in brain white matter. *Magnetic Resonance in Medicine*, 52(5):965–978, 2004. ISSN 1522-2594. doi: 10.1002/mrm.20274. URL http://dx.doi.org/10.1002/mrm.20274.

Y. Assaf, T. Blumenfeld-Katzir, Y. Yovel, and P. J. Basser. Axcaliber: A method for measuring axon diameter distribution from diffusion mri. *Magnetic Resonance in Medicine*, 59(6):1347–1354, 2008. ISSN 1522-2594. doi: 10.1002/mrm.21577. URL http://dx.doi.org/10.1002/mrm.21577.

Y. Assaf, D. C. Alexander, D. K. Jones, A. Bizzi, T. E. Behrens, C. A. Clark, Y. Cohen, T. B. Dyrby, P. S. Huppi, T. R. Knoesche, D. LeBihan, G. J. Parker, and C. Poupon. The {CONNECT} project: Combining macro- and micro-structure. *NeuroImage*, 80 (0):273 – 282, 2013. ISSN 1053-8119. doi: http://dx.doi.org/10.1016/j.neuroimage.2013.05.055. ¡ce:title¿Mapping the Connectome¡/ce:title¿.

H.-E. Assemlal, D. Tschumperlé, and L. Brun. Efficient and robust computation of {PDF} features from diffusion {MR} signal. *Medical Image Analysis*, 13(5):715 – 729, 2009. ISSN 1361-8415. doi: http://dx.doi.org/10.1016/j.media.2009.06.004. URL http://www.sciencedirect.com/science/article/pii/S1361841509000486. Includes Special Section on the 12th International Conference on Medical Imaging and Computer Assisted Intervention.

J. C. Ayus, S. G. Achinger, and A. Arieff. Brain cell volume regulation in hyponatremia: role of sex, age, vasopressin, and hypoxia. *American Journal of Physiology - Renal Physiology*, 295(3):F619–F624, 2008. doi: 10.1152/ajprenal.00502.2007. URL http://ajprenal.physiology.org/content/295/3/F619.

B. Balinov, B. Jonsson, P. Linse, and O. Soderman. The {NMR} self-diffusion method applied to restricted diffusion. simulation of echo attenuation from molecules in spheres and between planes. *Journal of Magnetic Resonance, Series A*, 104(1):17 – 25, 1993. ISSN 1064-1858. doi: http://dx.doi.org/10.1006/jmra.1993.1184. URL http://www.sciencedirect.com/science/article/pii/S1064185883711848.

D. Barazany, P. J. Basser, and Y. Assaf. In-vivo measurement of the axon diameter distribution in the rat's corpus callosum. *Brain*, 2009.

A. J. Barkovich. Concepts of myelin and myelination in neuroradiology. *American Journal of Neuroradiology*, 21(6):1099–1109, 2000.

N. Barnea-Goraly, H. Kwon, V. Menon, S. Eliez, L. Lotspeich, and A. L. Reiss. White matter structure in autism: preliminary evidence from diffusion tensor imaging. *Biological Psychiatry*, 55(3):323 – 326, 2004. ISSN 0006-3223. doi: http://dx.doi.org/10.1016/j.biopsych.2003.10.022. URL http://www.sciencedirect.com/science/article/pii/S000632230301151X.

P. Basser, J. Mattiello, and D. Le Bihan. Estimation of the effective self-diffusion tensor from the nmr spin echo. *Journal of Magnetic Resonance B*, 103(3), 1994.

P. J. Basser. Fiber-tractography via diffusion tensor mri (dt-mri).

P. J. Basser, S. Pajevic, C. Pierpaoli, J. Duda, and A. Aldroubi. In vivo fiber tractography using dt-mri data. *Magnetic Resonance in Medicine*, 44(4):625–632, 2000. ISSN 1522-2594. doi: 10.1002/1522-2594(200010)44:4⟨625::AID-MRM17⟩3.0.CO;2-O. URL http://dx.doi.org/10.1002/1522-2594(200010)44:4<625::AID-MRM17>3.0.CO;2-O.

T. Behrens, M. Woolrich, M. Jenkinson, H. Johansen-Berg, R. Nunes, S. Clare, P. Matthews, J. Brady, and S. Smith. Characterization and propagation of uncertainty in diffusion-weighted mr imaging. *Magnetic Resonance in Medicine*, 50(5):1077–1088, 2003. ISSN 1522-2594. doi: 10.1002/mrm.10609. URL http://dx.doi.org/10.1002/mrm.10609.

H. Benveniste, L. W. Hedlund, and G. A. Johnson. Mechanism of detection of acute cerebral ischemia in rats by diffusion-weighted magnetic resonance microscopy. *Stroke*, 23(5):746–54, 1992. doi: 10.1161/01.STR.23.5.746. URL http://stroke.ahajournals.org/content/23/5/746.abstract.

J. I. Berman, S. Chung, P. Mukherjee, C. P. Hess, E. T. Han, and R. G. Henry. Probabilistic streamline q-ball tractography using the residual bootstrap. *NeuroImage*, 39(1):215 – 222, 2008. ISSN 1053-8119. doi: http://dx.doi.org/10.1016/j.neuroimage.2007.08.021. URL http://www.sciencedirect.com/science/article/pii/S1053811907007185.

M. A. Bernstein, D. M. Thomasson, and W. H. Perman. Improved detectability in low signal to noise ratio magnetic resonance images by means of a phase corrected real reconstruction. *Medical Physics*, 16 (5):813–817, 1989. doi: http://dx.doi.org/10.1118/1.596304. URL http://scitation.aip.org/content/aapm/journal/medphys/16/5/10.1118/1.596304.

C. Bhushan, J. Haldar, A. Joshi, and R. Leahy. Correcting susceptibility-induced distortion in diffusion-weighted mri using constrained nonrigid registration. In *Signal Information Processing Association Annual Summit and Conference (APSIPA ASC), 2012 Asia-Pacific*, pages 1–9, Dec 2012.

F. Bloch. Nuclear induction. *Phys. Rev.*, 70:460–474, Oct 1946. doi: 10.1103/PhysRev.70.460. URL http://link.aps.org/doi/10.1103/PhysRev.70.460.

V. Brion. *Towards real-time diffusion imaging : noise correction and inference of the human brain connectivity*. PhD thesis, University of Paris Sud, France, 2013.

D. L. Buckley, J. D. Bui, M. I. Phillips, T. Zelles, B. A. Inglis, H. D. Plant, and S. J. Blackband. The effect of ouabain on water diffusion in the rat hippocampal slice measured by high resolution nmr imaging. *Magnetic Resonance in Medicine*, 41(1):137–142, 1999. ISSN 1522-2594. doi: 10.1002/(SICI)1522-2594(199901)41:1⟨137::AID-MRM19⟩3.0.CO;2-Y. URL http://dx.doi.org/10.1002/(SICI)1522-2594(199901)41:1<137::AID-MRM19>3.0.CO;2-Y.

F. Calamante, J.-D. Tournier, R. E. Smith, and A. Connelly. A generalised framework for super-resolution track-weighted imaging. *NeuroImage*, 59(3):2494 – 2503, 2012. ISSN 1053-8119. doi: http://dx.doi.org/10.1016/j.neuroimage.2011.08.099.

P. Callaghan. Pulsed-gradient spin-echo {NMR} for planar, cylindrical, and spherical pores under conditions of wall relaxation. *Journal of Magnetic Resonance, Series A*, 113(1):53 – 59, 1995. ISSN 1064-1858. doi: http://dx.doi.org/10.1006/jmra.1995.1055. URL http://www.sciencedirect.com/science/article/pii/S1064185885710558.

P. T. Callaghan. *Principles of nuclear magnetic resonance microscopy*. Oxford University Press, 1991.

P. T. Callaghan. A simple matrix formalism for spin echo analysis of restricted diffusion under generalized gradient waveforms. *Journal of Magnetic Resonance*, 129(1):74 – 84, 1997. ISSN 1090-7807. doi: http://dx.doi.org/10.1006/jmre.1997.1233. URL http://www.sciencedirect.com/science/article/pii/S1090780797912337.

P. T. Callaghan and M. E. Komlosh. Locally anisotropic motion in a macroscopically isotropic system: displacement correlations measured using double pulsed gradient spin-echo nmr. *Magnetic Resonance in Chemistry*, 40(13):S15–S19, 2002. ISSN 1097-458X. doi: 10.1002/mrc.1122. URL http://dx.doi.org/10.1002/mrc.1122.

H. Y. Carr and E. M. Purcell. Effects of diffusion on free precession in nuclear magnetic resonance experiments. *Phys. Rev.*, 94:630–638, May 1954. doi: 10.1103/PhysRev.94.630. URL http://link.aps.org/doi/10.1103/PhysRev.94.630.

Y.-P. Chao, J.-H. Chen, K.-H. Cho, C.-H. Yeh, K.-H. Chou, and C.-P. Lin. A multiple streamline approach to high angular resolution diffusion tractography. *Medical engineering & physics*, 30:989–996, 2008.

R. Chen, Y. Jiao, and E. H. Herskovits.

A. Cherubini, P. Peran, G. E. Hagberg, A. E. Varsi, G. Luccichenti, C. Caltagirone, U. Sabatini, and S. G. Characterization of white matter fiber bundles with t2 × relaxometry and diffusion tensor imaging. *Magnetic Resonance in Medicine*, 61(5): 1066–1072, 2009. ISSN 1522-2594. doi: 10.1002/mrm.21978.

C. A. Clark and D. Le Bihan. Water diffusion compartmentation and anisotropy at high b values in the human brain. *Magnetic Resonance in Medicine*, 44(6):852–859, 2000. ISSN 1522-2594. doi: 10.1002/1522-2594(200012)44:6⟨852::AID-MRM5⟩3.0.CO;2-A. URL http://dx.doi.org/10.1002/1522-2594(200012)44:6<852::AID-MRM5>3.0.CO;2-A.

J. S. Clegg. Properties and metabolism of the aqueous cytoplasm and its boundaries. *American Journal of Physiology - Regulatory, Integrative and Comparative Physiology*, 246(2):R133–R151, 1984. URL http://ajpregu.physiology.org/content/246/2/R133.

Y. Cointepas, C. Poupon, and J.-F. Mangin. A spin glass based framework to reconstruct brain fiber bundles from images of the water diffusion process. *Information Processes*, 2(1):30–36, 2002.

Y. Cointepas, C. Poupon, R. Maroy, D. Riviere, D. PapadopoulosOrfanos, D. L. Bihan, and J.-F. Mangin. A freely available anatomist/brainvisa package for analysis of diffusion mr images. In *Proceedings of the 9th HBM*, June 2003.

C. D. Constantinides, E. Atalar, and E. R. McVeigh. Signal to noise measurements in magnitude images from nmr phased arrays. *Magnetic Resonance in Medicine*, 38(5):852–857, 1997. ISSN 1522-2594. doi: 10.1002/mrm.1910380524. URL http://dx.doi.org/10.1002/mrm.1910380524.

P. A. Cook, Y. Bai, S. Nedjati-Gilani, K. K. Seunarine, M. G. Hall, G. J. Parker, and D. C. Alexander. Camino: Open-source diffusion-mri reconstruction and processing. In *Proceedings of the International Society Magnetic Resonance in Medicine*, 2006.

I. Corouge, P. T. Fletcher, S. Joshi, S. Gouttard, and G. Gerig. Fiber tract-oriented statistics for quantitative diffusion tensor {MRI} analysis. *Medical Image Analysis*, 10(5):786 – 798, 2006. ISSN 1361-8415. doi: http://dx.doi.org/10.1016/j.media.2006.

07.003. The Eighth International Conference on Medical Imaging and Computer Assisted Intervention – {MICCAI} 2005 The Eighth International Conference on Medical Imaging and Computer Assisted Intervention – {MICCAI} 2005.

D. Cory. Applications of spin transport as a probe of local geometry. *Polymere Preprints*, 149(31), 1990.

S. De Santis, M. Drakesmith, S. Bells, Y. Assaf, and D. Jones. Why diffusion tensor {MRI} does well only some of the time: Variance and covariance of white matter tissue microstructure attributes in the living human brain. *NeuroImage*, 89(0):35 – 44, 2014. ISSN 1053-8119. doi: http://dx.doi.org/10.1016/j.neuroimage.2013.12.003. URL http://www.sciencedirect.com/science/article/pii/S105381191301207X.

S. Deoni. Quantitative relaxometry of the brain. *Topics in Magnetic Resonance Imaging*, 21:101–113, april 2010.

S. Deoni, T. M. Peters, and B. K. Rutt. High resolution t1 and t2 mapping of the brain in a clinically acceptable time with despot1 and despot2. *Magnetic Resonance in Medicine*, 53:237–241, 2005a.

S. C. Deoni, B. K. Rutt, and T. M. Peters. Rapid combined t1 and t2 mapping using gradient recalled acquisition in the steady state. *Magnetic Resonance in Medicine*, 49(3):515–526, 2003. ISSN 1522-2594. doi: 10.1002/mrm.10407. URL http://dx.doi.org/10.1002/mrm.10407.

S. C. Deoni, M. J. Josseau, B. K. Rutt, and T. M. Peters. Visualization of thalamic nuclei on high resolution, multi-averaged t1 and t2 maps acquired at 1.5 t. *Human Brain Mapping*, 25(3):353–359, 2005b. ISSN 1097-0193. doi: 10.1002/hbm.20117.

S. C. Deoni, B. K. Rutt, T. Arun, C. Pierpaoli, and D. K. Jones. Gleaning multicomponent t1 and t2 information from steady-state imaging data. *Magnetic Resonance in Medicine*, 60(6):1372–1387, 2008. ISSN 1522-2594. doi: 10.1002/mrm.21704. URL http://dx.doi.org/10.1002/mrm.21704.

S. C. Deoni, E. Mercure, A. Blasi, D. Gasston, M. Johnson, S. C. Williams, , and D. G. Murphy. Investigating the relationships between t1 and t2 relaxation times and myelin water fraction during neurodevelopment. In *Proceedings of the International Society Magnetic Resonance in Medicine*, volume 18, 2010.

S. C. Deoni, D. C. D. III, J. O'Muircheartaigh, H. Dirks, and B. A. Jerskey. Investigating white matter development in infancy and early childhood using myelin water faction and relaxation time mapping. *NeuroImage*, 63(3):1038 – 1053, 2012. ISSN 1053-8119. doi: http://dx.doi.org/10.1016/j.neuroimage.2012.07.037. URL http://www.sciencedirect.com/science/article/pii/S1053811912007665.

M. Descoteaux. *High Angular Resolution Diffusion MRI: from Local Estimation to Segmentation and Tractography*. PhD thesis, Université de Nice-Sophia-Antipolis, France, 2008.

M. Descoteaux, E. Angelino, S. Fitzgibbons, and R. Deriche. Regularized, fast and robust analytical q-ball imaging. *Magn. Reson. Med.*, 58:497–510, 2007.

M. Descoteaux, R. Deriche, T. Knosche, and A. Anwander. Deterministic and probabilistic tractography based on complex fibre orientation distributions. *Medical Imaging, IEEE Transactions on*, 28(2):269–286, Feb 2009a. ISSN 0278-0062. doi: 10.1109/TMI.2008.2004424.

M. Descoteaux, R. Deriche, T. Knosche, and A. Anwander. Deterministic and probabilistic tractography based on complex fibre orientation distributions. *Medical Imaging, IEEE Transactions on*, 28(2):269–286, Feb 2009b. ISSN 0278-0062. doi: 10.1109/TMI.2008.2004424.

M. Descoteaux, R. Deriche, D. L. Bihan, J.-F. Mangin, and C. Poupon. Multiple q-shell diffusion propagator imaging. *Medical Image Analysis*, 15(4):603 – 621, 2011. ISSN 1361-8415. doi: http://dx.doi.org/10.1016/j.media.2010.07.001. URL http://www.sciencedirect.com/science/article/pii/S1361841510000939. Special section on {IPMI} 2009.

D. C. Douglass and D. W. McCall. Diffusion in paraffin hydrocarbons. *The Journal of Physical Chemistry*, 62(9):1102–1107, 1958. doi: 10.1021/j150567a020. URL http://pubs.acs.org/doi/abs/10.1021/j150567a020.

I. Drobnjak and D. C. Alexander. Optimising time-varying gradient orientation for microstructure sensitivity in diffusion-weighted {MR}. *Journal of Magnetic Resonance*, 212(2):344 – 354, 2011. ISSN 1090-7807. doi: http://dx.doi.org/10.1016/j.jmr.2011.07.017. URL http://www.sciencedirect.com/science/article/pii/S1090780711002497.

I. Drobnjak, B. Siow, and D. C. Alexander. Optimizing gradient waveforms for microstructure sensitivity in diffusion-weighted mr. *Journal of Magnetic Resonance*, 206(1):41 – 51, 2010. ISSN 1090-7807. doi: http://dx.doi.org/10.1016/j.jmr.2010.05.017. URL http://www.sciencedirect.com/science/article/pii/S1090780710001606.

J. Dubois, C. Poupon, F. Lethimonnier, and D. Le Bihan. Optimized diffusion gradient orientation schemes for corrupted clinical dti data sets. *Magnetic Resonance Materials in Physics, Biology and Medicine*, 19(3):134–143, 2006. ISSN 0968-5243. doi: 10.1007/s10334-006-0036-0. URL http://dx.doi.org/10.1007/s10334-006-0036-0.

J. Dubois, C. Poupon, F. Leroy, G. Santoro, L. Mangin, J-F.and Hertz-Pannier, and G. Dehaene-Lambertz. Quantification of tissues' maturation in the infant brain with multi-parametric mri. In *Proceedings of the International Society Magnetic Resonance in Medicine*, volume 18, page 740, 2010.

D. Duclap, A. Lebois, B. Schmitt, O. Riff, P. Guevara, M. L, B. V, P. F, M. J-F, and P. C. Connectomist-2.0: a novel diffusion analysis toolbox for brainvisa. In *Proceedings of the European Society Magnetic Resonance in Medicine and Biology*, 2012.

D. Duclap, P. Hubbard, H. Zhang, P. Guevara, A. Lebois, D. Le Bihan, J.-F. Mangin, D. Alexander, G. Parker, and C. Poupon. A novel microstructural atlas of the white matter bundles. In *ISMRM Workshop: Diffusion as a Probe of Neural Tissue Microstructure*, 2013a.

D. Duclap, B. Schmitt, A. Lebois, P. Guevara, H. Zhang, Y. Assaf, P. F, R. Denis, Y. Cointepas, D. Le Bihan, J.-F. Mangin, and C. Poupon. A novel probabilistic connectivity atlas for the human connectome: the connect/archi atlas. In *Proceedings of the International Society Magnetic Resonance in Medicine*, 2013b.

D. Duclap, B. Schmitt, A. Lebois, P. Guevara, H. Zhang, C. Dos Santos, D. Le Bihan, J.-F. Mangin, and C. Poupon. Towards a super-resolution connect/archi atlas of the white matter connectivity. In *Proceedings of the International Society Magnetic Resonance in Medicine*, 2013c.

S. Durrleman, P. Fillard, X. Pennec, and N. Trouvé, A. andAyache. Registration, atlas estimation and variability analysis of white matter fiber bundles modeled as currents. *NeuroImage*, 55(3):1073–1090, 2011.

T. B. Dyrby, L. V. Sogaard, M. G. Hall, M. Ptito, and D. C. Alexander. Contrast and stability of the axon diameter index from microstructure imaging with diffusion mri. *Magnetic Resonance in Medicine*, 70(3):711–721, 2013. ISSN 1522-2594. doi: 10.1002/mrm.24501. URL http://dx.doi.org/10.1002/mrm.24501.

A. Einstein. Über die von der molekularkinetischen theorie der wärme geforderte bewegung von in ruhenden flüssigkeiten suspendierten teilchen. *Annalen der Physik*, 322(8):549–560, 1905. ISSN 1521-3889. doi: 10.1002/andp.19053220806. URL http://dx.doi.org/10.1002/andp.19053220806.

P. Fillard, C. Poupon, and J.-F. Mangin. A novel global tractography algorithm based on an adaptive spin glass model. In G.-Z. Yang, D. Hawkes, D. Rueckert, A. Noble, and C. Taylor, editors, *Medical Image Computing and Computer-Assisted Intervention – MICCAI 2009*, volume 5761 of *Lecture Notes in Computer Science*, pages 927–934. Springer Berlin Heidelberg,

2009. ISBN 978-3-642-04267-6. doi: 10.1007/978-3-642-04268-3_114. URL http://dx.doi.org/10.1007/978-3-642-04268-3_114.

P. Fillard, M. Descoteaux, A. Goh, S. Gouttard, B. Jeurissen, J. Malcolm, A. Ramirez-Manzanares, M. Reisert, K. Sakaie, F. Tensaouti, T. Yo, J.-F. Mangin, and C. Poupon. Quantitative evaluation of 10 tractography algorithms on a realistic diffusion {MR} phantom. *NeuroImage*, 56(1):220 – 234, 2011. ISSN 1053-8119. doi: http://dx.doi.org/10.1016/j.neuroimage.2011.01.032. URL http://www.sciencedirect.com/science/article/pii/S105381191100067X.

H. E. S. Francesco Sciortino, Alfons Geiger. Effect of defects on molecular mobility in liquid water. *Nature*, (6350):218–221, 1991.

O. Friman, G. Farneback, and C.-F. Westin. A Bayesian approach for stochastic white matter tractography. *TMI*, 25(8):965–978, 2006.

D. Gallichan, J. Scholz, A. Bartsch, T. E. Behrens, M. D. Robson, and K. L. Miller. Addressing a systematic vibration artifact in diffusion-weighted mri. *Human Brain Mapping*, 31(2):193–202, 2010. ISSN 1097-0193. doi: 10.1002/hbm.20856. URL http://dx.doi.org/10.1002/hbm.20856.

B. Ghadirian, A. M. Torres, N. N. Yadav, and W. S. Price. Restricted diffusion in annular geometrical pores. *The Journal of Chemical Physics*, 138(9):094202, 2013. doi: http://dx.doi.org/10.1063/1.4793525. URL http://scitation.aip.org/content/aip/journal/jcp/138/9/10.1063/1.4793525.

G. Gong, T. Jiang, C. Zhu, Y. Zang, F. Wang, S. Xie, J. Xiao, and X. Guo. Asymmetry analysis of cingulum based on scale-invariant parameterization by diffusion tensor imaging. *Human Brain Mapping*, 24(2):92–98, 2005. ISSN 1097-0193. doi: 10.1002/hbm.20072.

C. B. Goodlett, P. T. Fletcher, J. H. Gilmore, and G. Gerig. Group analysis of {DTI} fiber tract statistics with application to neurodevelopment. *NeuroImage*, 45(1, Supplement 1):S133 – S142, 2009. ISSN 1053-8119. doi: http://dx.doi.org/10.1016/j.neuroimage.2008.10.060. Mathematics in Brain Imaging.

J. C. Gore, J. Xu, D. C. Colvin, T. E. Yankeelov, E. C. Parsons, and M. D. Does. Characterization of tissue structure at varying length scales using temporal diffusion spectroscopy. *NMR in Biomedicine*, 23(7):745–756, 2010. ISSN 1099-1492. doi: 10.1002/nbm.1531. URL http://dx.doi.org/10.1002/nbm.1531.

D. S. Grebenkov. Analytical solution for restricted diffusion in circular and spherical layers under inhomogeneous magnetic fields. *The Journal of Chemical*

Physics, 128(13):134702, 2008. doi: http://dx.doi.org/10.1063/1.2841367. URL http://scitation.aip.org/content/aip/journal/jcp/128/13/10.1063/1.2841367.

M. A. Griswold, P. M. Jakob, R. M. Heidemann, M. Nittka, V. Jellus, J. Wang, B. Kiefer, and A. Haase. Generalized autocalibrating partially parallel acquisitions (grappa). *Magnetic Resonance in Medicine*, 47(6):1202–1210, 2002. ISSN 1522-2594. doi: 10.1002/mrm.10171. URL http://dx.doi.org/10.1002/mrm.10171.

P. Guevara, D. Duclap, L. Marrakchi-Kacem, D. Rivière, Y. Cointepas, C. Poupon, and J.-F. Mangin. Accurate tractography propagation mask using t1-weighted data rather than fa. In *Proceedings of the International Society Magnetic Resonance in Medicine 19*, 2011a.

P. Guevara, C. Poupon, D. Rivière, Y. Cointepas, M. Descoteaux, B. Thirion, and J.-F. Mangin. Robust clustering of massive tractography datasets. *NeuroImage*, 54(3):1975 – 1993, 2011b. ISSN 1053-8119. doi: http://dx.doi.org/10.1016/j.neuroimage.2010.10.028.

P. Guevara, D. Duclap, C. Poupon, L. Marrakchi-Kacem, P. Fillard, D. L. Bihan, M. Leboyer, J. Houenou, and J.-F. Mangin. Automatic fiber bundle segmentation in massive tractography datasets using a multi-subject bundle atlas. *NeuroImage*, 61(4):1083 – 1099, 2012. ISSN 1053-8119. doi: http://dx.doi.org/10.1016/j.neuroimage.2012.02.071. URL http://www.sciencedirect.com/science/article/pii/S105381191200256X.

E. L. Hahn. Spin echoes. *Phys. Rev.*, 80:580–594, Nov 1950. doi: 10.1103/PhysRev.80.580. URL http://link.aps.org/doi/10.1103/PhysRev.80.580.

K. M. Hasan, I. S. Walimuni, L. A. Kramer, and P. A. Narayana. Human brain iron mapping using atlas-based t2 relaxometry. *Magnetic Resonance in Medicine*, 67(3):731–739, 2012. ISSN 1522-2594. doi: 10.1002/mrm.23054. URL http://dx.doi.org/10.1002/mrm.23054.

R. Hashemi, W. G. Bradley Jr, and C. J. Lisanti. *MRI : the basics*. Lippincott Williams & Wilkins, 2010.

P. Herve, E. Cox, A. Lotfipour, O. Mougin, R. Bowtell, P. Gowland, and T. Paus. Structural properties of the corticospinal tract in the human brain: a magnetic resonance imaging study at 7 tesla. *Brain Structure and Function*, 216(3):255–262, 2011. ISSN 1863-2653. doi: 10.1007/s00429-011-0306-0.

J. R. Highley, M. M. Esiri, B. McDonald, M. Cortina-Borja, B. M. Herron, and T. J. Crow. The size and fibre composition of the corpus callosum with respect to gender and

schizophrenia: a post-mortem study. *Brain*, 122(1):99–110, 1999. doi: 10.1093/brain/122.1.99. URL http://brain.oxfordjournals.org/content/122/1/99.abstract.

J. R. Highley, M. A. Walker, M. M. Esiri, T. J. Crow, and P. J. Harrison. Asymmetry of the uncinate fasciculus: A post-mortem study of normal subjects and patients with schizophrenia. *Cerebral Cortex*, 12(11):1218–1224, 2002. doi: 10.1093/cercor/12.11.1218.

K. Hugdahl and R. Westerhausen. Information processing in the cerebral hemispheres. In K. Hugdahl and R. Westerhausen, editors, *The two halves of the brain- Information processing in the cerebral hemispheres*, pages 469 – 499. Cambridge, MA, 2010. ISBN 0262014130.

A. Ianuş, B. Siow, I. Drobnjak, H. Zhang, and D. C. Alexander. Gaussian phase distribution approximations for oscillating gradient spin echo diffusion {MRI}. *Journal of Magnetic Resonance*, 227(0):25 – 34, 2013. ISSN 1090-7807. doi: http://dx.doi.org/10.1016/j.jmr.2012.11.021. URL http://www.sciencedirect.com/science/article/pii/S1090780712003655.

K. Jansons and D. Alexander. Persistent angular structure: New insights from diffusion mri data. dummy version. In C. Taylor and J. Noble, editors, *Information Processing in Medical Imaging*, volume 2732 of *Lecture Notes in Computer Science*, pages 672–683. Springer Berlin Heidelberg, 2003. ISBN 978-3-540-40560-3. doi: 10.1007/978-3-540-45087-0_56. URL http://dx.doi.org/10.1007/978-3-540-45087-0_56.

S. Jbabdi, P. Bellec, G. Marrelec, V. Perlbarg, and H. Benali. A level set method for building anatomical connectivity paths between brain areas using dti. In *Biomedical Imaging: Nano to Macro, 2004. IEEE International Symposium on*, pages 1024–1027 Vol. 1, April 2004. doi: 10.1109/ISBI.2004.1398715.

S. Jbabdi, M. Woolrich, J. Andersson, and T. Behrens. A bayesian framework for global tractography. *NeuroImage*, 37(1):116 – 129, 2007. ISSN 1053-8119. doi: http://dx.doi.org/10.1016/j.neuroimage.2007.04.039. URL http://www.sciencedirect.com/science/article/pii/S1053811907003503.

S. Jbabdi, P. Bellec, R. Toro, J. Daunizeau, M. Pélégrini-Issac, and H. Benali. Accurate anisotropic fast marching for diffusion-based geodesic tractography. *Journal of Biomedical Imaging*, 2008:2:1–2:12, Jan. 2008. ISSN 1687-4188. doi: 10.1155/2008/320195. URL http://dx.doi.org/10.1155/2008/320195.

I. O. Jelescu, L. Ciobanu, F. Geffroy, P. Marquet, and D. Le Bihan. Effects of hypotonic stress and ouabain on the apparent diffusion coefficient of water at cellular and tissue

levels in aplysia. *NMR in Biomedicine*, 27(3):280–290, 2014. ISSN 1099-1492. doi: 10.1002/nbm.3061. URL http://dx.doi.org/10.1002/nbm.3061.

J. H. Jensen, J. A. Helpern, A. Ramani, H. Lu, and K. Kaczynski. Diffusional kurtosis imaging: The quantification of non-gaussian water diffusion by means of magnetic resonance imaging. *Magnetic Resonance in Medicine*, 53(6):1432–1440, 2005. ISSN 1522-2594. doi: 10.1002/mrm.20508. URL http://dx.doi.org/10.1002/mrm.20508.

S. N. Jespersen, C. D. Kroenke, L. Østergaard, J. J. Ackerman, and D. A. Yablonskiy. Modeling dendrite density from magnetic resonance diffusion measurements. *NeuroImage*, 34(4):1473 – 1486, 2007. ISSN 1053-8119. doi: http://dx.doi.org/10.1016/j.neuroimage.2006.10.037. URL http://www.sciencedirect.com/science/article/pii/S1053811906010950.

S. N. Jespersen, C. R. Bjarkam, J. R. Nyengaard, M. M. Chakravarty, B. Hansen, T. Vosegaard, L. Østergaard, D. Yablonskiy, N. C. Nielsen, and P. Vestergaard-Poulsen. Neurite density from magnetic resonance diffusion measurements at ultrahigh field: Comparison with light microscopy and electron microscopy. *NeuroImage*, 49(1):205 – 216, 2010. ISSN 1053-8119. doi: http://dx.doi.org/10.1016/j.neuroimage.2009.08.053. URL http://www.sciencedirect.com/science/article/pii/S1053811909009665.

P. Jezzard and R. S. Balaban. Correction for geometric distortion in echo planar images from b0 field variations. *Magnetic Resonance in Medicine*, 34 (1):65–73, 1995. ISSN 1522-2594. doi: 10.1002/mrm.1910340111. URL http://dx.doi.org/10.1002/mrm.1910340111.

B. Jian and B. Vemuri. Multi-fiber reconstruction from diffusion mri using mixture of wisharts and sparse deconvolution. In N. Karssemeijer and B. Lelieveldt, editors, *Information Processing in Medical Imaging*, volume 4584 of *Lecture Notes in Computer Science*, pages 384–395. Springer Berlin Heidelberg, 2007. ISBN 978-3-540-73272-3. doi: 10.1007/978-3-540-73273-0_32. URL http://dx.doi.org/10.1007/978-3-540-73273-0_32.

H. Johansen-Berg and T. E. Behren. *Diffusion MRI : From quantitative measurement to in-vivo neuroanatomy*. Heidi Johansen-Berg and Timothy E.J. Behrens, 2009.

D. Jones and S. Deoni. Visualization of t1 and t2 along specific white matter tracts. In *Proceedings of the International Society Magnetic Resonance in Medicine*, volume 14, page 2744, 2006.

B. Kastler, D. Vetter, Z. Patay, and P. Germain. *Comprendre l'IRM. Manuel d'auto-apprentissage*. Masson, 2001.

S. Keihaninejad, H. Zhang, N. Ryan, I. Malone, C. Frost, M. Cardoso, M. Modat, J. Thornton, D. Cash, S. Ourselin, and N. Fox. White matter tract changes in mild-to-moderate alzheimer's disease revealed by tensor-based registration analyses of diffusion tensor imaging. *Alzheimer's & Dementia*, 8(4, Supplement):P31 – P32, 2012. ISSN 1552-5260. doi: http://dx.doi.org/10.1016/j.jalz.2012.05.079. URL http://www.sciencedirect.com/science/article/pii/S1552526012002117. Alzheimer's Association International Conference 2012 Alzheimer's Association International Conference 2012.

M. A. Koch and J. Finsterbusch. Double wave vector diffusion weighting in the human corticospinal tract in vivo. In *Proceedings of the International Society Magnetic Resonance in Medicine 19*, 2011.

M. E. Komlosh, E. Ozarslan, M. J. Lizak, F. Horkay, V. Schram, N. Shemesh, Y. Cohen, and P. J. Basser. Pore diameter mapping using double pulsed-field gradient mri and its validation using a novel glass capillary array phantom. *J Magn Reson*, 208(1):128–35, 2011. ISSN 1096-0856. URL http://www.biomedsearch.com/nih/Pore-diameter-mapping-using-double/21084204.html.

B. Kreher, I. Mader, and V. Kiselev. Gibbs tracking: A novel approach for the reconstruction of neuronal pathways. *Magnetic Resonance in Medicine*, 60(4):953–963, 2008. ISSN 1522-2594. doi: 10.1002/mrm.21749. URL http://dx.doi.org/10.1002/mrm.21749.

P. C. Lauterbur. Image formation by induced local interactions: Examples employing nuclear magnetic resonance. *Nature*, (5394):190–191, 1973. doi: 10.1038/242190a0. URL http://www.nature.com/nature/journal/v242/n5394/full/242190a0.html.

D. Le Bihan. The 'wet mind': water and functional neuroimaging. *Physics in Medicine and Biology*, 52, 2007.

D. Le Bihan, R. Turner, P. Douek, and D. Patronas. Diffusion mr imaging: clinical applications. *American Journal of Roentgenology*, 159(3):591–599, 1992.

D. Le Bihan, C. Poupon, A. Amadon, and F. Lethimonnier. Artifacts and pitfalls in diffusion mri. *Journal of Magnetic Resonance Imaging*, 24(3):478–488, 2006. ISSN 1522-2586. doi: 10.1002/jmri.20683. URL http://dx.doi.org/10.1002/jmri.20683.

D. Lebihan and E. Breton. Imagerie de Diffusion In Vivo par Résonance Magnétique Nucléaire. *XXX CR Académie des Sciences de Paris*, 301:1109–1112, 1985.

A. Lebois, B. Schmitt, D. Duclap, F. Poupon, and C. Poupon. A novel diffusion weighted arbitrary spin echo pulse sequence to customize diffusion gradient shapes. In *Proceedings of the European Society Magnetic Resonance in Medicine and Biology*, 2012.

A. Lebois, D. Duclap, B. Schmitt, C. Dos Santos, P. Guevara, H. Zhang, D. Le Bihan, J.-F. Mangin, and C. Poupon. Towards probabilistic atlases of the t1/t2 relaxation times from the connect/archi database. In *Proceedings of the International Society Magnetic Resonance in Medicine*, 2013a.

A. Lebois, C.-H. Yeh, , D. Le Bihan, J.-F. Mangin, C.-P. Lin, and C. Poupon. Cell diameter mapping : Gaussian phase distribution approximation of the diffusion signal attenuation using a two pool thick layer sphere model. In *Proceedings of the International Society Magnetic Resonance in Medicine Workshop : Diffusion as a probe of neural tissue microstructure*, 2013b.

A. Lebois, C.-H. Yeh, , D. Le Bihan, J.-F. Mangin, C.-P. Lin, and C. Poupon. Axon diameter mapping : Gaussian phase distribution approximation of the diffusion signal attenuation using a two pool thick layer cylinder model. In *Proceedings of the International Society Magnetic Resonance in Medicine Workshop : Diffusion as a probe of neural tissue microstructure*, 2013c.

A. Lebois, C.-H. Yeh, , D. Le Bihan, J.-F. Mangin, C.-P. Lin, and C. Poupon. On the use of the two pool model to improve axon radius estimation. In *Proceedings of the International Society Magnetic Resonance in Medicine*, 2014.

C. Lee, E. H. Baker, and D. M. Thomasson. Normal regional t1 and t2 relaxation times of the brain at 3t. In *Proceedings of the International Society Magnetic Resonance in Medicine*, volume 14, page 959, 2006.

C. Liu, R. Bammer, and M. E. Moseley. Generalized diffusion tensor imaging (gdti): A method for characterizing and imaging diffusion anisotropy caused by non-gaussian diffusion. *Israel Journal of Chemistry*, 43(1-2):145–154, 2003. ISSN 1869-5868. doi: 10.1560/HB5H-6XBR-1AW1-LNX9. URL http://dx.doi.org/10.1560/HB5H-6XBR-1AW1-LNX9.

M. Liu, Z. Chen, C. Beaulieu, and D. W. Gross. Disrupted anatomic white matter network in left mesial temporal lobe epilepsy. *Epilepsia*, 55(5):674–682, 2014. ISSN 1528-1167. doi: 10.1111/epi.12581. URL http://dx.doi.org/10.1111/epi.12581.

J. Mangin, C. Poupon, C. Clark, D. Lebihan, and I. Bloch. Eddy-current distortion correction and robust tensor estimation for mr diffusion imaging. In *in Medical Image Computing and Computer-Assisted Intervention - MICCAI '01*, pages 186–194. Springer Verlag, 2001.

P. Mansfield. Multi-planar image formation using nmr spin echoes. *Journal of Physics C: Solid State Physics*, 10(3):L55, 1977. URL http://stacks.iop.org/0022-3719/10/i=3/a=004.

Marrakchi-Kacem. *Connectivit 'e anatomique des noyaux gris centraux : d 'eveloppements m 'ethodologiques et application aux troubles moteurs*. PhD thesis, University of Paris Sud, France, 2011.

J. A. McNab, T. Witzel, H. Bhat, B. Keil, J. Cohen-Adad, M. D. Tisdall, and L. L. Wald. In vivo human brain measurements of axon diameter distributions in the corpus callosum using 300 mt/m maximum gradient strengths.

P. P. Mitra. Multiple wave-vector extensions of the nmr pulsed-field-gradient spin-echo diffusion measurement. *Phys. Rev. B*, 51: 15074–15078, Jun 1995. doi: 10.1103/PhysRevB.51.15074. URL http://link.aps.org/doi/10.1103/PhysRevB.51.15074.

D. M. Morris, K. V. Embleton, and G. J. Parker. Probabilistic fibre tracking: Differentiation of connections from chance events. *NeuroImage*, 42(4):1329 – 1339, 2008. ISSN 1053-8119. doi: http://dx.doi.org/10.1016/j.neuroimage.2008.06.012. URL http://www.sciencedirect.com/science/article/pii/S1053811908007301.

M. Moseley, J. Mintorovitch, Y. Cohen, H. Asgari, N. Derugin, D. Norman, and J. Kucharczyk. Early detection of ischemic injury: Comparison of spectroscopy, diffusion-, t2-, and magnetic susceptibility-weighted mri in cats. In H.-J. Reulen, A. Baethmann, J. Fenstermacher, A. Marmarou, and M. Spatz, editors, *Brain Edema VIII*, volume 51 of *Acta Neurochirurgica*, pages 207–209. Springer Vienna, 1990. ISBN 978-3-7091-9117-0. doi: 10.1007/978-3-7091-9115-6_70. URL http://dx.doi.org/10.1007/978-3-7091-9115-6_70.

J. Mårtensson, M. Nilsson, F. Ståhlberg, P. Sundgren, C. Nilsson, D. Westen, E.-M. Larsson, and J. Lätt. Spatial analysis of diffusion tensor tractography statistics along the inferior fronto-occipital fasciculus with application in progressive supranuclear palsy. *Magnetic Resonance Materials in Physics, Biology and Medicine*, 26(6):527–537, 2013. ISSN 0968-5243. doi: 10.1007/s10334-013-0368-5. URL http://dx.doi.org/10.1007/s10334-013-0368-5.

C. H. Neuman. Spin echo of spins diffusing in a bounded medium. *The Journal of Chemical Physics*, 60(11):4508–4511, 1974. doi: http://dx.doi.org/10.1063/1.1680931. URL http://scitation.aip.org/content/aip/journal/jcp/60/11/10.1063/1.1680931.

T. Niendorf, R. M. Dijkhuizen, D. G. Norris, M. van Lookeren Campagne, and K. Nicolay. Biexponential diffusion attenuation in various states of brain tissue: Implications for diffusion-weighted imaging. *Magnetic Resonance in Medicine*, 36(6):847–857, 1996. ISSN 1522-2594. doi: 10.1002/mrm.1910360607. URL http://dx.doi.org/10.1002/mrm.1910360607.

D. S. Novikov and V. G. Kiselev. Surface-to-volume ratio with oscillating gradients. *Journal of Magnetic Resonance*, 210(1):141 – 145, 2011. ISSN 1090-7807. doi: http://dx.doi.org/10.1016/j.jmr.2011.02.011. URL http://www.sciencedirect.com/science/article/pii/S1090780711000723.

L. J. O'Donnell, C.-F. Westin, and A. J. Golby. Tract-based morphometry for white matter group analysis. *NeuroImage*, 45(3):832 – 844, 2009. ISSN 1053-8119. doi: http://dx.doi.org/10.1016/j.neuroimage.2008.12.023.

E. Ozarslan and P. J. Basser. Microscopic anisotropy revealed by NMR double pulsed field gradient experiments with arbitrary timing parameters. *The Journal of chemical physics*, 128(15), Apr. 2008. ISSN 0021-9606. doi: 10.1063/1.2905765. URL http://dx.doi.org/10.1063/1.2905765.

E. Özarslan, T. M. Shepherd, B. C. Vemuri, S. J. Blackband, and T. H. Mareci. Resolution of complex tissue microarchitecture using the diffusion orientation transform (dot). *NeuroImage*, 31(3):1086 – 1103, 2006. ISSN 1053-8119. doi: http://dx.doi.org/10.1016/j.neuroimage.2006.01.024. URL http://www.sciencedirect.com/science/article/pii/S1053811906000656.

E. Panagiotaki, T. Schneider, B. Siow, M. G. Hall, M. F. Lythgoe, and D. C. Alexander. Compartment models of the diffusion {MR} signal in brain white matter: A taxonomy and comparison. *NeuroImage*, 59(3):2241 – 2254, 2012. ISSN 1053-8119. doi: http://dx.doi.org/10.1016/j.neuroimage.2011.09.081. URL http://www.sciencedirect.com/science/article/pii/S1053811911011566.

G. Parker and D. Alexander. Probabilistic monte carlo based mapping of cerebral connections utilising whole-brain crossing fibre information. In C. Taylor and J. Noble, editors, *Information Processing in Medical Imaging*, volume 2732 of *Lecture Notes in Computer Science*, pages 684–695. Springer Berlin Heidelberg, 2003. ISBN 978-3-540-40560-3. doi: 10.1007/978-3-540-45087-0_57. URL http://dx.doi.org/10.1007/978-3-540-45087-0_57.

M. Perrin, C. Poupon, Y. Cointepas, B. Rieul, N. Golestani, C. Pallier, D. Rivière, A. Constantinesco, D. Bihan, and J.-F. Mangin. Fiber tracking in q-ball fields using regularized particle trajectories. In G. Christensen and M. Sonka, editors, *Information Processing in Medical Imaging*, volume 3565 of *Lecture Notes in Computer Science*, pages 52–63. Springer Berlin Heidelberg, 2005a. ISBN 978-3-540-26545-0. doi: 10.1007/11505730_5.

M. Perrin, C. Poupon, Y. Cointepas, B. Rieul, N. Golestani, C. Pallier, D. Rivière, A. Constantinesco, D. L. Bihan, J. f. Mangin, and C. H. Strasbourg. Fiber tracking

in q-ball fields using regularized particle trajectories. In *Proc. of IPMI*, pages 52–63, 2005b.

C. Poupon. *Détection des faisceaux de fibres de la substance blanche pour l'étude de la connectivité anatomique cérébrale*. PhD thesis, Ecole Nationale Supérieure des Télécommunications, Paris , France, Dec. 1999.

C. Poupon, B. Rieul, I. Kezele, M. Perrin, F. Poupon, and J.-F. Mangin. New diffusion phantoms dedicated to the study and validation of high-angular-resolution diffusion imaging (hardi) models. *Magnetic Resonance in Medicine*, 60(6):1276–1283, 2008. ISSN 1522-2594. doi: 10.1002/mrm.21789. URL http://dx.doi.org/10.1002/mrm.21789.

C. Poupon, J. Dubois, L. Marrakchi, V. Brion, J.-F. Mangin, and F. Poupon. Real-time epi t1, t2 and t2* mapping at 3t. In *Proceedings of the International Society Magnetic Resonance in Medicine*, volume 18, page 4983, 2010.

W. S. Price. Pulsed-field gradient nuclear magnetic resonance as a tool for studying translational diffusion, part 1: Basic theory. *Magn. Reson.: Educ. J.*, 9(5):299–336, Aug. 1997. ISSN 1043-7347. doi: 10.1002/(SICI)1099-0534(1997)9:5⟨299::AID-CMR2⟩3.3.CO;2-2. URL http://dx.doi.org/10.1002/(SICI)1099-0534(1997)9:5<299::AID-CMR2>3.3.CO;2-2.

K. P. Pruessmann, M. Weiger, M. B. Scheidegger, and P. Boesiger. Sense: Sensitivity encoding for fast mri. *Magnetic Resonance in Medicine*, 42(5):952–962, 1999. ISSN 1522-2594. doi: 10.1002/(SICI)1522-2594(199911)42:5⟨952::AID-MRM16⟩3.0.CO;2-S. URL http://dx.doi.org/10.1002/(SICI)1522-2594(199911)42:5<952::AID-MRM16>3.0.CO;2-S.

E. M. Purcell, H. C. Torrey, and R. V. Pound. Resonance absorption by nuclear magnetic moments in a solid. *Phys. Rev.*, 69:37–38, Jan 1946. doi: 10.1103/PhysRev.69.37. URL http://link.aps.org/doi/10.1103/PhysRev.69.37.

J. D. Quirk, G. L. Bretthorst, T. Q. Duong, A. Z. Snyder, C. S. Springer, J. J. Ackerman, and J. J. Neil. Equilibrium water exchange between the intra- and extracellular spaces of mammalian brain. *Magnetic Resonance in Medicine*, 50(3):493–499, 2003. ISSN 1522-2594. doi: 10.1002/mrm.10565. URL http://dx.doi.org/10.1002/mrm.10565.

D. Raffelt, J.-D. Tournier, J. Fripp, S. Crozier, A. Connelly, and O. Salvado. Symmetric diffeomorphic registration of fibre orientation distributions. *NeuroImage*, 56(3):1171 – 1180, 2011. ISSN 1053-8119. doi: http://dx.doi.org/10.1016/j.neuroimage.2011.02.014. URL http://www.sciencedirect.com/science/article/pii/S1053811911001534.

T. Reese, O. Heid, R. Weisskoff, and V. Wedeen. Reduction of eddy-current-induced distortion in diffusion mri using a twice-refocused spin echo. *Magnetic Resonance in Medicine*, 49(1):177–182, 2003. ISSN 1522-2594. doi: 10.1002/mrm.10308. URL http://dx.doi.org/10.1002/mrm.10308.

D. Reich, S. Smith, C. Jones, K. Zackowski, P. Van Zijl, P. Calabresi, and S. Mori. Quantitative characterization of the corticospinal tract at 3t. *American Journal of Neuroradiology*, 27(10):2168–2178, 2006.

M. Reisert, I. Mader, C. Anastasopoulos, M. Weigel, S. Schnell, and V. Kiselev. Global fiber reconstruction becomes practical. *NeuroImage*, 54(2):955 – 962, 2011. ISSN 1053-8119. doi: http://dx.doi.org/10.1016/j.neuroimage.2010.09.016. URL http://www.sciencedirect.com/science/article/pii/S1053811910011973.

S. Rice. Mathematical analysis of random noise - and appendixes. Technical report, Bell Telephone Labs Inc. New York, 1952.

D. Rivière, J. Mangin, D. Papadopoulos-Orfanos, J.-M. Martinez, V. Frouin, and J. Régis. Automatic recognition of cortical sulci of the human brain using a congregation of neural networks. *Medical Image Analysis*, 6(2):77 – 92, 2002. ISSN 1361-8415. doi: http://dx.doi.org/10.1016/S1361-8415(02)00052-X.

W. D. Rooney, G. Johnson, X. Li, E. R. Cohen, S.-G. Kim, K. Ugurbil, and C. S. Springer. Magnetic field and tissue dependencies of human brain longitudinal 1h2o relaxation in vivo. *Magnetic Resonance in Medicine*, 57(2):308–318, 2007. ISSN 1522-2594. doi: 10.1002/mrm.21122. URL http://dx.doi.org/10.1002/mrm.21122.

H. E. Rorschach, C. Lin, and C. F. Hazlewood. Diffusion of water in biological tissues. *Scanning Microscopy Supplement*, 5(S1-S9), 1991.

B. Russell-Schulz, C. Laule, D. K. B. Li, and A. MacKay. What causes the hyperintense t2-weighting and increased short t2 signal in the cortico-spinal tract? *Magnetic Resonance Imaging*, 31:329–335, April 2013.

J. V. Sehy, J. J. Ackerman, and J. J. Neil. Evidence that both fast and slow water adc components arise from intracellular space. *Magnetic Resonance in Medicine*, 48(5):765–770, 2002. ISSN 1522-2594. doi: 10.1002/mrm.10301. URL http://dx.doi.org/10.1002/mrm.10301.

R. Seizeur, E. Magro, S. Prima, N. Wiest-Daesslé, C. Maumet, and X. Morandi. Corticospinal tract asymmetry and handedness in right- and left-handers by diffusion tensor tractography. *Surgical and Radiologic Anatomy*, pages 1–14, 2013. ISSN 0930-1038. doi: 10.1007/s00276-013-1156-7.

P. N. Sen. Time-dependent diffusion coefficient as a probe of geometry. *Concepts in Magnetic Resonance Part A*, 23A(1):1–21, 2004. ISSN 1552-5023. doi: 10.1002/cmr.a.20017. URL http://dx.doi.org/10.1002/cmr.a.20017.

P. N. Sen and P. J. Basser. A model for diffusion in white matter in the brain. *Biophysical Journal*, 89(5):2927 – 2938, 2005.

D. P. Shelton. Collective molecular rotation in water and other simple liquids. *Chemical Physics Letters*, 325(5–6):513 – 516, 2000. ISSN 0009-2614. doi: http://dx.doi.org/10.1016/S0009-2614(00)00734-X. URL http://www.sciencedirect.com/science/article/pii/S000926140000734X.

N. Shemesh, E. Özarslan, P. J. Basser, and Y. Cohen. Measuring small compartmental dimensions with low-q angular double-pgse nmr: The effect of experimental parameters on signal decay. *Journal of Magnetic Resonance*, 198(1):15 – 23, 2009. ISSN 1090-7807. doi: http://dx.doi.org/10.1016/j.jmr.2009.01.004. URL http://www.sciencedirect.com/science/article/pii/S1090780709000081.

B. Siow, I. Drobnjak, A. Chatterjee, M. F. Lythgoe, and D. C. Alexander. Estimation of pore size in a microstructure phantom using the optimised gradient waveform diffusion weighted {NMR} sequence. *Journal of Magnetic Resonance*, 214(0):51 – 60, 2012. ISSN 1090-7807. doi: http://dx.doi.org/10.1016/j.jmr.2011.10.004. URL http://www.sciencedirect.com/science/article/pii/S1090780711003806.

B. Siow, I. Drobnjak, A. Ianus, I. Christie, M. Lythgoe, and D. Alexander. Axon radius estimation with oscillating gradient spin echo (ogse) diffusion mri. *The Open-Access Journal for the Basic Principles of Diffusion Theory, Experiment and Application*, 18: 1–6, 2013.

E. Sorolla, J. Mosig, and M. Mattes. Algorithm to calculate a large number of roots of the cross-product of bessel functions. *Antennas and Propagation, IEEE Transactions on*, 61(4):2180–2187, April 2013. ISSN 0018-926X. doi: 10.1109/TAP.2012.2231929.

S. N. Sotiropoulos, T. E. Behrens, and S. Jbabdi. Ball and rackets: Inferring fiber fanning from diffusion-weighted {MRI}. *NeuroImage*, 60(2):1412 – 1425, 2012. ISSN 1053-8119. doi: http://dx.doi.org/10.1016/j.neuroimage.2012.01.056. URL http://www.sciencedirect.com/science/article/pii/S1053811912000730.

G. J. Stanisz. Diffusion mr in biological systems: Tissue compartments and exchange. *Israel Journal of Chemistry*, 43(1-2):33–44, 2003. ISSN 1869-5868. doi: 10.1560/E0WU-7FFH-31M6-VLYT. URL http://dx.doi.org/10.1560/E0WU-7FFH-31M6-VLYT.

G. J. Stanisz, G. A. Wright, R. M. Henkelman, and A. Szafer. An analytical model of restricted diffusion in bovine optic nerve. *Magnetic Resonance in Medicine*, 37(1):103–111, 1997. ISSN 1522-2594. doi: 10.1002/mrm.1910370115. URL http://dx.doi.org/10.1002/mrm.1910370115.

E. O. Stejskal and J. E. Tanner. Spin diffusion measurements: Spin echoes in the presence of a time dependent field gradient. *The Journal of Chemical Physics*, 42(1):288–292, 1965a. doi: http://dx.doi.org/10.1063/1.1695690. URL http://scitation.aip.org/content/aip/journal/jcp/42/1/10.1063/1.1695690.

E. O. Stejskal and J. E. Tanner. Spin diffusion measurements: Spin echoes in the presence of a time dependent field gradient. *The Journal of Chemical Physics*, 42(1):288–292, 1965b. doi: http://dx.doi.org/10.1063/1.1695690. URL http://scitation.aip.org/content/aip/journal/jcp/42/1/10.1063/1.1695690.

V. Stevenson, G. Parker, G. Barker, K. Birnie, P. Tofts, D. Miller, and A. Thompson. Variations in t1 and t2 relaxation times of normal appearing white matter and lesions in multiple sclerosis. *Journal of the neurological sciences*, 178:81–87, 2000.

I. V. Stiopkin, C. Weeraman, P. A. Pieniazek, F. Y. Shalhout, J. L. Skinner, and A. V. Benderskii. Hydrogen bonding at the water surface revealed by isotopic dilution spectroscopy. *Nature*, 474(7350):192–5, 2011. ISSN 1476-4687. URL http://www.biomedsearch.com/nih/Hydrogen-bonding-at-water-surface/21654801.html.

H. C. Torrey. Bloch equations with diffusion terms. *Phys. Rev.*, 104:563–565, Nov 1956. doi: 10.1103/PhysRev.104.563. URL http://link.aps.org/doi/10.1103/PhysRev.104.563.

J.-D. Tournier, F. Calamante, D. G. Gadian, and A. Connelly. Direct estimation of the fiber orientation density function from diffusion-weighted {MRI} data using spherical deconvolution. *NeuroImage*, 23(3):1176 – 1185, 2004. ISSN 1053-8119. doi: http://dx.doi.org/10.1016/j.neuroimage.2004.07.037. URL http://www.sciencedirect.com/science/article/pii/S1053811904004100.

J.-D. Tournier, F. Calamante, and A. Connelly. Robust determination of the fibre orientation distribution in diffusion mri: Non-negativity constrained super-resolved spherical deconvolution. *NeuroImage*, 35(4):1459 – 1472, 2007. ISSN 1053-8119. doi: http://dx.doi.org/10.1016/j.neuroimage.2007.02.016. URL http://www.sciencedirect.com/science/article/pii/S1053811907001243.

D. S. Tuch. *Diffusion MRI of complex tissue structure*. PhD thesis, Massachusetts Institute of Technology, Cambridge, MA, Jan. 2002.

D. S. Tuch. Q-ball imaging. *Magnetic Resonance in Medicine*, 52(6): 1358–1372, 2004. ISSN 1522-2594. doi: 10.1002/mrm.20279. URL http://dx.doi.org/10.1002/mrm.20279.

D. S. Tuch, T. G. Reese, M. R. Wiegell, N. Makris, J. W. Belliveau, and V. J. Wedeen. High angular resolution diffusion imaging reveals intravoxel white matter fiber heterogeneity. *Magn. Reson. Med.*, 48(4):577–582, 2002. URL http://www3.interscience.wiley.com/cgi-bin/fulltext/98518419/HTMLSTART.

P. Van Gelderen, D. DesPres, P. van Zijl, and C. Moonen. Evaluation of restricted diffusion in cylinders. phosphocreatine in rabbit leg muscle. *J.Magn.Reson B*, 103: 255–260, 1994.

F. Wang, Z. Sun, L. Cui, X. Du, X. Wang, H. Zhang, Z. Cong, N. Hong, and D. Zhang. Anterior cingulum abnormalities in male patients with schizophrenia determined through diffusion tensor imaging. *Am J Psychiatry*, 161(3):573–5, 2004. ISSN 0002-953X.

Y. Wang, A. Gupta, Z. Liu, H. Zhang, M. L. Escolar, J. H. Gilmore, S. Gouttard, P. Fillard, E. Maltbie, G. Gerig, and M. Styner. {DTI} registration in atlas based fiber analysis of infantile krabbe disease. *NeuroImage*, 55(4):1577 – 1586, 2011. ISSN 1053-8119. doi: http://dx.doi.org/10.1016/j.neuroimage.2011.01.038. URL http://www.sciencedirect.com/science/article/pii/S1053811911000735.

J. P. Wansapura, S. K. Holland, R. S. Dunn, and W. S. Ball. Nmr relaxation times in the human brain at 3.0 tesla. *Journal of Magnetic Resonance Imaging*, 9(4):531–538, 1999. ISSN 1522-2586. doi: 10.1002/(SICI)1522-2586(199904)9:4⟨531::AID-JMRI4⟩3.0.CO;2-L. URL http://dx.doi.org/10.1002/(SICI)1522-2586(199904)9:4<531::AID-JMRI4>3.0.CO;2-L.

V. Wedeen, T. Reese, D. Tuch, M. Weigel, J.-G. Dou, R. Weiskoff, and D. Chessler. Mapping fiber orientation spectra in cerebral white matter with fourier-transform diffusion mri. In *Proceedings of the International Society Magnetic Resonance in Medicine 8*, 2000.

R. Westerhausen, R. J. Huster, F. Kreuder, W. Wittling, and E. Schweiger. Corticospinal tract asymmetries at the level of the internal capsule: Is there an association with handedness? *NeuroImage*, 37(2):379 – 386, 2007. ISSN 1053-8119. doi: http://dx.doi.org/10.1016/j.neuroimage.2007.05.047.

S. D. Wolff and R. S. Balaban. Magnetization transfer contrast (mtc) and tissue water proton relaxation in vivo. *Magnetic Resonance in Medicine*, 10

(1):135–144, 1989. ISSN 1522-2594. doi: 10.1002/mrm.1910100113. URL http://dx.doi.org/10.1002/mrm.1910100113.

J. Xu, M. D. Does, and J. C. Gore. Quantitative characterization of tissue microstructure with temporal diffusion spectroscopy. *Journal of Magnetic Resonance*, 200(2):189 – 197, 2009. ISSN 1090-7807. doi: http://dx.doi.org/10.1016/j.jmr.2009.06.022. URL http://www.sciencedirect.com/science/article/pii/S109078070900189X.

X. H. Xu and E. S. Yeung. Long-range electrostatic trapping of single-protein molecules at a liquid-solid interface. *Science*, 281(5383):1650–3, 1998. ISSN 0036-8075. URL http://www.biomedsearch.com/nih/Long-range-electrostatic-trapping-single/9733506.ht

P.-T. Yap, Y. Chen, H. An, Y. Yang, J. H. Gilmore, W. Lin, and D. Shen. Sphere: {SPherical} harmonic elastic {REgistration} of {HARDI} data. *NeuroImage*, 55(2):545 – 556, 2011. ISSN 1053-8119. doi: http://dx.doi.org/10.1016/j.neuroimage.2010.12.015. URL http://www.sciencedirect.com/science/article/pii/S1053811910015971.

J. D. Yeatman, R. F. Dougherty, N. J. Myall, B. A. Wandell, and H. M. Feldman. Tract profiles of white matter properties: Automating fiber-tract quantification, 2012.

C. Yeh, B. Schmitt, D. Le Bihan, J. Li-Schlittgen, C. Lin, and P. C. Diffusion microscopist simulator: A general monte carlo simulation system for diffusion magnetic resonance imaging. *PLoS ONE*, 8(10), 2013.

H. Zhang, P. A. Yushkevich, D. C. Alexander, and J. C. Gee. Deformable registration of diffusion tensor {MR} images with explicit orientation optimization. *Medical Image Analysis*, 10(5):764 – 785, 2006. ISSN 1361-8415. doi: http://dx.doi.org/10.1016/j.media.2006.06.004. ¡ce:title¿The Eighth International Conference on Medical Imaging and Computer Assisted Intervention – {MICCAI} 2005¡/ce:title¿ ¡xocs:full-name¿The Eighth International Conference on Medical Imaging and Computer Assisted Intervention – {MICCAI} 2005¡/xocs:full-name¿.

H. Zhang, S. P. Awate, S. R. Das, J. H. Woo, E. R. Melhem, J. C. Gee, and P. A. Yushkevich. A tract-specific framework for white matter morphometry combining macroscopic and microscopic tract features. *Medical Image Analysis*, 14(5):666 – 673, 2010. ISSN 1361-8415. doi: http://dx.doi.org/10.1016/j.media.2010.05.002. Special Issue on the 12th International Conference on Medical Image Computing and Computer-Assisted Intervention (MICCAI) 2009.

H. Zhang, P. L. Hubbard, G. P. J.M., and D. C. Alexander. Axon diameter mapping in the presence of orientation dispersion with diffusion mri. *NeuroImage*, 56(3):1301–1315, 2011a.

H. Zhang, P. L. Hubbard, G. J. Parker, and D. C. Alexander. Axon diameter mapping in the presence of orientation dispersion with diffusion {MRI}. *NeuroImage*, 56(3):1301 – 1315, 2011b. ISSN 1053-8119. doi: http://dx.doi.org/10.1016/j.neuroimage.2011.01.084. URL http://www.sciencedirect.com/science/article/pii/S1053811911001376.

H. Zhang, T. Schneider, C. A. Wheeler-Kingshott, and D. C. Alexander. Noddi: Practical in vivo neurite orientation dispersion and density imaging of the human brain. *NeuroImage*, 61(4):1000 – 1016, 2012. ISSN 1053-8119. doi: http://dx.doi.org/10.1016/j.neuroimage.2012.03.072. URL http://www.sciencedirect.com/science/article/pii/S1053811912003539.

W. Zhou and W. Laidlaw. Measurement of axon radii distribution in orientationally unknown tissue using angular double-pulsed gradient spin echo (double-pgse) nmr, 2011.

E. Özarslan. Compartment shape anisotropy (csa) revealed by double pulsed field gradient {MR}. *Journal of Magnetic Resonance*, 199(1):56 – 67, 2009. ISSN 1090-7807. doi: http://dx.doi.org/10.1016/j.jmr.2009.04.002. URL http://www.sciencedirect.com/science/article/pii/S1090780709000962.

E. Özarslan and P. J. Basser. Mr diffusion–"diffraction" phenomenon in multi-pulse-field-gradient experiments. *Journal of Magnetic Resonance*, 188(2):285 – 294, 2007. ISSN 1090-7807. doi: http://dx.doi.org/10.1016/j.jmr.2007.08.002. URL http://www.sciencedirect.com/science/article/pii/S1090780707002364.